

**CHARMONIUM PRODUCTION AND
DETECTION IN HIGH ENERGY NUCLEAR
COLLISIONS AT FAIR**

By

Partha Pratim Bhaduri

Enrollment No. PHYS04201104001

Variable Energy Cyclotron Centre, Kolkata

A thesis submitted to the

Board of Studies in Physical Sciences

In partial fulfillment of requirements

for the Degree of

DOCTOR OF PHILOSOPHY

of

HOMI BHABHA NATIONAL INSTITUTE



November, 2014

Homi Bhabha National Institute¹

Recommendations of the Viva Voce Committee

As members of the Viva Voce Committee, we certify that we have read the dissertation prepared by Partha Pratim Bhaduri entitled "CHARMONIUM PRODUCTION AND DETECTION IN HIGH ENERGY NUCLEAR COLLISIONS AT FAIR" and recommend that it may be accepted as fulfilling the thesis requirement for the award of Degree of Doctor of Philosophy.

Chairman - Prof. S. R. Banerjee



Date: 03/11/2014

Guide / Convener - Prof. Subhasis Chattopadhyay



Date: 3/11/14

Co-guide - <Name> (if any)

Date:

Member 1 - Prof. Asis K. Chaudhuri



Date: 3/11/2014

Member 2- Prof. Prashant Shukla



Date: 3/11/14

Member N - Prof. Manjit Kaur
(External)



Date: 3.11.2014

Final approval and acceptance of this thesis is contingent upon the candidate's submission of the final copies of the thesis to HBNI.

I/We hereby certify that I/we have read this thesis prepared under my/our direction and recommend that it may be accepted as fulfilling the thesis requirement.

Date:

3/11/14

Place:

Kolkata

<Signature>

Co-guide (if applicable)

<Signature>

Guide

¹ This page is to be included only for final submission after successful completion of viva voce.

STATEMENT BY AUTHOR

This dissertation has been submitted in partial fulfillment of requirements for an advanced degree at Homi Bhabha National Institute (HBNI) and is deposited in the Library to be made available to borrowers under rules of the HBNI.

Brief quotations from this dissertation are allowable without special permission, provided that accurate acknowledgement of source is made. Requests for permission for extended quotation from or reproduction of this manuscript in whole or in part may be granted by the Competent Authority of HBNI when in his or her judgement the proposed use of the material is in the interests of scholarship. In all other instances, however, permission must be obtained from the author.

Partha Pratim Bhaduri

DECLARATION

I, hereby declare that the investigation presented in the thesis has been carried out by me. The work is original and has not been submitted earlier as a whole or in part for a degree/diploma at this or any other Institution/University.

Partha Pratim Bhaduri

List of Publications arising from the thesis

Journal

1. “Participation in the compressed baryonic matter experiment at FAIR”
S. Chattopadhyay, Y. P. Viyogi, **Partha Pratim Bhaduri** and A. K. Dubey
Current Science, **2011**, *100*, 682 - 689.
2. “ J/ψ production in proton induced collisions at FAIR”
Partha Pratim Bhaduri, A. K. Chaudhuri and S. Chattopadhyay
Phys. Rev. C., **2011**, *84*, 054914-1 - 054914-16.
3. “ J/ψ suppression in a dense baryonic medium”
Partha Pratim Bhaduri, A. K. Chaudhuri and S. Chattopadhyay
Phys. Rev. C., **2012**, *85*, 064911-1 - 0649211-5.
4. “Charmonium suppression in a baryon rich quark-gluon plasma”
Partha Pratim Bhaduri, A. K. Chaudhuri and S. Chattopadhyay
Phys. Rev. C., **2013**, *88*, 061902-1 - 061902-5 (Rapid Communication).
5. “Parton shadowing and J/ψ -to-Drell-Yan ratio in nuclear collisions at energies available at CERN-SPS and GSI-FAIR”
Partha Pratim Bhaduri, A. K. Chaudhuri and S. Chattopadhyay
Phys. Rev. C., **2014**, *89*, 044912-1 - 044912-8.

Chapters in books and lecture notes

1. “An Introduction to the Spectral Analysis of the QGP”
Partha Pratim Bhaduri, Prasad Hedge, Helmut Satz and Prithwish Tribedy
Lect. Notes. Phys., **2010**, *785*, 179-197; e-Print: arXiv:0812.3856 [hep-ph]

Conferences

1. “Development of a trigger algorithm for the measurement of rare probes in the CBM Experiment at FAIR”
Partha Pratim Bhaduri, S. Chattopadhyay, P. Ghosh and P. Tribedy
Proceedings of the DAE SYMPOSIUM ON NUCLEAR PHYSICS, **2008**, *53*, 739-740.
2. “Di-muon measurements with the CBM Experiment at FAIR”
Partha Pratim Bhaduri, S. Chattopadhyay *et. al.*
Proceedings of the DAE SYMPOSIUM ON NUCLEAR PHYSICS, **2008**, *53*, 631-632.
3. “Development of a trigger algorithm for the measurement of rare probes in the CBM Experiment at FAIR”
Partha Pratim Bhaduri, S. Chattopadhyay, A. Prakash, B. K. Singh
Proceedings of the DAE SYMPOSIUM ON NUCLEAR PHYSICS, **2010**, *55*, 640-641.
4. “Geometry optimization for dimuon detection system in CBM Experiment at FAIR”
A. Prakash, **Partha Pratim Bhaduri**, S. Chattopadhyay, B. K. Singh
Proceedings of the DAE SYMPOSIUM ON NUCLEAR PHYSICS, **2010**, *55*, 641-642.
5. “Sector layout of muon chambers (MUCH): first results”
Subhasis Chattopadhyay, **Partha Pratim Bhaduri**, Zubayer Ahammed, and Arun Prakash
Proceedings of the DAE SYMPOSIUM ON NUCLEAR PHYSICS, **2011**, *56*, 998-999.
6. “Di-muon measurements with the CBM experiment at FAIR”
A. Kiseleva, **Partha Pratim Bhaduri** *et. al.*
Proceedings of Quark Matter 2008
Indian J. Phys., **2011**, *85*, 211-216.

7. “Di-muon measurements in CBM experiment at FAIR”
A. Prakash, **Partha Pratim Bhaduri**, S. Chattopadhyay, A. Dubey , B.K. Singh
Proceedings of ICPAQGP-2010
Nucl. Phys. A, **2011**, *862*, 493-496; e-Print: arXiv:1102.0882 [nucl-ex].
8. “Response simulation of the GEM detector for the CBM experiment”
Partha Pratim Bhaduri and Subhasis Chattopadhyay
Proceedings of the DAE SYMPOSIUM ON NUCLEAR PHYSICS, **2012**, *57*, 848-849.
9. “Charmonium suppression in a baryon-rich quark-gluon plasma”
Partha Pratim Bhaduri, A. K. Chaudhuri and Subhasis Chattopadhyay
Proceedings of the DAE SYMPOSIUM ON NUCLEAR PHYSICS, **2013**, *58*, 696-697.
10. “Parton shadowing and J/ψ suppression in nuclear collisions at SPS energy regime”
Partha Pratim Bhaduri, A. K. Chaudhuri and Subhasis Chattopadhyay
Proceedings of the DAE SYMPOSIUM ON NUCLEAR PHYSICS, **2013**, *58*, 718-719.

Technical Reports

1. “Development of a trigger algorithm for the measurement of charmonia with the CBM experiment at FAIR”
Partha Pratim Bhaduri and S. Chattopadhyay
CBM Progress Report 2009, Darmstadt 2010, p. 68
2. “Much layout optimization for SIS-100”
Partha Pratim Bhaduri, A. Prakash and S. Chattopadhyay
CBM Progress Report 2010, Darmstadt 2011, p. 34
3. “Segmentation optimization for the MUCH detector”
A. Prakash, **Partha Pratim Bhaduri**, B. K. Singh and S. Chattopadhyay
CBM Progress Report 2010, Darmstadt 2011, p. 35

4. “Sector layout of Muon Chambers (MUCH): First results”
S. Chattopadhyay, **Partha Pratim Bhaduri**, Z. Ahammed and A. Prakash
CBM Progress Report 2010, Darmstadt 2011, p. 43
5. “ J/ψ detection via di-muon channel in the CBM experiment at FAIR”
Partha Pratim Bhaduri, Subhasis Chattopadhyay
CBM Progress Report 2013, Darmstadt 2014, p. 117
6. “Estimation of J/ψ multiplicity in the CBM Experiment at FAIR”
Partha Pratim Bhaduri, Subhasis Chattopadhyay
CBM Progress Report 2013, Darmstadt 2014, p. 126

Dedicated to my family

Mr. Plaban Kumar Bhaduri

Mrs. Ruby Bhaduri

Mrs. Kaushani Banerjee Bhaduri

Master Parthib Bhaduri

ACKNOWLEDGEMENTS

This thesis is an outcome of my last six years work at Variable Energy Cyclotron Centre, Kolkata. There are many individuals who have had tremendous contributions in helping me to reach this milestone. I take this opportunity to thank all of them. First and foremost, I would like to express my sincere gratitude to my thesis supervisor Prof. Subhasis Chattopadhyay, for his constant guidance, support, encouragement and careful supervision throughout the research period. He has always been open for scientific conversations and given me absolute freedom to choose the research topic and to pursue it in the direction I want. The second person without whom this work will not take its present shape is Prof. Asis Kumar Chaudhuri. All the phenomenological works that I have done for this thesis has only become possible because of his kind support, guidance and inspiration. I am grateful to Prof. D. K. Srivastava (Director, V.E.C.C.) for giving us immense support for doing research in nuclear physics and for his fantastic teaching in various SERC schools. I would also like to thank Prof. Jane Alam (Dean, Physical Sciences, HBNI) and Prof. Sourav Sarkar who taught me the physics of quark-gluon plasma. I thank Prof. Premomoy Ghosh for his useful lessons on detector simulation. The two persons who deserve a special mention in my research career as well as in my life are Dr. Jhilam Sadhukhan and Dr. Jajati Kesari Nayak. I would also like to thank Prof. Tapan Kumar Nayak for his valuable suggestions and encouragements. I have learnt a lot from the countless discussions I have, over the past several years, with my dear friends Mr. Vineet Kumar, Mr. Prithwish Tribedy and Mr. Sanjib Muhuri. I express my sincere gratitude to Prof. Ajit Mohan Srivastava, Prof. Raghava Varma, Prof. Ajit Mohanty, Prof. Prashant Shukla, Prof. R. S. Bhalerao and Mr. G. S. N. Murthy for their teachings, valuable suggestions and encouragements. It was indeed a great opportunity to work with Prof. Helmut Satz and Prof. Sourendu Gupta and I express my deepest gratitude to both of them. I thank Prof. Buddhadeb Bhattacharjee, Dr. Rupa Chatterjee, Dr. Siddharth K. Prasad, Dr. Tapasi Ghosh, Dr. Saikat Biswas, Dr. Mriganka M. Mandal, Dr. Sayantan Sharma, Dr. Debasish Banerjee, Dr. Victor Roy, Dr. Santosh Das, Dr. Anand K. Dubey, Dr. Zubayer Ahamed, Dr. Susant K.

Pal, Mr. R. Singaraju, Mr. Vikas Singhal, Mr. J. Saini, Dr. Nihar Ranjan Sahoo, Dr. Sudipan De, Dr. Arun Prakash, Dr. Prakhar Garg, Dr. Prashant K. Srivastava, Mr. Kalyan Dey, Mr. Subikash Chowdhury, Mr. Sumit Basu, Mr. Debojit Sarkar, Mr. Arindam Roy and Mr. Shabir Bhat for the illuminating discussions at various occasions, on different aspects of heavy ion physics. Over past one year I have learnt a lot from Dr. Purnendu Chakraborty. I also express my deepest respect to my higher secondary teacher Mr. Gautam Bhattacharya because of whom I had dared to pursue a career in physics. I recall the inspiration I got from my ex-colleague Mr. Mihir Ranjan Dutta Majumder, who motivated me by his selfless devotion towards scientific research. It has been a pleasure to work in the CBM collaboration and I thank all the members of the CBM community. Particularly I would like to acknowledge Prof. Peter Senger, Dr. Volker Friese, Dr. Florian Uhlig, Dr. Iouri Vassiliev, Dr. Evgeny Kryshen, Dr. Sudip Chatterji, Dr. Andrey Lebedev, Dr. Anna Kisseleva, Dr. Tetyana Galatyuk for their suggestions and guidance. The VECC grid-computing facility and GSI computing facility is gratefully acknowledged.

The list will be incomplete without the mention of the members of my beautiful family. I express my deepest gratitude to my grand parents late Jatindra Mohan Bhaduri and late Bina Rani Bhaduri and Mr. Birendra Kumar Talukder and late Renuka Talukder for their love and blessings. I thank my parents Mr. Plaban Kumar Bhaduri and Mrs. Ruby Bhaduri for their unconditional love, support and blessings. It is because of their hard work and sacrifice that I am able reach the culminating point of my academic career. My humble regards and thanks also go to my in-laws Mr. Kalyan Bandyopadhyay, Mrs. Indrani Bandyopadhyay, Mr. Partha Sarathi Mukherjee and Mrs. Illora Mukherjee for their support, blessings and encouragement during my PhD period. My little son Parthib has been my constant source of delightment and joy. The person who has been with me at all the times giving me her love, encouragement and constant support in all the ups and downs over the last five years is my wife Kaushani. With the completion of the thesis I have fulfilled the long cherished dream of my family.

Contents

Synopsis	13
List of Figures	17
List of Tables	21
1 Relativistic Heavy Ion Collisions and Quark-Gluon Plasma	22
1.1 Introduction	22
1.2 Historical background	28
1.3 Phase Diagram of Strongly Interacting Matter	30
1.4 Relativistic Heavy Ion Collisions	31
1.4.1 Space-time picture of relativistic heavy ion collisions	32
1.4.2 Theoretical formulation	34
1.4.3 Relativistic heavy ion Experiments	37
1.5 Signatures of QGP in Relativistic Nuclear Collisions	39
1.5.1 Global Observables	40
1.5.2 Strangeness enhancement	41
1.5.3 Electromagnetic radiations: Photons and Dilepton	42
1.5.4 Quarkonium suppression	48
1.5.5 Jet Quenching	50
1.5.6 Anisotropic Flow	51
1.5.7 Correlation and Fluctuations	52
1.6 Motivation and Organization of the thesis	53
2 The Compressed Baryonic Matter Experiment	56
2.1 Introduction	56
2.2 The Facility for Antiproton and Ion Research (FAIR)	59
2.3 Diagnostic probes of the high-density fireball	60
2.4 CBM physics cases and observables	62
2.5 The Compressed Baryonic Matter (CBM) experimental setup	64
2.6 Dilepton measurements at FAIR	71
2.7 Running scenario	73
3 An overview of Charmonium production in nuclear collisions	74
3.1 Introduction	74
3.2 Charmonium spectroscopy in vacuum	76
3.3 Charmonium dissociation in a thermal medium	77
3.3.1 Potential models for charmonium dissociation	78
3.3.2 Lattice studies of charmonium correlator	81
3.4 Overview of Charmonium Production in Nuclear Collisions	83

3.4.1	Charmonium Production in Hadronic Collisions	84
3.4.2	Charmonium production in $p + A$ collisions	92
3.4.3	Charmonium production in heavy ion collisions	99
3.5	Summary	114
4	Charmonium production in nuclear collisions within QVZ approach	116
4.1	Introduction	116
4.2	QVZ model and J/ψ production in nuclear collisions	117
4.3	The Drell-Yan process	128
4.4	Summary	130
5	Analysis of inclusive J/ψ production cross sections using QVZ model	131
5.1	Introduction	131
5.2	Analysis of the existing data at different fixed target energies	132
5.2.1	Proton-proton ($p + p$) interactions	132
5.2.2	Proton-nucleus ($p + A$) interactions	135
5.2.3	Nucleus-Nucleus collisions	146
5.3	Summary	156
6	Prediction of J/ψ production and suppression at FAIR energy collisions	159
6.1	Introduction	159
6.2	J/ψ production in proton-induced collisions	160
6.2.1	$p + p$ collisions	160
6.2.2	$p + A$ collisions	161
6.3	J/ψ production in heavy-ion collisions	167
6.4	Anomalous J/ψ suppression at FAIR	172
6.4.1	J/ψ suppression in a dynamically evolving medium	177
6.5	Summary	203
7	J/ψ detection at FAIR	206
7.1	Introduction	206
7.2	Conceptual layout of the CBM muon detection system	207
7.3	Simulation procedure of MUCH	220
7.3.1	Simulation framework	220
7.3.2	Detector segmentation, digitization, clustering and hit formation	222
7.3.3	MUCH Track Reconstruction	229
7.3.4	Muon identification and analysis	233
7.4	Physics performance studies	237
7.4.1	Input	237
7.4.2	Results for SIS-300 collisions	245
7.4.3	Results for SIS-100 collisions	250
7.4.4	Estimation of J/ψ collection rate	251
7.5	Data rate on chambers	254
7.6	Trigger simulation with MUCH	256
7.7	Summary	258
8	Summary and discussions	260
	References	268

SYNOPSIS

The Compressed Baryonic Matter (CBM) experiment is a dedicated relativistic heavy-ion collision experiment to investigate the properties of the highly compressed baryonic matter as it is anticipated to be produced at the Facility for Anti-proton and Ion Research (FAIR) accelerator center, in GSI, Darmstadt, Germany. The primary objective of the CBM experiment is the exploration of the QCD phase diagram in the region of moderate temperatures but very high net baryon densities, by colliding heavy-ions in the beam energy range $E_b = 10 - 35$ A GeV. Model calculations performed so far, based on transport as well as hydrodynamical equations, indicate that for central ($b = 0$) collisions highest net baryon densities $\rho_B = (6 - 12)\rho_0$ (where $\rho_0 = 0.17/\text{fm}^3$ is the density of normal nuclear matter) are expected to be produced at the center of the collision zone. The experiment will thus provide us the unique possibility to create and investigate extremely dense nuclear matter in the laboratory through measurements of bulk as well as rare probes. Such measurements will enable us to have deeper insight on some of the fundamental issues of QCD like hadronic properties in dense nuclear matter which might be connected to the chiral phase transition, de-confinement phase transition from hadronic to partonic matter driven by high baryon densities and the nuclear equation of state (EOS) at high baryon densities. The approach is complementary to the ongoing scientific activities at RHIC (BNL) and LHC (CERN), which concentrate on the regions of high temperatures and vanishingly small net baryon densities of the QCD phase diagram.

Charmonium production has been identified as one of the most promising diagnostic probes to indicate the occurrence of the de-confinement phase transition. Due to their relatively large masses charmonia are predominantly produced in the early stages of collision. In the CBM experiment, different charmonium states ($J/\psi, \psi'$) will be identified via their decay into lepton pairs. At FAIR energies ($E_b = 10 - 35$ A GeV) charmonium production will occur close to their kinematic thresholds and thus production cross sections will be extremely small. The main experimental challenge is thus the measurement of these rare probes in an environment typical for heavy-ion collisions. Till date no data exist on charmonium production in heavy-ion collisions below 158 A GeV. At FAIR,

such measurements will be enabled for the first time in the world, mainly with the help of unprecedented high heavy-ion beam intensities ($\sim 10^9/\text{sec}$) which would result in high interaction rates (10 MHz) and detectors with very high rate capabilities and radiation hardness. A muon detection system is under development by VECC and its collaborators, for identification of charmonia through their di-muon decay channel.

Work presented in this thesis is based on the study of the production and detection of J/ψ mesons in the FAIR energy domain. The thesis is broadly divided into two parts. The first part deals with the development of phenomenological models to calculate the J/ψ production in low energy nuclear collisions relevant for FAIR. The second part gives a detailed description of the design simulation of a muon detector system for identification of J/ψ mesons in the di-muon channel. A brief discussion on each of these topics and the main results are given below.

1. J/ψ production in high energy nuclear collisions at FAIR

(a) The QVZ model and charmonium production in nuclear collisions

Under this topic, we have developed a model framework to calculate J/ψ production cross sections in $p + p$, $p + A$ and $A + A$ collisions. For this purpose, we have adopted and adapted the originally proposed two component QVZ model. The model describes the J/ψ production in hadronic collisions as a factorisable two step process: (i) the production of the $c\bar{c}$ pairs which involves a short time scale and can be accounted by perturbative QCD (pQCD) ii) formation of the J/ψ mesons from the initially produced $c\bar{c}$ pairs which is non-perturbative in nature and can be conveniently parametrized through a function $F(q^2)$ where $F(q^2)$ represents the transition probability of a color averaged $c\bar{c}$ pair to form a J/ψ meson. Following the existing schemes of color neutralization, different functional forms of $F(q^2)$ (q^2 being the relative 4 momentum between c and \bar{c}) is constructed. Out of them two form namely the Gaussian form ($F^{(G)}(q^2)$) and power-law ($F^{(P)}(q^2)$) respectively bears the essential features of color-singlet model (CSM) and color octet model (COM) of hadronization.

In case of $p+A$ and $A+A$ collisions the model takes into account for both initial state modification of the parton distribution functions inside the nucleus (nPDF) and final state dissociation of the produced pre-resonant $c\bar{c}$ pairs with the prevailing cold nuclear

matter. The dissociation is modeled in an unconventional way through the multiple scattering of the $c\bar{c}$ pairs inside the nuclear medium which in turn increases the energy of the $c\bar{c}$ pair. Dissociation is characterized through a parameter e defined as the energy absorbed by the $c\bar{c}$ pair per unit path length of the medium.

(b) Analysis of the existing SPS data on J/ψ production cross sections within the QVZ approach

Before applying to the FAIR energy domain, the QVZ model described earlier is calibrated using the existing data on J/ψ production in $p + A$ and $A + A$ collisions at SPS energies. All the model parameters and their kinematic dependence are fixed from the comparison with the p+A data at different collision energies. Both the ratio of absolute cross sections as well as J/ψ to Drell-Yan ratio are analyzed. In case of $A + A$ collisions we have analyzed both the centrality dependence of nuclear modification factor R_{AA} and J/ψ to Drell-Yan ratio as available for Pb+Pb and In+In collisions measured by NA50 and NA60 Collaborations of CERN-SPS respectively. Our analysis shows that all the data, for both $p + A$ and $A + A$ collisions available from SPS, can be reasonably described by cold nuclear matter effects alone. The model does not allow for any additional suppression mechanism to set in even for most central Pb+Pb collisions.

(c) Prediction at FAIR energies

The QVZ model calibrated using the SPS data is extrapolated to the FAIR energy domain to predict J/ψ suppression at FAIR energies. Model calculations indicate a larger CNM suppression at FAIR energies. It has also observed that data to be collected from p+A collisions alone can help in experimental distinction of different mechanisms of color neutralization scenarios. In case of heavy-ion (Au+Au) collisions a detailed study of different nuclear effects indicate that almost 90% of the initially produced J/ψ are suppressed to the CNM effects, out of which around 15 – 20% can be attributed to the shadowing effects of nuclear parton densities whereas rest comes from nuclear dissociation of the pre-resonant $c\bar{c}$ pairs.

In addition, we have also studied the effects of Debye screening in a hot baryonic plasma anticipated to be produced at FAIR energy nuclear collisions. Debye screening is implemented through a variant of threshold model with the in-medium screening mass

deciding the fate of a particular charmonium state implanted inside the QGP medium. Comparison of different time scales related to the formation of the J/ψ mesons and that of the plasma indicates that J/ψ mesons will be formed earlier to the formation of the plasma. Hence J/ψ mesons which survive the cold matter suppressions will be subject to the plasma screening effects. Realistic space-time evolution of the plasma suggests that Debye screening would induce a rather weak dissociation effect ($\sim 15 - 20\%$) compared to the nuclear dissociations.

2. J/ψ detection in di-muon channel at FAIR energy collisions

Under this topic a detailed description has been given about the design simulation of a muon detection system for the CBM experiment. The muon system is aimed to be used for identification of J/ψ mesons produced at FAIR energies through their di-muon decay channel. The main objective of such simulation is to find out an optimized version of the muon detection system which would make the above measurements feasible. The novel feature of the muon system for CBM compared to other High Energy Physics (HEP) experiments previous or planned is that the total absorber is sliced and sensitive detectors (high resolution gas chambers) are placed in between the absorbers to facilitate the momentum dependent track identification. The chapter depicts about the optimization of the muon system in terms of absorbers material, their thickness, placement, number of chambers in between the absorbers etc. The optimized muon system is used to study the feasibility of J/ψ measurements in central Au+Au collisions at beam energy of 25 A GeV. The feasibility studies are performed within CBMROOT simulation framework which allows for full event simulation and reconstruction. Signal (J/ψ decaying to di-muon) and background particles are generated by event generators PLUTO and UrQMD-3.3 respectively. The primary particles are transported through the CBM detector set-up for muon identification using GEANT3. The produced primary and secondary tracks are reconstructed using realistic reconstruction packages. Reconstructed muon tracks are selected for analysis applying different track quality cuts including length of the track and track χ^2 . The reconstructed di-muon invariant mass spectra shows a clearly identifiable peak over the continuum which comprises the combinatorial background coming from the weak decay of pions and kaons.

List of Figures

1.1	Phase diagram of water	23
1.2	QGP formation under extreme conditions	24
1.3	Schematic view of QCD phase diagram	30
1.4	Space-time picture of the relativistic heavy ion collision	33
2.1	Layout of the Facility for Antiproton and Ion Research (FAIR)	58
2.2	Baryon density as function of elapsed time for central Au+Au collisions .	59
2.3	Three stages of a U+U collision at 23 AGeV calculated with UrQMD. . .	61
2.4	Particle yields in 25 A GeV Au+Au collisions	61
2.5	The CBM experimental setup	65
3.1	Lattice QCD results for charmonium dissociation	81
3.2	Perturbative production of $c\bar{c}$ pairs	84
3.3	J/ψ formation in nuclear collisions	91
3.4	x_F dependence of $\alpha_{J/\psi}$	95
3.5	Sequential charmonium suppression	101
3.6	J/ψ suppression at SPS	109
3.7	J/ψ suppression at RHIC	111
3.8	J/ψ suppression at LHC	113
4.1	The MSTW 2008 LO PDF	120
4.2	Energy dependence of the sub threshold $c\bar{c}$ production cross section . . .	122
4.3	Relative contributions of different partonic sub-processes to $c\bar{c}$ production	122
4.4	EPS09 LO nPDF inside Au nucleus	125
5.1	Model results on the excitation of J/ψ production in $p + p$ collisions . . .	135

5.2	J/ψ production cross section at mid rapidity in $p + p$ collisions	136
5.3	J/ψ cross section ratios for $p + A$ collisions	137
5.4	Energy evolution of the mid-rapidity shadowing functions	141
5.5	Nuclear path length dependence of the shadowing factor at SPS	142
5.6	J/ψ rapidity distributions in $p + A$ collisions	144
5.7	J/ψ -to-Drell-Yan ratio in $p + A$ collisions at SPS	145
5.8	Effect of projectile shadowing on ψ -to-Drell-Yan ratio	147
5.9	J/ψ production in Pb+Pb collisions at SPS	151
5.10	Effect of local shadowing corrections on J/ψ production	153
5.11	Impact parameter dependence of the shadowing factors at SPS	154
5.12	Rapidity dependence of the shadowing factor	155
5.13	Results on centrality dependence of $R_{AA}^{J/\psi}$ at SPS	156
6.1	J/ψ rapidity distributions in $p + p$ collisions at FAIR	160
6.2	Dependence of ε^2 on beam energy	161
6.3	J/ψ production in $p + A$ collisions at FAIR	162
6.4	Nuclear path length dependence of the shadowing factors at FAIR	164
6.5	Rapidity distribution of J/ψ mesons in $p + A$ collisions at FAIR	165
6.6	Energy dependence of the mass distribution of the initial $c\bar{c}$ pairs	167
6.7	Energy dependence of mass distribution of the final $c\bar{c}$ pairs	168
6.8	Impact parameter dependence of the shadowing functions at FAIR	170
6.9	Centrality dependence of J/ψ production in Au+Au collisions at FAIR	171
6.10	Anomalous J/ψ suppression at FAIR	173
6.11	Different scenarios for anomalous J/ψ suppression	175
6.12	Time evolution of the central densities	179
6.13	J/ψ survival within threshold scenario	182
6.14	Radial dependence of J/ψ escape time and plasma life time	186
6.15	Local T and μ_B in the transverse plasma plane	188
6.16	Time evolution plasma T and μ_B	189
6.17	μ_B dependence of the J/ψ dissociation temperature	190
6.18	Anomalous charmonium suppression in an expanding baryon dense plasma	191

6.19	Sensitivity of J/ψ suppression to the plasma EOS	192
6.20	Dependence of J/ψ survival on the QGP formation time	193
6.21	Effect of transverse dynamics on J/ψ survival probability	194
6.22	Dependence of the plasma parameters for expansion dynamics	195
6.23	Variation of the plasma life time on the medium expansion dynamics . . .	196
6.24	Effect of non-perturbative corrections in the Debye screening mass	197
6.25	Centrality dependence of $R_{AA}^{J/\psi}$ in heavy ion collisions at FAIR	198
6.26	Charmonium suppression in a high baryon density hadronic medium . . .	200
6.27	Hadronic dissociation of J/ψ for various expansion dynamics	201
6.28	Anomalous J/ψ suppression: plasma screening versus hadronic dissociation	202
6.29	Model predictions for inclusive J/ψ suppression at FAIR	202
7.1	Particle absorption pattern inside iron	209
7.2	Particle production inside iron	211
7.3	Effect of iron absorber in generation of fake tracks	212
7.4	Sensitivity of the combinatorial background to the absorber thickness . .	213
7.5	Comparison of iron and carbon as absorber materials:I	213
7.6	Comparison of iron and carbon as absorber materials:II	214
7.7	Optimization of air gaps	215
7.8	Radial distribution of hit densities	216
7.9	Schematic view of MUCH SIS-300 configuration	217
7.10	Schematic view of MUCH SIS-100 configuration	218
7.11	Layout of the trapezoidal sectors	220
7.12	Simulation chain in MUCH	221
7.13	Segmentation of muon chambers	223
7.14	Signal generation inside GEM	224
7.15	Digitization in MUCH	226
7.16	Charge deposition by the incident tracks	227
7.17	Response of MIP	227
7.18	Hit finding in MUCH	229
7.19	Clusterization in MUCH	229

7.20	Tracks in central Au+Au collisions	230
7.21	Performance of different tracking algorithms	233
7.22	Distribution of various kinematic variables of J/ψ generated by PLUTO .	239
7.23	Kinematic distributions of signal muons	240
7.24	Centrality dependence of J/ψ multiplicity	243
7.25	Reconstructed invariant mass spectra of J/ψ mesons	244
7.26	Acceptance plot for reconstructed J/ψ mesons	245
7.27	Particle composition of the reconstructed background	246
7.28	Momentum distribution of the reconstructed signals	247
7.29	Phase space distribution of the reconstructed J/ψ mesons	249
7.30	Reconstructed invariant mass spectra of J/ψ in minimum bias collisions .	250
7.31	J/ψ identification in p+Au collisions	250
7.32	Radial distribution of the density of the MUCH points	254
7.33	Radial distribution of occupancy for different MUCH stations	255
7.34	Schematic of the trigger logic	257

List of Tables

1.1	Relativistic heavy ion collision facilities	38
2.1	Experiments to explore super-dense nuclear matter	56
3.1	Quarkonium spectroscopy in vacuum	75
3.2	J/ψ production in elementary collisions	89
3.3	$\alpha_{J/\psi}$ from different experiments	93
3.4	Energy dependence of σ_{abs} for different charmonium states	97
5.1	Experiments reporting J/ψ production cross sections in $p + N$ collisions .	132
5.2	Optimized parameters of the QVZ model	134
5.3	Different fixed target experiments measuring J/ψ production in $p + A$ collisions	136
5.4	Optimum values of ε^2 at different beam energies	138
5.5	Comparison between ε^2 values and the corresponding absorption cross sections	140
5.6	List of parameters for J/ψ rapidity distributions at SPS	146
6.1	Nuclear absorption cross sections of J/ψ at FAIR energies	163
6.2	List of parameters for J/ψ rapidity distributions at FAIR	166
7.1	Properties of hadron absorbers	210
7.2	J/ψ production cross sections in elementary collisions	242
7.3	Optimization of track selection cuts	245
7.4	J/ψ measurement by NA50 Collaboration	253
7.5	Characteristics of the trigger logic	258

Chapter 1

Relativistic Heavy Ion Collisions and Quark-Gluon Plasma

1.1 Introduction

Matter, in statistical physics, is defined as a system of many constituents in thermal equilibrium whose average properties are specified by a few global or macroscopic observables (eg : temperature, pressure, density etc.). For different values of these observables, the system may exhibit fundamentally different average properties, and so there exist different states of matter, with “phase” transitions occurring when the system changes from one state to the other. Often transitions from one phase to another are accompanied by drastic and abrupt changes in the physical properties of the material like its electrical resistivity, opacity, elastic properties among the others. Thermodynamic properties of any macroscopic system is most readily expressed in the form of a *phase diagram*, a graphical representation, in which different manifestations or phases of any substance occupy different regions of a plot whose axes are calibrated in terms of the external conditions or *control parameters*. Each point on the diagram corresponds to a stable thermodynamic state. The most familiar example is of course water whose phases are (partly) accessible to the everyday experience, as shown in Fig. 1.1. The control parameters in this case are temperature (T) and pressure (P) and the three regions correspond to the three phases of ice (solid), water (liquid) and steam (gas). The lines mark the

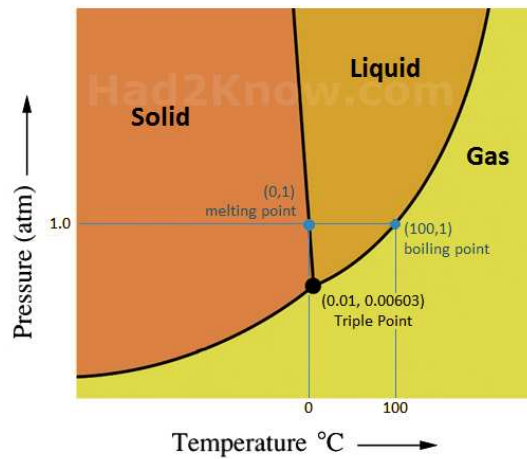


Figure 1.1: The phase diagram of water (H_2O) in the (P, T) plane. The diagram is taken from [1].

various coexistence curves $P(T)$ where two phases are in equilibrium; a phase transition such as melting or boiling is observed when moving along a path in the (T, P) plane which intersects such curves. Two special points in the diagram are the *triple point* where all three phases coexist, and the *critical point* where the meniscus separating liquid from vapor disappears, and the two fluid phases become indistinguishable. For $T < T_c$ the transition between liquid and vapor is *first-order*, implying discontinuities in entropy and volume respectively leading to non-vanishing latent heat and interface tension. This classification follows because entropy and volume are both first derivatives of the Gibbs free energy $G(T, P)$. At the critical point the transition becomes *second order*, which means that singularities instead occur in specific heat C_P and isothermal compressibility κ_T of the fluid, which are related to second derivatives of the free energy. Another interesting phenomenon is *critical opalescence*: the size of droplets of the liquid phase within the vapor (or *vice versa*) becomes comparable with the wavelength of visible light, implying large optical path differences between adjacent parallel rays of light and hence strong scattering – the system thus becomes opaque near the critical point. Just beyond the critical point, thermodynamic observables still vary very rapidly but continuously as one moves about the (T, P) plane due to the large values of C_P and κ_T ; this is known as a *crossover region*.

When sufficiently heated, water and for that matter any other substance, goes over into a new ionized state, a 'plasma', consisting of ions and free electrons. This transition

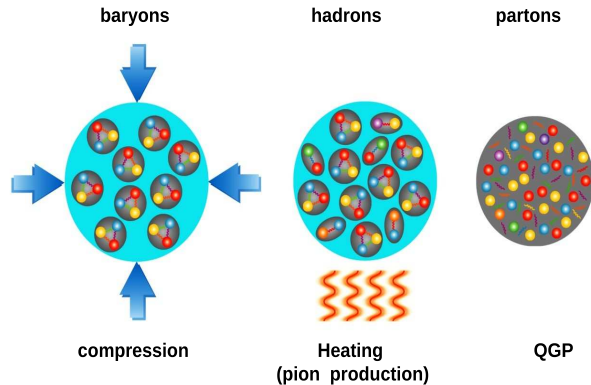


Figure 1.2: Schematic view of the QGP formation due to extreme compression and excessive heating.

is mediated by molecular or atomic collisions. It is continuous and hence not a true phase transition in the strict thermodynamic sense. A true phase transition is characterized by the singularity of the thermodynamic variables. Under certain conditions there may also be a true plasma phase transition [2]. On the other hand, the plasma exhibits new collective phenomena such as screening and 'plasma oscillations' [3]. Plasma states can also be induced by high compression, where electrons are delocalized from their orbitals and form a conducting 'degenerate' quantum plasma. In contrast to a hot plasma there exists in this case a true phase transition, the 'metal-insulator' transition [4, 5]. Some natural examples include white dwarfs, stars at the end of their evolution which are stabilized by the degeneracy pressure of free electrons [6, 7], that balances the inward gravitational pull and stabilizes them from further collapse.

Exploration of the different states of matter, their characterization and transitions among them has always been one of the most intriguing problems in physics research. Strongly interacting matter opens up a new window in these studies. Nuclear matter governed by strong interaction, one of the four fundamental forces in nature, is believed to have a rich phase structure. Ever since the discovery of the strong force and the multiple hadron production it may lead to, physicists are fascinated with the question of ultimate fate of the strongly interacting matter as it is heated to extremely high temperatures or compressed to extremely high densities [8, 9, 10, 11, 12]. In the Stan-

dard Model of particle physics the strong interaction is described in the framework of a relativistic quantum field theory called Quantum Chromodynamics (QCD), introduced in 1973 [13]. This relativistic field theory is formulated in close analogy to Quantum Electrodynamics (QED) as a gauge theory of massive fermionic matter fields interacting with massless bosonic gauge fields. In QCD, point-like quarks and gluons are the elementary degrees of freedom. Aside from the relativistic quantum numbers dictated by Lorentz invariance, quarks come in six 'flavors' (up, down, strange, charm, bottom, top). To obtain the correct quantum statistics for hadronic wave functions it turns out that quarks as well as gluons also have to carry 'color' as an additional quantum number [14, 15]. Unlike QED, where the photons do not carry any electric charge, gluons in QCD carry color charge. This gives rise to gluon self-interactions which in turn lead to the running of the QCD coupling constant $\alpha_s = g_s^2/4\pi$ with (space-time) distance or momentum transfer Q , such that α_s decreases logarithmically with the increase in Q (or reduction in the separation r) [16]. This phenomenon called **asymptotic freedom** simplifies the description of certain high energy processes and is the reason behind the success of perturbative QCD (pQCD). Conversely at large distances (or small Q), comparable to the size of the nucleon, the interaction between two quarks is strong. The amplification of the strong force with increasing distance is known as **infrared slavery**. In this sense the QCD vacuum is an 'anti-screening' medium in contrast to the QED vacuum, where the photon, although uncharged, can create virtual electron-positron pairs, causing partial screening of the charge of a test electron. Even though a mathematical proof is still missing, it is generally believed that the increase of the strong coupling constant for low values of Q is responsible for the permanent **confinement** of quarks and gluons inside the composite hadrons. Due to growing α_s toward small Q , the standard techniques of perturbative expansion breaks down and QCD enters the "strong" regime where "non-perturbative" phenomena occur. Phase transitions in strongly interacting matter occurs in the non-perturbative domain of QCD. Statistical QCD predicts that in the realm of very high temperature and/or net baryon density strongly interacting matter undergoes a transition from a color-confining hadronic phase to a plasma of deconfined colored quarks and gluons. The situation is schematically shown in Fig. 1.2

and can be understood at least qualitatively through following simple picture: normal nuclei or nuclear matter is made up of finite size nucleons ($r_N \sim 1$ fm) bound together by residual strong force, having density $\rho = \rho_0 = 0.16/\text{fm}^3$ and temperature $T = 0$. If we now start heating nuclear matter initially the thermal energy supplied to the system would increase the kinetic energy of the nucleons. At sufficiently high temperatures nuclei eventually dissolve into protons and neutrons (nucleons). At the same time light hadrons (preferentially pions) are created thermally, which increasingly fill the space between the nucleons. Because of their finite spatial extent ($r_\pi \sim 0.6$ fm) the pions and other thermally produced hadrons begin to overlap with each other and with the bags of the original nucleons such that a network of zones with quarks, antiquarks and gluons is formed. At a certain critical temperature T_c these zones fill the entire volume in a 'percolation' transition. We thus have a dense multi-quark environment where description of the system in terms of nucleonic or mesonic degrees of freedom is no longer possible. This new state of quark matter is the quark-gluon plasma (QGP). There is, however, a fundamental difference to ordinary electromagnetic plasmas in which the transition is caused by ionization and therefore gradual. Because of confinement there can be no liberation of quarks and radiation of gluons below the critical temperature. Thus a relatively sharp transition with $\Delta T/T_c \ll 1$ is expected. A similar picture emerges when matter is strongly compressed. In this case with increasing density nucleons start more and more overlapping with each other. At a critical number density $\rho_c \gg \rho_0$ a typical nucleonic volume would be occupied by several nucleons; a particular quark has no way to identify which of these had been its partners in a specific nucleon at some previous state of lower density. This will lead to a cold degenerate QGP consisting mostly of quarks. Since this deconfinement transition leads to a color-conducting state it is considered as the QCD counterpart of the insulator-conductor transition in atomic matter [17]. A further transition phenomenon, also expected from the behavior of atomic matter, is a shift in the effective constituent mass. At $T = 0$, in vacuum, quarks dress themselves with gluons to form the constituent quarks that make up hadrons. As a result, the bare quark mass $m_q \simeq 0$ is replaced by a constituent quark mass $M_q \sim 300$ MeV. In a hot and dense medium, this dressing melts and $M_q \rightarrow m_q$. Since the QCD

Lagrangian for $m_q = 0$ is chirally symmetric, $M_q \neq 0$ implies spontaneous chiral symmetry breaking. The melting $M_q \rightarrow 0$ thus corresponds to chiral phase transition leading to the restoration of chiral symmetry.

Presently the theoretical efforts of studying phase transitions and other non-perturbative aspects of QCD are mainly pursued in two directions. The first one is the development of various QCD inspired effective models with degrees of freedom appropriately adapted to specific problems. They are rather successful in describing the physics within their applicable energy range. For example in the low-energy regime of QCD, chiral perturbation theory was developed with hadrons, rather than quarks and gluons, as the effective degrees of freedom. The interaction term is dictated by the chiral symmetry, which is approximately respected by the original QCD Lagrangian. After the effective coupling constants are determined by fitting to experimental data, chiral perturbation theory gains predictive power for low energy hadronic reactions/decays. Another example is Non-Relativistic QCD, in which the heavy quarks are described by a Schrödinger field theory while the gluons and light quarks are modeled by the usual relativistic Lagrangian of QCD. The other approach is the only known way to solve the QCD equations in the region of strong coupling ($\alpha_s \sim 1$) from first principle calculations. The method is known as lattice QCD (lQCD) [18], where the QCD Lagrangian density is discretized on a discrete Euclidian space-time lattice. Here one makes use of the formal analogy between Feynman's path-integral formulation of a quantum field theory in imaginary time $\tau = it$ and the statistical mechanics of a system with temperature $T = 1/\tau$. With this method the partition function of the grand canonical ensemble, in the path integral formulation,

$$\mathcal{Z}(V, T, \mu_q) = \int \mathcal{D}[A, q] e^{-\int_0^{1/T} d\tau \int_V d^3x (\mathcal{L}_{\text{QCD}}^E - i\mu_q q^\dagger q)} \quad (1.1)$$

is evaluated stochastically via Monte Carlo sampling of field configurations, at least at vanishing μ_q . From the partition function, the thermodynamic state functions such as energy density and pressure can be determined, in the thermodynamic limit ($V, N \rightarrow$

$\infty; N/V = \text{const}$), using standard thermodynamic relations:

$$\varepsilon \equiv \frac{E}{V} = \frac{T^2}{V} \left(\frac{\partial \ln \mathcal{Z}}{\partial T} \right)_{V, \mu_q} + \mu_q \frac{N}{V}; \quad p = T \left(\frac{\partial \ln \mathcal{Z}}{\partial V} \right)_{V, \mu_q} \quad (1.2)$$

For matter with an equal number of baryons and anti-baryons i.e. for vanishing baryochemical potential $\mu_b = 3\mu_q$ one obtains in this way quantitative predictions for the temperature dependence of thermodynamic quantities [19]. These ab-initio numerical findings clearly show for $\mu_q = 0$, the existence of a 'cross over' QGP transition at $T_c \sim 154 \pm 9$ MeV. While at $\mu_q = 0$ the lattice results are relatively precise, the ab-initio evaluation of the phase boundary in the (T, μ_q) -plane poses major numerical difficulties. This is basically related to the Fermi-Dirac statistics of the quarks and is known in many-body physics as the 'fermion-sign problem'. For the integral (1.1) this implies that the integrand becomes an oscillatory function and, hence, Monte-Carlo sampling methods cease to work. New methods are being developed [20, 21, 22, 23] to go into the region of finite μ_q .

The study of the different states of strongly interacting matter is interesting not only from a purely academic point of view but it does have practical relevance. So far as natural occurrences are concerned our universe according to the Big Bang theory is believed to have passed through a very high temperature and vanishingly small net baryon density quark matter phase at the age of a few microseconds. Inside compact stars such as neutron star the temperature is far lower compared to the earlier case, but the high density makes it possible that the inside matter is in the color-conducting phase. Since the properties of quark matter are characterized by the strong interactions, new insights about the strong interaction is expected to be obtained by studying these novel states of matter.

1.2 Historical background

In 1951 Pomeranchuk [10] conjectured that hadrons have an intrinsic size, with a radius $r_h \simeq 1$ fm, and hence a hadron needs a space of volume $V_h \simeq (4\pi/3)r_h^3$ in order to exist. This suggests a limiting density $n_c = 1/V_h \simeq 0.24 \text{ fm}^{-3}$ of hadronic matter. Beyond

this point, hadrons overlap more and more, so that eventually they cannot be identified any more. Later in 1965 Hagedorn first addressed the question of the fate of matter at very high temperature in a seminal paper [12] which was subsequently elaborated by Frautschi [24]. The analysis was based on the (pre-QCD) statistical 'bootstrap model' in which strongly interacting particles (hadrons) were viewed as composite 'resonances' of lighter hadrons. A natural consequence of this model is the exponential growth in the density of mass states: $\rho(M_h) \propto M_h^{-5/2} e^{M_h/T_H}$. M_h denotes the hadron mass. This is well verified by summing up the hadronic states listed by the Particle Data Group. A fit to the data yields $T_H \sim 160 - 180$ MeV. All thermodynamic quantities diverge when $T = T_H$, which implies that matter cannot be heated beyond this limiting 'Hagedorn temperature'. The energy that is supplied is used entirely for the production of new particles. In the early and mid of 1970's it had gradually started becoming clear that hadrons are not elementary objects rather they are built from quarks and gluons and hence have substructure. However, the elementary building blocks of QCD, the quarks and gluons (carrying an extra quantum number called "color") have not been directly observed in experiments, although their fingerprints have been clearly identified in deep-inelastic collisions and jet production. The paradox of Hagedorn was taken up in 1975 by Cabibbo and Parisi [25] who noted that the quark-gluon substructure of hadrons opened the possibility for a phase transition to a new state of deconfined quark-gluon matter. Within this picture, the limiting temperature T_H is in reality close to or even coincides with the critical temperature for the phase transition between colorless finite size hadrons and colorful point like quarks and gluons. They demonstrated that the exponential mass spectrum of hadronic states is a feature of any hadronic system which undergoes a second order phase transition with critical temperature T_c , since thermodynamical quantities exhibit singularities at T_c . This is realized in models that include "quark containment" [25], so is in agreement with QCD principles. It is interesting to note that Ref. [25] contains the first sketch of a phase diagram of nuclear matter. In the same year Collins and Perry [26] demonstrated that asymptotically free QCD is also realized for large densities. However the question that remained was how to produce such exotic states of the strongly interacting matter in laboratory. Already in 1974, T. D. Lee in collaboration

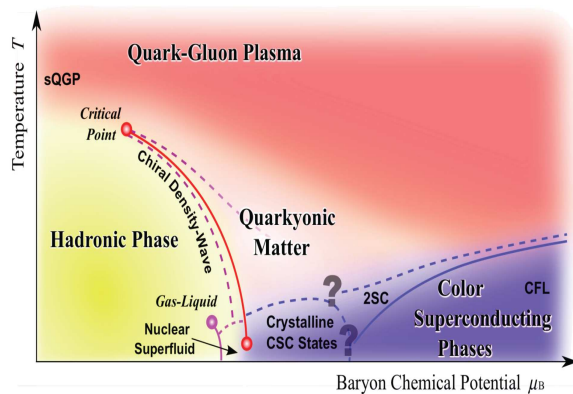


Figure 1.3: Schematic view of QCD phase diagram following current understanding, in terms of the baryon chemical potential μ_B and temperature T . Figure taken from Ref. [30].

with G. C. Wick, first proposed [27, 28] that in high energy heavy ion collisions one may possibly create the novel abnormal states of dense nuclear matter by distributing high energy or high nucleonic density over a large volume that could temporarily restore broken symmetries of physical vacuum. The term **quark-gluon plasma (QGP)** along with initial ideas about the space-time picture of hadronic collisions were first introduced by Shuryak [29] in 1978. QGP is now believed to be defined as: *A locally thermally equilibrated state of matter in which quarks and gluons are deconfined from hadrons, so that color degrees of freedom become manifest over nuclear rather than merely nucleonic volumes.*

1.3 Phase Diagram of Strongly Interacting Matter

Over past three decades substantial experimental and theoretical efforts worldwide are devoted to the exploration of the phase diagram of nuclear matter. As per contemporary wisdom, a sketch of the possible phase diagram of the strongly interacting matter as a function of the temperature T and the baryo-chemical potential μ_B including several partially speculative new phases and their boundaries is presented in Figure 1.3. For very low net baryon densities where the numbers of particles and anti-particles are approximately equal, QCD predicts that hadrons dissolve into quarks and gluons above

a temperature of about 160 MeV [31, 19]. The inverse process happened in the universe during the first few microseconds after the big bang: the quarks and gluons were confined into hadrons. In this region of the phase diagram the transition is expected to be a smooth crossover from partonic to hadronic matter [32]. Calculations suggest a critical endpoint at relatively large values of the baryon chemical potential [33]. Beyond this critical endpoint, for larger values of net baryon densities (and for lower temperatures), one expects a first order phase transition from hadronic to partonic matter with a phase coexistence region in between. A new phase of so called quarkyonic matter has been proposed to exist beyond the first order phase transition at large baryon chemical potentials and moderate temperatures [34]. This is an intermediate state in which baryons dissolve into quarks, but mesons remain as confined states. The compression of baryonic matter at low temperature could result in another type of transition. This would set in if an attractive interaction between quarks in the deconfined baryon-rich phase results in the formation of colored bosonic diquark pairs, the counterpart of Cooper pairs in QCD. At sufficiently low temperature, these diquarks can then condense to form a color superconductor. For a medium of quarks with color and flavor degrees of freedom, the diquark state can in fact consist of phases of different quantum number structures like CFL [35] phase where color degree of freedom couples strongly with flavor degree of freedom. The large degree of compression without heating, required for formation color superconductor presently seems to be impossible to achieve in the laboratory. However such high-density strongly interacting cold matter is expected to exist in the core of neutron stars, a few seconds after its birth in the supernova explosion. Heating will dissociate the diquark pairs and turn the color superconductor into a normal color conductor. The main goal of modern heavy ion experiments at intermediate energies is to shed more light on the very interesting region of high net baryon densities.

1.4 Relativistic Heavy Ion Collisions

Relativistic heavy ion collisions make it possible to study the properties of strongly interacting matter at energy densities far above those of normal nuclear matter. The idea

is that by accelerating heavy nuclei to very high speed and then colliding them a large amount of their kinetic energy is deposited into a small spatial region and converted to thermal energy resulting in extremely high temperature. In laboratory by colliding heavy ions at various energies one can produce nuclear matter over a range of temperatures and densities. Thus in principle the phase diagram of strongly interacting matter can be accessed experimentally in nucleus-nucleus collisions at relativistically high energies.

1.4.1 Space-time picture of relativistic heavy ion collisions

The large body of experimental and theoretical research conducted over the past decades at different experimental facilities like AGS, SPS, and RHIC has led to the following “standard model” of heavy ion collisions. The time evolution of a typical heavy ion collision at relativistic energies is understood to proceed through the following stages:

- **Initial state and pre-equilibrium** Two highly energetic lorentz-contracted nuclei travel along the light cone for $t < 0$ and they collide with each other, with an impact parameter b , at $t = 0$ at the origin ($z = 0$). Depending on the impact parameter, the two colliding nuclei overlap either partially in non-central collisions ($b > 0$) or fully in central ($b \simeq 0$) collision and dump a large fraction of their kinetic energy due inelastic collisions between the nucleons, inside a small volume in the centre of the collision zone. A large number of partons (quarks and gluons) are liberated from the high energy deposited in the overlap region of the two nuclei.
- **Thermalization:** These highly energetic partons interact among themselves with a characteristic mean free path much smaller compared to the size of the system. After sufficient reinteractions for $\tau_0=0.5-1\text{fm}/c$ the quarks and gluons undergo equilibration and a Quark-Gluon Plasma (QGP) is supposedly created. Driven by the pressure gradient the QGP expands and cools (for a duration of $\tau_{QGP} \sim 3-5\text{fm}/c$).
- **Hadronization and Freeze-out:** The hadronization then follows as the energy density falls below the critical value ($\epsilon_c \sim 1 \text{ GeV}/\text{fm}^3$) required for plasma formation by crossing the phase boundary. Further expansion occurs in the hadronic

study of the distributions of these particles which depending on their nature are emitted from the different stages of the evolution of the fireball. Whether any information on the phase transition can be gleaned from these investigations will be discussed below.

1.4.2 Theoretical formulation

Direct detection of free quarks and gluons is impossible due to the confining nature of QCD. It is thus utmost important to model the dynamical evolution of heavy ion reactions for getting insights about the interesting early stage of the reaction from the final state particle distributions and for a rigorous interpretation of the experimental observations. Theoretical models that have been developed to study the QGP production and its subsequent evolution in relativistic heavy ion collisions are based on Lorentz-covariant dynamical framework. They can be broadly classified into two categories: (i)relativistic transport models and (ii) relativistic hydrodynamics models. They represent two opposite limits in their underlying assumptions.

Models based on transport approach aims at the description of heavy ion reactions consistently from the initial state to the final state. They provide a microscopic description of the system in all stages of the collision on the basis of an effective solution of the relativistic Boltzmann equation [36]

$$p^\mu \cdot \partial_\mu f_i(x^\nu, p^\nu) = \mathcal{C}_i \quad . \quad (1.3)$$

This equation describes the time evolution of the phase space distribution functions $f_i(x^\nu, p^\nu)$, for particle species i and includes the full collision term on the right hand side. The advantage of such a microscopic description is that it is applicable to non-equilibrium situations and the full phase space information is available at all stages of the heavy ion reaction. However mostly the transport models are restricted to $2 \rightarrow n$ scattering processes to keep the calculation numerically tractable. The restriction to binary collisions assumes large mean free paths of the particles. However if the particle density increases in the system it becomes questionable if a restriction to two-particle interaction is still justified. Another lacuna of this approach is to find an appropriate

prescription to explain hadronization and the phase transition between the hadronic and the partonic phase on a microscopic level. Different transport based dynamical Monte-Carlo models are found in literature to simulate the relativistic heavy ion reactions over a broad energy range. They are mostly based on hadronic and string degrees of freedom. Some models are also available which additionally include partonic degrees of freedom in the initial stage of the collisions. Some of the typical transport based calculations are A Multi Phase Transport (AMPT) model [37], Ultra Relativistic Quantum Molecular Dynamics (UrQMD) [38] model, Hadron String Dynamics (HSD) [39] model, Parton Hadron String Dynamics model (PHSD) [40], Quark Gluon String Model (QGSM) etc.

Hydrodynamics, on the other hand, has been proposed many years ago as a tool for the description of the hot and dense stage of heavy ion reactions on a macroscopic level with a primary assumption of local thermal equilibrium of the produced system[41, 42, 43]. In this approach it is possible to model phase transitions explicitly because one of the major inputs to a hydrodynamic calculation is the equation of state (EoS). Ideal relativistic one fluid dynamics is based on the conservation of energy, momentum and the net baryon number current. For the hydrodynamical evolution local equilibrium is assumed and zero viscosity which corresponds to zero mean free path. The two conservation equations that govern the evolution are the energy-momentum conservation and net baryon density conservation for given initial conditions, i.e. spatial distributions of energy and net baryon number densities. The coordinate space is divided into small cells in which the distribution functions correspond to equilibrium distributions (Fermi or Bose distribution). The conservation equations read as [11, 44]

$$\partial_\mu T^{\mu\nu} = 0 \quad \text{and} \quad \partial_\mu N^\mu = 0, \quad (1.4)$$

where $T^{\mu\nu}$ is the energy-momentum tensor and N^μ is the baryon current. For an ideal fluid the energy-momentum tensor and the net baryon number current take the simple form

$$T^{\mu\nu} = (\epsilon_{\text{lrf}} + P) u^\mu u^\nu - P g^{\mu\nu} \quad \text{and} \quad N^\mu = \rho_{\text{lrf}} u^\mu \quad (1.5)$$

where ϵ_{lrf} , P and ρ_{lrf} are the local rest frame energy density, pressure and net baryon density, respectively. $u^\mu = \gamma(1, \vec{v})$ is the four velocity of the cell and $g^{\mu\nu} = \text{diag}(+, -, -, -)$ is the metric tensor. The local rest frame is defined as the frame where $T^{\mu\nu}$ has diagonal form, (i.e. all off-diagonal elements vanish). The four-velocity of the cells is calculated via the transformation into the local rest frame. In this macroscopic approach the propagated quantities are net baryon number and energy densities which can be translated into information about the temperature and chemical potential via the specific equation of state (EoS). Since the evolution is driven by pressure gradients and the pressure is determined via the EoS, the EoS is the essential ingredient for the hydrodynamical evolution. Thus, hydrodynamics is a good tool to describe collective behavior. Ideal hydrodynamics applies to systems with small mean free path, otherwise viscous effects have to be taken into account [11]. A general advantage of hydrodynamics is the feature to explicitly incorporate phase transitions by changing the EoS. The hydrodynamic description has gained importance over the last few years because the high elliptic flow values that have been observed at RHIC seem compatible with some ideal hydrodynamic predictions [45, 46, 47]. The initial conditions and freeze-out prescription are the boundary conditions for a hydrodynamic calculation and therefore a further crucial input. Thus, the hydrodynamic results depend strongly on the initial and final state prescription that is applied in the specific calculation. An obvious disadvantage of the hydrodynamic calculations are a priori assumption of local thermalization which prevents their use in the pre-equilibrium phase as well as in the late stage of the heavy ion reaction when the system gets too dilute to maintain equilibrium. A proper modeling of the hadronic rescatterings and resonance decays requires description in some non-equilibrium prescription like transport theory.

To get a more consistent picture of the whole dynamics of heavy ion reactions various so called microscopic plus macroscopic (micro+macro) hybrid approaches have been developed [48, 49, 50] during the last decade where a transport model is coupled to a hydrodynamic model such that non-equilibrium initial conditions are simulated by the transport approach and the intermediate hot and dense stage of the collision is described by hydrodynamical evolution. Subsequent freeze-out dynamics including the separation

of chemical and kinetic freeze-out and final state interactions like resonance decays and rescatterings are again accounted into the transport model.

1.4.3 Relativistic heavy ion Experiments

Till date the only laboratories providing sufficiently energetic nuclear beams are the Brookhaven National Laboratory (BNL) at Long Island, New York (USA) and the European Organization for Nuclear Research (CERN) in Geneva (Switzerland). Both began experimentation in 1986, using existing accelerators. BNL had the Alternating Gradient Synchrotron (AGS), designed for 30 GeV/c proton beams, CERN the Super Proton Synchrotron (SPS) for 450 GeV/c protons. The injectors available at that time allowed only the acceleration of nuclei containing equal numbers of protons and neutrons ($A=2Z$), so that the beams were restricted to light ions ($A \lesssim 40$). Both laboratories have in the meantime built new injectors, allowing the acceleration of arbitrarily heavy nuclei in AGS and SPS. The AGS program [51], carried out over a period of about 15 years by several experiments (E802/864,917 E810, E814/877, E864, E895). The SPS program has also been concluded. Compelling evidence for the production of a “New State of Matter”, has been claimed to be found in central Pb+Pb collisions [52] studied by seven experiments: WA80/98, NA35/49, NA38/50/60, NA44 NA45/CERES, WA97/NA57, and NA52. The currently running experimental facilities include the Relativistic Heavy Ion Collider (RHIC) at at Brookhaven National Laboratory (BNL) [53] and the Large Hadron Collider (LHC) at CERN [54]. A vigorous research program, started with the first data taking in 2001, is still on-going at RHIC with four experiments, BRAHMS, PHENIX, PHOBOS and STAR. Among them BRAHMS and PHOBOS have already stopped taking data whereas rest two are still running. The data collected at RHIC is believed to lead to the discovery that quark-gluon matter in the vicinity of the phase boundary behaves more like an ideal liquid, the so called strongly coupled quark-gluon plasma (sQGP) rather than a weakly-interacting plasma. The strongly coupled quark-gluon plasma is in many ways similar to certain kinds of conventional electromagnetic plasmas consisting of electrically charged particles (electrons, ions) which also exhibit liquid or even solid-like behavior. Strongly coupled systems are characterized by the

Table 1.1: Experimental facilities for high energy nuclear collisions which have already taken data. For each machine we have quoted the starting year of experimentation

Start Year	Machine	Type	Collision system	$\sqrt{s_{NN}}$ [GeV]
1986	BNL-AGS	Fixed Target	Si+Au	5
1986	CERN-SPS	Fixed Target	S+Pb, O+Pb	19
1992	BNL-AGS	Fixed Target	Au+Au	5
1994	CERN-SPS	Fixed Target	Pb+Pb	17
2000	BNL-RHIC	Collider	Au+Au	200
2010	CERN-LHC	Collider	Pb+Pb	2760

coupling parameter Γ defined as the ratio of the average potential energy to the average kinetic energy per particle. The strong coupling regime corresponds to $\Gamma > 1$.

A new era of experimental quark matter research has begun in 2009 with the start of the experimental program at the LHC. At LHC the ALICE experiment is fully dedicated for QGP research. Other experiments having ultra-relativistic heavy ion physics in their research program are ATLAS and CMS. A summary of the past and existing heavy ion collision experiments is given in Table 1.1. The forthcoming experimental facilities include the dedicated fixed-target Facility for Antiproton and Ion Research (FAIR) at Gesellschaft für Schwerionenforschung (GSI), expected to be operational in 2018 [55], the NA61 experiment at CERN-SPS ring and the nuclear collider (NICA) at Dubna. So far at SPS, collisions have been conducted between various ion beams, such as proton (p), deuteron (d), O, S, Pb, and different targets such as S, Si, Cu, W, Pb, U, at different energies from 20 AGeV to 158 AGeV (for a proton beam it can reach up to 450 GeV). RHIC has produced collisions between p+p, d+Au, Cu+Cu and Au+Au at different energies ranging from $\sqrt{s}=7.7$ A GeV to 200 A GeV. In near future Pb+Pb collisions will be performed at LHC with up to $\sqrt{s}=5.5$ ATeV. FAIR will carry out heavy ion collisions with \sqrt{s} close to 10 AGeV. Different heavy ion experiments, with different beam energies, probe different regions in the QCD phase diagram: the matter created in the central region of collisions with higher beam energies is more symmetric between baryons and antibaryons, while the lower energy experiments (such as FAIR) enable to study the properties of dense baryonic matter.

1.5 Signatures of QGP in Relativistic Nuclear Collisions

In this section we plan to briefly describe some of the different signatures that would indicate the formation of QGP in relativistic heavy ion collisions. The central problem connected with the detection of QGP in relativistic heavy ion collisions is the transient life time of the fireball which prevents any direct measurement and one has to look for the signals to search for the evidence for the QGP formation via indirect means. It is consequently of particular relevance to find experimental observables which carry information (preferentially) from one particular stage, in particular about the QGP phase. Over the decades specific probes of QGP have been proposed [56, 57, 58, 59, 60] which are believed to carry unambiguous and experimentally signatures for deconfinement transition in nuclear collisions.

But before making any conclusion on the possibility of plasma formation, it is essential to study the modification of all the proposed signals by the corresponding non-QGP, nuclear effects. Nuclear effects are generally constrained from the measurements of $p+A$ where no secondary medium is expected to be formed. Experimentally one tries to understand the onset of all the signals in terms of different handles available namely the collision centrality (by selecting multiplicity or transverse or forward energy), collision species (a controlled variation of system size) and the center of mass energy.

The specific questions which one aims to address via measurements of these probes are the following:

- Are the initial energy densities, necessary to form QGP, reachable in heavy ion collisions?
- Are the relevant space and time scales sufficiently large to achieve equilibrium?

Depending on the energy of the collision, two simple models are generally found in literature two estimate the initial energy densities. They are known as Landau model [61] and Bjorken model [62] and are based on the degree of stopping of the participant nucleons during the collision in the central region. The Landau model is based on the

complete stopping of the colliding nuclei in the central rapidity region is valid for low energy nuclear collisions. On the other hand in the Bjorken model two highly accelerated colliding nuclei completely pass through each other leaving a large fraction of their kinetic energy in the mid rapidity region which is subsequently used in particle production.

We will now discuss briefly some of the experimental signals which have been proposed over the years to probe the matter created in heavy ion collisions.

1.5.1 Global Observables

Global observables like transverse energy E_T , particle multiplicities (N_γ, N_{ch} etc.), p_T -spectra of the produced particles and their pseudo-rapidity distributions with mass number and beam energy provide insight about the dynamics of the system and regarding the formation of QGP [62, 63]. It is also proposed that the correlation of transverse momentum p_T and the multiplicity of the produced particles may serve as a probe for the EoS of hot hadronic matter [64]. According to Landau's hydrodynamic model [11], the rapidity density (dN/dy), reflects the entropy and the mean transverse momentum ($\langle p_T \rangle$) the temperature of the system. Except at the phase transition points, the rapidity density linearly scales with $\langle p_T \rangle$. If the phase transition is of first order, then the temperature remains constant at the coexistence of the hadron gas and the QGP phase, thereby increasing the entropy density. So $\langle p_T \rangle$ will show a plateau with increase of entropy. Hence the global observables like dN/dy and $\langle p_T \rangle$ will give indication of QGP phase and the order of phase transition. $dE_T/d\eta$ gives the maximum energy density produced in the collision process which is necessary to understand the reaction dynamics. The formation of QGP may also change the shape of the pseudo-rapidity distribution [65, 66]. The event multiplicity distribution gives information of the centrality and energy density of the collision. The scaling of multiplicity with number of participant nucleons (N_{part}) reflects the particle production due to soft processes (low p_T). Whereas, at high energy when hard processes (high- p_T) dominate, it's expected that the multiplicity will scale with number of elementary nucleon-nucleon collision (N_{coll}). There are models [67] to explain the particle production taking a linear combination of N_{part} and N_{coll} (called a two-component model).

1.5.2 Strangeness enhancement

Strangeness enhancement is one of the important probes of QGP formation [68, 69]. An abundant production of strange hadrons in heavy ion collisions, than in similar energy $p + p$ or $p + A$ collisions, was proposed as a potential signature for the QGP formation in the relativistic nuclear collisions way back in 1980 [70]. In a nucleus-nucleus collision, no valence strange quarks are present in the initial colliding nucleons. The strangeness, which is created during the collisions, in the partonic or in the hadronic phase thus provides information on the reaction dynamics.

In a thermally and chemically equilibrated QGP medium, the energy levels for u or d quarks are almost filled up to the Fermi surface. Thus following Pauli's exclusion principle creation of an additional $u\bar{u}$ or $d\bar{d}$ pair to the system would cost a minimum of $2\epsilon_F$ energy (ϵ_F being the Fermi energy of the light quarks). However creation of $s\bar{s}$ pairs is relatively much easier which are now considerably lighter due to chiral symmetry restoration. Since the current mass for the strange quarks is in the range $m_s \sim 100 - 150$ MeV, the maximum threshold energy for producing a $s\bar{s}$ pair in the plasma phase is $\sim 2m_s \sim 300$ MeV.

In a purely hot hadronic medium, the production of particles containing strange quarks is normally exponentially suppressed due to the high mass of strange quark compared to the particles composed of light u and d quarks. The dominant channels for strange hadron production are: $N + N \rightarrow N + \Lambda + K$ and $\pi + \pi \rightarrow K + \bar{K}$ having Q values around 670 MeV and 700 MeV, which is much larger than $s\bar{s}$ production threshold. Thus strangeness production is much easier in partonic phase compared to the hadronic phase. In the QGP phase, strangeness production predominantly occurs through the two gluon fusion ($g + g \rightarrow s\bar{s}$). This should be reflected in an enhanced production of strange hadrons in the QGP phase compared to a purely hadronic scenario, at the same temperature. Due to the initial conditions in the heavy ion collisions, light quarks (u, d) will be more abundantly available than the corresponding anti quarks (\bar{u}, \bar{d}). Hence during hadronization the $s\bar{s}$ pairs can combine with each other to form a ϕ meson. Otherwise a \bar{s} can combine with a u quark to form a $K^+(u\bar{s})$ or a s quark can find a u and d quark to form a $\Lambda(uds)$ (note that due to initial conditions it is easier

for a s quark to form a baryon rather than forming a meson by combining with a \bar{u} or \bar{d} quark). The higher number of $s\bar{s}$ pairs in the plasma phase will finally show up in an enhanced production of strange particles (ϕ , Λ , K^+ etc) in nuclear collisions compared to $p + p$ collisions. The important observables in this respect are the yields of strange as well as multi-strange hadrons and the ratios of the number of strange hadrons to non-strange hadrons produced in the collision process. Strangeness enhancement has been experimentally observed in experiments at SPS and RHIC. Strangeness enhancement is a more useful probe particularly for plasmas having finite baryon chemical potential ($\mu_B > 0$)

1.5.3 Electromagnetic radiations: Photons and Dilepton

Photons real or virtual (i.e. lepton pairs e^+e^- and $\mu^+\mu^-$) produced in relativistic heavy ion collisions are collectively called as electromagnetic probes. Emission of electromagnetic radiation is believed to be one of the most promising and efficient tool to characterize the initial state of heavy ion collisions. In 1976 Feinberg [71] first pointed out the importance of the electromagnetic probes. Photons and dileptons are produced in all stages of the evolution of the fireball right from the early pre-equilibrium stage up to the freeze-out. Once produced they interact with the surrounding medium dominantly via electromagnetic interactions ($\alpha_e \ll \alpha_s$). Even at the highest temperatures and compression reached in relativistic heavy ion collisions the mean free path ($\lambda = \frac{1}{n\sigma}$) of photons is typically $10^2 - 10^4$ fm [72], which is much larger than the size of the fireball (~ 10 fm). Consequently once produced they do not suffer any further interactions before reaching the detectors and thus carry the unscathed information about the interiors of the fireball where they are produced. Dileptons and photons are thus called the “penetrating” probes of the hot and dense matter produced in the collisions. In the beginning photons and dileptons were studied with the hope to get information the temperature of the fireball. Eventually they have also been found to provide useful informations about several other important aspects of the collision. For example photons can be used to study (i) evolution of the system size by intensity interferometry [73], (ii) momentum anisotropy of the initial partons [74] as well as formation time of quark-gluon

plasma [75] using elliptic flow of thermal photons, (iii) an accurate check on jet quenching and other aspects of the collision dynamics by photons due to passage of high energy jets through plasma [76] among the others. Dileptons, on the other hand are considered as the most reliable messengers of the medium modification of vector mesons [77]. In addition, studying the mass dependence of the dilepton interferometry in relativistic heavy ion collisions has also been recently proposed as a tool for characterization of QGP phase [78].

We here briefly discuss both the signals photons and dileptons useful for QGP diagnostics in relativistic nuclear collisions. More details can be found in [79, 80, 81]

In relativistic nuclear collisions, production of photons is a result of convolution of the various emission sources from the entire evolution history of the fireball. Photons are emitted from the pre-equilibrium stage, from QGP phase, from hadronic phase and also from the decay of hadrons produced at the time of freeze-out. Depending on the production mechanism photons can be broadly classified into two categories namely (i) direct photons and (ii) decay photons. In a heavy ion collision experiment, the detector captures all the emitted photons and the resultant spectrum is the inclusive photon spectrum, with more than 90% of the photons coming from hadron decay.

Photons which are directly produced from a particle collision are called 'direct photons'. Depending on their origin they can be classified into several categories, namely, (1) prompt photons, which originate from initial hard scatterings, (2) pre-equilibrium photons, produced before the medium gets thermalized, (3) thermal photons from quark-gluon plasma as well as by hadronic reactions in the hadronic phase, and (4) photons from passage of jets through plasma. In relativistic heavy ion collisions, prompt photons are produced in the initial stage due to hard partonic collisions from the colliding nucleons. The corresponding partonic sub-processes include quark gluon Compton scattering ($q + g \rightarrow g + \gamma$), quark anti-quark annihilation process ($q + \bar{q} \rightarrow g + \gamma$), and quark fragmentation ($q \rightarrow q + \gamma$) following scattering of partons of the nucleons in the colliding nuclei. At lowest order in $\alpha_e \alpha_s$, quark gluon Compton scattering and quark anti-quark annihilation processes dominate the photon production. Since produced in hard process, prompt photons have a very high p_T and their contribution to the inclusive

single photon spectrum in heavy ion collisions can be estimated by standard techniques of pQCD, provided the nuclear effects are properly taken into account. Thermal photons are likely to have two distinct origins namely thermal radiation from a QGP medium or that from a hot hadronic medium. Photons radiated from the QGP phase are expected to carry information on the thermodynamical state of the medium at the instant of their production. The same partonic subprocesses responsible for prompt photons are also the dominant sources for thermal photon radiation from a QGP phase. The only difference is that in the later case the momentum distributions of quarks and gluons obey thermal distribution whereas in the previous they are determined from the nuclear structure functions. Hot hadronic matter in thermal equilibrium produced after the hadronization of the quark-gluon plasma may also lead to production of thermal photons due to hadronic reactions. These photons will dominate the spectrum at lower p_T (< 1 GeV). In a hot hadronic gas (having temperature of the order of pion mass), typical reactions for photon production are pion annihilation ($\pi + \pi \rightarrow \gamma + \rho$) and Compton scattering ($\pi + \rho \rightarrow \gamma + \rho$) [72]. Apart from the thermal photons, the other possible source of direct photons are jet-conversion photons, relevant for the ultra-relativistic heavy ion collisions like RHIC and LHC. A quark (antiquark) jet during its passage through QGP may annihilate with a thermal antiquark (quark) or undergo a Compton scattering with a thermal gluon and lead to the production of high energy jet-conversion photon.

In addition to the directly produced photons, they are also produced copiously from the decay of final state hadrons emitted from the freeze out surface (eg: $\pi^0 \rightarrow \gamma + \gamma$, $\eta \rightarrow \gamma + \gamma$ etc.). Decay photons can be subtracted from the inclusive spectrum through invariant mass analysis [82, 83]. Theoretical models are required to identify the different sources of direct photons and their relative importance in the spectrum [84]. Depending on the source, the momentum distributions for different classes of photons would be different. Higher the p_T of the photons earlier they are produced in the collisions. One thus needs to identify a suitable p_T window where photons from QGP dominates over its hadronic counter part [85, 86, 87, 88], which in turn can be used for determination of initial temperature of the plasma [87, 89, 90, 91, 92, 93]. Calculation of jet-conversion photons on the other hand is particularly interesting, as there are indications that they

measure the initial spatial anisotropy of the system [94].

Dileptons on the other hand, are sometimes believed to be more advantageous over the photons due to their massive nature. The dilepton invariant mass M and the transverse momentum p_T are the two parameters available for dileptons, which can be tuned to investigate the different stages of the expanding fireball. Similar to photons dileptons are also emitted from every stage of heavy ion collisions and from different sources [57, 58, 80, 81]. Dileptons having large invariant mass and high p_T , are emitted very early, soon after the collision when the temperature of the system is very high. On the other hand, those having lower invariant masses come out later from a relatively cooler stages. The most significant physical source for di-lepton signal in the partonic phase is the annihilation of quark-antiquark pairs ($q + \bar{q} \rightarrow l^+ + l^-$, $q + \bar{q} \rightarrow g + l^+ + l^-$) and Compton scattering ($q(\bar{q}) + g \rightarrow q(\bar{q}) + l^+ + l^-$). In the hadronic sector, it is, $\pi^+ \pi^-$ ($\pi^+ + \pi^- \rightarrow l^+ + l^-$) annihilation. They are also produced from the direct decay of hadronic resonances like ρ , ω , ϕ , J/Ψ , ψ' etc as well as from Drell-Yan process. In the Drell-Yan process, a valence quark from a nucleon in the projectile nucleus interacts with a sea anti-quark from a nucleon in the target nucleus to form a virtual photon, which decays into a lepton pair. Apart from the direct hadronic decays there are contributions from Dalitz decay like $\pi^0 \rightarrow e^+ + e^- + \gamma$, $\omega \rightarrow \pi^0 + e^+ + e^-$, $\eta \rightarrow e^+ + e^- + \gamma$ etc. Depending on the pair invariant mass, the entire dilepton spectrum can be classified into three distinct regimes:

a) Low Mass Region (LMR): $M \leq M_\phi (= 1.024 \text{ GeV})$: In this mass range, vector meson decays are the dominating source of dilepton production and medium modified spectral density is one of the key issues which needs to be addressed.

b) Intermediate Mass Region (IMR): $M_\phi < M < M_{J/\Psi} (= 3.1 \text{ GeV})$: In intermediate mass region, continuum radiation from QGP dominates the dilepton mass spectrum and thus this region is important for getting a pure QGP signature.

c) High Mass Region (HMR): $M \geq M_{J/\Psi}$: In the HMR, the most interesting phenomenon are the primordial emission and heavy quarkonia like J/Ψ and Υ suppression.

Apart from the above signals the experimentally measured di-lepton spectrum contains a background continuum having contributions from both physical and unphysical

sources. The unphysical source is the combinatorial background mainly due to weak meson decays. Combinatorial background can be subtracted from the raw spectrum using invariant mass analysis techniques. The physical background is constituted mainly from the Drell-Yan scattering which mostly populate the high mass regime and the correlated semileptonic decay of heavy flavor mesons (D, \bar{D} etc.) that form a continuum in the intermediate mass regime. Dileptons from Dalitz decay also form a continuum and populate the low mass region. Contribution from the hard process like Drell-Yan production occurring in the initial stage of the collisions, can be estimated from pQCD calculations. The yield from Dalitz decays can be estimated from the hadronic spectra measured in heavy-ion collisions. A study of the p_T dependence of various mass windows might perhaps help to disentangle the different contributions to the spectrum and the regime where radiation from the plasma phase rides over all the other non-QGP sources. It has been found that the invariant mass spectrum of thermal dilepton is dominated by QGP radiation above ϕ mass and hadronic radiation outshines the QGP contribution for $M \leq M_\phi$. Theoretical calculations have also shown that ratio of the thermal photons to dileptons can be used to estimate the initial temperature of the fireball by a suitable selection of the p_T and invariance mass window (of the lepton pair) [95]. The ratio can also be used to extract the radial flow of the medium, non-monotonic variation of which with pair mass is argued to be indicative of the quark-hadron phase transition at SPS and RHIC energies [96]. Recently in [97], the authors have studied the variation of elliptic flow of thermal dileptons with transverse momentum and invariant mass of the pairs for Pb+Pb collisions at LHC energies. They found that a judicious selection of M and p_T windows can be used to extract the collective properties of quark matter, hadronic matter and also get a distinct signature of medium effects on vector mesons. Their results indicate a reduction of elliptic flow (v_2) for M beyond ϕ mass, which if observed experimentally would give the measure of v_2 of the partonic phase.

On the other hand, low mass vector mesons (ρ, ω, ϕ) decaying into dileptons are considered as the most reliable experimental probes to study the medium modification of hadrons. Among them particularly interesting is $\rho(770)$ meson. The low mass region of the dilepton spectra is largely mediated by $\rho(770)$, a broad vector meson, as a result

of its strong coupling to the $\pi\pi$ channel and a short lifetime, which is about $1.3 \text{ fm}/c$. ω meson was also predicted to behave as chronometer and thermometer in hot and dense hadronic matter due to opening up of the new in-medium decay channels forbidden in vacuum [98]. The ultimate goal of the study of in-medium hadrons, is to find some connection with the chiral phase transition. At high temperatures and large chemical potentials, in addition to deconfinement transition, chiral symmetry (a fundamental symmetry of QCD in the massless limit), spontaneously broken in the hadronic world, is believed to get restored. According to our current understanding chiral symmetry gets restored near (or at) the deconfinement phase boundary. The in-medium electromagnetic response, which is dominated by the vector mesons ρ, ω and ϕ , provides a direct link to chiral symmetry and its restoration near the transition temperature T_c . Restoration of chiral symmetry implies a strong reduction ('melting') of the quark condensate near T_c . Furthermore, at the phase boundary, the vector- and axial-vector correlation functions corresponding to the ρ meson and its chiral (parity) partner, the a_1 meson, must become identical in the limit of vanishing quark masses [99, 100]. Theoretical calculations [101] indicate that the dilepton yield calculated using the hadronic in-medium correlation function near the phase boundary coincides remarkably well with that obtained from lowest-order $q\bar{q}$ annihilation in the QGP, where chiral symmetry is restored. Since a strong increase of the ρ -meson width is seen in the present di-lepton data [102, 103], it thus seems that the signal for chiral symmetry restoration in the electromagnetic response of hot and dense matter is a smooth 'melting' of the ρ meson into a featureless quark-antiquark continuum. It might also important to note in this context, that in the recent data there is no evidence for a possible downward shift of the ρ mass, as had been predicted early-on [104] based on a scaling relation between the ρ mass and the in-medium quark condensate. In a chirally symmetric world, the spectral distribution of ρ meson should become degenerate with that of its chiral partner a_1 meson. Hence also the a_1 meson has to melt smoothly into a quark-antiquark continuum. Experimentally this is highly unfeasible to check as the dominant electromagnetic decay of the a_1 meson involves, besides a virtual or real photon, a pion which suffers strong rescattering and absorption in the fireball and hence the early stages of the collision are hard to probe.

Thus so far as experimental detection of chiral phase transition is concerned, di-leptons appears to be the only probe.

1.5.4 Quarkonium suppression

The bound states of a heavy quark (Q) and its anti-quark (\bar{Q}) which are stable with respect to strong decay into open charm or bottom hadrons are collectively called *quarkonia*. Depending on the heavy quark infrastructure, charm (c) or bottom (b), the corresponding bound states are known as *charmonia* or *bottomonia*, respectively. Due to their close analogy with positronium atom (bound state of e^+ and e^-), the heavy quark bound states are so named and contain a spectrum of resonances corresponding to various excitations of the heavy quark pair. However unlike its analog governed mainly by electrostatic Coulomb force, properties of the quarkonium states are determined by the strong interaction. The vector (spin-one) ground state of of charmonium ($c\bar{c}$) family is known as J/ψ and that of the bottomonium family is called Υ . Apart from these vector ground states both the $c\bar{c}$ and $b\bar{b}$ systems give rise to a number of other stable bound states of different quantum numbers [105].

Quarkonia are some what different from the usual hadrons. The masses of the lighter hadrons particularly in those of the non-strange mesons and baryons, almost entirely arise from the interaction of their nearly massless quark constituents. In contrast, the quarkonium masses are largely determined from the bare quark masses of charm or bottom quark, coming from the electroweak sector of the standard model via Higgs mechanism. Large quark masses enable the use of non-relativistic quantum theory to calculate many basic properties of these quarkonium states. A specific characteristic of quarkonia (particularly the ground and lower excited states) is their small size. While the typical hadron radius is ~ 1 fm, the radii of charmonia and bottomonia range from 0.1–0.3 fm, resulting a large binding energy compared to the normal hadrons. Again the stability of the $c\bar{c}/b\bar{b}$ quarkonium states implies that their masses satisfy $M_{c\bar{c}} < 2M_D$ and $M_{b\bar{b}} < 2M_B$, where $D = c\bar{u}$ and $B = b\bar{u}$ are the corresponding “open” mesons. Hence their strong decays into $D\bar{D}/B\bar{B}$ pairs are forbidden.

In 1986, Matsui and Satz in their seminal paper [106] argued that in a QGP, due

to Debye screening by the free color charges, production of J/ψ and other quarkonium resonances would be suppressed. The magnitude of the suppression for different quarkonium states should depend on their binding energy, with strongly bound states such as the Υ showing less or no modification [107]. Suppression does not imply that the $c\bar{c}$ pairs will not be produced. Rather it would indicate a depletion of the J/ψ yield either because an evolving $c\bar{c}$ pair fails to form a J/ψ or the J/ψ produced is destroyed due to its subsequent interactions with the medium. This suppression was thought to be an ideal test of deconfinement phase transition as no other mechanism apart from plasma screening could be identified that would lead to J/ψ suppression in nuclear collisions. Since then measuring J/ψ suppression in nuclear collisions had been one of the major experimental goals. A reduction of the J/ψ yield was indeed observed in different heavy ion collision experiments with the first ever nuclear suppression was measured with Oxygen beams at the SPS [108]; now attributed to cold nuclear matter (CNM) effects rather than deconfinement [109].

However over the years many other hadronic mechanisms have been identified that could also lead to the observed J/ψ suppression in experiments. Thus J/ψ suppression in nuclear collisions is no longer a “smoking-gun” signature for deconfinement transition. But the source of the observed J/ψ plasma or hadrons, has still remained controversial. Calculations of J/ψ suppression by a QGP as well as by a purely hadronic medium had both been previously shown to be consistent with the measurements. At higher energies in addition to the suppression, charmonium regeneration has also been proposed as an alternative mechanism for J/ψ production due to recombination of the exogenous c, \bar{c} quarks in the plasma phase. Often the discussions were focused on whether one could describe all the existing measurements simultaneously using hadronic models. No QGP mechanism can be soundly established until all plausible hadronic scenarios have been systematically excluded from the data. Till date the issue remains unsettled.

We will not discuss here any more detail about quarkonium suppression as a possible signal for QGP formation in relativistic heavy ion collisions. In chapter 3, we will present a brief overview on charmonium suppression in nuclear collisions. One of the main goals of the present thesis is to estimate the J/ψ production and its suppression in the low

energy collisions at the FAIR accelerator facility. In the heavy ion collisions at FAIR a dense baryonic medium is anticipated to be produced which might lead to the formation of a baryon rich QGP. We will come back to this issue in detail in chapter 6 where we first discuss about the CNM effects prevailing in $p + A$ and $A + A$ collisions and leading to the “normal” nuclear J/ψ suppression. This will be followed by a discussion on the possible “anomalous” suppression effects in nuclear collisions, presumably induced either by a hot baryonic plasma or by a compressed baryonic medium.

1.5.5 Jet Quenching

Jet production in hadronic collisions is an archetypical hard QCD process. An elastic ($2 \rightarrow 2$) or inelastic ($2 \rightarrow 2 + X$) scattering of two partons from each of the colliding hadrons (or nuclei) results in production of two or more partons in the final state. The two outgoing partons have a large virtuality Q which they reduce by subsequently radiating gluons and/or splitting into quark-antiquark pairs. Such a parton branching evolution is governed by the QCD radiation probabilities given by the Dokshitzer-Gribov-Lipatov-Altarelli-Parisi (DGLAP) equations [111] down to virtualities $\sim 1 \text{ GeV}^2$. At this point the produced partons fragment non-perturbatively into a set of final state hadrons. The characteristic collimated spray of hadrons resulting from the fragmentation of an outgoing parton is called a ‘jet’. When the jets propagate through the hot and dense medium produced in the relativistic nuclear collisions due to multiple scattering they suffer further interaction with the medium and lose their energy. The resulting attenuation or disappearance of the spray of hadrons coming out from the fragmentation of a hard parton due to energy loss in the dense medium is called ‘jet quenching’. It was one of the first proposed ‘smoking gun’ signature of QGP formation in relativistic heavy ion collisions. Jets lose their energy both via radiative as well as collisional processes. The energy loss is proportional to the both initial gluon density and life time of the dense matter. Results from Au+Au collisions at $\sqrt{s_{NN}} = 200 \text{ GeV}$ at RHIC exhibited striking evidences for quenching effect through the suppression of the high p_T hadrons. Experimentally suppression is quantified in terms of nuclear modification factor R_{AA} defined as the ratio of yield the Au+Au collisions to that in p+p collisions,

scaled by the number of binary collisions. In absence of any medium effect, $R_{AA} = 1$ which indicates that the nucleus-nucleus collision is an incoherent superposition of elementary nucleon-nucleon collisions. A value less than unity signifies the suppression of high energy jets due to their interaction with the thermal medium. The p_T dependence of R_{AA} for different particles was measured in RHIC [112] at mid-rapidity for central Au+Au collisions. A large suppression was visible in the data for π^0 , η and ϕ mesons with a maximum of $R_{AA} \sim 0.2$ indicating a suppression by a factor of five compared to p+p collisions. Similar level of suppression for different mesons with different quark infrastructure indicate that the suppression occurs at the partonic level where the dense medium scatterers the partons at high p_T and thus degrading their momenta. On the other hand direct photons which undergo only electromagnetic interactions do not suffer from the suppression effects. They follow the binary scaling exhibiting $R_{AA} \sim 1$. This observation puts a strong evidence that the suppression is not an initial state effect but a final state effect caused by the dense medium made up of unbound color charges. This observation lends further support from the d+Au collision measurements at the same energy, where $R_{AA}(p_T) \sim 1$ for pions at mid rapidity and at sufficiently high p_T .

1.5.6 Anisotropic Flow

One of the key observables in relativistic collisions of heavy nuclei is anisotropic flow, which confirms the collectivity and early thermalization in the hot and dense fireball created in the collisions. In non-central heavy ion collisions initial spatial anisotropy of the nuclear overlap zone is converted into momentum space anisotropy of particle distribution via the operation of azimuthally anisotropic pressure gradient. This leads to an anisotropic azimuthal distribution $dN/d\varphi$ of particles emitted from the collision zone. Anisotropic particle distributions were first suggested in [113] as a signal of collective flow in ultra-relativistic heavy ion collisions. In usual practice, the flow pattern is quantified via a Fourier expansion [114]:

$$E \frac{d^3N(b)}{d^3p} = \frac{1}{2\pi} \frac{d^2N(b)}{p_T dp_T dy} \left(1 + 2 \sum_{n=1}^{\infty} v_n(p_T, b) \cos [n(\varphi - \Psi_n)] \right) \quad (1.6)$$

The Fourier (or flow) coefficients v_n depend on N_{part} and are given by

$$v_n(p_T, b) = \langle \cos [n(\varphi - \Psi_n)] \rangle, \quad (1.7)$$

where the brackets denote an average over particles in a given p_T bin and over events in a given centrality class. In the above equations, n is the order of the harmonic, φ is the azimuthal angle of the particle, and Ψ_n is the reaction plane angle of harmonic n , the plane which maximizes the expectation value of v_n in each event. Among different Fourier coefficients, most attention was given in the past to v_2 , the *elliptic flow*, which is very strong in non-central collisions and is believed to signify the formation of a thermalized medium in the early stages of the collision. Magnitude of v_2 is found to be sensitive to the initial condition and the equation of state (EOS) of the hot and dense fireball produced in the collisions. The elliptic flow magnitude increases continuously with \sqrt{s} from SPS to RHIC [115, 116]. At top RHIC energy, v_2 reaches a value compatible with the one predicted by hydrodynamics for a “perfect fluid”, i.e. a fluid without internal friction and vanishing shear viscosity [117, 118, 119, 120, 121]. Large elliptic flow found at RHIC indicates the possibility of early thermalization of a partonic phase. The matter created at LHC is also seen to behave like the (almost) perfect liquid discovered at RHIC [124, 125]. Higher-order harmonics (v_3, v_4, v_5 etc.) have usually been neglected because they were expected to be small for symmetry reasons. However recent investigations have shown their importance to study the initial state fluctuations in heavy ion collisions. A comprehensive study of all the flow harmonics is also found to be useful to derive to η/s ratio (shear viscosity η over entropy density s), [122, 123] of the fluid produced in the collisions.

1.5.7 Correlation and Fluctuations

Phase transition being a critical phenomenon, is associated with divergence of susceptibilities and hence fluctuations in corresponding observables. Hence, observable fluctuations could be used as probes of deconfinement phase transitions. Fluctuations are very sensitive to the nature of the phase transition. First-order phase transition is ex-

pected to lead to large fluctuations due to droplet formation or more generally density or temperature fluctuations. In case of a second-order phase transition the specific heat diverges, and this has been argued to reduce the fluctuations drastically if the matter freezes out at the critical temperature. Even if the transition is not of first order, fluctuations may still occur in the matter that undergoes a transition. The fluctuations may be in density, chiral symmetry, strangeness or other quantities and show up in particle multiplicities. The “anomalous” fluctuations depend not only on the type and order of the phase transition, but also on the speed by which the collision zone goes through the transition, the degree of equilibration, the subsequent hadronization process, the amount of re-scattering between hadronization and freeze-out [128].

There have been efforts to use observable fluctuations like, ratios of charged particles [129, 130], baryon number multiplicity [131], net charge [132], mean p_T [133], transverse energy [134], strangeness [135], isospin [136] etc., to probe the deconfinement phase transition. It is necessary to understand the role of statistical fluctuations, in order to extract new physics associated with fluctuations. The sources of these fluctuations include impact parameter fluctuations, fluctuations in the number of primary collisions and in the results of such collisions, fluctuations in the relative orientation during the collision of deformed nuclei, effects of re-scattering of secondaries and QCD color fluctuations.

1.6 Motivation and Organization of the thesis

The focal aim of the relativistic heavy ion collision experiments is to explore the QCD phase diagram and to identify the formation of quark-gluon plasma in the laboratory. The CBM experiment at FAIR is designed to unravel the phase structure of nuclear matter in the region of moderate temperatures and extremely high net baryon densities. J/ψ suppression has been identified as one of the promising diagnostic probe to indicate the possible occurrence of deconfinement phase transition in super dense nuclear medium. The CBM experimental program thus includes a detailed plan to measure the J/ψ mesons via their decay into di-lepton channels. The measurements are particularly challenging due to extremely low production cross section of the J/ψ mesons in the

CBM energy regime ($E_b = 2-35A$ GeV), which is close to the J/ψ kinematic production threshold ($E_{th} \sim 12.3A$ GeV). This in turn demands accelerators with unprecedentedly high heavy ion beam intensities and detectors with extremely large rate-capabilities. India along with Russia jointly holds the responsibility to design and build a muon detector system for the CBM experiment which will be dedicated for measurement of entire di-muon spectrum including the J/ψ mesons. The main objective of the present work is to study the J/ψ production in the FAIR energy domain and its detection under CBM experimental conditions via di-muon channel. The work done for the thesis can be broadly divided into the following parts:

- The first part is devoted to the theoretical estimation of J/ψ production and its possible suppression in the FAIR energy regime. A theoretical model has been developed for this purpose which has been calibrated by analyzing the available data on J/ψ production cross section at SPS energies. In case of $p + A$ collisions suppression induced by different possible cold nuclear effects are taken into account. In case of heavy ion collisions additional suppression effects induced by a hot and dense secondary medium has been estimated. We have explored the two possible cases namely the suppression due to high density hadronic medium and the dissociation due to baryonic plasma.
- In the second part of the thesis we have investigated the feasibility of J/ψ measurements using the CBM muon detector setup. Different steps for optimization of the muon detector system has been investigated in detail. The optimized setup is then used for J/ψ detection in p+Au and Au+Au collisions.

The organization of the thesis is the following. Chapter 2 describes the outline of the CBM experiment at FAIR including a brief description of the FAIR accelerator facility, the major physics goals and the corresponding potential observables of CBM and the different detector sub-systems of the CBM experimental set-up. In chapter 3 we give a detailed overview of charmonium production in nuclear collisions. Chapter 4 will be dedicated to describe our theoretical formulation for calculation of J/ψ production in nuclear collisions. In chapter 5 we discuss the analysis of existing data on J/ψ from

different SPS experiments within our model framework. In chapter 6 we present the predictions for inclusive J/ψ productions and expected level suppressions for different probable scenario, in FAIR energy collisions. The detailed description on the design simulation of the muon detector system for the CBM experiment and its physics capabilities for detection of J/ψ in di-muon channel are depicted in chapter 7. Finally we present our thesis summary and discussions in chapter 8.

Chapter 2

The Compressed Baryonic Matter

Experiment

2.1 Introduction

Statistical QCD predicts that at high temperature and/or density, hadronic matter undergoes a de-confining phase transition to a new state, where strongly interacting matter shows partonic behavior. Relativistic heavy ion collision experiments give us the opportunity to produce and study such a novel state of matter in the laboratory. The upcoming Compressed Baryonic Matter (CBM) experiment [137], at the future accelerator facility FAIR at GSI, aims at the production and characterization of super dense nuclear matter in the laboratory. CBM is one of the four major scientific pillars of the upcoming FAIR project. The primary goal of the CBM experiment is the exploration of the phase diagram of nuclear matter in the region of moderate temper-

Table 2.1: Experiments investigating the high net-baryon density region in the QCD phase diagram, their energy range and reaction rates which triggers the limitation. The reaction rate of CBM is orders of magnitude higher in comparison to the other experiments.

Experiment	Energy range	Reaction rate (Hz)	Limitation by
STAR-BES @ RHIC BNL	$\sqrt{s} = 7 - 200$ GeV	1 - 800	luminosity
NA61 @ SPS CERN	$E_k = 20 - 160$ A GeV	80	detector
MPD @ NICA Dubna	$\sqrt{s} = 4 - 11$ GeV	1000	luminosity
CBM @ FAIR Darmstadt	$E_k = 2 - 35$ A GeV	$10^5 - 10^7$	detector

atures and extremely high densities. In the laboratory hot and dense nuclear matter can be generated over a wide range of temperatures and densities by colliding atomic nuclei at relativistic energies. In the interior of the collision zone, matter is heated and compressed for a very short time. At moderate temperatures and densities, nucleons are excited to short-lived states (baryonic resonances) which decay by the emission of mesons. At higher temperatures, baryon-antibaryon pairs are also created. This mixture of baryons, antibaryons and mesons, all strongly interacting particles, is generally called hadronic matter, or baryonic matter if baryons prevail. At very high temperatures or densities the hadrons melt, and their constituents, the quarks and gluons, form a new phase: the Quark-Gluon Plasma (QGP). The goal of the experiments at RHIC and LHC is to investigate the properties of deconfined QCD matter at very high temperatures and almost zero net-baryon densities. Several experimental programs are devoted to the exploration of the QCD phase diagram at high net-baryon densities. Table 2.1 summarizes such current and upcoming experiments in the low and intermediate energy region. The STAR collaboration at RHIC scanned the beam energies in order to search for the QCD critical endpoint [138]. For the same reason, measurements are performed at the CERN-SPS with the upgraded NA49 detector (NA61) using light and medium size ion beams [139]. At the Joint Institute for Nuclear Research (JINR) in Dubna, a heavy ion collider project (NICA) is planned with the goal to search for the coexistence phase of nuclear matter [140]. However, due to luminosity or detector limitations these experiments are constrained to the investigation of particles which are abundantly produced. In contrast, the Compressed Baryonic Matter (CBM) experiment at the Facility for Antiproton and Ion Research (FAIR) in Darmstadt is designed for precision measurements of multidimensional observables including particles with very low production cross sections using the high-intensity heavy ion beams provided by the FAIR accelerators.

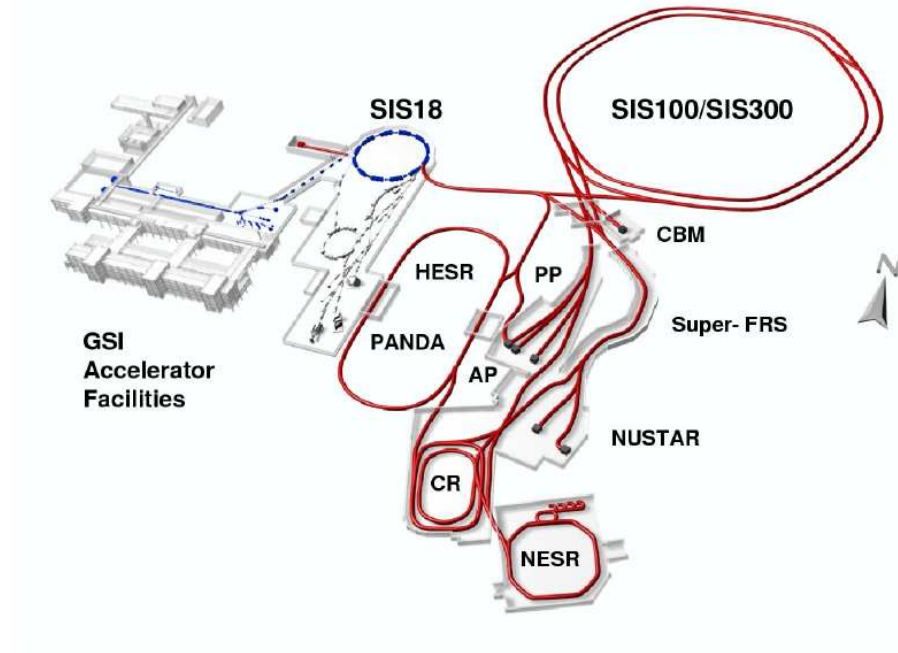


Figure 2.1: Layout of the Facility for Antiproton and Ion Research (FAIR). [141]. The double synchrotron SIS-100/300 directly provides the nuclear beams for the CBM experiment. In parallel operation it transports the secondary beams of antiprotons or rare nuclear isotopes from a production target to the new fragment separator (super FRS). These beams are subsequently stored and further manipulated in special purpose storage rings, like the HESR for antiproton research at PANDA detector or for nuclear structure and atomic and plasma physics investigations at other rings.

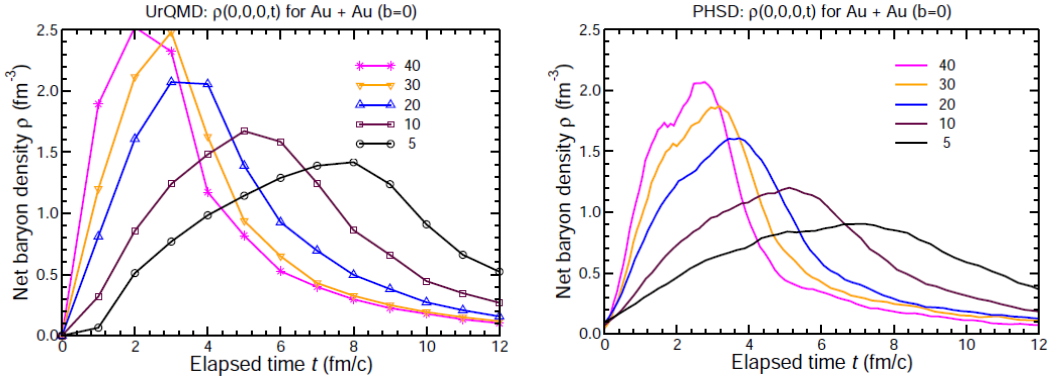


Figure 2.2: Evolution of net baryon density as function of elapsed time for central Au+Au collisions, at the centre of the collision zone, at different beam energies. Calculations are performed with two different transport models namely PHSD [40] and UrQMD [38]. The figure is taken from [291].

2.2 The Facility for Antiproton and Ion Research (FAIR)

The international Facility for Antiproton and Ion Research (FAIR), the new accelerator facility coming up in Darmstadt will provide unique research opportunities in the fields of nuclear, hadron, atomic and plasma physics [141]. The research program devoted to the exploration of compressed baryonic matter will start with primary beams from the SIS100 synchrotron (protons up to 29 GeV, Au up to 11 AGeV, nuclei with $Z/A = 0.5$ up to 14 AGeV), and will be continued with beams from the SIS300 synchrotron (protons up to 90 GeV, Au up to 35 AGeV, nuclei with $Z/A = 0.5$ up to 45 AGeV). The layout of FAIR is presented in Fig. 2.1. The beam extracted to the CBM cave reaches intensities up to 10^9 Au ions per second.

The SIS100/300 accelerators at FAIR are very well suited to create high net-baryon densities. This is illustrated in Fig. 2.2 which depicts results of transport code calculations for central Au+Au collisions. According to these calculations, densities of up to 7 times saturation density can be produced already at beam energies of 10 AGeV. Under these conditions the nucleons overlap, and theory predicts a transition to a mixed phase of baryons and quarks.

2.3 Diagnostic probes of the high-density fireball

Figure 2.3 depicts three snapshots of the evolution of a heavy ion collision at FAIR energies as calculated with the UrQMD transport code [38], and illustrates the time of production and eventual emission of various particle species. Particles containing charm quarks are expected to be created in the very first stage of the reaction. Then, D mesons and J/ψ mesons may serve as probes for the dense fireball and its degrees of freedom. Vector mesons like ω , ρ and ϕ mesons are produced continuously via $\pi\pi$ annihilation during the course of the reaction, and decay either again into mesons, or into a pair of leptons. However, as leptons are not affected by final-state interactions, the dileptonic decay offers the possibility to look into the fireball. In particular, the short-lived ρ meson is a promising diagnostic probe of hot and dense nuclear matter. Due to their small hadronic cross sections, also multi-strange hyperons and ϕ mesons carry information on the dense phase of the collision, in particular via their collective flow. Finally, the bulk of the particles freezes out at densities below saturation density. Up to date, essentially these freeze-out particles have been measured in heavy ion collisions at beam energies between 2 and 40 AGeV (on stationary target). Diagnostic probes of the dense stage of the fireball such as multi-strange baryons, dilepton pairs and charmed particles will be measured for the first time by the CBM experiment in this beam energy range. Therefore, the CBM experiment has a unique discovery potential both at SIS100 and SIS300 energies.

The experimental challenge is to measure multi-differential observables and particles with very low production cross sections such as multi-strange (anti-) hyperons, particles with charm and lepton pairs with unprecedented precision. The situation is illustrated in Fig. 2.4 which depicts the product of multiplicity times branching ratio for various particle species produced in central Au+Au collisions at 25 AGeV. The data points are calculated using either the HSD transport code [142] or the thermal model based on the corresponding temperature and baryon-chemical potential [143]. Mesons containing charm quarks are about 9 orders of magnitude less abundant than pions (except for the ψ' meson which is even more suppressed). The dilepton decay of vector mesons is suppressed by the square of the electromagnetic coupling constant $(1/137)^2$, resulting

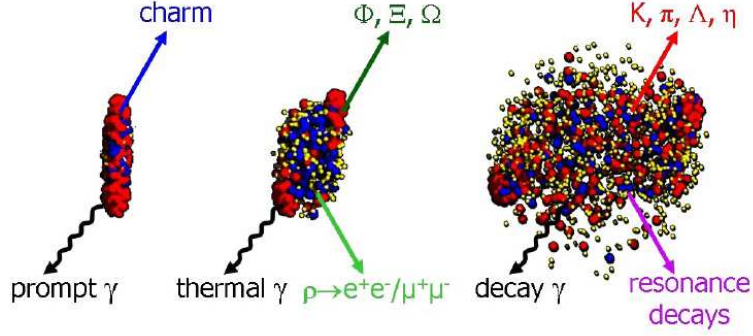


Figure 2.3: Three stages of a U+U collision at a laboratory beam energy of 23 AGeV as calculated with the UrQMD model [38]: the initial stage where the two Lorentz-contracted nuclei overlap (left), the high density phase (middle), and the final stage (“freeze-out”) when all hadrons have been formed (right). Different particles are created in different stages of the collisions or escape from the interaction region at different times (see text). Almost 1000 charged particles are created in such a collision, most of them are pions.

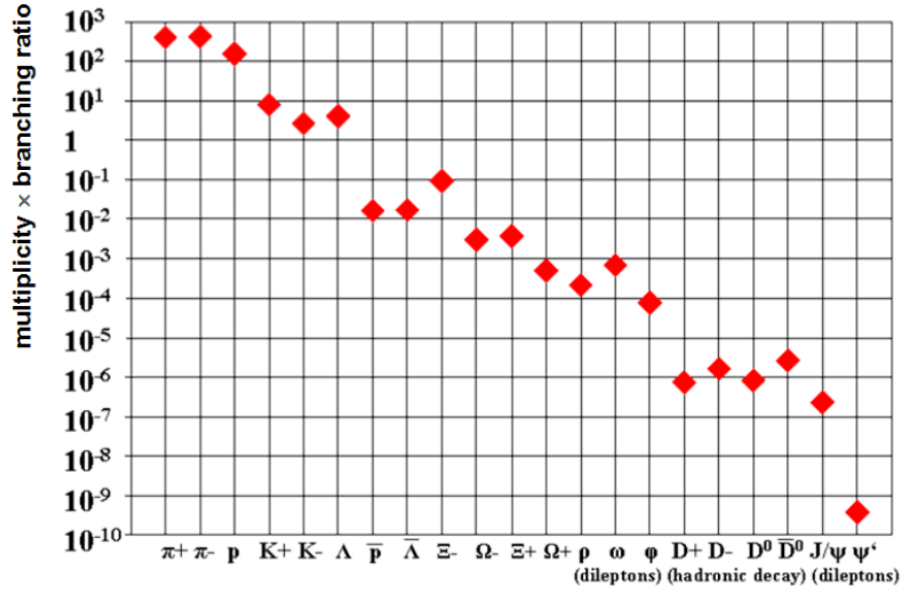


Figure 2.4: Particle multiplicities times branching ratio for minimum bias Au+Au collisions at 25 AGeV as calculated with the HSD transport code [142] and the statistical model [143]. For the vector mesons (ρ , ω , ϕ , J/ψ , ψ') the decay into lepton pairs was assumed, for D mesons the hadronic decay into kaons and pions.

in a dilepton yield which is 6 orders of magnitude below the pion yield, similar to the multiplicity of multi-strange anti-hyperons.

In order to produce high statistics data even for the particles with the lowest production cross sections, the CBM experiment is designed to run at reaction rates of 100 kHz up to 1 MHz. For charmonium measurements - where a trigger on high-energy lepton pairs can be generated - reaction rates up to 10 MHz are envisaged.

2.4 CBM physics cases and observables

The CBM research program is focused on the following physics cases:

The equation-of-state of baryonic matter at neutron star densities.

The relevant measurements are:

- The excitation function of the collective flow of hadrons which is driven by the pressure created in the early fireball (SIS100);
- The excitation functions of multi-strange hyperon yields in Au+Au and C+C collisions at energies from 2 to 11 AGeV (SIS100). At sub-threshold energies, Ξ and Ω hyperons are produced in sequential collisions involving kaons and Λ 's, and, therefore, are sensitive to the density in the fireball.

In-medium properties of hadrons.

The restoration of chiral symmetry in dense baryonic matter will modify the properties of hadrons. The relevant measurements are:

- The in-medium mass distribution of vector mesons decaying in lepton pairs in heavy ion collisions at different energies (2 - 45 AGeV), and for different collision systems. Leptons are penetrating probes carrying the information out of the dense fireball (SIS100/300);
- Yields and transverse mass distributions of charmed mesons in heavy ion as a function of collision energy (SIS100/300).

Phase transitions from hadronic matter to quarkyonic or partonic matter at high net-baryon densities.

Already at SIS100 energies densities of up to 7 times ρ_0 are reached in central collisions between heavy ions. A discontinuity or sudden variation in the excitation functions of sensitive observables would be indicative of a transition. The relevant measurements are:

- The excitation function of yields, spectra, and collective flow of strange particles in heavy ion collisions from 6 - 45 AGeV (SIS100/300);
- The excitation function of yields, spectra, and collective flow of charmed particles in heavy ion collisions from 6 - 45 AGeV (SIS100/300);
- The excitation function of yields and spectra of lepton pairs in heavy ion collisions from 6 - 45 AGeV (SIS100/300);
- Event-by-event fluctuations of conserved quantities like baryons, strangeness, net-charge etc. in heavy ion collisions with high precision as function of beam energy from 6 - 45 AGeV (SIS100/300).

Hypernuclei, strange dibaryons and massive strange objects.

Theoretical models predict that single and double hypernuclei, strange dibaryons and heavy multi-strange short-lived objects are produced via coalescence in heavy ion collisions with the maximum yield in the region of SIS100 energies. The planned measurements include:

- The decay chains of single and double hypernuclei in heavy ion collisions at SIS100 energies;
- Search for strange matter in the form of strange dibaryons and heavy multi-strange short-lived objects. If these multi-strange particles decay into charged hadrons including hyperons they can be identified via their decay products.

Charm production mechanisms, charm propagation, and in-medium properties of charmed particles in (dense) nuclear matter.

The relevant measurements are:

- Cross sections and momentum spectra of open charm (D-mesons) in proton-nucleus collisions at SIS100/300 energies. In-medium properties of D mesons can be derived from the transparency ratio $T_A = (\sigma_{pA} \rightarrow DX) / (A \times \sigma_{pN} \rightarrow DX)$ measured for different size target nuclei;
- Cross sections, momentum spectra, and collective flow of open charm (D-mesons) in nucleus-nucleus collisions at SIS300 energies;
- Cross sections, momentum spectra, and collective flow of charmonium (J/ψ) in proton-nucleus and nucleus-nucleus collisions at SIS100/300 energies.

As discussed above, a substantial part of the CBM physics cases can be addressed already with beams from the SIS100 synchrotron. The intended measurements at SIS100 including the results of simulations and count rate estimates are described in [144]. A general review of the physics of compressed baryonic matter, the theoretical concepts, the available experimental results, and predictions for relevant observables in future heavy ion collision experiments can be found in the CBM Physics Book [145].

2.5 The Compressed Baryonic Matter (CBM) experimental setup

In order to realize the physics goals presented in the previous section, the CBM experimental strategy is to perform systematic both integral and differential measurements of almost all the particles produced in nuclear collisions (i.e. yields, phase-space distributions, correlations and fluctuations) with unprecedented precision and statistics. These measurements will be performed in nucleus-nucleus, proton-nucleus, and - for baseline determination - proton-proton collisions at different beam energies. The identification of multi-strange hyperons, hypernuclei, particles with charm quarks and vector mesons decaying into lepton pairs requires efficient background suppression and very high interaction rates up to 10 MHz with charge particle multiplicities up to 1000 per event.. In order to select events containing those rare observables, the tracks of each collision have to be reconstructed and filtered online with respect to physical signatures. This

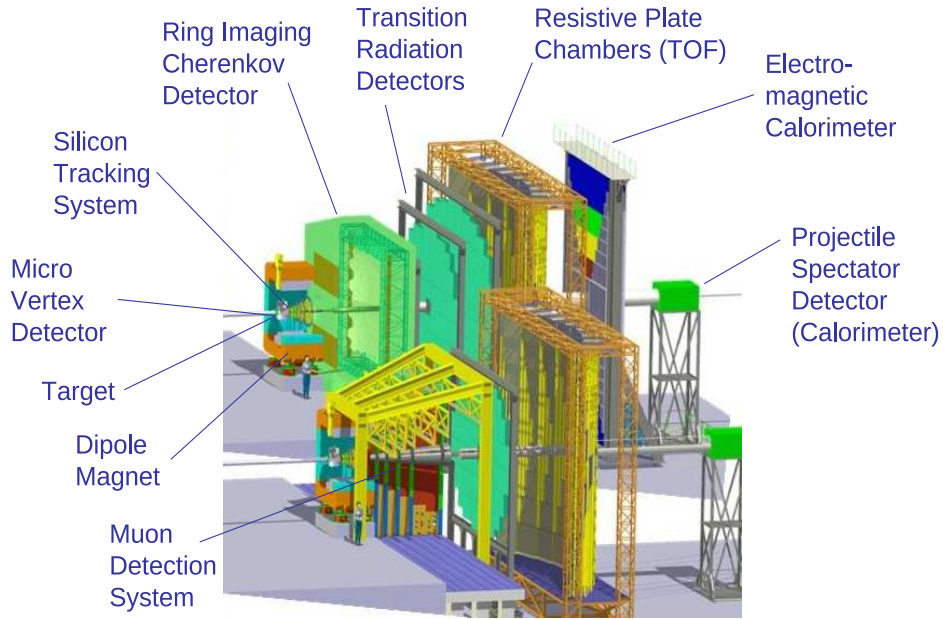


Figure 2.5: The conceptual layout of the CBM experimental facility. Both the electron mode (RICH and TRD) and muon mode (MUCH) are shown.

concept represents a paradigm shift for data taking in high-energy physics experiments: CBM will run without hierarchical trigger system. Self-triggered read-out electronics, a high-speed data processing and acquisition system, fast algorithms, and, last but not least, radiation hard detectors are indispensable prerequisites for a successful operation of the experiment. Figure 2.5 depicts the CBM experimental setup with electron detectors (at the top) and the muon detection system (at the bottom). The CBM experiment comprises the following components:

Dipole magnet

The dipole magnet has the bending power in the region of $1 - 2 \text{ Tm}$. In order to restrict the size of the tracking detectors located inside the field, the field region is confined within 1 m along the beam axis. It has a large aperture (acceptance) of $\pm 25^\circ$ polar angle, which results in a gap width of 1 m. Estimation of coil requirements assuming a perfect yoke to close the field lines results in 2 coils with 800000 A^* turns each to provide a field of 2 T. To reduce the operation cost superconducting coils will be used. The current in the coils to generate the required field distribution is $\sim 3000 \text{ A}$ which

generates a maximum field of 3 T in the inner edge of the coil. Indirect cooling will be done using liquid He at 4.5° K. To minimise the eddy currents the ram-up/down time is chosen to be 1/2 an hour. The coil shape consists of two half-circles (radius= 0.5 cm) connected by a 12 cm long straight section. This geometry is found to optimize the field configuration.

Micro-Vertex Detector (MVD)

The determination of the decay vertices of open charm particles ($c\tau = 123 \mu\text{m}$ for D^0 mesons and $c\tau = 314 \mu\text{m}$ for D^\pm mesons) requires detectors with excellent position resolution and a very low material budget in order to reduce multiple scattering. These requirements are met by Monolithic Active Pixel Sensors (MAPS). The pixel size will be between $18 \times 18 \mu\text{m}^2$ and $20 \times 40 \mu\text{m}^2$. A position resolution of $\sigma = 3.5 - 6 \mu\text{m}$ can be achieved depending on the pixel size. The goal of the detector development is to construct a vacuum compatible MAPS detector stations with a total thickness of about 300 - 500 μm silicon equivalent for sensors and support structures, depending on the size of the stations. The MVD consists of 3 MAPS layers located at 5, 10, and 15 cm downstream of the target in the vacuum. This detector arrangement permits to determine the secondary decay vertex of a D-meson with a resolution of about 50-100 μm along the beam axis.

Silicon Tracking System (STS)

The STS is being designed for charged particle tracking in a magnetic field. Its task is to provide track reconstruction and the standalone determination of the event multiplicity. The system will be operated in the magnetic field in order to determine the momentum of the charged particles from the track curvature. From simulations we have seen that the typical track multiplicity of charged particles is up to 700 per central Au+Au collisions at 25 A GeV within the detector acceptance. The STS consists of 8 tracking layers of silicon detectors covering the aperture between the polar angles $2.5^\circ < \theta < 25^\circ$. They are located downstream of the target at distances between 30 cm and 100 cm inside the magnetic dipole field. The number of tracking stations is a tradeoff between precision of a track fit on one hand and special constraints like cost as well as requirement of minimal material budget to reduce the distortion of tracks by multiple Coulomb scattering. The

required momentum resolution is of the order of $\Delta p/p = 1\%$. An essential prerequisite for this is hit reconstruction with efficiency $\epsilon > 95\%$. This performance can only be achieved with an ultra-low material budget not exceeding $1\%X_0$ per tracking station (X_0 being the radiation length of silicon), imposing particular restrictions on the location of power-dissipating front-end electronics in the fiducial volume. Such ultra-thin material budget helps to minimize the multiple Coulomb scattering achieving a momentum resolution of required precision. The STS extends about 1 m along the beam and will be installed in a $\sim 1 \text{ m}^3$ volume inside the 1 T dipole magnet to generate sufficient bending power for momentum measurements and suppress the low energy δ electrons. The concept of the STS tracking is based on silicon microstrip sensors mounted onto lightweight mechanical support ladders. The sensors will be read out through multi-line micro-cables with fast electronics at the periphery of the stations where cooling lines and other infrastructure can be placed. The micro-strip sensors will be double-sided with a stereo angle of 7.5° , a strip pitch of $58 \mu\text{m}$, strip lengths between 20 and 60 mm, and a thickness of $300 \mu\text{m}$ of silicon (equivalent to $0.3\%X_0$). The micro-cables will be built from sandwiched polyimide-Aluminum layers of several $10 \mu\text{m}$ thickness ($0.17\%X_0$).

Ring Imaging Cherenkov Detector (RICH)

The RICH detector is designed to provide identification of electrons and suppression of pions in the momentum range below 10 GeV/c. This will be achieved using a gaseous RICH detector build in a standard projective geometry with focusing mirror elements and a photo detector. CO_2 with a pion threshold for Cherenkov radiation of 4.65 GeV/c will be used as radiator gas. The detector will be positioned behind the dipole magnet about 1.6 m downstream of the target. It will consist of a 1.7 m long gas radiator (overall length approximately 2 m) and two arrays of mirrors and photo detector planes. The mirror plane is split horizontally into two arrays of spherical glass mirrors, $(4 \times 1.5) \text{ m}^2$ each. The 72 mirror tiles have a curvature of 3 m radius, a thickness of 6 mm and a reflective $\text{AL}+\text{MgF}_2$ coating. Rings of Cherenkov radiation will be projected onto two photo detector planes $(2 \times 0.6) \text{ m}^2$ each located behind the CBM dipole magnet and shielded by the magnet yokes. The design of the photo detector plane is based on MAPMTs (e.g. H8500 from Hamamatsu) in order to provide high granularity, high

geometrical acceptance, high detection efficiency of photons also in the near UV region and a reliable operation. In-beam tests with a prototype RICH of real size length showed that 22 photons are measured per electron ring. On the order of 100 rings are seen in central Au+Au collisions at 25 AGeV beam energy due to the large material budget in front of the RICH detector. Still, due to the high granularity (approx. 55 000 channels) and high number of photons per ring, a pion suppression on the order of 500 is expected to be achieved according to simulations.

Muon Chamber System (MUCH)

The experimental challenge for muon measurements in heavy ion collisions at FAIR energies is to identify low-momentum muons in an environment of high particle densities. The CBM concept is to track the particles through a hadron absorber system, and to perform a momentum-dependent muon identification. This concept is realized by segmenting the hadron absorber in several layers, and placing triplets of tracking detector planes in the gaps between the absorber layers. The absorber/detector system is placed downstream of the Silicon Tracking System (STS) which determines the particle momentum. In order to reduce meson decays into muons the absorber/detector system has to be as compact as possible. The actual design of the muon detector system consists of 6 hadron absorber layers (carbon 60 cm, iron plates of 2×20 cm, 30 cm, 35 cm and 100 cm thickness) and 18 gaseous detector planes located in triplets behind each absorber slab. The identification of a muon depends on its momentum which varies with the mass of the vector mesons and with beam energy. The challenge for the muon detectors and for the track reconstruction algorithms is the very high particle density up to a maximum of 0.3 hits/cm^2 per central event in the first detector layers after 20 cm of iron. In case of minimum bias collisions the numbers are factor of 4 down. Hence for a minimum bias reaction rate of 10 MHz this hit density translates into a hit rate of 0.75 MHz/cm^2 . Prototype detectors based on gas electron multiplier (GEM) technology were operated successfully at rates of about 1.4 MHz/cm^2 as measured by anode currents using X-rays. In total, the muon chambers cover an active area of about 70 m^2 subdivided into about half a million channels. The low particle multiplicities behind the muon absorber favors the implementation of a trigger on muon pairs. The trigger

concept is based on the measurement of short track segments in the last tracking station triplet, and extrapolation of these tracks to the target. After selection of tracks with good vertices the event rate can be reduced already by a factor of about 1000 for J/ψ measurements in minimum bias Au+Au collisions. For J/ψ measurements at SIS100 a MUCH start version with 3 chamber triplets is sufficient.

Transition Radiation Detector (TRD)

Three Transition Radiation Detector stations each consisting of 3 detector layers will serve for particle tracking and for the identification of electrons and positrons with $p > 1.5 \text{ GeV}/c$ ($\gamma \geq 1000$). The detector stations are located at approximately 5 m, 7.2 m and 9.5 m downstream the target, the total active detector area amounts to about 600 m^2 . For example, at small forward angles and at a distance of 5 m from the target, we expect particle rates on the order of $100 \text{ kHz}/\text{cm}^2$ for 10 MHz minimum bias Au+Au collisions at 25 AGeV. In a central collision, particle densities of about $0.05/\text{cm}^2$ are reached. In order to keep the occupancy below 5% the minimum size of a single cell should be about 1 cm^2 . The TRD detector readout will be realized in rectangular pads giving a resolution of 300-500 μm across and 3 - 30 mm along the pad. Every second TR layer is rotated by 90 degree. Prototype gas detectors based on multi-wire proportional chamber (MWPC) and GEM technology have been built and tested with particle rates of up to $400 \text{ kHz}/\text{cm}^2$ without deterioration of their performance. The pion suppression factor obtained with 9 TRD layers is estimated to be well above 100 at an electron efficiency of 90%. For measurements at SIS100 only one station with 3 detector layers will be used as an intermediate tracker between the STS and the time of flight (TOF) wall.

Timing Multi-gap Resistive Plate Chambers (MRPC)

An array of Resistive Plate Chambers will be used for hadron identification via TOF measurements. The TOF wall covers an active area of about 120 m^2 and is located about 6 m downstream of the target for measurements at SIS100, and at 10 m at SIS300. The required time resolution is on the order of 80 ps. For 10 MHz minimum bias Au+Au collisions the innermost part of the detector has to work at rates up to $20 \text{ kHz}/\text{cm}^2$. Prototype MRPCs built with low-resistivity glass have been tested with a

time resolution of about 40 ps at 20 kHz/cm². At small deflection angles the pad size is about 5 cm² corresponding to an occupancy of below 5% for central Au+Au collisions at 25 AGeV.

Electromagnetic Calorimeter (ECAL)

A “shashlik” type calorimeter as installed in the HERA-B, PHENIX and LHCb experiments will be used to measure direct photons and neutral mesons (π^0, η) decaying into photons. The ECAL will be composed of modules which consist of 140 layers of 1mm lead and 1mm scintillator, with cell sizes of 3×3 cm², 6×6 cm², and 12×12 cm². The shashlik modules can be arranged either as a wall or in a tower geometry with variable distance from the target.

Projectile Spectator Detector (PSD)

The PSD will be used to determine the collision centrality and the orientation of the reaction plane. A precise characterization of the event is of crucial importance for the analysis of event-by-event observables. The study of collective flow requires a well-defined reaction plane which has to be determined by a method not involving particles participating in the collision. The detector is designed to measure the number of non-interacting nucleons from a projectile nucleus in nucleus-nucleus collisions. The PSD is a full compensating modular lead-scintillator calorimeter which provides very good and uniform energy resolution. The calorimeter comprises 44 individual modules, each consisting of 60 lead/scintillator layers with a surface of 20×20 cm². The scintillation light is read out via wavelength shifting (WLS) fibers by Multi-Avalanche Photo-Diodes (MAPD) with an active area of 3×3 mm² and a pixel density of 10⁴/mm².

Online event selection and data acquisition

High statistics measurements of particles with very small production cross sections require high reaction rates. The CBM detectors, the online event selection systems, and the data acquisition will be designed for event rates of 10 MHz, corresponding to a beam intensity of 10⁹ ions/s and a 1% interaction target, for example. Assuming an archiving rate of 1 GByte/s and an event volume of about 10 kByte for minimum bias Au+Au collisions, an event rate of 100 kHz can be accepted by the data acquisition. Therefore, measurements with event rates of 10 MHz require online event selection algorithms (and

hardware) which reject the background events (which contain no signal) by a factor of 100 or more. The event selection system will be based on a fast on-line event reconstruction running on a high-performance computer farm equipped with many-core CPUs and graphics cards (GSI GreenIT cube). Track reconstruction, which is the most time consuming combinatorial stage of the event reconstruction, will be based on parallel track finding and fitting algorithms, implementing the Cellular Automaton and Kalman Filter methods. For open charm production the trigger will be based on an online search for secondary vertices, which requires high speed tracking and event reconstruction in the STS and MVD. The highest suppression factor has to be achieved for J/ψ mesons where a high-energetic pair of electrons or muons is required in the TRD or in the MUCH. For low-mass electron pairs no online selection is possible due to the large number of rings/event in the RICH caused by the material budget of the STS. In the case of low-mass muon pairs some background rejection might be feasible.

2.6 Dilepton measurements at FAIR

The CBM experimental program puts a special emphasis on measurement of di-leptons. Importance of the lepton pair measurements is discussed in chapter 1. The comparison of precision data with theoretical models has demonstrated that dilepton pairs emitted in energetic heavy ion collisions provide valuable information on the evolution and on the properties of the hot and dense fireball. It was shown, that the in-medium mass distribution of short-lived vector mesons decaying in lepton pairs is modified both due to their coupling to baryon resonances, and by their interaction with the chiral condensate. A careful analysis of the measured dilepton excess yield - i.e. the dilepton mass distribution with the contribution from vector mesons subtracted - allows to extract the thermal radiation, and, hence, the temperature evolution of the fireball. At top SPS energies, the dilepton mass distribution in the intermediate mass range is dominated by radiation from a deconfined phase. Analysis of the latest dimuon data from NA60 collaboration shows that the effective temperature (or inverse slope parameter) T_{eff} , extracted from the pair p_T distribution, of the dimuon excess yield (Drell-Yan contribution subtracted)

is found to increase with invariant mass in the low-mass range. This effect is attributed to the increase of collective flow in the late phase of the collision. In the intermediate mass range, the effective temperature drops. This observation suggests that the intermediate mass dimuons are emitted in the early (partonic?) phase of the collision where the collective flow is not yet developed. The comparison of charmonium yields measured in proton-nucleus and nucleus-nucleus collisions has led to the observation of an anomalous dissociation of charmonium in central collisions of heavy nuclei which was explained by color screening in the quark-gluon phase. This observation still is considered as one of the convincing experimental facts hinting towards the existence of partonic degrees of freedom in the fireball at top SPS energies. The dilepton measurements at the CERN-SPS have been performed mainly at 158 A GeV, except for one spectrum taken in Pb+Au at 40 A GeV by the CERES collaboration where even an increased excess yield has been observed [148]. Similarly there is no data on J/ψ production in heavy ion collisions below top SPS energy. A systematic beam energy scan in order to search for the onset of in-medium mass modifications of vector mesons or for partonic contributions to the dilepton yield or onset of anomalous J/ψ suppression has not been performed yet. Up to date, no dilepton data have been measured in heavy ion collisions in the FAIR energy range, i.e. between about 2 AGeV (with DLS at LBL [146] and HADES at GSI [147]), and 40 A GeV (with CERES at CERN-SPS [148]). With the dilepton measurements in heavy ion collisions at FAIR energies the CBM collaboration will open a new era of dilepton experiments. Moreover, CBM will enter terra incognita: in the beam energy range between 2 and 40 A GeV where the highest net-baryon densities can be created in the laboratory no dileptons have been measured in heavy ion collisions. The CBM experiment will systematically measure both dielectrons and dimuons in p+p, p+A and A+A collisions as function of beam energy and size of the collision system. The dielectron and dimuon high-precision data will complement each other, and will provide a complete picture on dilepton radiation off dense baryonic matter. Therefore, the CBM experiment has a large discovery potential both at SIS100 and SIS300. The experimental challenge in dilepton measurements is to suppress the huge combinatorial background of lepton pairs. In the case of muon measurements, which is one of the major goals of

this thesis work, the muon background is generated by weak decays of pions and kaons, by mismatches of hadrons upstream and muons downstream the hadron absorber, and by hadrons punching through the absorber.

2.7 Running scenario

The total running time at SIS100 is about 10 months beam on target. A large fraction of the physics program can be achieved with event rates between 10^5 and 10^6 collisions/s. Some aspects, like charmonium production at top SIS100 energies or excitation functions of multi-strange baryon and hypernuclei production, require event rates of up to 10^7 collisions/s. The total dose for the STS is dominated by these high-rate runs, equivalent to about 2 month of running at 10^7 Au+Au collisions/s. About 5-10% of the silicon sensors will accumulate a total non-ionising dose of about 6×10^{12} $n_{eq}(1 \text{ MeV})/\text{cm}^2$. At SIS300 the expected running time is about 30 month including at least 15 month of measurements at high rates. The resulting total non-ionising dose accumulated by the sensors close to the beam pipe is in the order of 10^{14} $n_{eq}(1 \text{ MeV})/\text{cm}^2$. The operation scenario foresees an exchange of those sensors in case of higher doses.

Chapter 3

An overview of Charmonium production in nuclear collisions

3.1 Introduction

The focal aim of the high energy heavy ion collisions is to study the color deconfinement and the resulting production of the quark-gluon plasma in the laboratory. However transient nature of the plasma led its identification difficult and it is important to identify a clear signature of the expected occurrence of phase transition to QGP. In this respect, quarkonia which itself is produced in the collision can serve as a potential probe to study the medium produced in the collision. Thus the study of quarkonium production in nuclear collisions, have long been of both theoretical and experimental interest. Survival probability of different quarkonium states depend on the density and (effective) temperature of the system leading to the expectation of progressively suppressed quarkonia yields with increasing collision centrality and/or centre-of-mass energy. Among the different charmonium states the most extensively studied state is the J/ψ meson. It was discovered on 11th November, 1974. J/ψ was the first observed resonance that contained previously unknown but anticipated charm quark and its anti-quark: $c\bar{c}$. However the discovery created a lot of controversy. Observation of J/ψ resonance was simultaneously and independently announced by the Brookhaven National Laboratory [149], in the proton-Beryllium collisions ($p + Be \rightarrow J/\psi \rightarrow e^+e^-$)

Table 3.1: Masses, sizes, mass defects and binding energies of the lowest $c\bar{c}$ and $b\bar{b}$ bound states, obtained within non-relativistic Schrödinger approach. The input parameters for these results are $m_c = 1.25$ GeV, $m_b = 4.65$ GeV, $\sqrt{\sigma} = 0.445$ GeV, $\alpha = \pi/12$.

state	J/ψ	χ_c	ψ'	Υ	χ_b	Υ'	χ'_b	Υ''
mass (GeV)	3.10	3.53	3.68	9.46	9.99	10.02	10.36	10.36
ΔE (GeV)	0.64	0.20	0.05	1.10	0.67	0.54	0.31	0.20
ΔM (GeV)	0.02	-0.03	0.03	0.06	-0.06	-0.06	-0.08	-0.07
r_0 (fm)	0.5	0.72	0.9	0.28	0.44	0.56	0.68	0.78

and by the Stanford Linear Accelerator Centre [150], in the process electron-positron scatterings ($e^+e^- \rightarrow \gamma \rightarrow J/\psi \rightarrow \mu^+\mu^-$). The priority of its discovery was so disputed that it was given two names, dubbed as the J particle at BNL and ψ at SLAC. It had also been realized that since in the SLAC experiment ψ was produced from e^+e^- annihilation through a virtual photon so it had to carry the same quantum numbers as γ , in particular spin 1. Thus it could not be the ground state charmonium rather the lowest lying state with total angular momentum 1 and thus identified as 1^3S_1 state of charmonium. The higher lying states of charmonium family like ψ' and χ_c were later discovered at SLAC. Discovery of J/ψ had been considered as a prominent landmark of particle physics as it confirmed the basic validity of the quark model.

12 years after its discovery, absence of J/ψ mesons in the final state of the high energy nuclear collisions had been suggested as an unambiguous and experimentally viable tool to confirm the production of quark-gluon plasma in the laboratory. In 1986, Matsui and Satz in their seminal paper argued that in a QGP, due to Debye screening by the free color charges, production of J/ψ and other quarkonium resonances would be suppressed.

At FAIR energies, which is our ultimate interest, the production of bottomonium resonances are not feasible. Hence from now onwards we restrict ourselves to charmonium production only. However most of the following discussions are applicable for bottomonia as well.

3.2 Charmonium spectroscopy in vacuum

Due to large mass of the charm quarks ($m_c \gg \Lambda_{QCD} \sim 200$ MeV), their speed is much smaller ($v_c \sim 0.6c$) compared to the light quarks. Hence one widely used approach in depicting charmonium states is to consider its dynamics analogous to atomic systems or positronium and to treat it in the non-relativistic limit by means of the Schrödinger equation with a central binding potential $V(r)$ [105, 151]. Being spherically symmetric, $V(r)$ depends only on the relative separation r between the quark and anti-quark. The equation can then be written as:

$$-\frac{1}{m_c} \{ \nabla^2(r) + V(r) \} \Psi_i(r) = (M_i - 2m_c) \Psi_i(r), \quad (3.1)$$

where $\Psi(r)$ denotes the charmonium wave function¹. Since Eq. (3.1) is a non-relativistic description of the binding, the total rest mass must be subtracted from the masses M_i of the bound states. Once we find the eigenvalues M_i of the system, we can also define the “binding energy” ΔE of each charmonium state, $\Delta E = 2M_D - M_i$. Lattice and spectroscopic studies suggest for the potential $V(r)$ has the form [152]

$$V(r) = \sigma r - \frac{\alpha}{r}, \quad (3.2)$$

generally known as the “Cornell potential”. It is spherically symmetric, and consists of two parts. The linearly rising part, which is dominant at long range, represents the confining force, given in terms of the *string tension* σ ; lattice studies put its value at around 0.2 (GeV)². The second part, dominant at short range is an effective Coulomb potential. It results from one gluon exchange and analogous to QED where the Coulomb interaction arises from single photon exchange. It includes transverse string oscillations; string theory suggests $\alpha = \pi/12$.

Exact solution of Eq. 3.1 gives a very good account of the full (spin-averaged) charmonium spectroscopy as given in Table 3.1 [105]. In addition the bottomonium states are also shown. The line labeled ΔM shows the differences between the experimental and

¹Note that the reduced mass of the $c\bar{c}$ pairs is $m_c/2$, so that we have $-\nabla^2/m$ instead of the usual $-\nabla^2/2m$, for the kinetic energy term.

the calculated values; they are in all cases less than 1 %. r_0 gives the $Q\bar{Q}$ separation for the state (i.e. twice the radius) in question. A fair estimate of the spin-averaged ground state properties can also be obtained by means of a semi-classical formulation. It shows that in vacuum the radius of the J/ψ , to a considerable extent, is still determined by the confining part of the potential. From the above table one can see that in particular J/ψ and lower-lying bottomonium states are very tightly bound ($\Delta E \gg \Lambda_{QCD}$) and of very small spatial size compared to the typical hadrons ($r_0 \ll 2r_h \simeq 2$ fm). When put inside a medium, the J/ψ mesons can only be resolved by a sufficiently hard probe.

3.3 Charmonium dissociation in a thermal medium

After discussing the basic spectroscopic properties of the different charmonium states in vacuum, we now turn to a description of the decay and dissociation of the charmonium states inside a static thermal medium. More details are available in [105, 151]. The basic idea behind this study is to gain insight about the modification of the charmonium properties in a fully equilibrated QCD medium and how that can help us to identify the state of the strongly interacting matter and transitions between different states in terms of observable quantities calculated in QCD. Having learnt this, one can then think of using charmonia as a sensitive probe for characterization of the hot and dense medium expected to be produced in the high energy heavy ion collisions. Till date most of the works related to the in medium spectral properties of charmonium are concentrated to the case of vanishing baryon density ($\mu_B \sim 0$). As alluded above, in vacuum the charmonium spectroscopy is well described by non-relativistic potential models. In a medium the heavy quark potential is subject to screening effects both in its strength and spatial range. The screening occurs with a characteristic radius, called Debye radius (r_D) which determines the range of the screening effect. It decreases with increasing temperature, as the medium increases in density, resulting in weakening of the binding between c and \bar{c} quarks. Eventually a situation arises when a charmonium resonance can longer remain as a bound state and gets melted.

We now turn to the question of how to determine quantitatively the charmonium

dissociation points in a hot QCD plasma. Two different approaches are in vogue to address this problem.

- The first one is the potential model approach where the Schrödinger equation for a charmonium resonance is solved with a temperature-dependent potential $V(r, T)$, obtained either through phenomenological consideration or from heavy quark lattice studies
- The alternative way is to calculate the charmonium spectrum directly in finite temperature lattice QCD.

Though the second approach is the only model independent way, the direct lattice study of charmonium spectra has become possible only a few years back. Much of what is known so far is based on the Schrödinger equation studies with various model inputs. We shall look at each of these approaches in turn.

3.3.1 Potential models for charmonium dissociation

The first quantitative assessment of charmonium dissociation at finite temperature due to color screening was made by Karsch, Mehr and Satz [153]. It was based on screening in the form obtained in one-dimensional QED, the so-called Schwinger model. In this approach, the Cornell potential, Eq. 3.2, operative in vacuum is generalized to non-zero temperature in the form

$$V(r, T) = \frac{\sigma}{\mu(T)} \{1 - e^{-\mu(T)r}\} - \frac{\alpha}{r} e^{-\mu(T)r} \quad (3.3)$$

known as the screened Cornell potential. The T -dependence of the medium is encoded in the “screening mass” $\mu(T) = 1/r_D(T)$, where $r_D(T)$ denotes the Debye screening length of the medium at temperature T . Eq. 3.3 gives the correct zero-temperature limit, Eq. 3.2, for $\mu(T) \rightarrow 0$ as $T \rightarrow 0$. In order to determine the dissociation points for different charmonium states, the corresponding Schrödinger equation with in-medium potential $V(r, \mu)$ is solved to obtain the in-medium binding energies $E_{n,l}(\mu)$ (n, l being the radial and orbital quantum number respectively) from the corresponding bound state masses $M_i(\mu)$. With increasing temperature, the binding energy starts decreasing (from

its vacuum value at $T = 0$) and at the dissociation point the binding energy vanishes, while the binding radius diverges. The result of this model is that the excited states (ψ' and χ_c) become dissociated around $T \simeq T_c$ while the J/ψ survives up to about $T \simeq 1.2T_c$.

Though the Schwinger model approach provides some first insight to the problem of charmonium dissociation in a thermal medium, it suffers from the following disadvantages: (i) The Schwinger form corresponds to the screening of the linear part of the potential (σr), in one space dimension and the actual form in three space dimension is quite different [154]. (ii) The screening mass $\mu(T)$ is calculated from leading order perturbative QCD; lattice studies indicate large non-perturbative corrections close to the deconfinement transition.

To overcome these shortcomings, a comparatively more rigorous approach was suggested where the heavy quark potential is directly calculated in lattice QCD simulations [155, 156, 157, 158, 159]. In this approach, lattice results for the temperature dependence of the free energy of a static quark-anti-quark pair is used to determine the required binding potential. The static $Q\bar{Q}$ studies start from the partition function Z , which is related to the free energy by $Z = \exp(-\beta F)$; this in turn gives the thermodynamic potentials, free energy $F(r, T)$ and internal energy $U(r, T)$. However it is not yet clear whether F , U or a linear combination thereof is to be identified with heavy quark potential $V(r, T)$. Assuming that $U(r, T)$ provides the temperature dependence of the heavy quark potential, and using results from $N_f = 2$ lattice QCD the corresponding Schrödinger equation can be solved. Dissociation temperatures are determined as earlier by the infinite size or zero binding energy of the system. The results obtained from such studies indicate that the ψ' and χ_c are dissociated around a temperature $T \simeq 1.1T_c$ but J/ψ survives in the medium up to a temperature $T \simeq 2 T_c$. Comparing these results to the ones from the Schwinger model, we see that while there is agreement in the case of the higher excited states, lattice potential models with $V = U$, predict a considerably higher dissociation temperature for the J/ψ . However if one directly uses the free energy, F of the static $c\bar{c}$ pair as the binding potential, resulting dissociation temperatures for all the charmonium states are in agreement with Schwinger model ap-

proach. F and U are thus better to be considered as the two limits of the heavy quark potential V , which corresponds to a slow and rapid charmonium dissociation inside hot deconfined medium. For a rapid dissociation process, there is no heat exchange between the heavy quarks and the medium and the potential is just the internal energy U of the pair; while for a slow dissociation process there is enough time for the heavy quarks to exchange heat with the medium and hence F represents the binding potential. The potential well is deeper for the case $V = U$ and leads to much stronger binding resulting higher dissociation temperatures. However it has also been realized that since the entropy changes rapidly across the deconfinement temperature, the internal energy computed on lattice provides more binding than vacuum potential. In literatures, a number of effective potentials between F and U having the form $aU + (1 - a)F$, with $0 \leq a \leq 1$, is used in the Schrödinger equation to evaluate charmonium evolution in a thermal QCD medium. Such potentials tend to reduce binding and lower the dissociation temperature as a is decreased. Recently attempts have been made to estimate effect of relativistic corrections to the dynamical evolution of charmonium in the hot medium [160]. For this purpose the covariant relativistic Schrödinger equation is solved and the ground and excited state wave functions are obtained for the charmonium states at finite temperature. Subsequent determination of dissociation temperature shows, T_d for J/ψ increases by 7% to 13% when the central potential is varied between free energy (F) and internal energy (U). Such corrections for bottomonium states are found to be negligible. Another important point to note is that the potential used in the dynamical equations to find the dissociation temperatures is calculated for a static $c\bar{c}$ pair. In practice, the charmonium produced in high energy nuclear collisions will be moving and it is important to investigate the velocity dependence of the charmonium dissociation temperature [161]. It has been observed that including the relaxation of the medium induced by the relative velocity between charmonia and the deconfined expanding matter, the Debye screening is reduced and the charmonium dissociation takes place at a higher temperature, compared to the static case. As a consequence of the velocity dependent dissociation temperature, the quarkonium suppression at high transverse momentum is significantly weakened in high energy nuclear collisions at RHIC and LHC.

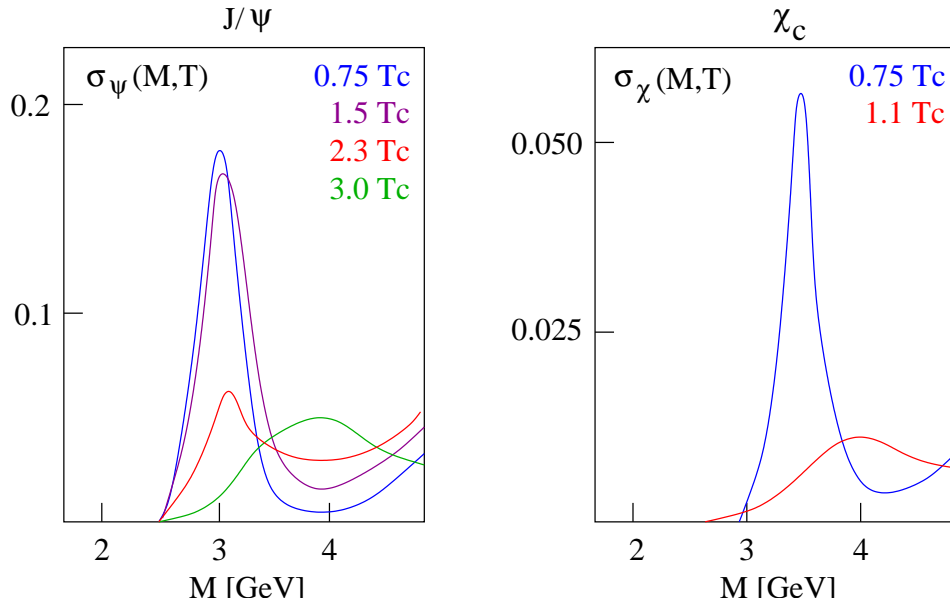


Figure 3.1: Schematic view of lattice results for charmonium dissociation. The figure is adopted from [151]

3.3.2 Lattice studies of charmonium correlator

The ideal way to resolve the above ambiguity would be to calculate the $c\bar{c}$ spectrum directly on the lattice, as is being done by the present state-of-the-art lattice studies [162, 163, 164, 165, 166, 167]. Effects of the hot medium are imprinted on the spectral function. More specifically, they calculate the $c\bar{c}$ spectrum $\sigma(\omega, T)$ in the appropriate quantum channel, as a function of the temperature T and the $c\bar{c}$ energy ω . Bound-states show up as resonances in a plot of σ versus ω . By performing simulations at different temperatures, one can determine the temperature at which a particular peak disappears into the background of continuum states which gives the clear indication of the melting of a bound-state. This in turn allows to determine the dissociation temperature (T_d) of that particular charmonium resonance. A schematic illustration is shown in Fig. 3.1. The results presently indicate that χ_c is dissociated for $T \geq 1.1T_c$ whereas J/ψ persists up to $1.5 < T/T_c < 2.3$. Thus, on the basis of lattice studies, the following picture emerges: The higher excited states dissociate around $T = T_c$, while the J/ψ survives up to much higher temperature, in accord with the potential model studies based on the internal energy $U(r, T)$.

There is, however, a caveat to these calculations. The discretization introduced by the lattice limits the resolution of the peak. Lattice methods are thus useful in deter-

mining the position and to some extent the amplitude of the peaks, but determining the peak *widths* remains a challenge, nor is it easy to study the spectrum in the continuum region ($\omega > 4$ GeV).

In all the above studies the estimation of dissociation temperatures for different charmonium states are precisely related to the zero binding of that particular state. However recently Laine and collaborators [168] have shown that the real time static $Q\bar{Q}$ potential has an imaginary part in addition to the real part. As a result the binding energy of the different charmonium states will also have both real and imaginary parts. The imaginary part endows the charmonium a thermal width at any finite temperature T . Explicit calculations indicate with increase of temperature while the real part of the in-medium binding energy $\epsilon_B(T)$ decreases its imaginary part increases. A state can then be considered as dissociated at the temperature when the two parts become comparable i.e. the thermal medium effects of $\sim T$ are comparable to the binding energy. Above this temperature the state will decay faster than it binds. At finite temperature this new definition of T_d [169] is considered more realistic than the older idea of zero binding condition which makes sense only at zero temperature.

In closing we note that all the above studies are performed in a baryon less medium. Though lattice QCD has emerged as the most reliable tool to address particularly the non-perturbative issues in QCD, progress in the application of the lattice computations in a baryon rich medium is hindered by yet unsolved sign problem. Over the years some techniques like Taylor series expansion, re-weighting and imaginary chemical potential have been suggested to bypass the sign problem and employ the lattice simulations at finite baryon density. However they are applicable in the domain of $\frac{\mu_B}{T} \lesssim 1$. In [170], the authors have studied the heavy quark free energies and screening at finite temperature and density, for 2-flavor QCD. A small but finite baryon number density is included via a 6th order Taylor expansion of the fermion determinant in the baryo-chemical potential μ_B , that circumvents the sign problem. The Taylor expansion coefficients of color singlet and color averaged free energies have been calculated and from this the expansion coefficients for the corresponding screening masses are determined. They have observed that for small μ_B the free energies of a static quark anti-quark pair decrease in

a medium with a net excess of quarks, to the first order in μ_B^2 and that screening is well described by a screening mass which increases with increasing μ_B . This suggests that the screening length in a baryon rich or anti-baryon rich quark-gluon plasma decreases with increasing net quark or anti-quark density. This is consistent with the common expectation that presence of non-zero μ_B shifts the deconfinement transition to lower temperatures. However these calculations suffer from the use of unrealistically large pion mass as input. Till date no results are available from lattice QCD for realistic values of pion mass or at large baryon densities. Due to lack of reliable direct lattice simulations, parallel efforts are underway way to study the charmonium dissociation a hot and baryon dense medium using potential model approach [171].

3.4 Overview of Charmonium Production in Nuclear Collisions

After a brief review of the charmonium spectroscopy in vacuum and in a static QCD medium, in this section we take a look on the different dynamical aspects of charmonium production in nuclear collisions. Thus study of charmonium or more specifically J/ψ production in nuclear collisions, as a potential probe for QGP formation, have long been of both theoretical and experimental interest. However to in order to unambiguously identify charmonia (or rather is depleted production) as a probe to the deconfined matter, one needs a clear understanding about its production in vacuum and how the production is affected in presence of a hadronic medium is essential. We thus first consider the issue of charmonium production in elementary $p + p$ collisions and then in $p + A$ collisions where the production is affected by the presence of the normal nuclear medium. Finally we shall describe the charmonium production in nuclear collisions. One may note in this respect that m_c is significantly larger than typical temperatures in the early stages of heavy-collisions, even at the highest currently available collision energies, $T_0 \simeq 0.5 - 0.6$ GeV at top LHC energy. Consequently, charm-quark production is expected to be dominated by primordial N-N collisions, and thus can be bench marked rather reliably via binary scaling from $p + p$ reactions.

3.4.1 Charmonium Production in Hadronic Collisions

Pedagogically charmonium production in hadron-hadron collisions, is believed to be a two stage process. The first stage is the production of $c\bar{c}$ pairs. Because of the large quark mass ($m_c \sim 1.5 \text{ GeV}$) this is a hard process, with the hard-scattering scale usually set by a large momentum transfer ($Q^2 \geq 4m_c^2$). Due to asymptotic freedom the running coupling $\alpha_s(Q^2)$ is correspondingly small which allows one to use perturbative QCD to calculate $c\bar{c}$ production cross section. A parton from the projectile interacts with one from the target; the (non-perturbative) parton distribution within the hadrons are determined empirically in other reactions eg. by deep inelastic lepton-hadron scattering. At sufficiently high collision energies $c\bar{c}$ production dominantly occurs by gluon fusion ($gg \rightarrow c\bar{c}$). In low energy collisions, in addition to gluon fusion, quark-anti-quark annihilation ($q\bar{q} \rightarrow c\bar{c}$) also plays a significant role. The $c\bar{c}$ so produced in general is in a color

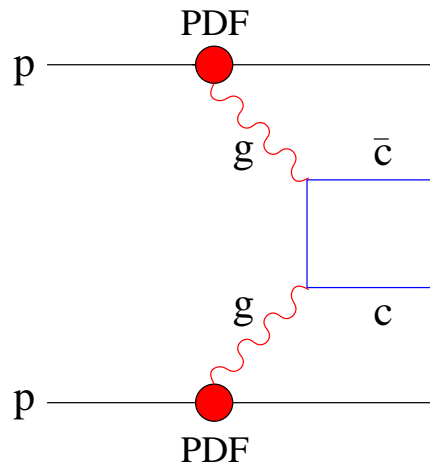


Figure 3.2: Feynman diagram showing the production of $c\bar{c}$ pairs in hadronic collision through gluon fusion, in leading order perturbative QCD.

octet state. It has to neutralize its color in order to leave the interaction zone and form a physical resonance like J/ψ or ψ' among the others. In the second stage, the color neutralization occurs by interaction with the surrounding color field which results finally forms the physical bound state. This stage is non perturbative in nature. Over the years, the main debate on the mechanism of J/ψ production is focused on this non-perturbative component of color neutralization, which is not yet fully understood on a fundamental theoretical level. However this nonperturbative evolution of the $c\bar{c}$ pair into an observed charmonium state has been discussed extensively in terms of phenomenological models

and in terms of the language of effective theories of QCD. Different treatments of this evolution have led to various theoretical models for inclusive charmonium production. Most notable among these are the color evaporation model (CEM) [172], and the non-relativistic QCD (NRQCD) [173] approach which can accommodate both color singlet model (CSM) [174] and the so-called color octet model (COM) [175]. Here we briefly describe each of them.

The color-singlet model

The Color Singlet model (CSM) was first proposed shortly after the discovery of the J/ψ . A detailed account of this model can be found in [176]. In this model, it is assumed that the $c\bar{c}$ pair that evolves into the quarkonium is in a color-singlet state and that it has the same spin and orbital angular-momentum quantum numbers as the quarkonium. The production rate for each quarkonium state is related to the absolute values of the color-singlet $c\bar{c}$ wave function and its derivatives, evaluated at zero $c\bar{c}$ separation. These quantities can be extracted by comparing theoretical expressions for quarkonium decay rates in the CSM with experimental measurements. Once this extraction has been carried out, the CSM has no free parameters. The CSM was successful in predicting quarkonium production rates at relatively low energy. However after the arrival of Tevatron data from CDF Collaboration [177], it was observed that CSM seriously underestimates the prompt J/ψ and ψ' production cross section, in $p + \bar{p}$ collisions, particularly in the high p_T domain. Recently, it has been found that, at high energies, very large corrections to the CSM appear at next-to-leading order (NLO) and next-to-next-to-leading order (NNLO) in α_s [178, 179, 180]. Consequently, the possibility that the CSM might embody an important production mechanism at high energies has re-emerged. However, given the very large corrections at NLO and NNLO, it is not clear that the perturbative expansion in α_s is convergent. Furthermore, in the production and decay of P -wave and higher-orbital-angular-momentum quarkonium states, the CSM is known to be inconsistent because it leads to uncanceled infrared divergences. (see Ref. [181] and references therein.) As we shall shortly see, the NRQCD factorization approach encompasses the color-singlet model, but goes beyond it.

The color-evaporation model

The color evaporation model (CEM) was proposed in 1977 [172] and has enjoyed considerable phenomenological success over the years. CEM (also known as semi-local duality approach) is motivated by the principle of quark-hadron duality. In the evaporation process, the $c\bar{c}$ can either combine with light quarks to form open charm mesons (D and \bar{D}) or bind with each other to form a hidden charm/charmonium state. A fixed fraction of the sub-threshold $c\bar{c}$ production is used in charmonium production. The basic quantity in this picture is the total sub-threshold charm cross section $S_{c\bar{c}}$, obtained by integrating the perturbative $c\bar{c}$ production cross section σ over the mass window from $2m_c$ to $2m_D$. Production cross section of any particular charmonium state H is then given by an empirical constant F_H that is energy-momentum and process independent. Once F_H has been fixed by comparison with the measured total cross section for the production of the resonance H , the CEM can predict, with no additional free parameters, the momentum distribution of the produced charmonium states. An immediate further consequence of the CEM is that the production ratios of different charmonium states, must be energy independent. Both these predictions have been compared in detail to charmonium hadro-production data over a wide range of energies [182]. They are found to be well supported, both in the energy dependence of the cross sections and the constancy of the relative species abundances. Although the color evaporation model provides a viable phenomenological description of the hadroproduction of quarkonia, leading to correct quantitative predictions up to the highest energies under consideration, it cannot predict the fractions f_i of the hidden charm cross sections. Moreover it does not give any insight to the space-time evolution of color neutralization process. However for charmonium production in proton-nucleus and nucleus-nucleus collisions, this evolution is crucial which in turn calls for a more detailed description of color neutralization absent in the evaporation approach.

The color-octet model

Another model used to describe the hadroproduction of J/ψ is the so called Color Octet Model (COM). In the color octet scenario, the $c\bar{c}$ pair produced in the first stage of the

collision, is assumed to be in the color-octet state $(c\bar{c})_8$. In order to form the physical resonance state it has to neutralize its color and attain the quantum numbers of that particular state. The color octet model proposes that the color octet $c\bar{c}$ state propagates in the medium together with a soft collinear gluon. After a short relaxation time τ_8 this pre-resonance state $(c\bar{c} - g)$ turns into physical resonance by absorbing the accompanying gluon, with similar formation processes for other resonances like χ_c and ψ' production. The color neutralization time τ_8 of the pre-resonant state can be essentially estimated by the lowest momentum possible for the confined gluons $\tau_8 \simeq \frac{1}{\sqrt{2m_c\Lambda_{QCD}}} \simeq 0.25$ fm. The formation time for actual physical ground state (say J/ψ) is presumably somewhat larger than τ_8 . Although $r_{J/\psi} \sim \tau_8$, the massive charm quarks move non-relativistically. For the larger higher excited states, depending on their size, the formation time will then be correspondingly larger. The color octet model encounters difficulties if the collinear gluons are treated perturbatively, indicating once more that color neutralization seems to require non-perturbative elements. However it does provide a conceptual basis for the evolution of the formation process.

The NRQCD factorization approach

The NRQCD (Non-Relativistic QCD) factorization approach [175] to heavy-quarkonium production is by far the theoretically most sound and phenomenologically most successful. NRQCD is an effective field theory obtained by integrating out the modes of energy and momentum from the QCD Green functions which describe the heavy quark-anti-quark ($Q\bar{Q}$) pairs. It is built in such a way that it describes the dynamics of $Q\bar{Q}$ pairs (not necessarily the same flavor) at energy scales in the center of mass frame much smaller than their masses. Since the heavy quark mass is much larger than Λ_{QCD} , the QCD running coupling constant is much less than unity ($\alpha_s(m_c) \sim 0.25, \alpha_s(m_b) \sim 0.18$) but perturbation theory can not directly applied due to the nonperturbative effects associated with the quarkonium bound state dynamics. Hence QCD factorization technique is explicitly used to separate out the short distance high momentum effects from long distance low momentum part. In the NRQCD factorization approach, the inclusive cross section for the direct production of a quarkonium state H is written as a sum of products

of these NRQCD matrix elements with the corresponding $Q\bar{Q}$ production cross sections:

$$\sigma(H) = \sum_n \sigma_n(\Lambda) \langle \mathcal{O}_n^H(\Lambda) \rangle. \quad (3.4)$$

Here Λ is the ultraviolet cutoff of the effective theory. The σ_n are process independent expansions in powers of v of the cross sections to produce a $Q\bar{Q}$ pair in the color, spin, and orbital-angular momentum state n . The σ_n are convolutions of parton-level cross sections at the scale p with parton distribution functions. (The former are short-distance quantities, while the latter are long-distance quantities that depend on the nonperturbative dynamics of the initial hadrons). The matrix elements $\langle \mathcal{O}_n^H(\Lambda) \rangle$ contain the nonperturbative physics associated with the $Q\bar{Q}$ evolution into a measurable quarkonium state. One may note that Eq. 3.4 represents both processes in which the $Q\bar{Q}$ pair is produced in a color-singlet state and processes in which the $Q\bar{Q}$ pair is produced in a color-octet state. The NRQCD factorization is sometimes erroneously called the 'Color Octet Model' since the color octet terms are expected to dominate in some specific situations, such as J/ψ production at large p_T in hadron colliders. However, there are situations where color singlet terms are expected to be most significant ones, as in J/ψ production in e^+e^- collisions.

A further important aspect of charmonium production in elementary collisions is that the observed (1S) ground state J/ψ is partially produced through feed-down from higher excited states [183]. Of the observed J/ψ rates, only some 60 % is a directly produced J/ψ (1S) state; about 30 % comes from $\chi_c(1P)$ and 10 % from $\psi'(2S)$ decay. Because of the narrow width of the excited states ($\Gamma \sim 100$ keV), their decay occurs well outside any interaction region. The presence of any medium in nuclear collisions would therefore affect these excited states themselves, and not their decay products.

So far as the experimental situation is concerned, J/ψ production in hadronic collisions has been measured over a wide range of energies, starting from the threshold up to the LHC energies. The kinematic threshold for J/ψ production in $p + p$ collision, is $\sqrt{s_0} \simeq 5$ GeV, in the CM frame. J/ψ is identified via its decay into lepton pair, through the peak in di-lepton invariant mass distribution. Both electron and muon channels had been explored in the experiments. They have almost identical branching

Table 3.2: Inclusive J/ψ production cross section in the di-lepton channel for $p + p$ collisions as measured by different fixed target experiments

Experiment	$\sqrt{s_{NN}}$ [GeV]	Cuts	channel	B. R (%)	$B\sigma$ [nb]
CERN-PS [184]	6.9	$p_T \leq 0.3$	e^+e^-	6.9 ± 0.9	$(3.86 \pm 1.1) \times 10^{-2}$
WA39 [185]	8.9	$x_F > 0.$	$\mu^+\mu^-$	7.0	$(7 \pm 0.35) \times 10^{-2}$
NA3 [186]	17.3	$x_F > 0$	$\mu^+\mu^-$	7.4 ± 1.2	–
NA3 [186]	20	$x_F > 0$	$\mu^+\mu^-$	7.4 ± 1.2	3.364 ± 0.464
NA51 [187]	30	$-0.18 \leq x_F \leq 0.14$	$\mu^+\mu^-$	-	5.5 ± 0.06

ratio. Hadroproduction of J/ψ mesons has been studied over many years and with a variety of hadronic systems like $p + p$ collisions, $\pi + p$ collisions and $\bar{p} + p$ collisions. Since our ultimate aim is to estimate J/ψ production in heavy ion collisions we stick to the $p + p$ collisions only. Quarkonium production cross sections in $p + p$ collisions are usually reported as a function of x_F and p_T . Total cross sections are never really measured in a single experiment since no experiment covers the entire phase space. However the experiments do report total cross sections, at least in the forward ($x_F > 0$) region. The required extrapolation to the unmeasured regions of phase space is very sensitive to the way the data has been characterized. In Table 3.2 we have given the inclusive J/ψ production cross section in the di-lepton channel, as measured by different experiments from the lowest up to the ISR energies, but not beyond. A global analysis of the data sets however requires the suitable corrections for limited kinematic acceptances and different value of the branching ratios.

The invariant cross section is usually assumed to be factorisable with the data fit to separate functional forms describing the x_F and p_T distributions,

$$E \frac{d\sigma}{d^3p} = \frac{1}{\pi} \frac{d\sigma}{dy dp_T^2} = \frac{1}{\pi} \frac{E}{p_{max}} \frac{d\sigma}{dy dp_T^2} = f(x_F) \times g(p_T) \quad (3.5)$$

where $p_{max} = \sqrt{s}/2$ and $-1 \leq x_F \leq 1$ in the centre of mass frame. The x_F distribution is assumed to be symmetric about $x_F = y = 0$ in $p + p$ interactions, the data are usually fit to the invariant form,

$$E \frac{d\sigma}{dx_F} \sim (1 - x_F)^d \quad (3.6)$$

or the non-invariant form ,

$$\frac{d\sigma}{dx_F} \sim (1 - x_F)^c \quad (3.7)$$

while the p_T distribution is usually parameterized as

$$g(p_T) \sim \exp(-bp_T) \text{ or } \exp(-ap_T^2) \quad (3.8)$$

The factorization given in Eq. 3.5 is difficult because x_F itself is a function of p_T , $x_F = \frac{2m_T}{\sqrt{s}} \sinh(y)$. Quarkonium production cross sections are usually reported either as integrated over forward region of phase space, ($x_F > 0$) in the center of mass or in the central rapidity region ($y_{c.m.} = 0$). Since the fixed target experiments are forward focused, most of the forward x_F region is accessible so that extrapolation to $x_F > 0$ is reasonable. The x_F distributions narrow down with increasing collision energy, so that at high energies the exponents d and c become large while the measurable x_F range shrinks. To expand information in the limited x_F range, the centre-of-mass rapidity of J/ψ meson is sometimes favored in collider experiments where the cross section is often reported only at mid-rapidity ($y_{c.m.} \approx 0$).

In literature, there are also different parameterizations available for inclusive J/ψ production in elementary NN collisions, from different fixed target experiments. We here review some of them below.

One of the oldest parameterizations available from E672 Collaboration [188] and valid for collision energies $\sqrt{s} \leq 31$ GeV is called Schuler parametrization. It gives the total cross section in the forward hemisphere ($x_F \geq 0$) without including the branching ratio to lepton pairs, as:

$$\sigma(x_F > 0) = \sigma_0 \left(1 - \frac{m_J}{\sqrt{s}}\right)^n \quad (3.9)$$

where $n = 12.0 \pm 0.9$ and $\sigma_0 = 638 \pm 104$ nb for a proton beam and $m_J = 3.097$ GeV is the J/ψ mass.

Slightly different parametrization is available from the E771 Collaboration [189] which studies J/ψ production in p+Si interactions with 800 GeV/c proton beam. Data were collected in the di-muon channel with an open geometry large acceptance fixed

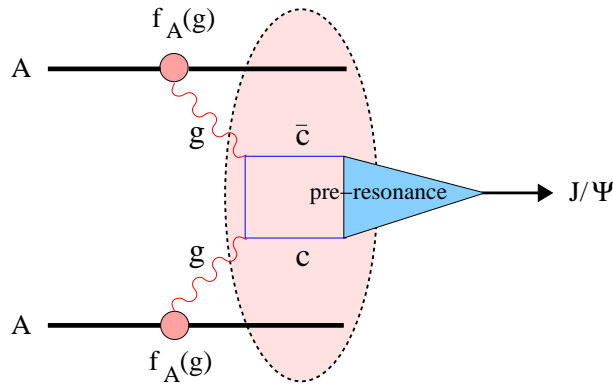


Figure 3.3: A schematic diagram showing the evolution of J/ψ production in nucleon-nucleus collision. The figure is adopted from [151]

target spectrometer. Inclusive cross section per nucleon are obtained with an atomic weight dependence A^α with $\alpha = 0.92 \pm 0.008$. The parametric form reads as :

$$B_{\mu\mu}\sigma = \sigma_0 \left(1 - \frac{m_J}{\sqrt{s}}\right)^\beta \quad (3.10)$$

where $\beta = 11.7 \pm 0.5$ and $\sigma_0 = 59 \pm 6$ nb and $B_{\mu\mu}$ is the branching ratio for di-muon channel.

Parametrization of a compilation of data by Lourenco [190] gives:

$$B_{\mu\mu}\sigma(x_F > 0) = 37 \left(1 - \frac{m_J}{\sqrt{s}}\right)^{12} \quad (3.11)$$

Finally we resort to a more recent calculation based on scaling analysis of near threshold quarkonium production off cold nuclear matter [191]. Following this analysis the J/ψ production in elementary $p + p$ collisions can be written as:

$$B_{\mu\mu}\sigma = B f_1 Y^{\beta_0} \quad (3.12)$$

where f_1 is a dimensionless parameter, $Y = \frac{1}{2} \log\left(\frac{s}{s_0}\right)$, with s_0 being the square of the threshold energy for J/ψ production, in equivalent NN center of mass frame.

All the above parametrizations have been found to describe the existing data corpus with reasonable accuracy.

3.4.2 Charmonium production in $p + A$ collisions

Proton-nucleus ($p + A$) collisions are believed to be an ideal measure of nuclear effects on charmonium production. In $p + A$ collision there is usually no formation time for the medium, so that such collisions provide a tool to probe charmonium production, evolution and absorption in confined matter. Since we eventually want to probe the effect which the ‘secondary’ medium produced by nucleus-nucleus collisions has on charmonium production, it is essential to account correctly for any effects of the ‘primary’ nuclear medium initially present. The nuclear effects can arise in all evolution stages of J/ψ production, and a number of different phenomena, collectively known as cold nuclear matter (CNM) effects have been identified studied in considerable detail. The two most important nuclear effects identified so far are:

- The presence of other nucleons in the nucleus can modify the initial state parton distribution functions, which enter in the perturbative $c\bar{c}$ production process. This can lead to a decrease (shadowing) or an increase (anti-shadowing) of the production rate.
- Once it is produced the $c\bar{c}$ pair will evolve through the nuclear matter during which it can undergo dissociation both in the pre-resonance as well as in the resonance stage, caused by successive interactions with the target nucleons.

Apart from these two effects another important effect is the energy loss of the partons before they fuse to produce a heavy quark pair. Due to these cold matter effects, charmonium production is expected to get modified inside the nuclear medium as compared to hadronic collisions. The modification occurs before any QGP formation takes place and is independent of the effects due to a deconfined medium having free quarks and gluons. So far as measurements of charmonium production in $p + A$ collisions are concerned one unambiguous feature observed in all the experiments is that the production cross section per nucleon decreases with increase of the target mass A .

Two approaches are commonly followed for quantification of nuclear effects in charmonium production in $p + A$ collisions. Traditional way to characterize the nuclear effects in charmonium production is the so called α -*parametrization*, which is generally

Table 3.3: Variation of the parameter α for J/ψ production, with beam energy in $p + A$ collisions, from different fixed target experiments. Measurements are performed either in di-muon or in di-electron channel.

Experiment	E_{CM} [GeV]	Targets	Phase space	α
CERN-PS [184]	6.9	p, C, W	$p_T \leq 0.3$	0.92 ± 0.09
NA60 [197]	17.3	Be, Al, Cu, In, W, Pb, U	$0.28 < y_{cm} < 0.78$	0.882 ± 0.009 ± 0.008
NA3 [186]	19.4	p, Pt	$x_F > 0$	0.94 ± 0.03
NA38 [192]	19.4	Cu, W, U	$0 < x_F < 0.5$	0.911 ± 0.034
E331 [193]	20.6	C, Sn	$x_F > 0.15$	0.91 ± 0.05
NA38 [192, 194]	29.1	C,Al,Cu, W	$-0.11 < x_F < 0.16$	0.919 ± 0.015 ± 0.02
NA38 [195]	29.1	C, Cu, W	$0 < x_F < 0.15$	0.95 ± 0.02
NA50 [196]	28.3	Be, Al, Cu, Ag, W, Pb	$-0.425 < y_{cm} < 0.575$	0.925 ± 0.009
NA60 [197]	28.3	Be, Cu, Ag, W, Pb,U	$-0.17 < y_{cm} < 0.33$ ± 0.009	0.927 ± 0.013
NA50 [198]	29.1	Be, Al, Cu, Ag, W	$-0.5 < y_{cm} < 0.5$	0.928 ± 0.015
E771 [189]	38.8	Si	$-0.1 < x_F < 0.3$	0.92 ± 0.008
E772 [199]	38.8	d, C, Ca, Fe, W	$-0.15 < x_F < 0.65$	0.92 ± 0.008
E789 [201]	38.8	Be, C, W	$-0.1 < x_F < 0.1$	0.888 ± 0.026
E789 [200]	38.8	Au	$-0.35 < x_F < 0.135$	0.9 ± 0.02
E866 [202]	40.0	Be, Fe, W	$-0.065 < x_F < 0.9$	0.96 ± 0.01
HERAB [203]	42.8	C, Ti, W	$-0.34 < x_F < 0.14$	0.981 ± 0.015

followed to study the nuclear target dependence of all the hard processes including charmonium production. In this method the target mass (A) dependence of the charmonium production cross section is fitted with a simple power law:

$$\sigma_{pA} = \sigma_0 \times A^\alpha \quad (3.13)$$

where the exponent α , extracted from the data encodes all the nuclear effects. Measured values of α are found to be less than unity which then indicates suppression of charmonium production in nuclear medium. Note that α is an effective quantity that includes all possible nuclear effects present in the initial and final stage, leading to the reduction of J/ψ yield in $p + A$ collisions compared to hadronic collisions. In case there are no initial state effects, the case $\alpha = 1$ is for particles which once produced do no interact with the surrounding medium. For example, this is almost true for the muon

pairs produced in Drell-Yan process at SPS energy regime. The NA50 Collaboration at SPS has measured the Drell-Yan production cross section in $p + A$ collisions with 400 GeV proton beam and a variety of targets from Be to Pb. Their analysis indicated $\alpha_{DY} = 0.982 \pm 0.021$, indicating small initial state effects. Different experiments had measured $\alpha_{J/\psi}$ in $p + A$ collisions using variety of targets and for different proton beam energies. In Table 3.3, we give the value of $\alpha_{J/\psi}$, integrated over the experimental kinematic acceptance, as reported by different fixed target experiments. Highest value of α are from experiments with hydrogen target. It was concluded subsequently that when results from $p + p$ collisions are considered together with $p + A$ data to extract α , results are often inconsistent with a fit to the $p + A$ data alone, with deuterium or beryllium as the lightest target [109]. Compared to J/ψ production less information is available for nuclear target mass dependence of ψ' production. The first significant result came from E772 Collaboration[199], which reported $\alpha_{\psi'}$ consistent with high statistics J/ψ result. This observation of lack of noticeable difference between ψ' and J/ψ suppressions in $p + A$ collisions was consistent with the color octet model of charmonium production. It indicated that the object being propagated and suppressed inside the target nucleus is not one of the two physical resonances rather a common precursor $(c\bar{c}g)_8$ colored state. This observation was contradicted once the results from E866/NuSea Collaboration [202] became available. They studied p+Be, p+Fe and p+W interactions with an incident proton beam energy of 800 GeV and found that over a broad range of x_F suppression patterns for J/ψ and ψ' are different with $\alpha_{\psi'} > \alpha_{J/\psi}$. Later the measurements available from HEBA-B Collaboration at DESY and NA50 and NA60 Collaborations at SPS also supported this observation.

The evolution of α with x_F and p_T has also been studied using differential measurements in order to have deeper insight of the nuclear suppression effects on J/ψ kinematics. A compilation of $\alpha_{J/\psi}$ values as a function of x_F as obtained from different fixed target experiments is available by NA60 Collaboration [197] and is plotted in Fig. 3.4.

Two main features that emerged from the comparison of different experiments are:

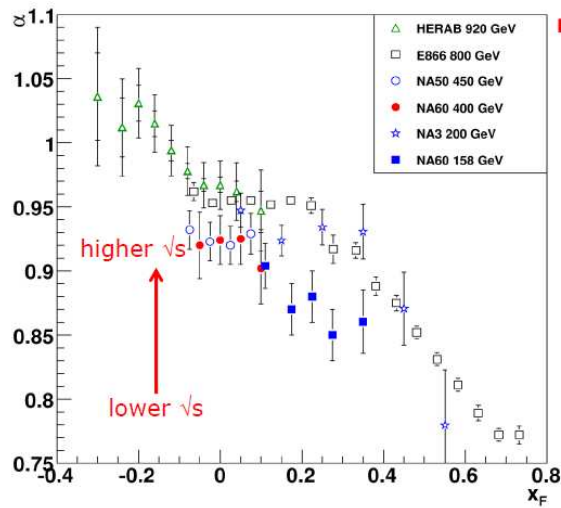


Figure 3.4: The evolution of α as a function of x_F for J/ψ production in $p + A$ collisions at different energies. The figure is adopted from [197]

1. While moving from negative x_F towards positive x_F regime, α steadily decreases, an effect which was already known from HERA-B and E866 measurements performed at close incident proton beam energies (920, 800 GeV).
2. At a given x_F , α is smaller when the incident proton energy is lowered, as seen by comparison of the HERA-B/E866 results with NA60 results at 400 and 158 GeV. On the other hand, α values extracted from the NA3 measurements of J/ψ production at 200 GeV $p + p$ and $p + \text{Pt}$ collisions has been found to be in partial disagreement. They are close to the values obtained from higher energy data samples (E866/HERA-B), even after correcting for the bias introduced by the use of hydrogen as the lighter target.

A satisfactory interpretation of the complex observed pattern is still missing. Various theoretical calculations have underlined the importance of several cold nuclear matter effects, including final state dissociation, initial state parton shadowing, initial and final state parton energy loss and the presence of a charm component in the nuclear wave function. Relative contributions of these effects are still under debate.

A much more rigorous formalism to describe the observed charmonium production cross-sections is provided by the Glauber model [204, 57, 58, 205]. The application of Glauber systematics to describe J/ψ production in nuclear collisions requires as input parameters the inelastic nucleon-nucleon cross section and density distributions for var-

ious nuclei. Having these quantities as input parameters the model gives as an output σ_{abs} , which represents the break-up cross section of the $c\bar{c}$ pair in its pre-resonance or resonance state due to inelastic collisions with the target nucleons along its path. Following Glauber systematics the charmonium production cross section in $p + A$ collisions can be written as:

$$\sigma_{pA} = \frac{\sigma_{NN}}{\sigma_{abs}^G} \int d\mathbf{b}_A [1 - (1 - T_A(\mathbf{b}_A)\sigma_{abs}^G)^A] \quad (3.14)$$

σ_{abs}^G represents the charmonium absorption cross section and σ_{NN} is the elementary nucleon-nucleon cross section for charmonium production. Its value is extracted from a fit to several nuclear targets and not from a single measurement done in $p + p$ collisions. $T_A(\mathbf{b})$ is the nuclear thickness function defined as the nuclear density per unit surface area. Often the detailed Glauber calculation, is approximated, in first order, by a simplified $\langle \rho L \rangle$ exponential parameterization:

$$\frac{1}{A}\sigma_{pA} = \sigma_{NN} \exp(-\sigma_{abs}^{\langle \rho L \rangle} \langle \rho L \rangle) \quad (3.15)$$

Here $\langle \rho L \rangle$ denotes the average amount of nuclear matter crossed by the pre-formed charmonium state from its production point up to exiting from the nucleus. One obtains this formula by expanding the term in square parentheses in powers of σ_{abs} and retaining up to the terms σ_{abs}^2 . $\langle \rho L \rangle$ can be calculated as:

$$\langle \rho L \rangle = \frac{A-1}{2} \int d\mathbf{b} [T_A(\mathbf{b})]^2 \quad (3.16)$$

The $\langle \rho L \rangle$ parametrization can be connected to the α parametrization through the relation:

$$\alpha \simeq 1 - \sigma_{abs} \frac{\langle \rho L \rangle}{\ln A} \quad (3.17)$$

We should take note of the fact that both α and σ_{abs} as reported by the experiments, are effective quantities, used to describe the convolution of all cold nuclear matter effects reducing the J/ψ yield. But they do not easily allow to disentangle the different

contributions (initial state shadowing, final state dissociation etc.) playing a role in this reduction. However such isolations of different cold nuclear matter effects is indeed theoretically possible. The commonly adopted procedure is the following [206]: (i) in absence of any final state dissociation effect, the charmonium production cross section per target nucleon is calculated using nuclear parton distribution functions (nPDF) for the partons inside the target nucleons and free proton pdf for the projectile partons. Depending on the collision kinematics, the production rate can thus be either enhanced or reduced, compared to $p + p$ collisions, mainly depending on the initial state nuclear modification of the gluon distribution functions. (ii) CEM predicts the production of the different charmonium states from the initially produced $c\bar{c}$ pair. (iii) the $c\bar{c}$ pair has thus been formed, with whatever nuclear modifications of the parton distribution functions applied for its formation rate, and now traverses the remaining part of the nucleus. The final state dissociation of the $c\bar{c}$ pairs in the pre-resonance or resonance stage can then be estimated using either versions of the Galuber model. σ_{abs} is then exclusively gives the final state absorption cross section rather than the effective cold nuclear suppression. However this method also suffered from an ambiguity. The amount of final state absorption cross section (σ_{abs}) is highly sensitive to the choice of the nPDF set used to model the initial state effects. For example, if for a given measurement a particular nPDF produce anti-shadowing effects, one requires a smaller value of σ_{abs} compared to the case where one chooses a different nPDF set in the initial state which does not include the anti-shadowing effects [206].

Table 3.4: Variation of the nuclear absorption cross section (σ_{abs}) for J/ψ production as function of beam energy in $p + A$ collisions.

Experiment	E_{CM} [GeV]	σ_{abs}^G [mb] (J/ψ)	σ_{abs}^G [mb] (ψ')
NA60 [197]	17.3	$7.6 \pm 0.7 \pm 0.6$	-
NA60 [197]	28.3	$4.3 \pm 0.08 \pm 0.6$	-
NA50 [196]	28.3	4.6 ± 0.6 (3.4 ± 1.2)	10.1 ± 1.6 (8.8 ± 2.3)
NA50 [198]	29.1 (HI)	4.4 ± 1.0 (4.3 ± 0.7)	7.6 ± 1.4 (7.8 ± 1.2)
NA50 [198]	29.1 (LI)	4.1 ± 0.4 (4.4 ± 1.0)	5.7 ± 2.7 (6.8 ± 1.7)

Analysis of charmonium production cross section using Glauber formalism has been extensively performed by the different experimental Collaborations at SPS. It was ini-

tiated by the NA38 Collaboration who had collected the charmonium events first time in 1988, with 450 GeV incident protons on various targets. Later both NA50 and NA60 Collaborations have extracted effective absorption cross section σ_{abs} from their measurements of charmonium production in $p + A$ collisions with incident proton beams of energies 450, 400 and 158 GeV. NA50 has extracted the nuclear absorption cross section both by fitting the data on absolute J/ψ production cross section as well as J/ψ -to-Drell-Yan ratio for different target nuclei. The advantage for the second quantity (ratio) is that since both the processes are measured simultaneously they give a much better control over the systematic uncertainties. However due to small production cross section of the Drell-Yan process statistical errors associated with the ψ -to-DY ratio are much larger. The estimated values of σ_{abs} for these two cases exhibit reasonable compatibility within errors. On the other hand due to large uncertainties associated with the Drell-Yan muon pairs, NA60 estimated the nuclear effects on J/ψ yield from the A dependence of the absolute production cross section ratios $\sigma_{J/\psi}^{pA}/\sigma_{J/\psi}^{pBe}$. Since the data for different targets were collected in the same run using a rotating target holder, this ratio also helps to cancel out most of the systematics. In Table 3.4, we summarize the numerical values of σ_{abs} for J/ψ and ψ' production, as reported by different experiments obtained with full Glauber model calculation, at different SPS energies. Since they are not corrected for initial state shadowing effects, they represent the overall global nuclear suppression. The main outcomes of these studies are:

- for a given beam energy, the loosely bound ψ' has larger absorption cross section compared to J/ψ , leading to around 20% less ψ' 's per J/ψ when going from $p + p$ to $p+W$ collisions
- for a given state the absorption cross section depend on the collision energy and increases with decreasing energy of the incident proton beam
- values of σ_{abs} obtained from full Glauber model calculation is $\sim 10\%$ (15%) larger for J/ψ (ψ').

Apart from these inclusive absorption cross section obtained at mid-rapidity, nuclear suppression effect is also measured at forward and backward rapidities, though

the measurements were challenged by statistics constraints and limited phase space acceptance of the di-muon spectrometer. Nevertheless ψ' is found to be more suppressed compared to J/ψ , as in the mid-rapidity case and strongest ψ' suppression is observed in the most negative x_F bin.

3.4.3 Charmonium production in heavy ion collisions

After discussing the J/ψ production in $p + p$ and $p + A$ collisions, finally we have come to the study of J/ψ production in nuclear collisions. Here one would look for suppressed production of J/ψ mesons which can then be related to the formation of QGP. However as we have seen earlier, J/ψ yield is already depleted in $p + A$ collisions owing to the cold nuclear matter effects. This nuclear suppression will also be present in case of heavy ion collisions, even at a higher degree due to the cold matter effects induced by both target as well as projectile nucleons. If some ‘anomalous’ suppression in addition to the normal nuclear suppression can be detected in the heavy ion data, then that can be connected to the presence of a secondary medium eventually produced in the collisions. A charmonium state produced in such a collision will in its early stages first be subject to the possible effects of the nuclear medium, just as it is in $p + A$ collisions, and then, after the nuclei have separated, encounter the newly produced medium.

Cold nuclear matter suppression

The systematics those have been developed for $p + A$ reactions to quantify the cold matter effects can also be extended to nuclear collisions. The ‘ α ’ parametrization in is written as:

$$\sigma_{AB} = \sigma_0 \times (AB)^\alpha \quad (3.18)$$

On the other hand, the Glauber formalism used above to calculate the survival probability of an evolving charmonium state in a $p + A$ collision can also be extended to $A + B$ interactions [205]. The survival probability at impact parameter b now becomes

$$\sigma_{AB} = \frac{\sigma_{NN}}{\sigma_{abs}^G \times \sigma_{abs}^G} \int d\mathbf{b}_A (1 - [1 - T_A(\mathbf{b}_A)\sigma_{abs}^G]^A) \int d\mathbf{b}_B (1 - [1 - T_B(\mathbf{b}_B)\sigma_{abs}^G]^B) \quad (3.19)$$

as extension of Eq. (3.14). With the dissociation cross sections σ_{diss}^i determined in $p + A$ collisions, Eq. (3.14) specifies the ‘normal’ survival probability, i.e., that due to only the nuclear medium. Like $p + A$ case, the detailed Glauber calculation can again be simplified in the ‘ $\rho < L >$ ’ parametrization as:

$$\sigma_{AB} = \sigma_{NN} A B \exp(-\sigma_{abs}^{<\rho L>} <\rho L >) \quad (3.20)$$

where $L = L_A + L_B$. The effective path length $L_A(L_B)$ through the nucleus $A(B)$, can again be calculated using Eq. 3.16.

It is important to note that the effect cold nuclear matter absorption depends strongly on the passing time $t_d \simeq \frac{2R_A}{\sinh Y_B}$ of the two colliding nuclei, where R_A is the nuclear radius and Y_B is their rapidity in the center-of-mass frame. While at SPS energy the collision time is about 1 fm/ c and normal suppression is large the cold nuclear matter effect in extremely energetic collisions should be small, due to the small collision time, for example $t_d \simeq 0.1$ fm/ c at RHIC and $t_d \simeq 1/200$ fm/ c at LHC.

In order to use J/ψ as a diagnostic probe for the produced medium, we now have to study how the behavior observed in nuclear collisions differs from this predicted pattern. Several possible and quite different effects have been considered as consequences of the produced medium on charmonium production.

Color screening and sequential quarkonium suppression

If the produced medium in nuclear collisions is indeed a hot and dense quark-gluon plasma (QGP), Debye color screening would set into operation. This will decrease the quarkonium binding, both in strength and in its spatial range compared to the vacuum binding. With increasing the temperature of the medium the binding potential weakens and the $c\bar{c}$ bound states dissociate at some characteristic Mott temperature T_d . If the maximum temperature of the medium produced in heavy ion collisions reaches

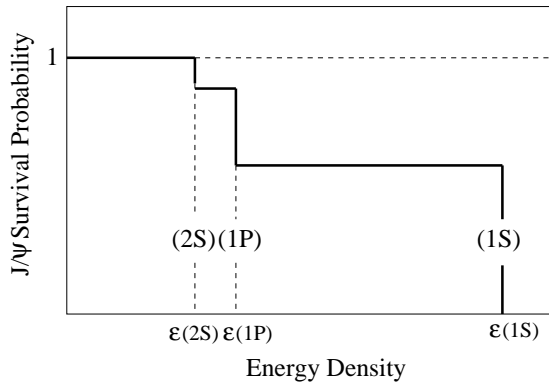


Figure 3.5: A schematic diagram showing sequential J/ψ suppression by color screening inside QGP medium. The figure is taken from [151]

the Mott temperature, the Debye screening effect results in anomalous charmonium suppression. Even though no quantitative conclusions on the precise value of the charmonium dissociation temperatures have been reached yet, a common conclusion from the phenomenological as well as lattice based calculations is that the different charmonium states owing to different binding energies, correspond to different dissociation temperatures. Since the larger and less tightly bound states melt at lower temperature or energy density than the ground states, color screening would produce *sequential suppression* [207, 208, 107, 209]. Considering the feed down contributions from the long lived excited states, to the inclusive J/ψ production, inside a QGP medium, J/ψ would exhibit a step like suppression pattern. With increasing medium energy density, after an initial threshold melting the ψ' and hence removing its feed-down component for J/ψ production, there will be a second threshold for χ_c melting and then finally a third, at which the direct J/ψ ($1s$) is dissociated. Such a step wise onset of suppression with specified threshold dissociation temperatures is perhaps the most characteristic feature predicted for charmonium production (as well as for bottomonium) in nuclear collisions. It is illustrated schematically in Fig. 3.5 where the J/ψ survival probability is defined to be unity if the production rate suffers only the estimated nuclear suppression. Theoretically, this is the chance of a J/ψ to persist as a bound state in a deconfined medium. How to properly define this quantity as a useful observable in experimental studies is still a subject of intense discussion. The generic suppression pattern shown here would of course be softened by nuclear profile effects, impact parameter uncertainties etc. On the other hand this could be partially compensated if there is a discontinuous onset of

deconfinement as a function of energy density of the medium.

In heavy ion collisions, J/ψ suppression in hot and dense medium induced by color screening is usually described within a geometrical threshold model without considering detailed microscopic dynamics [210, 211]. In this model, the J/ψ inclusive survival probability for a collision at an impact parameter b can be written as

$$S_{J/\psi}^{tot}(b) = \int d^2s S_{J/\psi}^{CNM}(\mathbf{b}, \mathbf{s}) \Theta(n_c - n_p(\mathbf{b}, \mathbf{s})) \quad (3.21)$$

where $S_{J/\psi}^{CNM}(b, \mathbf{s})$ is the J/ψ survival probability after cold nuclear matter suppression, and \mathbf{s} is the transverse position of the J/ψ . The transverse participant density $n_p(\mathbf{b}, \mathbf{s})$ in the step function is assumed to be proportional to the local energy density of the medium at a point (b, \mathbf{s}) . In the hot and dense interior of the fireball where n_p is larger than the critical density n_c , all the J/ψ 's are dissolved due to strong screening effects and those outside this region only suffer normal nuclear suppression effects. The threshold density n_c in this model is a parameter that can be fixed by comparing with the data. If the matter with $n_p > n_c$ is QGP, the critical density n_c can be considered as the threshold value to create QGP. Despite its simplicity, the threshold model was found successful to describe the anomalous J/ψ suppression observed in Pb+Pb collisions at SPS [210, 211]. Though found successful, the threshold model gives a crude description of the partonic medium. It is a geometrical model applicable for a static medium. However the volume of the produced fireball in relativistic heavy ion collisions is relatively small and expands very rapidly, implying rather fast cooling and dilution and short fireball lifetimes. To include the medium dynamics several variants of the threshold model had been proposed in literature [212, 213]. For example to describe the data on centrality dependence of J/ψ suppression at mid-rapidity in Au+Au collisions ($\sqrt{s_{NN}} = 200$ GeV) at RHIC, in [212], the J/ψ survival probability at a point inside the plasma is modeled in terms of the instantaneous thermal J/ψ decay width $\Gamma_{dis}(T(\mathbf{x}(\tau)))$ at a local temperature T at the space time point (\mathbf{x}, τ) . Following simple threshold ansatz the decay width is parametrized such that it is either zero for $T < T_d$ or infinity for $T > T_d$. The space-time evolution of the hot and dense partonic matter was described either by (3+1)-D ideal relativistic hydrodynamics or (2+1)-D relativistic viscous hydrodynamics, with

the assumption of local thermal equilibrium. J/ψ is treated as an impurity traversing through the medium. A detailed treatment of the matter evolution and J/ψ suppression within a threshold scenario at energies available from SPS and future FAIR facility had also been carried out in the hadronic transport model HSD [213], where the J/ψ motion is traced microscopically throughout the medium.

The above pictures utilizing Debye screening effect were typically based on the existence of characteristic constant dissociation temperatures depending on which the suppression is either total or absent. Attempts were also made to smear the step functions [211, 212] modeling the survival probabilities in the plasma to incorporate the effect of gradual thermal broadening of J/ψ rather than its abrupt change. This was motivated by the fact that deconfinement, instead of abrupt one, is a continuous process.

In addition to Debye screening effects, another essentially important effect was found to be the collisional dissociation of J/ψ due to hard partons which leads to sizable inelastic reaction rates comparable to the fireball expansion rate. In particular in a real system, charmonia can be destroyed below the characteristic dissociation temperature. Debye screening would be still operative by controlling the binding energy which in turn determines the phase space (and thus the width) of the dynamic dissociation reactions [214]. An important such process in the QGP at leading order is the gluon dissociation process [105] $g + J/\psi \rightarrow c + \bar{c}$, in analogy to the photon dissociation process of the electromagnetic bound states [215]. Close to the dissociation temperatures, the binding energies of the charmonium states are small and the gluon dissociation becomes kinematically unfavorable due to shrinking of phase space. As a result, the next-to-leading order (NLO) processes take over [214, 216], most notably inelastic parton scattering: $g(q, \bar{q}) + J/\psi \rightarrow g(q, \bar{q}) + c + \bar{c}$. Debye screening being a macroscopic effect, remains operative as the deconfined medium is in thermal equilibrium. On the other hand collisional dissociation can be effective in the preequilibrium phase also as long as the medium is in the deconfined state.

Suppression by Comover Collisions

In addition to the hard partons, anomalous J/ψ suppression can also be induced due to inelastic collisions with the secondary hadrons like π , ρ and ω produced in the nuclear collisions and co-moving with J/ψ [217, 218, 219, 220]. The suppression due to comover effect in a hot and dense hadronic phase can be schematically written as:

$$S_{co} = \exp\left[-\int_{\tau_0}^{\tau_F} d\tau \langle \sigma_{co} v_{rel} \rangle n_{co}(\tau)\right] \quad (3.22)$$

where $n_{co}(\tau)$ is the comover density at some proper time τ at the position of J/ψ , and the σ_{co} denotes inelastic hadro- J/ψ dissociation cross section (multiplied by the relative velocity) and is averaged over various kinds of co-moving species and interaction energies. τ_0 and τ_f respectively denotes the co-mover formation time and freeze-out time at which the inelastic interactions stop. Not all the hadrons produced in nucleus-nucleus collisions (co)move with the J/ψ . So the number density of comoving hadrons is given by $n_{co} = f_c n_h$, where n_h is density of produced hadrons and f_c is the fraction that (co)moves with the J/ψ . The comover density, $n_{co}(\tau)$, is generally obtained through some kind of evolution mechanism of the matter. Generally the evolution is assumed to be described by Bjorken's boost invariant 1-D hydrodynamic scaling solutions [62], so that co-moving density becomes inversely proportional to the proper time τ and fitted to the measured final state hadron yield dN_{ch}/dy [221, 57, 58]. The co-mover dissociation cross section is an adjustable parameter in the calculation. Charmonium dissociation by interaction with hadronic comovers has received considerable attention in the past [222]. However in some calculations the comover densities turned out to be rather high, corresponding to energy densities well above the critical one computed in lattice QCD. Consequently the pertinent comover interaction cross sections assumed rather small values like $\sigma_{co} \sim 0.65$ mb which are more suitably interpreted as partonic comover interactions. A more detailed treatment of the medium evolution together with a dynamical description of the interactions between charmonia and comovers were carried out in the framework of hadronic transport models like UrQMD and HSD [213]. Charmonia hadron cross sections were input parameters to these models.

Charmonium Regeneration

The normal and anomalous suppression mechanisms discussed above are applicable to the primordial J/ψ mesons produced in initial hard nucleon-nucleon collisions. In case of heavy ion collisions at SPS energy and below, there is typically no more than one $c\bar{c}$ pair produced per central Pb+Pb collisions ($N_{c\bar{c}} \simeq 0.2$ at $E_{Lab} = 158$ A GeV). Hence if the two quarks can not form a (pre-resonant) charmonium bound state close to their creation point, the probability to recombine in the medium and form a resonant state is very small and can be safely neglected. However for nuclear collisions at collider energies like those available from RHIC and LHC, the situation becomes quite different. In a central Au+Au collision at the top RHIC energy, about 10-20 $c\bar{c}$ pairs are produced [223], while the number is around 100 at LHC. Hence the uncorrelated c and \bar{c} from different pairs have a significant probability (proportional to $N_{c\bar{c}}^2$) to meet and form charmonium bound states in the medium. The J/ψ regeneration in partonic and hadronic (or mixed) phases arises as a possible new mechanism for charmonium production in heavy ion collisions at RHIC and LHC. Regeneration is generally employed in two classes of models. Within the *statistical hadronization model*, charm quarks are assumed to be equilibrate kinetically and secondary charmonium production entirely occurs at the hadronization transition. It further assumes in accord with color screening and the resulting suppression, that at sufficiently high energies there is an almost complete dissociation of the J/ψ 's produced in primary nucleon-nucleon interactions. On the other hand, at such collision energies, these interactions lead to abundant $c\bar{c}$ production; the rate for this process grows faster than that for the production of light quarks, and if the $c\bar{c}$ pairs remain present in the evolution of the medium, the system will at the hadronisation point show an over saturation of charm, compared to the predicted thermal abundance. If these charm quarks have become part of an equilibrated medium and as such undergo hadronisation in the form of statistical combination, then such secondary charmonium formation can convert more $c\bar{c}$ pairs into J/ψ 's than the dynamical primary production mechanism, provided the binding force between charm quarks from different sources is large enough. This would lead to an effective J/ψ enhancement in $A + A$ collisions relative to $p + p$ results scaled by binary collisions. The statistical hadronization model has been found

successful in describing the mid-rapidity J/ψ suppression in Au+Au collisions at top RHIC energy. Extrapolation of the model calculations to the LHC domain led to a striking prediction of *increase* of the enhancement with collision centrality [225], because of the corresponding increase in the number of collisions and hence of the number of $c\bar{c}$ pairs thermalized in QGP. On the other hand recent lattice calculations of charmonium spectral functions suggest that directly produced J/ψ mesons can exist in a thermal environment at temperatures well above the deconfinement phase transition. Hence unlike in the statistical model, charmonia in the kinetic formation model [224] can be regenerated continuously throughout the QGP region and the formed J/ψ 's reflect the initially produced charm-quark spectra and their modification due to the interaction in the medium. In the kinetic approach, the J/ψ production during the entire lifetime of the deconfined phase is dynamically calculated through (related) formation and dissociation processes at finite temperature and density. The simplest dissociation reaction utilizes absorption of the individual deconfined gluons in the medium to ionize the color singlet J/ψ , $g + J/\psi \rightarrow c + \bar{c}$, resulting in a color octet $c\bar{c}$ pair. The inverse of this process serves as the corresponding formation reaction, in which a $c\bar{c}$ pair in a color-octet state emits a gluon and falls into the color-singlet J/ψ bound state. The competition between the J/ψ formation and suppression is characterized by a kinetic rate equation that decides the effective number of J/ψ at any instant τ .

One common assumption of the statistical hadronization model and the kinetic model is that the initially produced charmonia are entirely destroyed due to color screening in the deconfined medium. Though it might be a reasonable approximation in central collisions at RHIC and LHC energies, but for nuclear collisions at SPS and lower energies, as well as for peripheral collisions and light ions one needs to include initial production together with normal and anomalous suppressions. This was first accounted in the two-component model [214], where the final charmonium yield is expressed as the sum of 'direct' and 'thermal' production. The direct component are the J/ψ mesons initially produced via hard processes with subsequent nuclear absorption and anomalous suppression in the QGP. Regeneration in this model is restricted to statistical hadronization at the boundary of the confinement phase transition, as in the statistical recombination models.

Both direct and thermal components are subsequently subject to hadronic dissociation processes. This approach incorporates inelastic processes beyond $2 \rightarrow 2$ scattering. This is particularly important for small charmonium binding energies where inelastic $2 \rightarrow 3$ processes like $g(q, \bar{q}) + J/\psi \rightarrow g(q, \bar{q}) + c + \bar{c}$, instead of gluo-dissociation generally used in kinetic models, become important. In the hadronic phase, inelastic interactions with pions ($\pi + J/\psi \rightarrow D + \bar{D}^*, \bar{D} + D^*$) and ρ mesons ($\rho + J/\psi \rightarrow D + \bar{D}^*, \bar{D} + D^*$) are accounted for which mostly affect the ψ' abundance. Regeneration of charmonia essentially occur at or before the hadronization transition. J/ψ regeneration may also occur in hadronic matter by considering the backward channels $D + \bar{D} \rightarrow J/\psi +$ mesons through detailed balance. While the regeneration is negligible at SPS energy, its contribution to the final J/ψ yield is essential and comparable to the dissociation by the comoving mesons at extremely relativistic energies. The two component model has been found successful to describe the data on J/ψ production from SPS to RHIC. At SPS energy, the direct production prevails over the thermal component for both S+U and Pb+Pb collisions at any centrality. The thermal contribution sets in when the temperature of the system reaches the critical value for deconfinement phase transition and grows with increasing open charm production. At RHIC energy, the J/ψ yield is still dominated by initial production for peripheral collisions, but regeneration becomes comparable (or even exceeds) direct production for semi-central/central collisions, though a significant uncertainty due to incomplete charm-quark thermalization remains.

It is important to note, so far J/ψ enhancement with centrality has not been observed in data collected at LHC. Moreover since our primary concern is the J/ψ production in the FAIR energy domain, where number of $c\bar{c}$ pairs per collision is $\approx 10^{-5}$, we can safely neglect the regenerating effects as far J/ψ production in nuclear collisions is concerned.

Apart from the inclusive charmonium production, transverse momentum (p_T) dependence of the J/ψ production can also provide information about the production process, the evolution of the resonance formation and of that of the produced medium. In case of $p + A$ and $A + A$ collisions, the p_T distribution of charmonia gets broadened in comparison to that in $p + p$ interactions, due to collision broadening of the incident gluons which fuse to make $c\bar{c}$ pairs. For heavy ion collisions, the amount of broadening depends on the

average number of collisions of a projectile parton in the target and vice versa as well as the average “kick” which the incident parton receives in each subsequent collision. As a result the $\langle p_T^2 \rangle_{AA}$ is found to rise linearly with the number of collisions. In the absence of any anomalous suppression, this would be the expected behavior of the average J/ψ transverse momentum. Now given the sequential suppression by color screening, the J/ψ ’s observed for energy densities in a range above the onset of anomalous suppression, $\epsilon(2S), \epsilon(1P) \leq \epsilon \leq \epsilon(1S)$ are the directly produced $1S$ states unaffected by the presence of the QGP. They should therefore still show the normal broadening pattern as long as $\epsilon < \epsilon(1S)$ [209]. This broadening is a memory of the initial state and hence essentially absent if the J/ψ is formed only at the hadronization point, where such memory has been destroyed. Thus J/ψ production through regeneration should show a flat distribution as function of the number of collisions [228], in contrast to the rise expected in the sequential suppression scenario. The behavior of $\langle p_T^2 \rangle_{AA}$ thus should provide a clear indication of how the observed J/ψ ’s were produced. A further interesting signal is how an anomalous suppression behaves as function of p_T . If the nascent J/ψ is formed as a small color singlet gradually expanding to its physical size, then it can be out of the deconfining medium either spatially or temporally before suffering serious suppression, provided it has a high enough transverse momentum. The “end” of anomalous suppression as function of p_T could thus give indication on the size or life-time of the QGP [229, 230, 231, 232, 233, 234]. More recently, calculations have appeared [235] which are based on the AdS/CFT correspondence applied to QCD; they indicate the opposite effect, suggesting that J/ψ ’s of high transverse momentum should suffer more suppression. It must be kept in mind, however, that binding and the dissociation of specific bound states are clearly non-conformal phenomena, so that such modeling is not necessarily valid.

Again it is important to note that in the low energy collisions at FAIR, anomalous suppression pattern might be independent of p_T , due to small p_T values of the produced J/ψ mesons. This issue is discussed at length in section 6.4 of chapter 6.

Over past 25 years, concentrated experimental efforts have produced a wealth of data on charmonium production in nuclear collisions. Measurement of J/ψ suppression

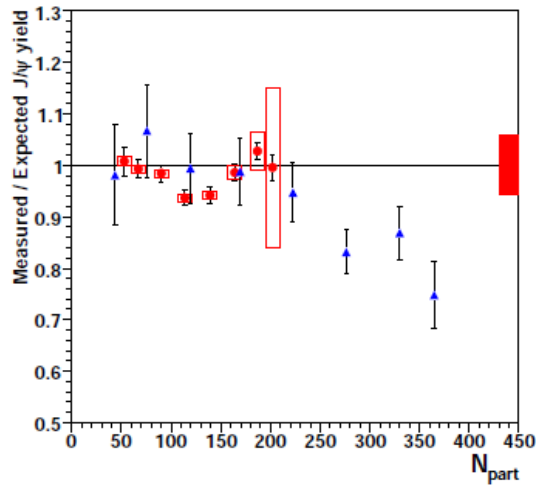


Figure 3.6: Measured-to-expected ratio of J/ψ production in 158 A GeV heavy ion collisions at SPS. The figure is taken from [236]

in heavy ion collisions was pioneered by the NA38 Collaboration at SPS in S+U and O+Cu collisions with sulfur and oxygen beams of energy 200 A GeV. Data were published in terms of J/ψ -to-Drell-Yan ratio ($\sigma_{J/\psi}/\sigma_{DY}$) as function of collision centrality measured through the variable $\langle L \rangle$. With increasing collision centrality, decrease in the height of the J/ψ mass peak with respect to Drell-Yan continuum was observed which then indicated suppression of J/ψ production. However the resulting centrality dependence of J/ψ suppression pattern was found to be completely compatible with the Glauber model calculations extrapolated from the previous $p + A$ measurements by the same group. The first significant measurement of J/ψ production in heavy ion collisions were subsequently came from the NA50 Collaboration who measured the J/ψ suppression in 158 A GeV Pb+Pb Collisions, in the di-muon kinematic domain $0 < y_{c.m.} < 1$. Data were published again in terms of J/ψ -to-DY ratio as a function of $\langle L \rangle$. Centrality bins and the corresponding $\langle L \rangle$ are were inferred from three independent measurements of forward energy, transverse energy and charged particle multiplicity. Suppressions above a certain centrality threshold were found to be about 20 – 40% larger than that suggested by extrapolations of the $p + A$ data measured by NA50 Collaboration with incident proton beams at energies 400 and 450 GeV, using Glauber formalism. Such anomalous suppression of J/ψ yield beyond that expected from cold nuclear matter effects were expected to carry the evidence for deconfinement transition at SPS. The onset of anomalous J/ψ suppression in Pb+Pb collisions and its absence in

S+U collisions suggested studying a lighter $A + A$ combination to obtain further insight about this phenomena. Hence the NA60 Collaboration measured the J/ψ suppression in In+In collisions at the same energy and kinematic domain of NA50 heavy ion collisions and again an onset of anomalous suppression was seen which appeared to occur at a centrality ($N_{part} \sim 80$) at which the corresponding S+U data do not show such effect. Due to poor statistics of the Drell-Yan muon pairs, the results are finally published in terms of measured-to-expected J/ψ ratio as a function of the number of participants (N_{part}), where the expected denotes the J/ψ cross section calculated using a purely nuclear absorption scenario. The Pb+Pb data within errors were found to be compatible with an earlier as well as a later onset position. However one common factor in both the measurements was that the corresponding value of $\sigma_{J/\psi}^{eff} \sim 4.2$ mb, which was extracted from the data collected in p+A collisions at 400 and 450 GeV and used to estimate the effect of normal nuclear absorption. With the new measurements of charmonium in p+A collisions at 158 GeV [236], where $\sigma_{J/\psi}^{eff}$ turned out to be almost twice as large as that at 400 GeV, the NA60 experiment reported the relative charmonium yield in In+In collisions to be compatible within errors with absorption in cold nuclear matter, as shown in Fig. 3.6. An anomalous suppression of about 25 - 30 % still remained visible in the most central Pb+Pb collisions. Apart from SPS, no other fixed target facility has measured J/ψ production in heavy ion collisions and hence till date there are no data on J/ψ suppression in nuclear collisions below 158 A GeV. However so far as heavy ion collider machines are concerned, J/ψ suppression has been observed at both RHIC and LHC.

The measurements of J/ψ production in p+p, d+Au, Au+Au and Cu+Cu and Cu+Au collisions at $\sqrt{s_{NN}} = 200$ GeV energy were performed by the PHENIX and STAR experimental Collaborations at RHIC [237, 238, 239, 240, 241, 242, 243, 244]. The observed suppression of J/ψ production for the first time was presented in terms of nuclear modification factor, R_{AA} , defined as the ratio of J/ψ production in $A + A$ collisions to the J/ψ production in $p + p$ collisions, normalized to the number of binary collisions, N_{coll} . R_{AA} had been calculated as a function of collision centrality expressed via number of participants, N_{part} (or multiplicity or energy density), transverse momen-

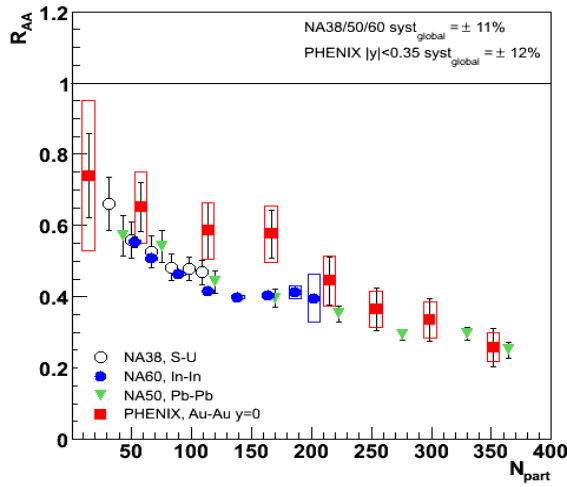


Figure 3.7: Centrality dependence of J/ψ suppression at SPS and RHIC. The figure is obtained from [246]

tum, p_T and so on. The most striking observation from RHIC measurements observed by PHENIX Collaboration was that in case of Au+Au collisions, suppression in forward rapidity range $1.2 < |y| < 2.2$ was found to be stronger than that in the central rapidity ($|y| < 0.35$). For the most central collisions, the suppression reaches a value near 80%. This phenomenon appeared contradictory with the models containing only initial production mechanisms as anomalous suppression in the central region where the highest temperatures are expected should be stronger than that at forward/backward rapidities. However this observation found a natural explanation from the regeneration effects since recombination mainly occurs in the central region and thereby compensating the initial suppression effects. The J/ψ production in Au+Au collisions at large transverse momentum $p_T > 5$ GeV/c for mid-rapidity range ($|y| < 1.0$) was also measured in STAR experiment at RHIC. The suppression of J/ψ production was smaller than measured at PHENIX and was near 50% for most central collisions. J/ψ data in Cu+Cu and Cu+Au collisions at RHIC exhibit a suppression close in magnitude to that observed in in Au+Au collisions. At lower RHIC energies, measurements show a J/ψ suppression similar in magnitude to that measured at top RHIC energy. For extraction of the CNM effects, the PHENIX data for Au+Au and d+Au collisions were analyzed simultaneously. It was suggested that in p+p, p+A and d+Au collisions the hot and dense nuclear matter is not formed and the observed suppression was purely due to the cold matter effects. The nuclear modification factor for cold nuclear matter,

$R_{AA}(CNM)$ in Au+Au collisions was obtained. The ratio $R_{AA}/R_{AA}(CNM)$ showed the anomalous suppression of the J/ψ production in the hot and dense nuclear matter produced in relativistic heavy ion collisions. At $\sqrt{s} = 200$ GeV the $R_{AA}/R_{AA}(CNM)$ ratio found to be approximately equal for different ranges of rapidity [245]. There is another interesting feature related to RHIC data. Once the RHIC data were available, the SPS data on Pb+Pb collisions from NA50 Collaboration were reanalyzed and published in terms of $R_{AA}^{J/\psi}$ as a function of N_{part} . Initial comparisons showed a similar suppression pattern at SPS and RHIC. This was explained either using the fact that the T_d value for directly produced J/ψ is too high ($T_d^{J/\psi} \sim 2T_c$) to get them melted either at SPS or RHIC energy collisions. Hence in both the cases the suppression is due to the melting of the excited states which contribute to the feed down production of J/ψ mesons. This finally leads to the identical suppression pattern. The other possible explanation of this observed feature was based on the recombination mechanism. Even though the suppression is more severe in the central rapidity region of RHIC, due to secondary production of J/ψ via exogamous regeneration mechanism, the initial suppression is compensated in such way that the overall observed reduction of J/ψ yield is same as that at SPS. However it is important to note that at SPS in calculation of $R_{AA}^{J/\psi}$, the corresponding $\sigma_{J/\psi}$ for $p + p$ collisions was not measured. Initial estimates of R_{AA} were based on the extrapolation of the then available 400 GeV $p + A$ data up to $A = 1$. Once the $p + A$ data were collected at 158 GeV, $\sigma_{J/\psi}$ for $p + p$ collisions was recalculated using this 158 GeV data set. Resulting suppression pattern for Pb+Pb collisions at SPS, was found to be different than that observed in Au+Au collisions at RHIC [246].

The latest results on J/ψ production in nuclear collisions have recently become available from the CERN LHC, which provides the opportunity to study the quarkonium production at a completely new energy domain more than ten times higher than that at RHIC. At LHC, the experiments ALICE [247], ATLAS [248], CMS [249] and LHCb [250] are measuring charmonium production at various rapidity and p_T ranges. During the years 2010-2012 J/ψ production was measured in p+p collisions at 2.76 TeV, 7 TeV and 8 TeV and in Pb+Pb collisions at 2.76 TeV. Measurement of J/ψ production in p+p collision at the same energy as in Pb+Pb collision, provides baseline for extraction

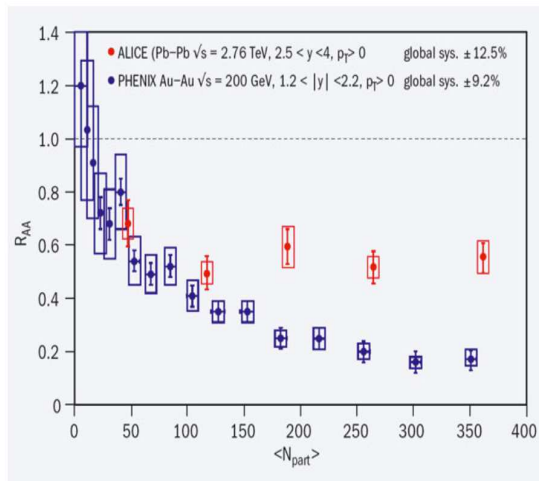


Figure 3.8: Centrality dependence of J/ψ suppression at LHC. The figure is obtained from [247]

of the nuclear modification factor R_{AA} . The mechanism of J/ψ production is investigated and the contribution of B-decay to J/ψ production is measured. There is a fair agreement for the p+p collision data obtained in ALICE, LHCb, CMS and ATLAS experiments in the same kinematical domains [251]. The J/ψ production cross section is found to depend on rapidity. For forward rapidity the cross section is smaller. By increasing the energy the mean p_T and production cross section of J/ψ becomes larger. The contribution of B-decay to J/ψ production cross section depends on rapidity and increases for larger J/ψ transverse momentum. This contribution is approximately 10% for $p_T \sim 1.5$ GeV/c [252]. Charmonium production in Pb+Pb collisions at 2.76 TeV was measured at LHC in ALICE, CMS and ATLAS experiments. In ALICE experiment the transverse momentum of inclusive J/ψ was measured from values zero up to 8 GeV/c in rapidity range $y < 0.9$ via di-electron channel and $2.5 < y < 4$ in di-muon channel. In ATLAS and CMS experiments charmonium production was measured in the rapidity range $|y| < 2.4$, but range of p_T values depend on rapidity. In ATLAS experiment only J/ψ mesons with large transverse momentum ($p_T > 6.5$ GeV/c) were measured. The R_{AA} dependence on centrality in ALICE experiment is not as strong as in PHENIX. In ALICE for the most central events and for forward rapidity ($2.5 < y < 4$) the R_{AA} value is two times larger than that measured in PHENIX, so the suppression of J/ψ production is smaller. But in CMS experiment [252] the suppression of prompt J/ψ production (directly produced and obtained from feed-down of excited charmonium states) for most

central event is approximately equal to the suppression measured at RHIC. A comparison of the centrality dependence of R_{AA} measured in ALICE was done with a statistical hadronization model calculation, which is in good agreement with the RHIC data. The model predicts larger values for R_{AA} at LHC than at RHIC in agreement with ALICE experimental data. The importance of J/ψ regeneration process is also seen from LHC experimental data. Another stark difference between LHC and RHIC data on J/ψ production is observed in the p_T dependence of R_{AA} . This is arguably the most prominent difference between LHC and RHIC data in all multitude of observables studied till date. With increasing p_T , R_{AA} of J/ψ was seen to increase at RHIC at both mid and forward rapidities, which is in accord within a screening scenario, where Debye screening mechanism is expected to be effective at low p_T (recall the discussions in the previous section). On the other hand at ALICE both in the mid and forward rapidities, the J/ψ R_{AA} is seen to decrease with increasing p_T . This gives a strong support to the interpretation of J/ψ production at LHC as dominated by the generation at hadronization or by regeneration throughout the QGP lifetime as the statistical hadronization model or the kinetic models respectively imply. It was shown with the transport models that as expected regeneration is predominantly a low p_T phenomenon since c and \bar{c} quarks spend more time inside the QGP to recombine. This translates to average values of p_T very different at the LHC compared to the lower energies. The measurement of J/ψ elliptic flow parameter (v_2) at the LHC brings another argument in favor of charmonium production from thermalized c and \bar{c} quarks. Transport model predictions describe the data well. Recent measurements by CMS Collaboration indicates that the prompt J/ψ mesons exhibit elliptic flow for p_T as large as 10 GeV/ c . It may be recalled that J/ψ data at RHIC are compatible with a null flow signal. A v_2 signal was measured for J/ψ at the SPS and was interpreted as a path length dependence of the plasma screening.

3.5 Summary

To summarize, in this chapter, we engage in a brief review of the physics of charmonium production in energetic nuclear collisions. Most of our discussions are concentrated on

J/ψ , the most extensively studied charmonium state. Starting with discovery of J/ψ meson, we first discuss the vacuum properties of different quarkonium bound states within non-relativistic potential model approach. This is followed by a short narration of the spectral analysis of the charmonium bound states in an equilibrated QCD medium. In particular we concentrate on the determination of the dissociation temperature of various charmonium states, estimated for a baryonless medium, within both potential model approach and lattice correlator method. Next we move on to the dynamical production of J/ψ mesons in nuclear collisions. We start with the case for elementary hadronic collisions, where various models accounting for resonance binding of the charmonium states are depicted in short. This is followed by a discussion on different aspects of charmonium production in $p + A$ collisions. These reactions are believed to be the looking glass to identify the effects of the nuclear medium. In such collisions, different cold nuclear matter effects come into play which modify the perturbative $c\bar{c}$ pair production as well as their evolution into physical bound states. We discuss in some detail the two most important CNM effects namely the initial state nuclear modification of the parton densities as well as the final state dissociation of the nascent $c\bar{c}$ pairs. Two conventional methods for quantification of the CNM suppression of J/ψ production are discussed along with the experimental results obtained from different fixed target experiments. Finally we go to the $A + A$ collisions. In this domain, we give a concise description of the different mechanisms both in the partonic and in the hadronic sectors that might give rise to the anomalous J/ψ suppression or its regeneration on top of the normal nuclear suppression induced by the cold nuclear matter. We end our review with a short summary of the experimental observations made so far on J/ψ suppression in heavy ion collisions.

Chapter 4

Charmonium production in nuclear collisions within QVZ approach

4.1 Introduction

In this chapter we discuss our theoretical formalism to calculate J/ψ production cross sections in proton-proton ($p + p$), proton-nucleus ($p + A$) and nucleus-nucleus ($A + A$) collisions. Our estimations are based on the QVZ model, originally proposed by Qiu, Vary and Zhang [253], for interpretation of centrality dependence of the then observed J/ψ suppression in 158 A GeV Pb+Pb collisions [254] measured by NA50 Collaboration at SPS. For our present work, we have made several modifications as and when required [255, 256], which will be detailed in the following discussion. Within the QVZ model, the generic nuclear absorption of J/ψ mesons, that affect their production in $p + A$ and $A + A$ collisions, is treated in a completely unconventional way. Generically the cold nuclear dissociation effects are evaluated within Glauber formalism, with σ_{abs} quantifying the J/ψ absorption cross section within nuclear matter arising due to J/ψ -nucleon inelastic collisions. On the other hand, in QVZ model, the nuclear dissociation of J/ψ is described in terms of the coherent multiple scattering of the pre-resonant $c\bar{c}$ pairs inside the nuclear medium. As a result some of the $c\bar{c}$ pairs can absorb enough energy from the medium to cross the open charm threshold to form $D\bar{D}$ pairs, which finally results in depleted production of J/ψ mesons both in $p + A$ and $A + A$ collisions.

The total energy gained by a $c\bar{c}$ pair is proportional to the path length traversed by the pair inside the medium. The model does not consider further suppression in the hot and dense secondary medium eventually created in the heavy ion collisions. Without incorporation of any additional anomalous suppression mechanism, the approach was found to be successful to reproduce the then available data on J/ψ suppression, the transverse energy (E_T) dependence of J/ψ over Drell-Yan ratio [254], in 158 A GeV Pb+Pb collisions [253, 257, 258]. These provocative results indicated a negligible additional J/ψ suppression (compared to CNM effects) even in the most central Pb+Pb collisions, contrary to the expected signatures of the dense parton plasma.

4.2 QVZ model and J/ψ production in nuclear collisions

In QVZ model, the J/ψ production in high energy hadronic collisions is believed to a factorisable two stage process. The first stage is as usual the production of a $c\bar{c}$ pair with relative momentum square q^2 , which is accounted by leading order perturbative QCD. The second stage involves the (non-perturbative) formation of the color neutral physical bound state J/ψ , from the initially compact $c\bar{c}$ pair, which is conveniently parameterized, following existing schemes of color neutralization. As discussed in the previous chapter the most common approaches are based either on color evaporation (CEM) or non-relativistic QCD (NRQCD) approach. However, data from the CDF Collaboration at Fermilab Tevatron seemed to be inconsistent with the predictions from both the approaches. The disagreement is thought be caused by radiation of semi-hard gluons from the $c\bar{c}$ pair during its evolution to form a J/ψ meson. The parameterizations incorporated in QVZ model are general enough to include the effect of semi-hard gluon radiation as well as mechanisms addressed by the conventional approaches. The production rate of the $c\bar{c}$ pairs with an invariant mass Q^2 , can be factorized into i) a convolution of two parton distributions from the two incoming hadrons and, ii) $d\hat{\sigma}_{a+b\rightarrow c\bar{c}+X}/dQ^2$, which represents the perturbatively calculable short-distance hard parts for the parton a and b to produce the $c\bar{c}$ pairs with mass Q^2 [259]. At the leading order in strong coupling, the

partonic contributions come from two subprocesses: quark annihilation ($q\bar{q} \rightarrow c\bar{c}$) and gluon fusion ($gg \rightarrow c\bar{c}$). With the K-factor accounting for effective higher order contributions, the single differential J/ψ production cross section in collisions of hadrons h_1 and h_2 , at the center of mass energy \sqrt{s} can be expressed as,

$$\frac{d\sigma_{h_1 h_2}^{J/\psi}}{dx_F} = K_{J/\psi} \int dQ^2 \left(\frac{d\sigma_{h_1 h_2}^{c\bar{c}}}{dQ^2 dx_F} \right) \times F_{c\bar{c} \rightarrow J/\psi}(q^2), \quad (4.1)$$

where $Q^2 = q^2 + 4m_C^2$ with m_C being the mass of the charm quark and x_F is the Feynman scaling variable. It can be related to x_a and x_b by $x_F = x_a - x_b$, with x_a and x_b being the momentum fractions carried by the incoming partons originating from the beam and the target respectively. In Eq. 4.1, $F_{c\bar{c} \rightarrow J/\psi}(q^2)$ is the transition probability that $c\bar{c}$ pair with relative momentum square q^2 evolve into a physical J/ψ meson, in hadronic collisions. Without isolating contributions from different color channels, $F_{c\bar{c} \rightarrow J/\psi}(q^2)$ in Eq. 4.1 represents the transition probability of a color averaged $c\bar{c}$ pair to form a physical resonance. Three alternatives have been proposed for parameterizing the transition probability, corresponding to the various physical mechanisms available for color neutralization. They are read as:

$$F_{c\bar{c} \rightarrow J/\psi}^{(C)}(q^2) = N_{J/\psi} \theta(q^2) \theta(4m_D^2 - 4m_C^2 - q^2) \quad (4.2)$$

$$F_{c\bar{c} \rightarrow J/\psi}^{(G)}(q^2) = N_{J/\psi} \theta(q^2) \exp[-q^2/(2\alpha_F^2)] \quad (4.3)$$

$$F_{c\bar{c} \rightarrow J/\psi}^{(P)}(q^2) = N_{J/\psi} \theta(q^2) \theta(4m_D^2 - 4m_C^2 - q^2) \times (1 - q^2/(4m_D^2 - 4m_C^2))^{\alpha_F} \quad (4.4)$$

where $2m_D$ is the mass scale for the open charm production threshold. In $F_{c\bar{c} \rightarrow J/\psi}(q^2)$, $N_{J/\psi}$ and α_F are the tunable parameters. They can be fixed by comparing the model results with the existing total production cross section data from hadron-hadron collisions. The different functional forms of the transition probability represent different mechanisms of color neutralization. The $F^{(C)}(q^2)$ implies that a constant fraction of all the produced $c\bar{c}$ pairs with invariant mass below the open charm production threshold evolves into the physical J/ψ mesons, and thus bears the central theme of the Color

Evaporation Model [172]. $F^{(G)}(q^2)$ carries the essential ingredients of the Color-Singlet Model [174]. It is assumed that the $c\bar{c}$ pair is produced in a color-singlet state. The transition amplitude $\langle c\bar{c}|J/\psi\rangle$ does not involve any radiation and interaction with the medium, and thus proportional to square of the J/ψ wave function at the origin, parameterized as Gaussian. If we neglect the q^2 -dependence in the production of the $c\bar{c}$ pairs in Eq. 4.1, and require the $c\bar{c}$ to be color-singlet, the total cross section with $F^{(G)}(q^2)$ is effectively the same as that from the Color-Singlet Model. In this approach, possibilities for the $c\bar{c}$ pairs having large invariant mass to form J/ψ mesons are strongly suppressed. Finally, $F^{(P)}(q^2)$ in Eq. 4.4, mimics the essential features of gluon radiation effects. In this scenario, the $c\bar{c}$ pairs are assumed to be produced in color-octet stage. Subsequent formation of color-singlet physical resonances occurs through the gradual expansion of the initially compact $c\bar{c}$ pairs. The expansion is associated with the radiation of soft gluons necessary for color neutralization. The phase space between the threshold for producing a $c\bar{c}$ pair and open charm meson is fairly large, $4m_D^2 - 4m_C^2 \simeq 5 \text{ GeV}^2$. Hence during formation of the resonance, $c\bar{c}$ pairs with large invariant mass can radiate semi-hard gluons. Though the heavy quark mass would suppress the radiation effect, it would help to reduce the pair's invariant mass and strongly enhances the probability for the nascent pair to form a J/ψ . The q^2 -dependence of the transition probability is assumed to be associated with that radiation, and a power-law (P) distribution, is believed to represent the transition probability. If we expand the transition probability at $q^2 \approx 0$, the normalization of $F^{(P)}(q^2)$ can be related to the combination of the matrix elements in the Color-Octet Model [175].

In principle, with a different functional form of $F(q^2)$, the factorized formula in Eq. 4.1 can be generalized to calculate the inclusive cross sections for producing other quarkonium states.

Instead of x_F , one can also express the single differential cross section, in terms of the center of mass rapidity $y_{c.m.}$, of the $c\bar{c}$ pair as,

$$\frac{d\sigma_{h_1 h_2}^{J/\psi}}{dy_{c.m.}} = (x_a + x_b) \frac{d\sigma_{h_1 h_2}^{J/\psi}}{dx_F} \quad (4.5)$$

The inclusive cross sections as reported by different experiments can then be esti-

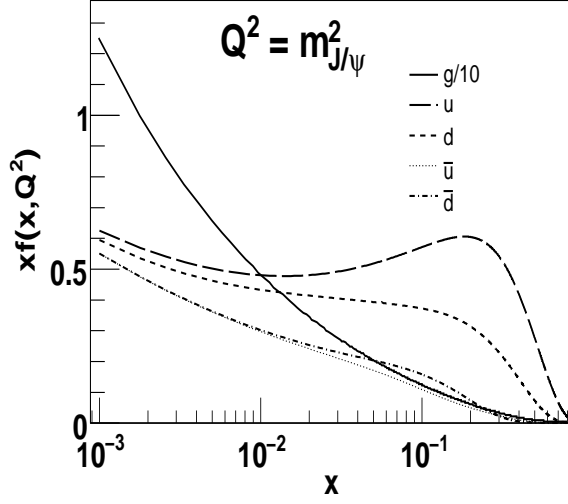


Figure 4.1: The MSTW 2008 leading order (LO) parton distribution functions in a free proton for gluon (continuous line), up quark (long dashed), down quark (short dashed), anti-up quark (dotted line) and anti-down quark (dashed-dot line). The parton densities are evaluated at a scale $Q = m_{J/\psi}$.

mated by integrating over corresponding kinematic range.

The double differential cross section for producing a $c\bar{c}$ pair can be decomposed into the individual contributions from different channels and at leading order is given by

$$\frac{d\sigma_{h_1 h_2}^{c\bar{c}}}{dQ^2 dx_F} = \frac{d\sigma_{h_1 h_2}^{q\bar{q}}}{dQ^2 dx_F} + \frac{d\sigma_{h_1 h_2}^{c\bar{c}_{int}}}{dQ^2 dx_F} + \frac{d\sigma_{h_1 h_2}^{gg}}{dQ^2 dx_F}, \quad (4.6)$$

where $\sigma^{q\bar{q}}$ is the contribution from annihilation of light quarks, $q = u, d, s$, $\sigma^{c\bar{c}_{int}}$ is the contribution from intrinsic charm quarks, and σ^{gg} is the contribution from fusion of two gluons. Due to very small charmed sea distribution appearing quadratically in the cross section calculation, the contribution of intrinsic component $\sigma^{c\bar{c}_{int}}$, is negligible compared to the other terms [260]. Hence the significant contributions from the other two leading terms read as

$$\frac{d\sigma_{h_1 h_2}^{q\bar{q}}}{dQ^2 dx_F} = \sum_{f=u,d,s} \frac{\hat{\sigma}^{q\bar{q}}(Q^2)}{Q^2} \frac{x_a x_b}{x_a + x_b} \times [q_{h_1}^f(x_a, Q^2) q_{h_2}^{\bar{f}}(x_b, Q^2) + q_{h_1}^{\bar{f}}(x_a, Q^2) q_{h_2}^f(x_b, Q^2)]$$

for light quark annihilation, and

$$\frac{d\sigma_{h_1 h_2}^{gg}}{dQ^2 dx_F} = \frac{\hat{\sigma}^{gg}(Q^2)}{Q^2} \frac{x_a x_b}{x_a + x_b} g_{h_1}(x_a, Q^2) g_{h_2}(x_b, Q^2), \quad (4.7)$$

for gluon fusion.

Here $q(x, Q^2)$, $\bar{q}(x, Q^2)$ and $g(x, Q^2)$ signify the quark, anti-quark and gluon distributions, respectively, in a hadron, evaluated at a scale Q^2 . In the present work, we have used the central set of MSTW 2008 [261] LO parton distribution functions for free protons. Uncertainties for a central set are minimum. In our all present and future calculations we have only considered the mean values of the PDF neglecting the errors associated with them. Fig. 4.1 shows the momentum distributions for up and down quarks, anti-quarks and gluons following MSTW 2008 LO central set, evaluated at the scale $Q = m_{J/\psi}$. Because of the two-parton final-state at the leading order, the incoming parton momentum fractions are fixed by the kinematics, and at a given \sqrt{s} , can be expressed in terms of x_F and Q^2 , by $x_a = (\sqrt{x_F^2 + 4Q^2/s} + x_F)/2$ and $x_b = (\sqrt{x_F^2 + 4Q^2/s} - x_F)/2$, respectively. The partonic cross sections appearing in Eqs. 4.7 and 4.7, in the leading log approximation, are given by [260, 262]

$$\hat{\sigma}^{q\bar{q}}(Q^2) = \frac{2}{9} \frac{4\pi\alpha_s^2}{3Q^2} \left(1 + \frac{1}{2}\gamma\right) \sqrt{1-\gamma}, \quad (4.8)$$

and

$$\hat{\sigma}^{gg}(Q^2) = \frac{\pi\alpha_s^2}{3Q^2} \left[\left(1 + \gamma + \frac{1}{16}\gamma^2\right) \log\left(\frac{1 + \sqrt{1-\gamma}}{1 - \sqrt{1-\gamma}}\right) - \left(\frac{7}{4} + \frac{31}{16}\gamma\right) \sqrt{1-\gamma} \right],$$

where $\alpha_s(Q^2)$ is the QCD running coupling constant, and $\gamma = 4m_c^2/Q^2$.

One important quantity in general for quarkonium production is the **sub-threshold** $Q\bar{Q}$ production. By sub-threshold $c\bar{c}$ pairs here we mean the $c\bar{c}$ pairs produced in the partonic collisions, with an invariant mass between $2m_C$ and $2m_D$ ($2m_C < Q < 2m_D$), i.e. the so called hidden charm interval. It should not be confused with particle production below kinematic production threshold. Thus it might be interesting to study the energy evolution of these sub-threshold $c\bar{c}$ pairs. In Fig. 4.2 we have thus plotted sub-threshold

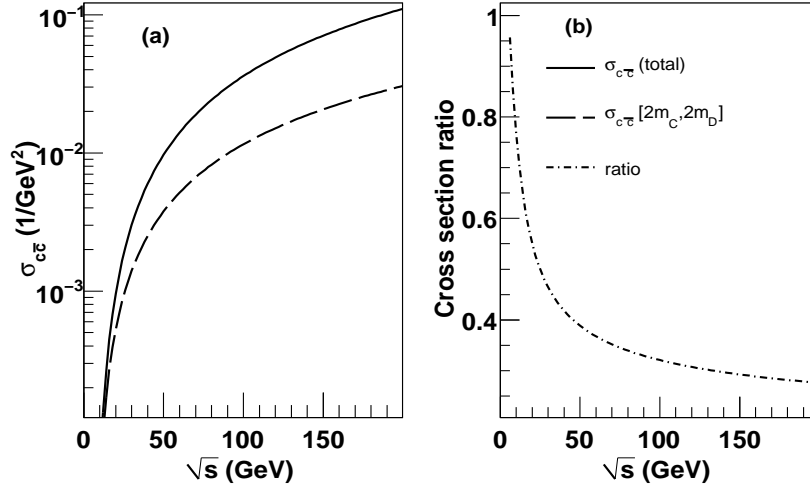


Figure 4.2: Variation of the sub-threshold (dashed line) and total (continuous line) $c\bar{c}$ production (left panel) and their ratio (sub-threshold fraction) (right panel) as a function of the center of mass energy of the colliding hadrons.

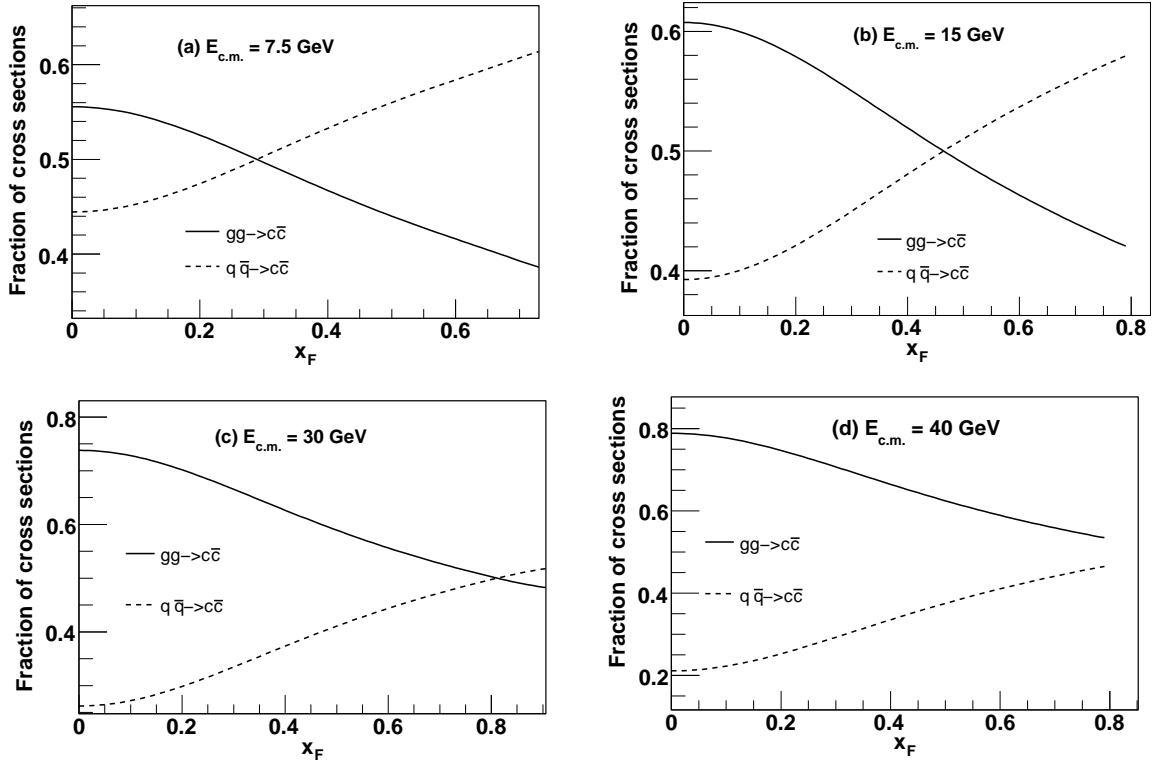


Figure 4.3: Ratio of light quark annihilation and gluon fusion cross sections for $c\bar{c}$ production in $p+p$ collisions to their sum as a function of the Feynman scaling variable x_F , at different values of the center of mass energies of the collision system. MSTW 2008 LO central PDF set is used as an input. The solid line is for quark contribution, and the dashed line is for gluonic contribution as indicated in the figures.

$\sigma_{c\bar{c}}[2m_C, 2m_D]$, and total $c\bar{c}$ production cross section and their ratio as a function of the center of mass energy \sqrt{s} of the colliding hadrons. For small values of \sqrt{s} , the two cross sections are almost indifferent indicating that all the $c\bar{c}$ pairs are predominantly produced within the hidden charm interval. However the sub-threshold cross section is found to rise less steeply with collision energy compared to the total cross section, resulting an increased separation between the two curves with increasing \sqrt{s} . The ratio of these two cross sections, the sub-threshold fraction is first seen to decrease with energy then gradually saturates for large \sqrt{s} . Thus higher be the energy of the collision, $c\bar{c}$ pairs are more likely to be produced with an invariant mass above the sub-threshold domain.

As pointed out earlier, at leading order, the significant contribution to $c\bar{c}$ production comes from the light quark annihilation and gluon-gluon fusions. Because of the larger color factors, the inclusive cross section, at a given energy, due to gluon fusion is always higher than that due to quark annihilation. However this may not be the case if one looks at the differential cross sections of these two processes. To estimate their relative size, we plot in Fig. 4.3, the fraction of the total differential cross section due to each sub-process in $p + p$ collision for different values of \sqrt{s} . At lower x_F , gluon fusion dominates the $c\bar{c}$ production whereas at higher x_F , quark annihilation also plays a crucial role. The critical value x_F^C , above which $q\bar{q}$ annihilation cross section rides over gg fusion is not fixed and depends on the underlying collision energy. Higher be the \sqrt{s} , larger is the contribution due to gluons. Consequently at RHIC ($\sqrt{s_{NN}} = 200$ GeV) or at LHC ($\sqrt{s_{NN}} = 5.5$ TeV), J/ψ production up to leading order can be reliably described by gg fusion alone. However, at the other end of the energy scale, in the FAIR energy domain, one needs to consider the light quark annihilation channel as well. This observation can be easily understood by looking at the behavior of parton distribution functions shown in Fig. 4.1. Larger x_F requires a beam parton at large x_a , which in turn means small \sqrt{s} . In this region the gluon distribution of a proton is very small compared to the valence quark distribution. Consequently, the J/ψ production cross section at large x_F is very sensitive to the sea quark distributions of the target.

Let us now turn to a description of J/ψ production in proton-nucleus collisions[255]. In this case, our model incorporates two most important cold nuclear matter (CNM)

effects, namely, i) the initial state nuclear modification of the parton distribution function affecting the perturbative $c\bar{c}$ pair production, ii) the final state dissociation of the nascent $c\bar{c}$ pair in the pre-resonance or resonance stage, due to its interactions with nucleons during its passage through the target nucleus.

The PDF in a nucleus with atomic number Z and mass number A is written as the sum of the proton ($f_i^{p/A}$) and the neutron ($f_i^{n/A}$) parton densities in a nucleus:

$$f_i^A = Z f_i^{p/A} + (A - Z) f_i^{n/A}, \quad (4.9)$$

where $f_i^{n/A}$ is obtained from $f_i^{p/A}$ by isospin conjugation: $u^{n/A} = d^{p/A}$, $d^{n/A} = u^{p/A}$, $s^{n/A} = s^{p/A}$. Deep inelastic scattering (DIS) and Drell-Yan measurements performed with nuclear targets have shown that the distributions of partons in nuclei are significantly modified relative to those in free protons. These nuclear modifications depend on the fraction of the total hadron momentum carried by the parton, x , on the momentum scale, Q^2 , and on the mass number of the nucleus, A . The mechanisms governing these modifications are not yet well understood. However based on global DGLAP analysis [111], several groups have produced parameterizations, $R_i(A, x, Q^2)$, that convert the free-proton distributions for each parton i , $f_i^p(x, Q^2)$, into nuclear ones, $f_i^A(x, Q^2)$, assuming factorization:

$$f_i^A(x, Q^2) = R_i(A, x, Q^2) \times f_i^p(x, Q^2) \quad (4.10)$$

For a recent comprehensive review of different available nuclear PDF sets one can see [263]. For our calculations, we have employed state-of-the-art EPS09 [264] interface, which is available for all mass numbers. Fig. 4.4 shows the ratio $R_i(A, x, Q^2)$ following EPS09 parameterization, again as a function of x , inside a Pb nucleus for valence up quarks, sea up quarks and gluons, calculated at the scale, $Q = m_{J/\psi}$. We note that there are essentially four different regimes. Near $x = 1$, Fermi motion inside the nucleus leads to an enhancement; following this is a suppression (the EMC effect) due to nucleon-nucleon interactions. Close to $x \simeq 0.1$, we then again have an enhancement (“anti-shadowing”), followed by a suppression at very small x (“shadowing”). Note that

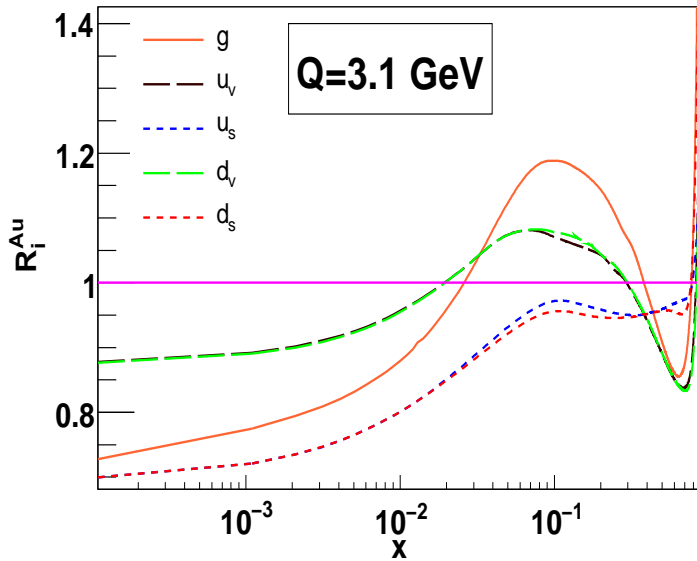


Figure 4.4: Nuclear modification of valence up (u_v) and down (d_v) quarks, sea up (u_s) and down (d_s) quarks and gluon (g) distributions inside a Au nucleus, following EPS09 interface. The parton densities are evaluated at the scale $Q = 3.1$ GeV, suitable for J/ψ production. EPS09 gives $R_i(Pb, x, Q^2)$, the scale dependent ratio of the distribution of the parton flavor i for a proton in a nucleus A , to the corresponding parton distribution in the free proton.

the particular x values where these PDFs switch from enhancement to suppression or vice versa depend on the parton type. High energy collisions generally access regions $x \leq 0.4$, so that anti-shadowing and shadowing are the phenomena of particular interest. Depending on the collision energy and the momentum of the observed J/ψ , the production rate can thus be either enhanced or reduced by the initial state nuclear modification of the gluon distribution function. It is important to note that, the quark and anti-quark distribution functions are directly probed by the nuclear DIS and Drell-Yan data, their nuclear effects are relatively well constrained and different parameterizations give almost similar results. The connection between the measurements and the nuclear gluon densities is much more indirect. Since gluon fusion plays the dominant role for $c\bar{c}$ production, a complete understanding of charmonium production in proton-nucleus collisions is presently lacking due to uncertainties in nuclear gluon distributions, as illustrated in [206]. It may also be mentioned here that in the original version of QVZ model, the nuclear effect to the parton distribution functions are ignored and free proton PDFs have been used to estimate the $c\bar{c}$ pair production in nucleon-nucleus and nucleus-nucleus collisions.

For simulating the final state interactions we closely follow the method advocated by Qiu *et al.* [253, 260], who have treated the conventional nuclear dissociation in somewhat unconventional way. In nucleon-nucleus collisions, the produced $c\bar{c}$ pairs are likely to interact with the nuclear medium before they exit. Observed anomalous nuclear enhancement of the momentum imbalance in di-jet production [265] indicates that a colored parton (quark or gluon) experiences multiple soft scatterings when it exits the target nucleus [266]. Hence, the colored $c\bar{c}$ pair produced through partonic hard scattering should also experience multiple soft scatterings when it passes through nuclear matter. These multiple soft scatterings will increase the relative transverse momentum between the c and \bar{c} , and consequently, increase the invariant mass of the $c\bar{c}$ pair. Some pairs can thus gain enough momentum to be pushed over the threshold and become two open charm mesons, and the J/ψ production cross section will in turn be reduced in comparison with nucleon targets. Larger be the size of the nucleus, more be the number of soft scatterings undergone by the pair and the reduction in the cross section for J/ψ production will be even larger. If the formation length for the J/ψ meson, which depends on the momenta of the $c\bar{c}$ pairs produced in the hard collision, is longer than the size of the nuclear medium, it is reasonable to assume that the transition probability $F_{c\bar{c}\rightarrow J/\psi}(q^2)$, defined in Eq. (4.1), can be factorized from the multiple scattering. Then, as far as the total cross section is concerned, the net effect of the multiple scattering of the $c\bar{c}$ pairs can be represented by a shift of q^2 in the transition probability,

$$q^2 \longrightarrow q^2 + \Delta q^2 = q^2 + \varepsilon^2 L(A) . \quad (4.11)$$

In Eq. 4.11, Δq^2 is the total shift, linear in $L(A)$, which effectively reduces the overlap between $c\bar{c}$ pair and $F(q^2)$. $L(A)$ is the effective length of nuclear medium traversed by the $c\bar{c}$ pair, from its point of production till it exits and depends on the details of the nuclear density distributions [205]. ε^2 represents the square of the relative momentum received by the pairs per unit length of the nuclear medium. It might be useful to note here that there are variants of QVZ model [258], where the multiple scattering is assumed to be a random walk, treated as a Krammer like process, resulting a new

prescription of momentum gain as $\Delta q^2 \rightarrow L^2$. However in all our following calculations we closely follow the original formulation of QVZ approach.

Finally we consider the J/ψ production in nucleus-nucleus ($A + B$) collisions [256]. In these collisions, parton densities are modified both inside projectile and target nuclei. Depending on the collision geometry, either the halo or the core of the nuclei will be mainly involved, and the resulting shadowing effects will be more important in the core than in the periphery. Hence the shadowing factors have to be calculated for various centrality intervals. Different prescriptions are available in literature to model the impact parameter dependent shadowing factors [267, 268, 269]. In the present calculations we implement the spatial dependence of shadowing functions assuming them to be proportional to the local nuclear density [267, 268], with Woods-Saxon (WS) profile chosen for nuclear density distributions, as:

$$R_{i,\rho}(A, x, Q^2, \mathbf{s}, z) = 1 + N_\rho^A (R_i(A, x, Q^2) - 1) \frac{\rho_A(\mathbf{s}, z)}{\rho_0}, \quad (4.12)$$

where N_ρ^A is the normalization constant. The constant is fixed so to ensure that $(1/A) \int ds dz R_{i,\rho}(A, x, Q^2, \mathbf{s}, z) = R_i(A, x, Q^2)$, for a nucleus of mass number A and radius R_A . For large values of radii, $r(= \sqrt{(s^2 + z^2)}) \gg R_A$ and $R_{i,\rho} \rightarrow 1$, while at the nuclear centre, the modifications are larger than the average R_i . Inhomogeneous shadowing effects inside the nucleus can also be invoked by postulating them to be linearly proportional to the density weighted longitudinal thickness of nucleus at the transverse position of the binary collision ($T_A(\mathbf{r}_T)$ defined as $T_A(\mathbf{r}_T) = \int \rho_A(\mathbf{r}_T, z) dz$, where $\rho_A(\mathbf{r}_T, z)$ is the local nuclear density at a point (\mathbf{r}_T, z) inside the nucleus A). However these two parameterizations of local shadowing have been found to give similar results at SPS energies, their difference lies within 2% – 3% [270]. Recently spatial dependence of the nPDFs has been studied in detail using the A -dependence of the spatially independent global EPS09 and EKS98 routines [269]. Spatial dependence is modelled as a power series of T_A , having terms up to $(T_A)^4$. Two spatially dependent nPDF sets namely EPS09s and EKS98s have also been released for public use.

The effective length of the nuclear matter $\langle L \rangle$, traversed by the $c\bar{c}$ pair, is also larger in nuclear collisions and depends on collision centrality. For a collision with an

impact parameter, \mathbf{b} , one can write $\langle L(b) \rangle = \langle L_A(b) + L_B(b) \rangle$.

In our modified version of the QVZ approach, apart from the above two nuclear effects, namely the initial state shadowing and final state dissociation no additional effect either due to colliding or due to produced medium is incorporated even for nuclear collisions.

4.3 The Drell-Yan process

In relativistic heavy-ion collisions the data on J/ψ measurements is often reported in terms of ratio of the cross sections for J/ψ production and Drell-Yan (DY) process ($\frac{\sigma_{J/\psi}}{\sigma_{DY}}$). In the Drell-Yan process, a valence quark from a nucleon in the projectile nucleus interacts with a sea anti-quark from a nucleon in the target nucleus (or vice versa) to form a virtual photon, which decays into a lepton pair ($\mu^+\mu^-$). Since the leptons interact only electromagnetically the Drell-Yan di-muons once produced do not get affected by any final state interaction of the surrounding medium. Hence Drell-Yan process is used for characterization of J/ψ suppression in nuclear collisions. A reduction in the J/ψ peak height compared to the Drell-Yan continuum with increasing collision centrality signifies larger J/ψ suppression in more central collisions. The NA50 Collaboration at CERN SPS measured first significant data on J/ψ suppression in heavy-ion collisions for 158 A GeV Pb+Pb interactions. In addition they also made significant measurements of J/ψ production in $p + A$ collisions at incident beam energies of 400 GeV and 450 GeV and for a variety of nuclear targets. For $p + A$ collisions they published two sets of data (i) first the absolute J/ψ production cross section and second the ψ -to-DY ratio for different $p + A$ systems. In case of $A + A$ collisions data is expressed in terms of ψ -to-DY ratio as a function of collision centrality. The advantage of measuring the ratio is that since the muon pairs from both the processes (i.e. J/ψ decay and Drell-Yan scattering) were collected in the same run systematic errors become minimal. However the disadvantage is the large statistical errors associated with the ratio due to much smaller production cross section (DY is a purely electromagnetic process) for Drell-Yan di-muons. Any how in the later chapters we will analyze the SPS data on $\frac{\sigma_{J/\psi}}{\sigma_{DY}}$ using

the QVZ model for J/ψ production. Since this also demands the calculation of DY production cross sections we here briefly outline the necessary formulae for the same. More details can be found in [57, 221]

As mentioned at the tree level the Drell-Yan process is the production of a lepton pair through the annihilation of a $q\bar{q}$ pair into a virtual photon. The partonic cross section is give by:

$$\frac{d\sigma}{dM^2} = \frac{4\pi\alpha^2}{3M^2} e_q^2 \delta(x_1 x_2 s - M^2) \quad (4.13)$$

where M is invariant mass of the produced dilepton, $\alpha = e^2/4\pi$ is the fine structure constant and x_1, x_2 respectively represent the projectile and target nucleons momentum fractions carried by partons with charge e_q in a collision of centre of mass energy \sqrt{s} .

In order to obtain the cross section in hadronic collisions, as a function of pair invariant mass M and pair rapidity y we need to convolute the partonic cross section with the quark and anti-quark distributions inside the colliding hadrons. The double differential cross section for production of Drell-Yan di-muons can be written as:

$$\begin{aligned} \frac{d^2\sigma(AB \rightarrow \mu^+ \mu^-)}{dy dM^2} &= \frac{1}{3} \frac{4\pi\alpha^2}{3M^2} \int_0^1 dx_1 dx_2 \delta(x_1 x_2 s - M^2) \delta(y - \frac{1}{2} \ln \frac{x_1}{x_2}) \\ &\times \sum_q e_q^2 [F_q^A(x_1, M^2) F_{\bar{q}}^B(x_2, M^2) + F_{\bar{q}}^A(x_1, M^2) F_q^B(x_2, M^2)] \end{aligned} \quad (4.14)$$

where the factor $\frac{1}{3}$ takes into account the quark and antiquark within the pair should share the same color. After integrating the delta functions to obtain $x_{1,2} = \frac{M}{\sqrt{s}} \exp(\pm y)$, the leading order cross section evaluated at a scale $Q^2 = M^2$, and taking into account that $\sigma_{pp}^{DY} \neq \sigma_{pn}^{DY} \neq \sigma_{np}^{DY} \neq \sigma_{nn}^{DY}$ becomes

$$\begin{aligned} \frac{d^2\sigma(AB \rightarrow \mu^+ \mu^-)}{dy dM} &= K_{DY} \frac{8\pi\alpha^2}{9M^3} \sum_q e_q^2 [(\frac{Z_A}{A} F_q^p(x_1, Q^2) + \frac{N_A}{A} F_q^n(x_1, Q^2)) \times (\frac{Z_B}{B} F_{\bar{q}}^p(x_2, Q^2) + \\ &\frac{N_B}{B} F_{\bar{q}}^n(x_2, Q^2)) + (\frac{Z_A}{A} F_{\bar{q}}^p(x_1, Q^2) + \frac{N_A}{A} F_{\bar{q}}^n(x_1, Q^2)) \\ &\times (\frac{Z_B}{B} F_q^p(x_2, Q^2) + \frac{N_B}{B} F_q^n(x_2, Q^2))] \end{aligned} \quad (4.15)$$

where $Z_{A,B}$ and $N_{A,B}$ are the numbers of protons and neutrons of the projectile and

nuclei having mass numbers A and B respectively. K_{DY} like earlier takes care of higher order contributions. The pdf sets used for free proton and nuclear structure functions are the same as they used for calculation of charmonium production cross section.

4.4 Summary

In this chapter, we have described our theoretical framework for calculation inclusive J/ψ production cross sections in nuclear collisions. Our formulation is based on the QVZ model. Within this model, the J/ψ production in hadronic collisions is assumed to be a factorizable two stage process. The first stage is the perturbative production of the hard $c\bar{c}$ pairs and second stage involves the non-perturbative binding of the $c\bar{c}$ pairs to the physical J/ψ resonance. The transition from $c\bar{c}$ pairs to J/ψ meson is simulated using parametric functions which incorporate various proposed mechanisms of color neutralization. In case of $p + A$ and $A + A$ collisions, two most important CNM effects that have been incorporated in our calculations are the initial state modifications of the parton densities inside target or projectile nucleus and the final state dissociation of the pre-resonant $c\bar{c}$ pairs during their passage through the nuclear medium. Nuclear modifications of the parton densities are different for the quarks and gluons and also depend on the kinematic region probed by an experiment. The final state dissociation of the pre-resonant $c\bar{c}$ pairs is incorporated through the multiple scatterings suffered by them inside the nuclear medium. Heavy quark rescattering inside the medium increases the relative four momentum between c and \bar{c} . Gain in momentum is linearly proportional to the average path length traversed by the $c\bar{c}$ pair in the nuclear medium. By this process, some of the pairs might have enough momentum to transmute to a $D\bar{D}$ pair. This results in a reduction of the charmonium yield in $p + A$ and $A + A$ collisions compared to $p + p$ collision. Even in case of heavy ion collision no additional medium effect is taken into consideration aside these CNM effects. In addition to the discussion of QVZ approach, we end this chapter with a brief description on the Drell-Yan process, often used for normalization of J/ψ data measured in nuclear collisions.

Chapter 5

Analysis of inclusive J/ψ production cross sections using QVZ model

5.1 Introduction

In the previous chapter we have introduced our theoretical formulation, the so called QVZ approach for estimation of J/ψ production in nuclear collisions. In this chapter we examine the inclusive J/ψ production cross sections for proton-proton ($p + p$), proton-nucleus ($p + A$) and nucleus-nucleus ($A + A$) collisions available from different fixed target experiments within our adapted version of the QVZ model framework. Different parameters of the model can be tuned by contrasting the model calculations with the existing data for $p + p$ and $p + A$ collisions. Note that our model, in case of heavy-ion collisions, does not incorporate any additional mechanism of J/ψ suppression apart from the cold nuclear matter effects. Thus all the model parameters can be fixed from the data available on total J/ψ production cross sections in proton induced collisions alone. Model so optimized will then be used to analyze the J/ψ production in heavy-ion collisions at SPS energy domain. Our ultimate goal is to estimate the level of J/ψ production and suppression that are expected to occur at FAIR energies. Hence in our present analysis we confine ourselves to the data corpus available from different low energy fixed target machines only. A large body of data is now available from both the collider machines RHIC and LHC, and in principle one can apply the model to such

high collision energies as well.

5.2 Analysis of the existing data at different fixed target energies

5.2.1 Proton-proton ($p + p$) interactions

Table 5.1: Basic features and results of the experiments measuring the J/ψ production cross sections in $p + p$ and $p + A$ collisions. For $p + A$ collisions results only from light target nuclei like Lithium (Li) having $A = 3$ and Beryllium (Be) having $A = 4$ and Carbon (C) with $A = 6$ are included. In case of nuclear target, the equivalent $p + N$ cross sections, estimated following α -parametrization (see text) are quoted. In addition to the inclusive forward ($x_F > 0$) production cross section, the mid-rapidity differential cross section in di-muon channel is also given.

Experiment	E_{CM} [GeV]	system	σ [nb]	$B_{\mu^+\mu^-} \frac{d\sigma}{dy}$
CERN-PS [184]	6.1	p-p	0.1 ± 0.05	≈ 0.01
CERN-PS [184]	6.7	p-p	0.31 ± 0.09	0.055 ± 0.02
AGS [149]	7.3	p-Be	1 ± 0.5	≈ 0.1
WA39 [185]	8.6	p-p	1.2 ± 0.6	0.2 ± 0.1
IHEP [271]	11.5	p-Be	11 ± 3	1.2 ± 0.4
E331 [272]	16.8	p-Be	–	5.6 ± 1.5
E331 [273]	16.8	p-Be	69 ± 23	1.2 ± 0.4
NA3 [186]	16.8	p-p	47 ± 10	–
NA3 [186]	19.4	p-p	61 ± 11	4.1 ± 0.3
E331 [193]	20.5	p-C	147 ± 7	14.3 ± 1.5
E331 [274]	20.5	p-C	95 ± 13	9.5 ± 1.0
E705 [275]	23.8	p-Li	162 ± 22	–
UA6 [276]	24.3	p-p	71.8 ± 9.3	6.2 ± 1.1
E288 [277]	27.4	p-Be	110 ± 27	8.9 ± 2.2
WA39 [278]	30	p-p	–	9.1 ± 2.5
WA39 [279]	30.6	p-Be	–	6.6 ± 1.8
E672 [188]	31.5	p-Be	161 ± 35	8 ± 2
WA39 [280]	52	p-p	–	7.5 ± 2.5
WA39 [281]	52	p-p	350 ± 160	12 ± 5
WA39 [282]	52	p-p	–	12.8 ± 3.2
WA39 [279]	52.7	p-p	–	11.0 ± 0.4
WA39 [278]	53	p-p	–	13.6 ± 3.1
WA39 [279]	62.4	p-p	–	10.2 ± 0.7
WA39 [278]	63	p-p	–	14.8 ± 3.3

Let us begin with J/ψ production in hadronic collisions [255]. As stated earlier, hadroproduction of J/ψ mesons has been studied over many years and with a variety

of hadronic systems like $p + p$ collisions, $\pi + p$ collisions and $p + \bar{p}$ collisions. Since our ultimate aim is to estimate J/ψ production in heavy-ion collisions we stick to the $p + p$ collisions only. In all these experiments, J/ψ had been detected via its decay into lepton pairs, through the peak in di-lepton invariant mass distribution. Both electron and muon channels had been explored in the experiments. They have almost identical branching ratio ($\sim 6\%$). Plethora of data exist today on J/ψ production in $p+p$ or more generally proton-nucleon ($p + N$) interactions. The experiments have used either liquid hydrogen or light nuclei as the target. The measurements have been performed over a time period spanning around 40 years, starting from the discovery experiment in 1974 in $p+\text{Be}$ collisions. Naturally over such a long period, several novel experimental techniques have been invented by different groups and different input information were available during the time of measurements. Hence comparing results of different experiments on an equal footing requires an update of the then published numbers on several aspects. To give an example, J/ψ branching ratio into di-leptons has changed with time and the treatments of nuclear effects are not homogeneous. Several attempts have been made to adjust the data from different experiments to a common framework. For a theoretical analysis one invariably needs a data set where all the measurements are readjusted using a common approach. Such compilations are available in Refs. [221, 283]. We take the data from [221] which is tabulated in Table 5.1. In addition to $p+p$ collisions, data from $p+A$ collisions for light ions are also included in the table. In case of the nuclear targets, the target mass dependence is accounted for assuming $A^{0.9}$ (recall α -parametrization) to obtain the equivalent $p + N$ cross sections. Total forward cross sections are obtained by assuming a symmetric x_F distribution around $x_F = 0$, assuming the form discussed in chapter 2. In addition to total inclusive forward cross section ($\sigma(x_F > 0)$), differential distribution at mid-rapidity ($y_{c.m.} = 0$) is also given in di-muon channel. The angular distributions are assumed always to be isotropic. All cross section data are per nucleon and adjusted with the same di-muon branching ratio ($B_{\mu^+\mu^-} = 0.0597 \pm 0.0025$). In case of inclusive cross sections branching ratio has been divided out.

We now use the data on the energy dependence of the total forward cross section to fix the relevant parameters of the model. In case of hadroproduction of J/ψ , the

Table 5.2: Values of fitting parameters $f_{J/\psi}$ and α_F used in the calculation of J/ψ production cross sections

	$F^{(C)}$	$F^{(G)}$	$F^{(P)}$
$f_{J/\psi}$	0.261	0.517	0.510
α_F	0	1.2 GeV	1.0

model contains three parameters namely, (i) $K_{J/\psi}$, the K-factor to take care of the contributions beyond leading order in perturbative $c\bar{c}$ production, (ii) α_F and (iii) $N_{J/\psi}$ both of which appear in the parametric function representing the transition of the $c\bar{c}$ pairs to physical J/ψ mesons. For optimizing the total number of parameters, we combine the K-factor with the overall normalization constant $N_{J/\psi}$. We are thus effectively left with two free parameters α_F and $f_{J/\psi} = K_{J/\psi}N_{J/\psi}$. The optimum values of these two parameters are given in Table 5.2. They are extracted by fitting the model results with the inclusive J/ψ production cross section data in the forward region ($x_F > 0$), exclusively for $p + p$ collisions given in Table 5.1. All the three parameterizations of $F_{c\bar{c} \rightarrow J/\psi}(q^2)$ are independently found to fit the available data reasonably well. Results are shown in Fig. 5.1. In addition to $p + p$ reactions, data points from equivalent $p + N$ collisions are also plotted, though they are not used in the fitting procedure. These nuclear target data points represent the forward cross section per nucleon from light targets (Li, Be, C). Their close agreement with the theoretical curves for $p + p$ collisions indicates that for light-ions J/ψ production is least affected by the nuclear effects due to the presence of few target nucleons. Theoretical curves from the model calculations are also found to be in agreement with Schuler parameterization of the \sqrt{s} dependence of inclusive J/ψ production.

Once the parameters are fixed, the model can now also be used to calculate the energy dependence of the cross section at mid-rapidity. This energy dependence has also been parameterized long ago by Craigie [221] as:

$$B \frac{d\sigma}{dy} = C \exp\left(\frac{-14.7m}{\sqrt{s}}\right) \quad (5.1)$$

where m is the mass of the particular resonance state, B is the branching ratio for di-muon channel and $C(J/\psi)=40.0$ nb. Fig. 5.2 thus shows the comparison of the data

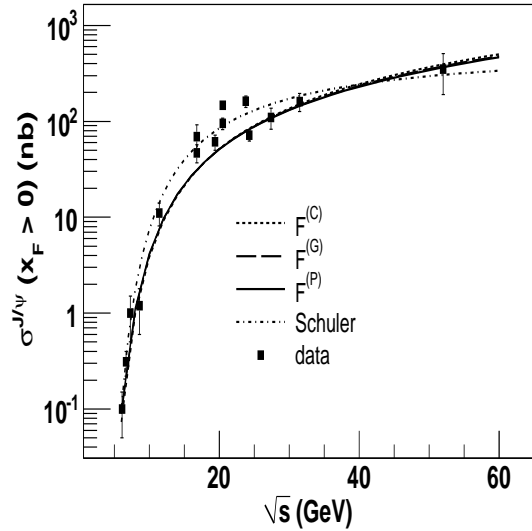


Figure 5.1: Total J/ψ production cross section in the forward region ($x_F > 0$) as a function of center of mass energy. In addition to $p + p$ collisions, the plot also contains the available data points for scaled $p + A$ collisions with light target nuclei from different fixed target experiments. The model parameters for each of the parametric forms of the transition probability $F(q^2)$ is however fixed from the $p + p$ data. The cross section as obtained from Schuler parameterization is also included.

for the mid-rapidity J/ψ production in $p + N$ collisions at fixed-target energies with the model calculations along with the parametric curve.

Thus we have seen that with all three parametric forms of the transition probabilities, representing three possible physical scenarios of color neutralization, the model gives a reasonable description of the data for J/ψ hadroproduction at the available fixed target energies. This observation is in line with the original studies made by Qiu *et al.* [253]. Note that particularly for hadronic collisions our present version of the model is exactly similar to the original version. Even then the explicit values of the model parameters obtained from fitting the data of hadronic collisions are different for the two cases. This can largely be attributed to the choice of different input set of parton densities for calculation of $c\bar{c}$ production cross sections.

5.2.2 Proton-nucleus ($p + A$) interactions

We now examine in detail the J/ψ production for nuclear targets [255]. Since the parameters α_F and $f_{J/\psi}$ are already fixed from the analysis of $p + p$ data, the only parameter that is left free in case of nuclear collisions is ϵ^2 that characterizes the square

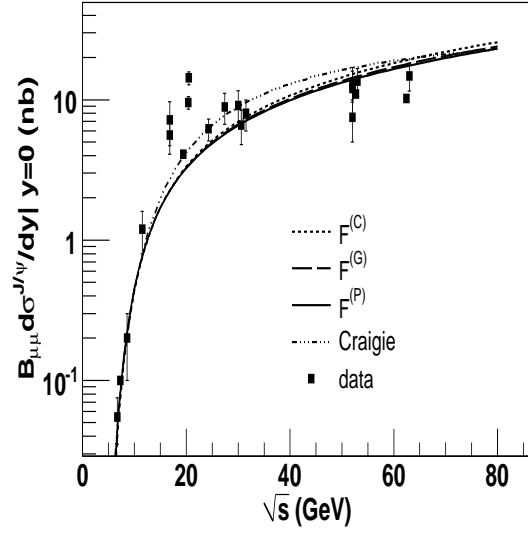


Figure 5.2: Evolution of the mid-rapidity J/ψ production cross section in di-muon channel for proton-nucleon collisions, as a function of collision energy. The Craigie parameterization of the differential cross section is also shown.

Table 5.3: Basic features of the experiments providing the inclusive J/ψ production cross sections (or their ratios) for various nuclear targets

Experiment	E_{lab} [GeV]	Collision systems	Phase space
NA60 [197]	158	p-Be, Al, Cu, In, W, Pb, U	$0.28 < y_{\text{c.m.}} < 0.78$
NA50 [110]	200	p-C, Al, Cu, Ag, Pb, U	$0.0 < y_{\text{c.m.}} < 1.0$
NA50 [196]	400	p-Be, Al, Cu, Ag, W, Pb	$-0.425 < y_{\text{c.m.}} < 0.575$
NA60 [197]	400	p-Be, Cu, Ag, W, Pb, U	$-0.17 < y_{\text{c.m.}} < 0.33$
NA50 [198]	450	p-Be, Al, Cu, Ag, W	$-0.50 < y_{\text{c.m.}} < 0.50$
E866 [202]	800	p-Be, W	$-0.10 < x_{\text{F}} < 0.93$
HERA-B [203]	920	p-C, W	$-0.34 < x_{\text{F}} < 0.14$

of the energy gained per unit path length, by the pre-resonant $c\bar{c}$ pairs due to their multiple scattering in the nuclear medium. In $p + A$ collisions the J/ψ production is influenced by the interplay of the variety of physical processes, as discussed earlier. For a thorough understanding of the involved mechanisms, we need to have accurate sets of data, spanning over large intervals of the incident proton beam energy and covering large x_{F} and p_{T} intervals. As far as present experimental situation is concerned, a wealth of high statistics J/ψ data samples have been collected over the years in several fixed target experiments covering different kinematic range and energy domains. The HERA-B [203] experiment at DESY has recorded J/ψ production in p+C, p+W reactions at 920 GeV incident proton beam energy. E866 [202] at FNAL has studied p+Be, p+Fe and

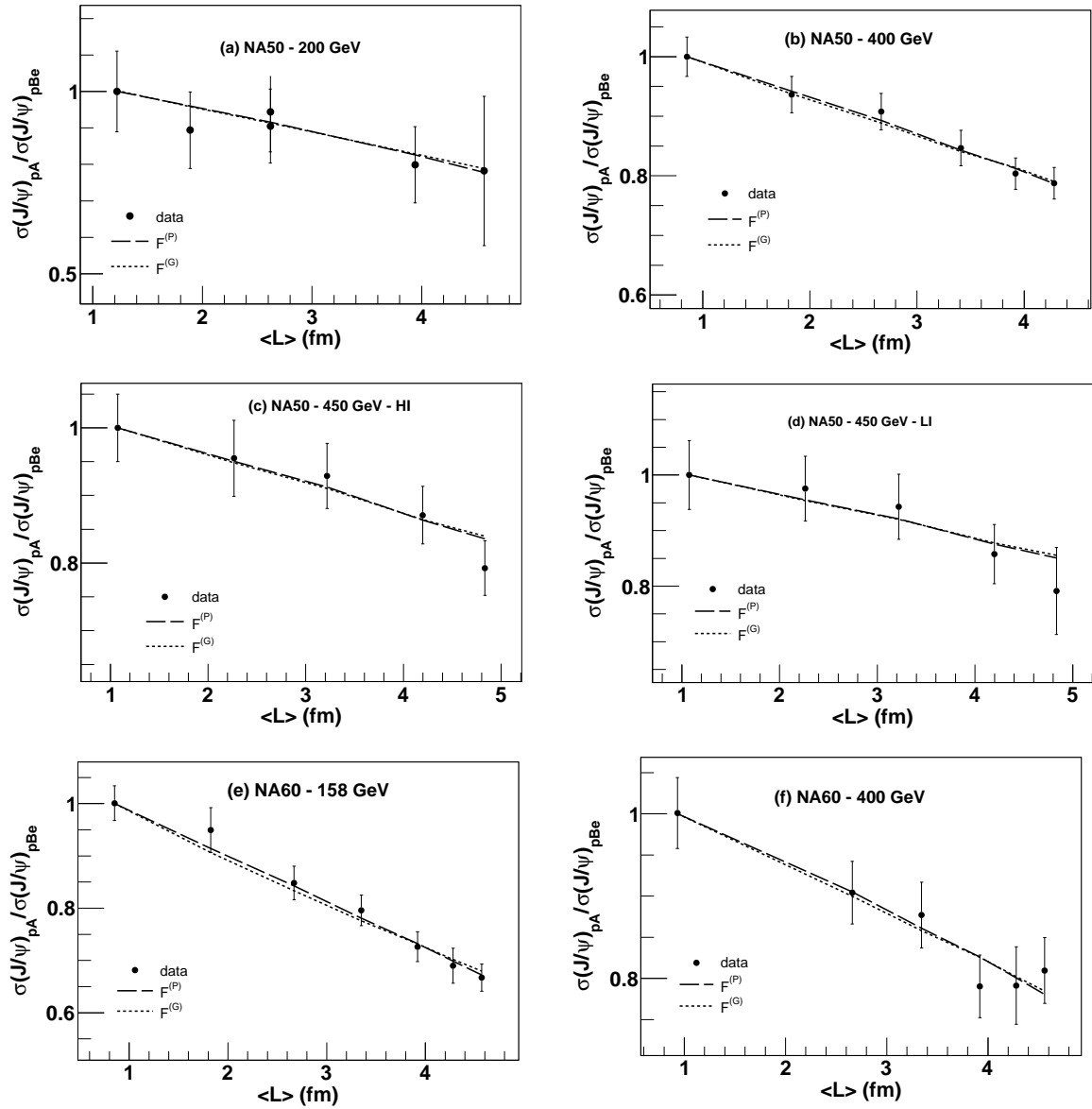


Figure 5.3: J/ψ cross section ratios for $p + A$ collisions at different energies of the incident proton beam from different fixed target experiments. Data are fitted with model calculations for two different forms of the transition probability representing two different physical mechanisms of J/ψ formation from an initial $c\bar{c}$ pair.

p+W collisions at 800 GeV, CERN-SPS experiment NA50 at 200 [110], 400 [196] and 450 [198] GeV and NA60 [197] at 158 and 400 GeV for several different nuclear targets. A unanimous feature observed in all such measurements is that at fixed collision energy, charmonium production rate per target nucleon decreases with increasing A, the mass number of target nucleus.

Table 5.4: The ε^2 values obtained from fitting the data of different fixed target experiments with different energy of the incident proton beam. ε_G^2 and ε_P^2 corresponds to $F^{(P)}(q^2)$ and $F^{(G)}(q^2)$ respectively. The errors correspond to fitting errors.

Experiment	E_{lab} [GeV]	ε_G^2 [GeV ² /fm]	ε_P^2 [GeV ² /fm]
NA60	158	$3.52 \times 10^{-1} \pm 1.72 \times 10^{-2}$	$2.47 \times 10^{-1} \pm 1.02 \times 10^{-2}$
NA50	200	$2.616 \times 10^{-1} \pm 8.72 \times 10^{-2}$	$1.9^{-1} \pm 5.67 \times 10^{-2}$
NA50	400	$2.65 \times 10^{-1} \pm 1.71 \times 10^{-2}$	$1.86 \times 10^{-1} \pm 1.07 \times 10^{-2}$
NA60	400	$2.617 \times 10^{-1} \pm 2.22 \times 10^{-2}$	$1.82 \times 10^{-1} \pm 1.37 \times 10^{-2}$
NA50	450 (HI)	$1.94 \times 10^{-1} \pm 2.46 \times 10^{-2}$	$1.38 \times 10^{-1} \pm 1.6 \times 10^{-2}$
NA50	450 (LI)	$1.79 \times 10^{-1} \pm 3.51 \times 10^{-2}$	$1.3 \times 10^{-1} \pm 2.35 \times 10^{-2}$
E866	800	$1.83 \times 10^{-1} \pm 3.28 \times 10^{-3}$	$1.31 \times 10^{-1} \pm 2.18 \times 10^{-3}$
HERA-B	920	$1.42 \times 10^{-1} \pm 1.19 \times 10^{-2}$	$1.04 \times 10^{-1} \pm 8.16 \times 10^{-3}$

In the present work, we have analyzed the J/ψ production cross section data measured in the energy range from 158 to 920 GeV. The data sets from different fixed target experiments, that have been used in the present analysis are given in Table 5.3 along with their phase space coverage. Among the listed experiments, NA50 presented their results in terms of J/ψ production cross section in di-muon channel for different nuclear targets as a function of the average nuclear path length $\langle L \rangle$. On the other hand NA60 has presented their results as the ratio of J/ψ production cross sections for a particular nucleus to that due to the lightest bombarded target nucleus beryllium (Be), as a function of $\langle L \rangle$. In case of any model study, one advantage to work with ratios is that we can get rid of the multiplicative parameters as they get cancelled. Hence for NA50 as well, we have fitted the model results with the cross section ratios rather than their absolute values. For 400 and 450 GeV we have used the lightest available target Be as the reference. In case of 200 GeV, we have chosen carbon nucleus (C) as our reference instead of hydrogen (H), as the nuclear suppression are found to be sensitive to the choice of the lightest target [206]. Fig. 5.3 illustrates our calculations fitted with the corresponding data sets from NA50 and NA60. On the other hand, for E866 and

HERA-B data we have fitted the ratio of J/ψ production cross section for W to C and Be respectively as a function of x_F , calculated from the parameter α and given in [206]. $L(A)$, as introduced in the description of the model in the preceding chapter, is replaced by the respective value $\langle L \rangle$ for a target nucleus, as used in the corresponding data set at a particular fixed target energy. The value of ε^2 (the relevant parameter in the model for quantifying the final state nuclear dissociation of J/ψ) at each energy is extracted by fitting the available data independently with the model results for both parameterizations of the transition probability namely the Gaussian distribution $F^{(G)}(q^2)$ (simulating the color singlet model) and the power law distribution $F^{(P)}(q^2)$ (mimicking the color octet formalism). The transition probability $F^{(C)}(q^2)$ containing the essential features of color evaporation model (CEM) [172], is a special case of $F^{(P)}(q^2)$ for $\alpha_F = 0$. It assumes that all the $c\bar{c}$ pairs with invariant mass less than open charm threshold has the same constant probability to evolve in a J/ψ meson. However the pairs just below the threshold should have a smaller probability to become J/ψ , than those far below the threshold. In other words, the power law parameterization $F^{(P)}(q^2)$, with $\alpha_F > 0$ is believed represent more accurate physics for J/ψ production since it includes gluon radiation effect which is essential for color neutralization of the octet channel and also for mass adjustment from $c\bar{c}$ pairs to final J/ψ eigen state. We thus refrain ourselves from further use of $F^{(C)}(q^2)$, while analyzing the J/ψ production in $p+A$ reactions. The best fit values of ε^2 as obtained separately for $F^{(G)}(q^2)$ and $F^{(P)}(q^2)$ are presented in Table 5.4. Both ε_G^2 and ε_P^2 show a non-negligible energy dependence with ε^2 increasing with decrease in the collision energy. This implies larger cold nuclear dissociation of J/ψ mesons at smaller collision energies. The observed energy dependence pattern of ε^2 for different mechanisms of J/ψ production, as emerged from our analysis is thus in line with the earlier observations of the energy dependence of the J/ψ absorption cross section in normal nuclear matter, both theoretically [206] and experimentally [197].

It might be interesting to note that for the gaussian parameterization $F^{(G)}(q^2)$ of the transition probability, as given in the previous chapter, a shift of q^2 to \bar{q}^2 , for the J/ψ suppression in $p+A$ collisions gives the following relation

Table 5.5: Comparison of the extracted ε^2 and the corresponding absorption cross section (σ_{abs}) values with free proton (p) and nuclear (n) parton distribution functions following EPS09 interface at different beam energies in case of Gaussian transition probability. The absorption cross sections extracted from the collected data from exponential $\rho < l >$ fitting are also included in the last column. The normal nuclear matter density is taken as $\rho_0 = 0.15/fm^3$.

Experiment	E_{lab} [GeV]	ε_p^2 [GeV ² /fm]	ε_n^2 [GeV ² /fm]	σ_{abs}^p [mb]	σ_{abs}^n [mb]	$\sigma_{abs}^{\rho < L >}$ [mb]
NA60	158	0.296 ± 0.0172	0.35 ± 0.0172	6.85 ± 0.4	8.1 ± 0.4	7.36 ± 0.7
NA50	200	0.22 ± 0.094	0.262 ± 0.087	5.09 ± 2.08	6.06 ± 2.01	4.68 ± 3.55
NA50	400	0.195 ± 0.017	0.265 ± 0.017	4.51 ± 0.39	6.13 ± 0.39	4.69 ± 0.75
NA60	400	0.187 ± 0.022	0.262 ± 0.022	4.3 ± 0.51	6.06 ± 0.51	4.44 ± 1.02
NA50-HI	450	0.15 ± 0.026	0.194 ± 0.0246	3.47 ± 0.6	4.49 ± 0.57	3.8 ± 1.1
NA50-LI	450	0.134 ± 0.038	0.179 ± 0.0351	3.1 ± 0.88	4.14 ± 0.81	3.71 ± 1.51

$$\sigma_{pA \rightarrow J/\psi}(\sqrt{s}) = \exp \left[-\frac{\varepsilon^2}{2\alpha_F^2} L(A) \right] \sigma_{NN \rightarrow J/\psi}(\sqrt{s}). \quad (5.2)$$

This relation is effectively the same as that accounted by the exponential $\rho < L >$ parameterization of Glauber formalism. From the equivalence of these two relations, one can thus calculate the corresponding absorption cross section as

$$\sigma_{abs} = \frac{(10 \times \varepsilon^2)}{(2 \times \alpha_F^2 \times \rho_0)} \quad (5.3)$$

where σ_{abs} is expressed in milli barn (mb). Using the relevant values for α_F and ε^2 at 158 GeV, and taking $\rho_0 \sim 0.15/fm^3$, the corresponding absorption cross section comes out to be $\sigma_{abs} \sim 8.15 \pm 0.4$ mb. Though close, it is still larger than 7.6 mb, the mean value of the J/ψ absorption cross section, that reported by NA60 Collaboration with a full Glauber model analysis. As pointed out earlier, the σ_{abs} as reported by different experimental groups are the effective quantities since they include both initial as well as final state effects. However in our calculation ε^2 and hence the corresponding σ_{abs} characterizes only the size of the final state dissociation, as the initial state effects are separately included by using the nuclear parton distributions in calculation of perturbative $c\bar{c}$ pair production. We can calculate the effective ε^2 (for $F^{(G)}(q^2)$) at different energies, following our adopted model, if we neglect the initial state effect in our calculation and use free proton pdfs without any nuclear modification for calculation of $c\bar{c}$ pair production cross section.

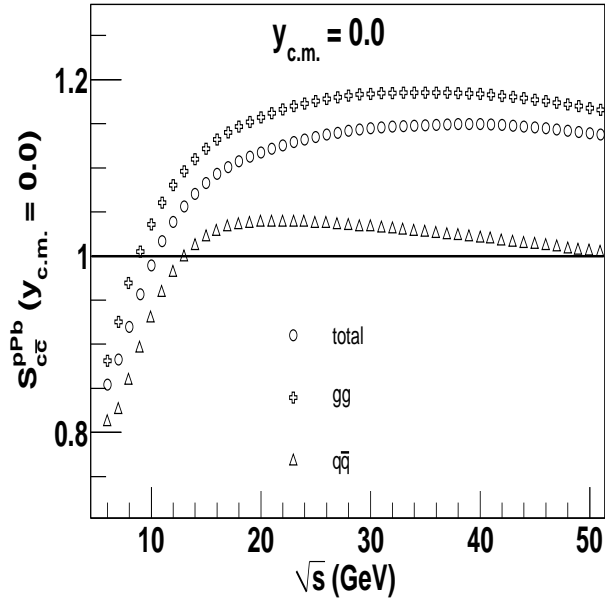


Figure 5.4: Energy evolution of the shadowing factor $S_{c\bar{c}}^{pPb}$ at mid-rapidity, following EPS09 parameterization. The individual contribution due to light quark annihilation (open triangles) and gluon fusion (open crosses) are shown separately along with their joint contribution (open circles).

Table 5.5 shows a comparison between the best fitted ε^2 values at different SPS energies with and without the nuclear modification of the parton distribution functions and along with the corresponding σ_{abs} calculated from Eq. 5.3. In addition, the effective absorption cross sections extracted from the exponential fitting of the experimentally measured data points are also shown.

It appears from the Table 5.5 that if we incorporate, as initial state effect, the nuclear modification of the parton densities following EPS09 interface, we need a higher value of ε^2 than that of a free proton pdf to reproduce the corresponding data, in the SPS energy regime. This can be understood by studying the influence of the nuclear modification of the parton distribution functions to the J/ψ production. For this purpose let us define the shadowing factor ($S_{J/\psi}^{pA}$) for a particular nucleus as the ratio between the per nucleon J/ψ production cross sections in $p + A$ and $p + p$ collisions:

$$S_{pA}^{J/\psi}(y_{c.m.}) = \frac{1}{A} \frac{d\sigma_{J/\psi}^{pA}/dy_{c.m.}}{d\sigma_{J/\psi}^{pp}/dy_{c.m.}} \quad (5.4)$$

Thus $S_{J/\psi}^{pA}$ less than unity indicates shadowing whereas $S_{J/\psi}^{pA}$ larger than unity signifies anti-shadowing. Since the pdfs enter as an input to the calculation of perturbative

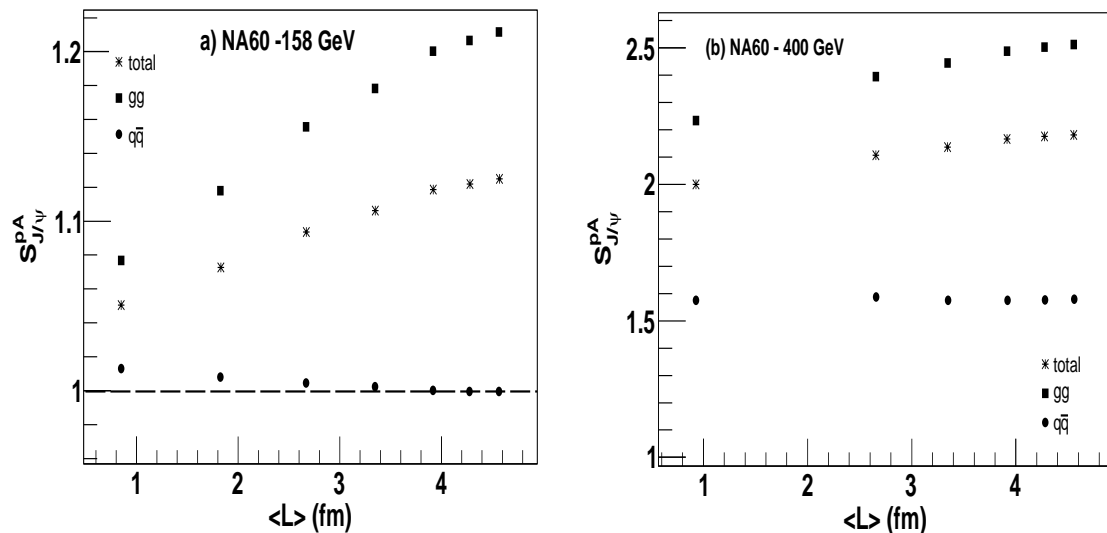


Figure 5.5: Variation of the shadowing factor $S_{J/\psi}^{pA}$ as function of $\langle L \rangle$ at NA60 for two different energies $E_b = 158$ GeV (left panel) and $E_b = 400$ GeV (right panel) of the incident proton beam. The contribution of the light quark annihilation and gluon fusion are separately shown along their sum. The inclusive production cross sections are obtained by integrating the differential cross sections over the respective rapidity windows corresponding to the two beam energies. The Gaussian form of transition probability is used for evolution of $c\bar{c}$ pairs into J/ψ mesons.

$c\bar{c}$ pair production cross section, hence in Fig. 5.4, we plot $S_{c\bar{c}}^{pPb}$ at mid-rapidity, as a function of center of mass energy, in the domain of different fixed target experiments. In the energy regime probed by the SPS experiments, charm production at mid-rapidity explores x (fraction of nucleon momentum carried by partons) values corresponding to the anti-shadowing region, where parton densities in the nuclei are enhanced with respect to those of free protons. In the absence of any final state interaction this would certainly result in enhancement of J/ψ production cross section per nucleon in $p + Pb$ collisions compared to $p + p$ collisions. To make our study more quantitative let us now calculate $S_{J/\psi}^{pA}$ for different nuclei as a function of $\langle L \rangle$ at NA60 beam energies, corresponding to their respective kinematic interval. The results are depicted in Fig. 5.5. As it appears from the figure, at both the energies we obtain an over all anti-shadowing for all the nuclei, resulting in an increment in the J/ψ production cross section compared to the $p + p$ reactions in absence of any final state dissociation. At 158 GeV, the $q\bar{q}$ fraction of the cross section shows a very weak shadowing for heavier nuclei, which is more than counterbalanced by the stronger contribution from gluon fu-

sion. Hence if nuclear modification of parton densities is taken into account, one needs a more severe amount of final state multiple scattering, than with a free proton pdf, to reproduce the measured data collected at SPS, which actually show a suppression in yield as a function of $\langle L \rangle$. Naturally the absorption cross section extracted from the corresponding ε^2 will also be larger if one takes into account the nuclear pdfs following EPS09 interface compared to the free proton (as well as the experimentally measured) case. The observation is in agreement with the earlier studies [197, 206]. The results are sensitive to the adopted parameterization of the nuclear parton densities. For example, the NA60 Collaboration has observed that if the initial state effects are evaluated with EKS98 [284] parameterization, a larger absorption cross section is required to fit the measured data ($\sigma_{abs}^{J/\psi}$ (158 GeV) = $9.3 \pm 0.7 \pm 0.7$ mb and $\sigma_{abs}^{J/\psi}$ (400 GeV) = $6.0 \pm 0.9 \pm 0.7$ mb). Slightly higher $\sigma_{abs}^{J/\psi}$ has been obtained using EPS08 [285] parameterization. To observation can be better understood by recalling the behavior of the evolution of the nPDFS as a function of x , given in the previous chapter for Au nucleus, at a momentum scale $Q = 3.1$ GeV suitable for J/ψ production. The rapidity coverage of NA60 at 158 GeV is $0.28 < y_{c.m.} < 0.78$. This roughly corresponds to a target x range, $x_b = \frac{m_{J/\psi}}{\sqrt{s}} e^{-y_{c.m.}} \sim 0.08 < x_b < 0.13$, where the gluon densities in a nucleon bound inside a nucleus is largely enhanced compared to a free nucleon. So far as quarks are concerned valence quark densities experience a small enhancement where as sea quark densities are highly depleted inside a bound nucleon. Since gluon fusion dominates over the quark-anti-quark annihilation hence we observe an overall anti-shadowing so far as J/ψ production is concerned. Due to this anti-shadowing effects, larger dissociation cross sections are required in order to reproduce the observed suppression in the data.

Apart from the inclusive production cross sections, NA60 has also measured the J/ψ rapidity distributions [197] for several target nuclei at 158 GeV as well as 400 GeV. Within the experimental coverage of NA60 di-muon spectrometer, the rapidity distributions are found to be well reproduced by Gaussian functions. Preliminary analysis reports that at 158 GeV, the distributions corresponding to the different p-A collisions can simultaneously be described, by a single Gaussian function, having mean (μ_y) = 0.05 ± 0.05 and sigma (σ) = 0.51 ± 0.02 . At 400 GeV the corresponding fit parameters

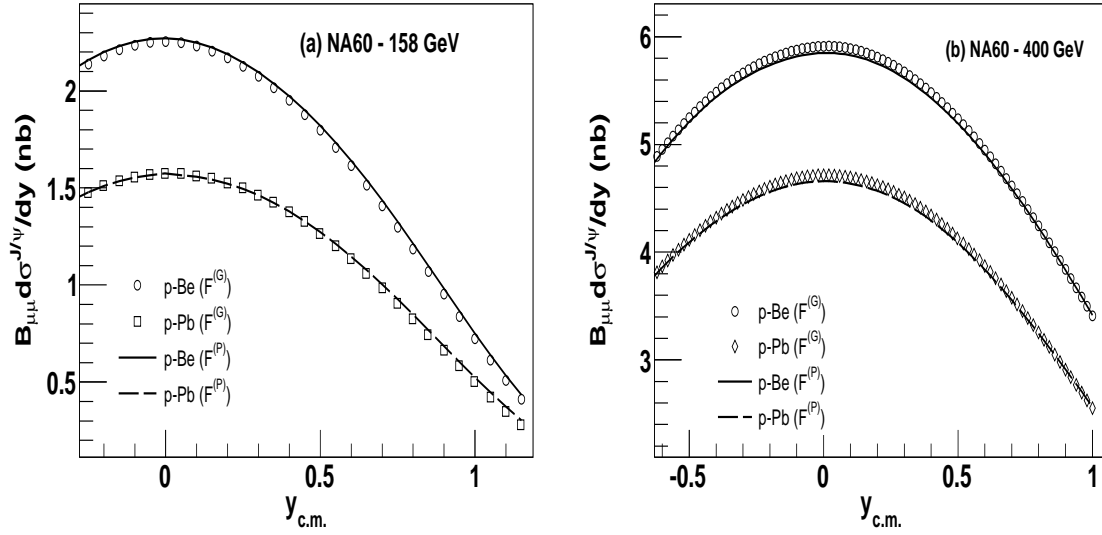


Figure 5.6: J/ψ rapidity distributions in $p + A$ collisions for Be and Pb targets at 158 GeV (left panel) and 400 GeV (right panel) as obtained in our calculations. Two different parametric forms of the transition probabilities produce almost similar results.

are mean (μ_y) ~ -0.2 (guided by the previous NA50 measurements at the same energy) and (σ) $= 0.81 \pm 0.03$. However the data for rapidity distribution are presented in arbitrary units. Cross section values have not yet been published. We thus compare the shape of rapidity distributions at both energies, as obtained from our calculations with the experimentally measured ones. The rapidity distributions for different collision systems are simultaneously fitted by a single three parameter Gaussian function. For an unbiased comparison we have also performed the Gaussian fitting of the experimental data points. Results are given in Table 5.6. At both the energies, the widths of the rapidity distribution are found to be higher in our model calculations in comparison with the measured values. Moreover our calculations can not reproduce the negative mean value of the rapidity distribution at 400 GeV. For illustration, we have shown the rapidity distributions for Be and Pb targets, following our model calculations in Fig. 5.6.

Apart from the absolute production cross sections, NA50 Collaboration has also published the data on J/ψ production in $p + A$ collisions as well as Pb+Pb collisions in terms of J/ψ to Drell-Yan (DY) ratio. It might be interesting to check the viability of our model analyzing the ratio in $p+A$ collisions [286]. The advantage of analyzing this ratio is that the cross-sections for both the processes are directly measured in the experiment and thus does not require any additional theoretical modeling or extrapolations. Moreover

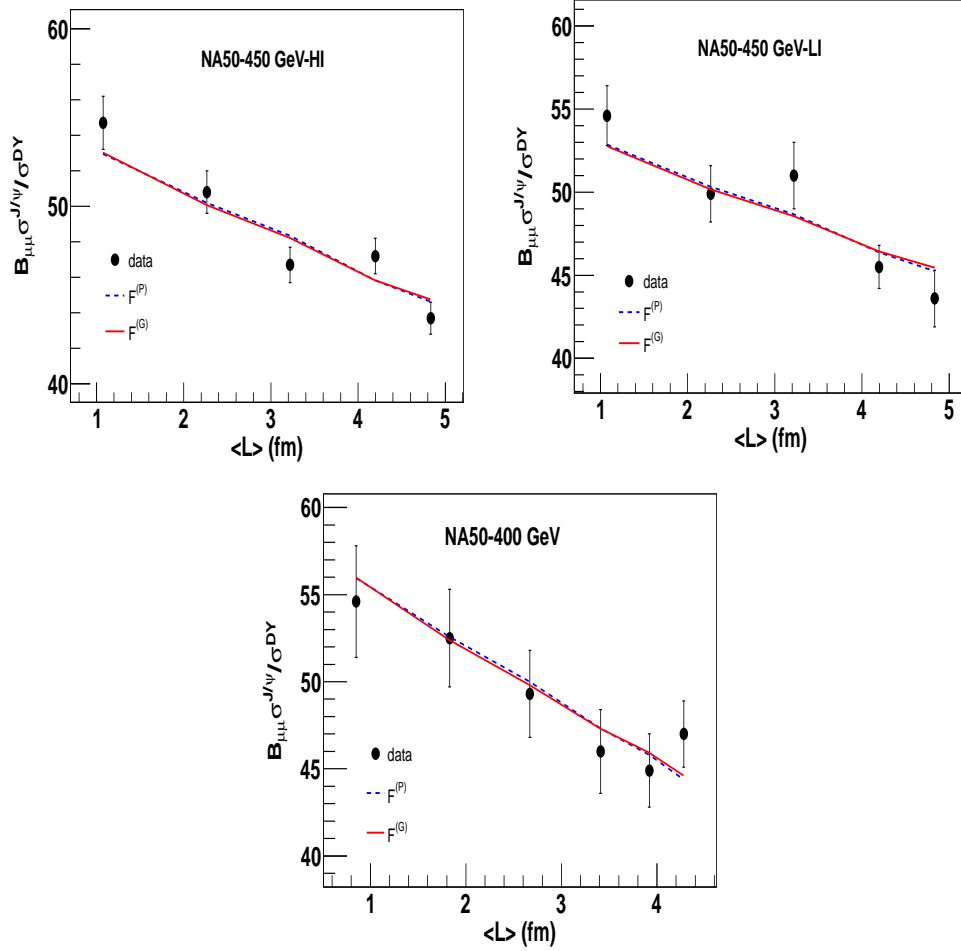


Figure 5.7: Model description of the data on ratio of the J/ψ -to-Drell-Yan production cross-sections in 450 GeV and 400 GeV $p + A$ collisions, measured by NA50 Collaboration at SPS. For 450 GeV proton beam energy, data for high intensity (HI) and low intensity (LI) run are separately shown. The two theoretical curves represents two different parametric forms of J/ψ formation probability ($F(q^2)$).

Table 5.6: Parameters of the Gaussian functions used to fit the J/ψ rapidity distributions in $p + A$ collisions at 158 GeV and 400 GeV. The superscripts (P) and (G) respectively denote the power law and Gaussian parameterizations.

E_{Lab} (GeV)	$\mu_y^{(Expt)}$	$\mu_y^{(P)}$	$\mu_y^{(G)}$	$\sigma_y^{(Expt)}$	$\sigma_y^{(P)}$	$\sigma_y^{(G)}$
158	0.044 ± 0.1	0.02 ± 0.087	0.02 ± 0.086	0.55 ± 0.06	0.66 ± 0.09	0.065 ± 0.096
400	-0.27 ± 0.16	0.0009 ± 0.037	-0.0002 ± 0.034	0.86 ± 0.2	0.97 ± 0.07	0.92 ± 0.059

since the muon pairs for both events were collected in the same run, it certainly gives a better control over the systematic uncertainties. However due to huge statistical uncertainty in measurement of Drell-Yan di-muons, NA60 never published the results of their analysis in terms of this ratio.

Fig. 5.7 shows the variation of the J/ψ to Drell-Yan cross section ratio as a function $\langle L \rangle$, in $p + A$ collisions measured by NA50 Collaboration. The two theory curves result from fitting the above data sets following two parameterizations of $F(q^2)$. The $\langle L \rangle$ values as published with the data are used to generate the theoretical curves. Note that for a given parameterization of $F(q^2)$ (power-law or Gaussian), our employed model contains three parameters. Two of them, namely ϵ^2 and α_F were already fixed earlier using inclusive J/ψ data on absolute production cross-sections in $p + A$ and $p + p$ collisions respectively. The only free parameter left in the present analysis is the K_{eff} defined as $K_{eff} = f_{J/\psi}/K_{DY}$ where $f_{J/\psi} = K_{J/\psi} \times N_{J/\psi}$. K_{DY} takes care of higher order effects in Drell-Yan production. As evident from the figure, both the curves can give a satisfactory description of the data. This is of course expected from our earlier observation, where we found that the J/ψ production in $p + A$ collisions at SPS energies is well described by both forms of $F(q^2)$. This more or less completes our analysis of J/ψ production in $p + A$ collisions within QVZ approach.

5.2.3 Nucleus-Nucleus collisions

We will now delve into the analysis of J/ψ production in heavy-ion collisions [256, 286]. Precisely we plan to examine the heavy-ion data available from CERN-SPS experiments. We would like to reemphasize here that measurement of J/ψ suppression in

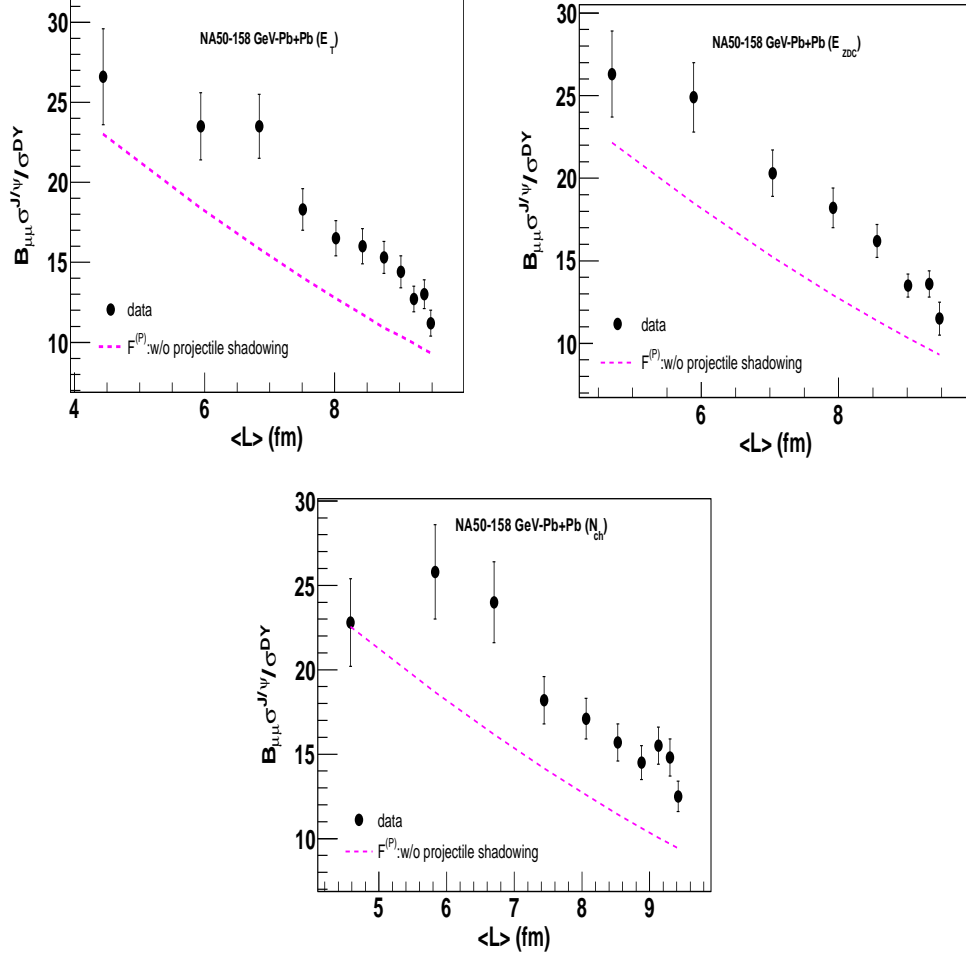


Figure 5.8: Centrality dependence of J/ψ -to-Drell-Yan ratio in 158 A GeV Pb+Pb collisions measured within the acceptance ($0 \leq y_{c.m.} \leq 1$ and $-0.5 \leq \cos(\theta_{cs}) \leq 0.5$) of the NA50 muon spectrometer. Data were published using three independent centrality estimators. The theoretical curve correspond to the power law ($F^{(p)}(q^2)$) parametric form of the J/ψ transition function. Model calculations do not include the shadowing corrections of the projectile nucleons into account and thus completely underestimate the data.

nucleus-nucleus collisions was initiated by the NA38 Collaboration at SPS in S+U and O+Cu collisions with sulphur and oxygen beams of energy 200 A GeV. However the data were later found to be well explained by conventional normal absorption mechanism in nuclear matter accounted by Glauber model formalism. Subsequently both NA50 and NA60 Collaborations at SPS measured J/ψ production respectively in 158 A GeV Pb+Pb and In+In collisions. Initially both the experiments observed significant anomalous suppression of J/ψ yield, above certain centrality thresholds, beyond the cold nuclear matter suppression modeled using Glauber formalism. Though the Pb+Pb data were found to be well explained by a variety of models [210, 211, 220, 287, 257, 258, 288], with or without incorporating deconfinement scenario, none of them satisfactorily reproduced the NA60 data. A coherent description of both the results were missing and the theorized origin of the additional suppression thus remained unsolved and debated. However in both the measurements, the corresponding value of normal nuclear absorption cross section ($\sigma_{J/\psi}^{eff} = 4.18 \pm 0.35$ mb) was extracted from the data collected in $p + A$ collisions at 400 GeV [196]. With the new measurements of charmonium in $p+A$ collisions at 158 GeV [236], where $\sigma_{J/\psi}^{eff}$ turned out to be almost twice as large as that at 400 GeV, the NA60 experiment reported the relative charmonium yield in In+In collisions to be compatible within errors with absorption in cold nuclear matter; an anomalous suppression of about 25 - 30 % still remains visible in the most central Pb+Pb collisions. Apart from SPS, J/ψ suppression has also been measured by now at RHIC and LHC. However in the present work we shall analyze the data available from NA50 and NA60 experiments only. In principle, our model can also be applied the higher \sqrt{s} available from the colliders like RHIC and LHC. However in nuclear collisions at those energies secondary production of charmonia due to regeneration effects should also be taken into account.

Let us now look at the data available from SPS in more detail. In case of NA50 Pb+Pb collisions we have selected the latest data set that corresponded to their new measurement of J/ψ production in year 2000, under improved experimental conditions with respect to their previous three heavy-ion runs between the time period 1995 to 1999. The target system was placed in a vacuum chamber and the setup was better adapted to

study in particular the most peripheral nuclear collisions with unprecedented accuracy, which was otherwise polluted by out-of-target interactions particularly Pb-air interactions. On the other hand use of a thin target compared to the previous runs helped to avoid the re-interactions of the target fragments and thus helped to have precise data in most central collisions. Data were originally published in terms of J/ψ -to-Drell-Yan ratio as a function of collision centrality expressed in terms of average path length $\langle L \rangle$. Data were collected in the di-muon kinematical domain $0 < y_{c.m.} < 1$ and $-0.5 < \cos(\theta_{cs}) < 0.5$. Drell-Yan differential cross-sections are integrated in the mass domain $2.9 - 4.5 \text{ GeV}/c^2$. Analysis has been performed using three independent centrality estimators, namely, neutral transverse energy (E_T) deposited in electromagnetic calorimeter, forward energy (E_{ZDC}) deposited in zero degree calorimeter and charge particle multiplicity per unit of pseudo-rapidity at mid-rapidity $(dN_{ch}/d\eta)_{max}$. For each centrality estimator, the centrality classes and the corresponding values of number of participant nucleons, N_{part} , of impact parameter, b , and of the average path length of nuclear matter traversed by the pre-resonant $c\bar{c}$ pair, $\langle L \rangle$ are given. We shall examine all three data sets and like $p + A$ case, we have used the published $\langle L \rangle$ values in our model calculations. It is also important to mention that for Pb+Pb collisions, no model parameter is tuned. All the model parameters are fixed from the present and previous analysis of $p + A$ data. The NA60 Collaboration on the other hand, used two different methods to analyze their data on J/ψ production in In+In collisions, in the same energy and kinematic domain as that of NA50. The first method followed the standard approach used by NA38/NA50 experiments where J/ψ yield is normalized to the corresponding Drell-Yan (DY) production and $\sigma_{J/\psi}/\sigma_{DY}$ was extracted in three centrality intervals. In contrast to NA50, centrality was inferred using only a zero degree calorimeter and is expressed in terms of N_{part} . However very poor statistics of the Drell-Yan pairs limited the statistical significance of the results and prevented any finer centrality binning. Hence in the second approach NA60 published their final results in terms of ratio between measured J/ψ yield and expected J/ψ yield which is calculated using Glauber model assuming absorption in cold nuclear matter is the only active suppression mechanism. However one obvious disadvantage of this so called measured-to-expected ratio that the

data becomes sensitive to the theoretical model inputs. Particularly the models like our present one where the cold nuclear dissociation are not accounted following Glauber framework can not directly compared with the data. We thus desist from examining the measured-to-expected J/ψ ratio available from NA60 experiment. However post RHIC era, the J/ψ data from both Pb+Pb and In+In colliding systems were reanalyzed and presented in terms of nuclear modification factor of J/ψ , $R_{AA}^{J/\psi}$ as a function of N_{part} , with the aim to compare results from different experiments on equal footing. However there is caveat as well. For both Pb+Pb and In+In systems the common input to calculate $R_{AA}^{J/\psi}$ is the J/ψ production cross section in $p + p$ collisions, $\sigma_{pp}^{J/\psi}$. But $\sigma_{pp}^{J/\psi}$ was not directly measured in either case, rather estimated from the extrapolation of the $p + A$ data up to $A = 1$. Hence initial estimations were based on the $p + A$ data collected at 400 GeV. Resulting suppression pattern for SPS Pb+Pb collisions ($\sqrt{s} \sim 17.3$ GeV) looked similar to that obtained in Au+Au collisions at RHIC ($\sqrt{s} \sim 200$ GeV). Subsequently they were corrected by using the NA60 $p + A$ data collected at 158 GeV and the suppression patterns look different. We shall compare our model results with these latest values of R_{AA} expressed as a function of N_{part} for both In+In and Pb+Pb systems. It is also important to reiterate that for nuclear collisions, no model parameter is tuned. All the model parameters are fixed from the analysis of the relevant $p + A$ data sets.

We start with the centrality dependence of J/ψ -to-Drell-Yan ratio available for Pb+Pb collisions. Alike $p + A$ systems, in this case also the production would be affected by the initial state effects like nuclear modification of the parton densities both inside target as well as projectile nucleons. To investigate the role played by parton shadowing in detail let us first compare the data with our model calculations with out incorporating the nuclear modifications of projectile nucleons. Results are illustrated in Fig. 5.8. Data for three different centrality estimators are shown differently. The theoretical curves correspond to the power law parametrization of $F(q^2)$. As evident from the figure, the theoretical curves completely underestimate the data (Same is true for the Gaussian though not shown explicitly). The dominant contribution to J/ψ production comes from gluon fusion and at the SPS kinematic domain gluons in the projectile nucleons are heavily anti-shadowed. Once these shadowing corrections of projectile partons are

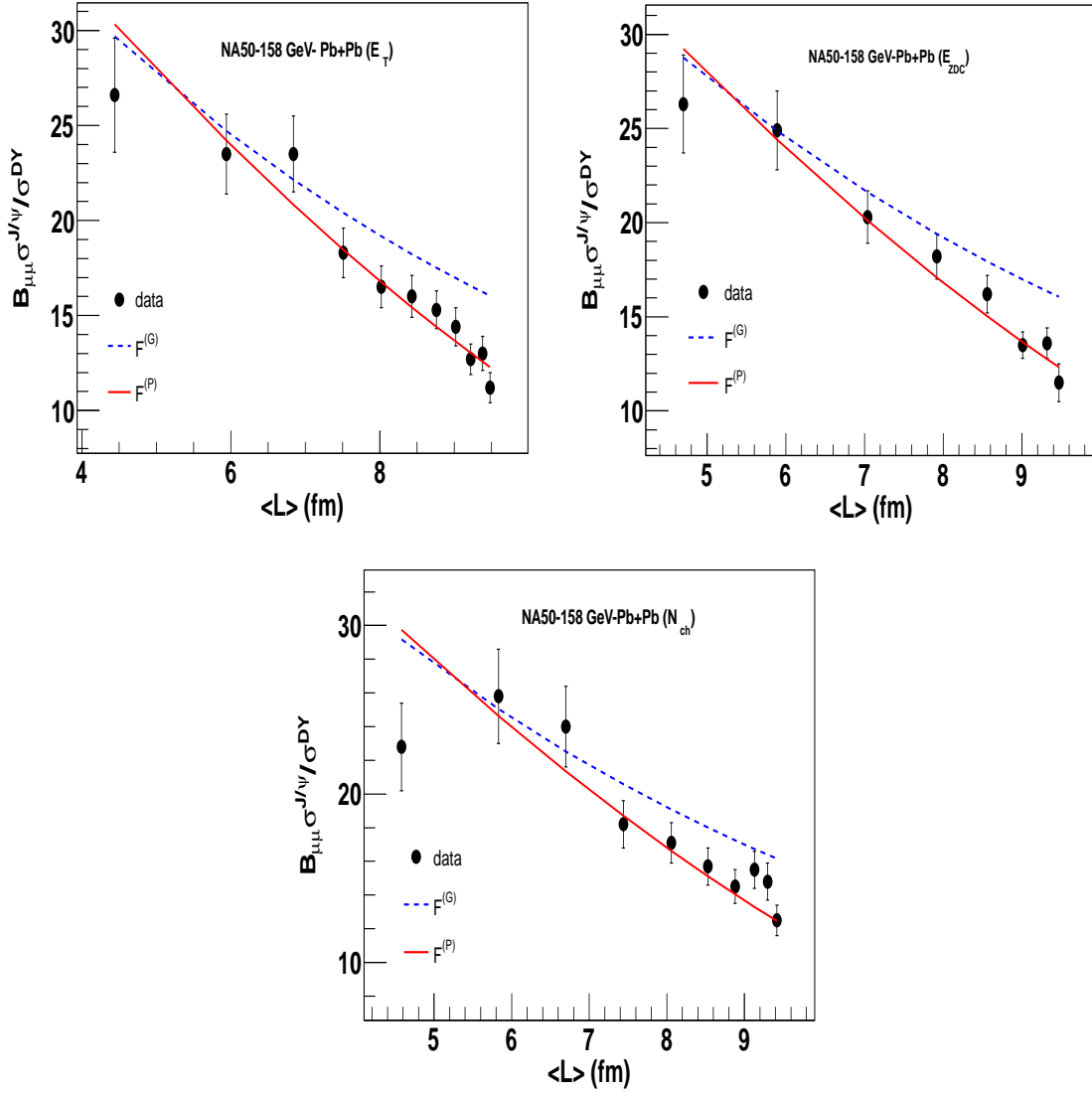


Figure 5.9: Centrality dependence of J/ψ production in Pb+Pb collisions measured at 158 A GeV beam energy. Three independent centrality estimators were used to analyze the data. Data sample were collected within the phase space window: $0 \leq y_{c.m.} \leq 1$ and $-0.5 \leq \cos(\theta_{cs}) \leq 0.5$. The theoretical curves correspond to the two different parametric forms of the J/ψ transition function. Global shadowing corrections of the projectile and target nucleons are taken into account.

taken into account, a much better description of the data is obtained as seen in Fig. 5.9. Here we have contrasted the data with both forms of the transition probability, $F(q^2)$. For both the cases we have considered global shadowing implying the shadowing factors are independent of the spatial location of the partons. The Gaussian form $F^{(G)}(q^2)$ gives lower suppression than that observed in data. However the power law form, $F^{(P)}(q^2)$ can fairly describe all the three data sets and for all centralities. It thus does not provide any additional room for any anomalous suppression mechanism either hadronic or partonic to set in. One might recall that for $F^{(G)}(q^2)$, the corresponding suppression is equivalent to that obtained in first order approximation of Glauber theory. Thus though it can account for the peripheral and semi-central collisions but fails to generate enough suppression for very central Pb+Pb collisions. On the other hand due to threshold effect power law form generates a much stronger suppression for collisions involving heavy nuclei. As all the model parameters namely α_F , K_{eff} and ε^2 , are constrained from the p+p and p+A data, in our present calculations, no free parameter is required to be tuned. The observed J/ψ suppression in Pb+Pb collisions can be fully accounted for by the heavy quark re-scattering in the cold nuclear medium, without considering further suppression in the hot medium created in the later expansion stages. Earlier the model has also been found successful to describe the then available NA50 data on J/ψ suppression in Pb+Pb collisions [257]. However in those studies shadowing corrections to nuclear parton densities were ignored and E_T fluctuations had to be explicitly incorporated, through a tunable parameter, for better reproduction of the data at large E_T .

Finally in Fig. 5.10, we have examined the effect of local shadowing. Shadowing factors are assumed to be proportional to local nuclear density as depicted in previous section. The effect of spatial dependence of shadowing is more visible for peripheral collisions. The dominant contribution to J/ψ production comes from the gluon fusion. At the SPS energy regime gluon densities in both target and projectile exhibit anti-shadowing and hence when a spatial dependence of the nuclear parton densities is incorporated in the model, gluons at the core are more effected compared to those near the surface. Hence in peripheral collisions the J/ψ production cross section is less

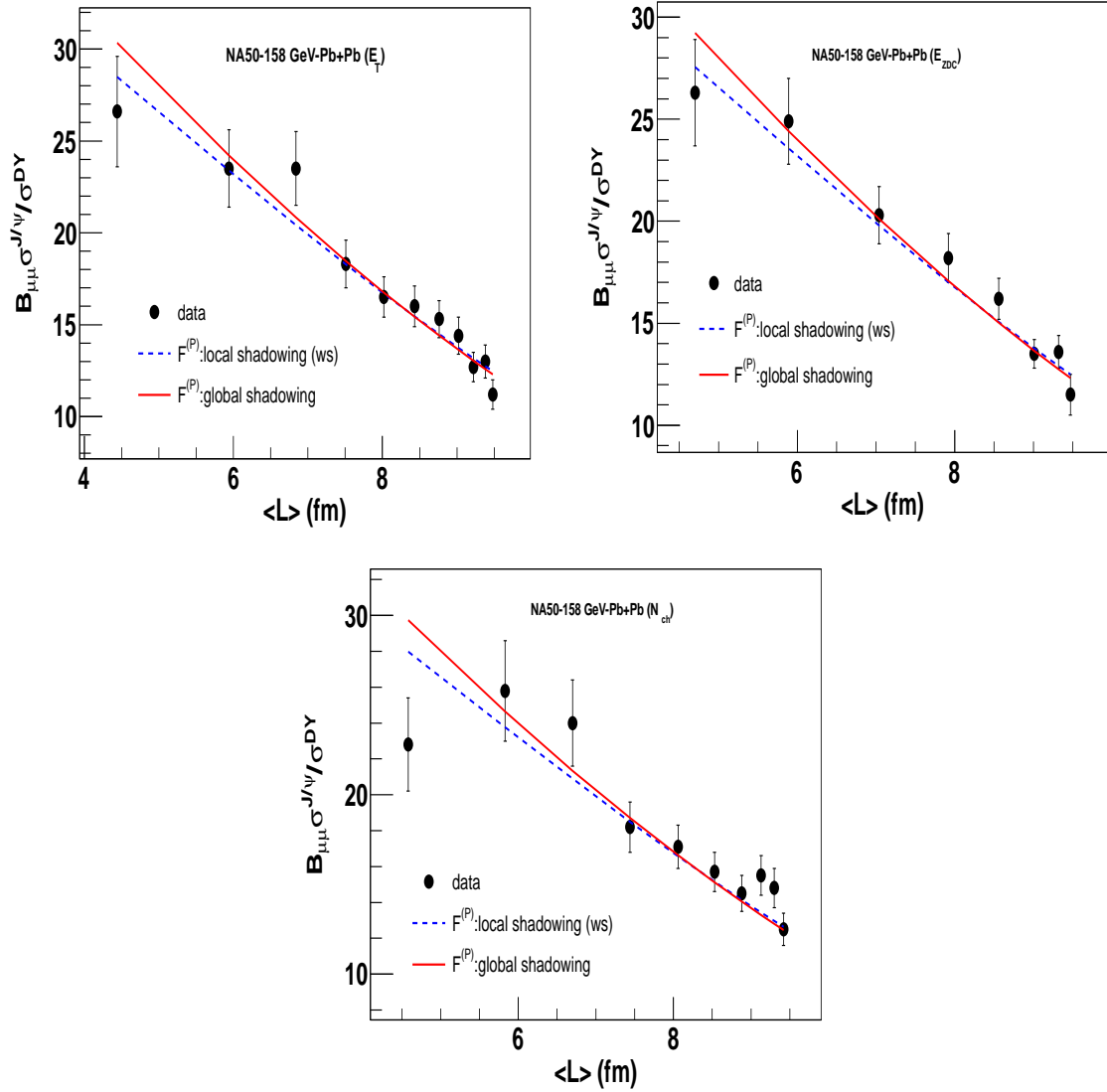


Figure 5.10: Model calculation of the centrality dependence of J/ψ production contrasted with the data for Pb+Pb collisions measured by NA50 Collaboration at 158 A GeV beam energy and in the kinematic domain: $0 \leq y_{c.m.} \leq 1$ and $-0.5 \leq \cos(\theta_{cs}) < 0.5$. Data sets corresponding to all three independent centrality estimators are shown. Shadowing corrections of the projectile and target nucleons as incorporated in the model, are assumed to be proportional to the local nuclear density. For completeness global shadowing corrections are also shown.

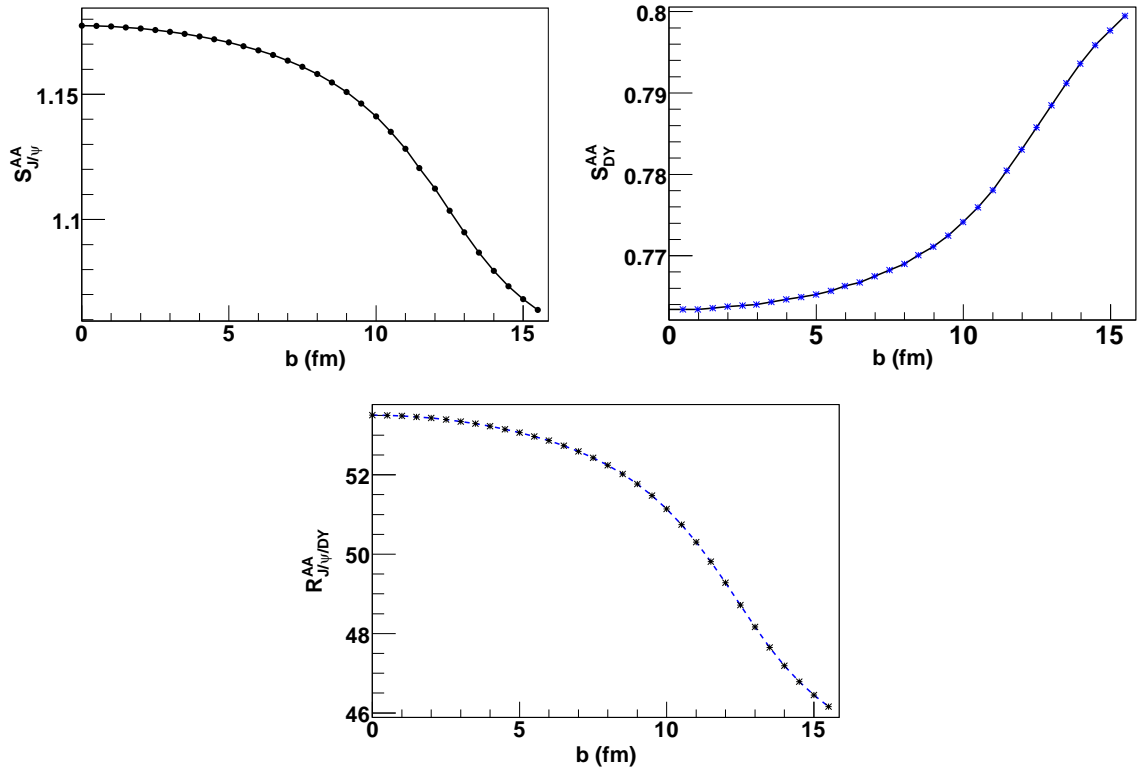


Figure 5.11: Centrality dependence of the shadowing factors for J/ψ (top left) and Drell-Yan productions (top right) and ratio of the two production cross sections in di-muon channel (bottom), in absence of any final state nuclear dissociation ($R_{J/\psi/DY}^{AA} = B_{\mu\mu}\sigma_{J/\psi}^{AA}(\varepsilon^2 = 0)/\sigma_{DY}^{AA}$) for J/ψ (right), in 158 A GeV Pb+Pb collisions. Total cross-sections are obtained by integrating the differential cross-section in the rapidity range $0 < y_{c.m.} < 1$, which corresponds to the rapidity coverage of the NA50 di-muon system for the Pb-Pb run.

for local shadowing compared to the global case (where the amount of anti-shadowing is independent of spatial position of the partons and thus same for different centrality intervals) and for most central collision it is more. To examine such geometrical effects in more detail, let us now calculate the shadowing function ($S_{J/\psi}(DY)$), defined as the ratio between J/ψ (or Drell-Yan) production cross-sections in Pb+Pb and p+p collisions in absence of any final state interaction. Since gluons and quarks are effected differently by shadowing effects behavior of the resulting shadowing functions for J/ψ and Drell-Yan productions will also be different. This is illustrated in Fig. 5.11, where we have plotted the variation of the shadowing functions in 158 A GeV Pb+Pb collisions as a function of impact parameter.

As evident from the figure, in the kinematic domain probed by SPS heavy-ion collisions, J/ψ production gets enhanced due to increasing gluon densities whereas the

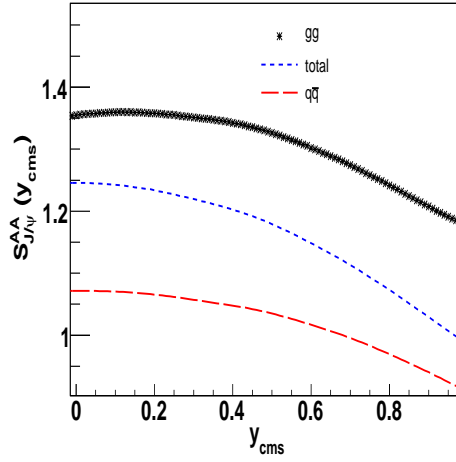


Figure 5.12: Rapidity dependence of the shadowing factor for J/ψ in 158 A GeV Pb+Pb collisions within the coverage of NA50 muon system. The contributions from quark annihilation and gluon fusion are shown separately.

shadowing effects in Drell-Yan production can be attributed to the depleted quark densities inside the Pb nucleus. Effects are maximum for central collisions, as explained above. We have also plotted the ratio $R_{J/\psi/DY}^{AA}$ defined as the ratio of the two production cross sections in di-muon channel, in absence of any final state nuclear dissociation ($R_{J/\psi/DY}^{AA} = B_{\mu\mu}\sigma_{J/\psi}^{AA}(\varepsilon^2 = 0)/\sigma_{DY}^{AA}$). Due to absence of final state dissociation the ratio exhibits a decreasing trend with decrease in collision centrality. Note for $b = 0$, the ratio assumes a value $R_{J/\psi/DY}^{AA} \simeq 53$. It is close to the normalization factor used in [210] to describe the J/ψ -to-DY ratio in 158 A GeV Pb+Pb collisions. This can be further illustrated by looking at the rapidity dependence of the shadowing function. In Fig. 5.12, we have shown the rapidity dependence of the shadowing function for J/ψ production. The contributions arising from the gluons fusion and quark annihilation are plotted separately along with the total. The shadowing effects for quark annihilation is more than compensated by gluon fusion.

We plan to close this section with analysis of the centrality dependence of $R_{AA}^{J/\psi}$ for In+In and Pb+Pb collisions. Like the previous case, our model does not contain any adjustable parameter for nuclear collisions. Since we are calculating the ratio of the production cross sections in $A + A$ and $p + p$ collisions, the corresponding K -factors get canceled out. Thus in this case the number of effective parameter are two, namely α_F and ε^2 both of which are fixed from $p + p$ and $p + A$ data. Fig. 5.13 shows the variation

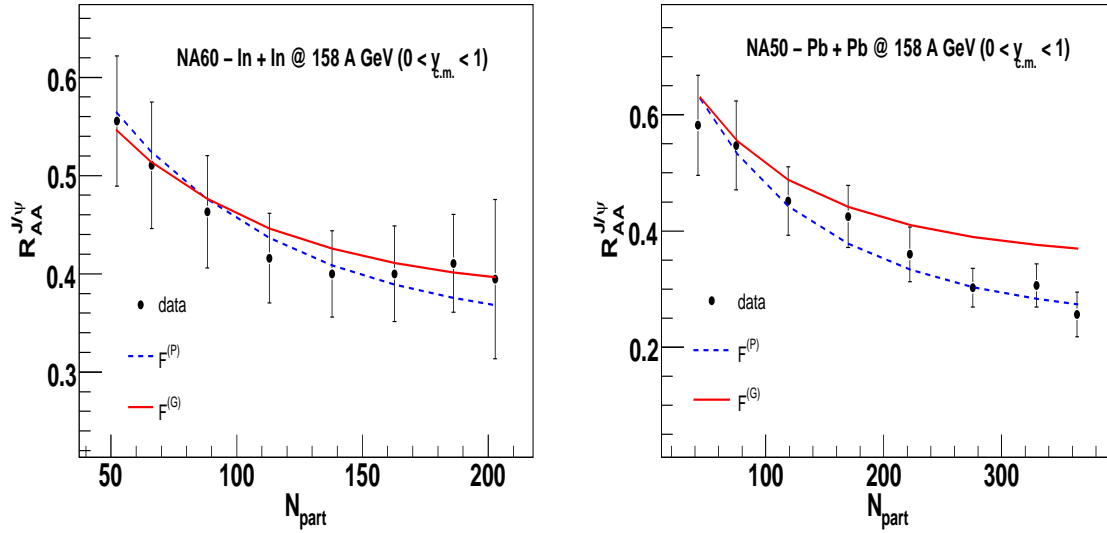


Figure 5.13: Centrality dependence of J/ψ production in In+In (left panel) and Pb+Pb (right panel) collisions measured at same energy ($E_b = 158$ A GeV) and kinematic domain ($0 < y_{c.m.} < 1$). Data are represented in terms of nuclear modification factor R_{AA} plotted as a function of N_{part} estimating the collision centrality. Error bars include both statistical and systematic uncertainties. Two different parametric forms of the transition function are used for generating the theoretical curves.

of $R_{AA}^{J/\psi}$ as a function of N_{part} for In+In and Pb+Pb collisions as calculated from our model in comparison with the available latest data [246]. The In+In data points can be reasonably described within errors by both Gaussian ($F^{(G)}(q^2)$) as well as power law ($F^{(P)}(q^2)$) forms of transition probability. In case of Pb+Pb collisions, as expected, $F^{(G)}(q^2)$ generates lower suppression than that observed in data though $F^{(P)}(q^2)$ can describe the data reasonably well. Note that for Gaussian form the corresponding value of ϵ_G^2 was obtained by analyzing the recent NA60 data for p+A collisions at 158 A GeV. Naturally it can account for the In+In data but fails to generate enough suppression for Pb+Pb case.

5.3 Summary

In summary, in this chapter we have examined the available data on J/ψ production cross sections for different colliding systems from different fixed target experiments. The J/ψ production cross sections are calculated within the ambit of the adapted version of the QVZ model described in the previous chapter. The model accounts for the cold

nuclear matter dissociation of J/ψ in an unconventional way. Contrary to the usual nuclear absorption picture quantified following Glauber formalism, our model describes nuclear suppression of J/ψ mesons in terms multiple scattering of the $c\bar{c}$ pairs inside the nuclear medium. The crucial quantity in this case is ε^2 defined as the gain in the square of the relative four momentum between $c\bar{c}$ pair per unit length which can be fixed from the data. On the other hand different form of J/ψ transition probability $F(q^2)$ allows one to accommodate a wide variety of physical mechanisms of color neutralization and resonance formation. Over a wide energy range the J/ψ production in proton induced reactions are found to be fairly well described by our model with different forms of $F(q^2)$. The data corpus for $p + A$ collisions, includes the ratio of the absolute J/ψ production cross sections $\left(\frac{\sigma_{J/\psi}^{pA}}{\sigma_{J/\psi}^{pBe}}\right)$ measured by both NA50 and NA60 Collaborations at different energies of the incident proton beam. In addition to the absolute cross sections our model also describe the ψ -to-DY ratio measured in by NA50 Collaboration in $p + A$ reactions. The same ε^2 values optimized from the $p + A$ data on the target mass dependence of $\frac{\sigma_{J/\psi}^{pA}}{\sigma_{J/\psi}^{pBe}}$ is also explain the target mass dependence of ψ -to-DY ratio which establishes the viability of our analysis. Data do not show any preference for a particular mechanism of resonance formation, over the other and same holds true for nuclear collisions with lighter nuclei. In addition to $p + A$ data, our calculations for both functional forms of $F(q^2)$ are found to match the J/ψ production cross sections in 158 A GeV In+In collisions measured by NA60 Collaboration and expressed in terms of R_{AA} . We have used the latest R_{AA} values where the J/ψ production cross sections in $p + p$ collisions are directly obtained from the extrapolation of the $p + A$ measurements (upto $A = 1$) performed at 158 A GeV, instead of rescaling any high energy data. However for heavier nuclei, gluon radiation effects are found to be mandatory for a complete description of the data, provided the initial state shadowing effects are correctly taken into account. We have analyzed the J/ψ cross sections in 158 A GeV Pb+Pb collisions, collected by NA50 Collaboration. Results of our analysis indicate antishadowing effects inside both target and projectile nucleons which unless properly taken into account, our calculations underestimate the data. A further investigation of the initial state effects indicates that in the kinematic regime probed by SPS heavy ion collisions quark densities show a shad-

owing behavior which is more than overcompensated by the antishadowing of the gluon densities. This ultimately leads to antishadowing enhancement for charmonium production whereas shadowing reduction for Drell-Yan production. With the initial state effects included, our model can explain the centrality dependence of J/ψ suppression in Pb+Pb collisions for all centrality bins with the power law form of $F(q^2)$ that incorporates the radiation of semi hard gluons from an evolving colored $c\bar{c}$ pair. In this case we have matched the data both for ψ -to-DY ratio as well as $J/\psi R_{AA}$. The Gaussian form of $F(q^2)$, which is equivalent to the usual Glauber systematics of course fails to explain the data for central collisions. However the reproduction of the heavy ion data within QVZ model, in principle, nullify the observation of any anomalous suppression at SPS even for most central Pb+Pb collisions. Note that in case of $A + A$ collisions no free parameter is required to be adjusted in our calculations. All parameters are fixed from the analysis of $p + A$ data. Another important observation is the beam energy dependence of the parameter ε^2 , came out from the analysis of the $p + A$ data. Larger values of ε^2 with decreasing beam energy implies magnification of the cold nuclear suppression effects at low energy collisions. This is also in agreement with the existing theoretical as well as experimental evidences where larger nuclear absorption cross section has been found at lower energies.

Chapter 6

Prediction of J/ψ production and suppression at FAIR energy collisions

6.1 Introduction

In this chapter we give predictions for J/ψ production and suppression expected to occur in the FAIR energy domain. We shall start with calculations of J/ψ production cross sections in proton induced collision. The modified QVZ model, previously calibrated using SPS data, will be extended to the FAIR energy collisions for this purpose. This will be followed by the estimation of possible J/ψ suppression effects in nuclear collisions. The cold nuclear matter suppressions will again be evaluated within the QVZ approach. However a very high baryon density medium is anticipated in the heavy-ion collisions at FAIR. Such a hot and baryon dense medium might induce additional suppression of J/ψ production. We will thus explore the issue of anomalous J/ψ suppression in a dense baryonic medium.

FAIR is being constructed so as to be operated in a modularized structure. In the first phase beams will be delivered by SIS-100 ring and one gets proton beams having momentum up to 30 GeV/c. In the final phase, beams will be accelerated by SIS-300 ring, which will deliver protons having momentum up to 90 GeV/c. For heavy-ions the

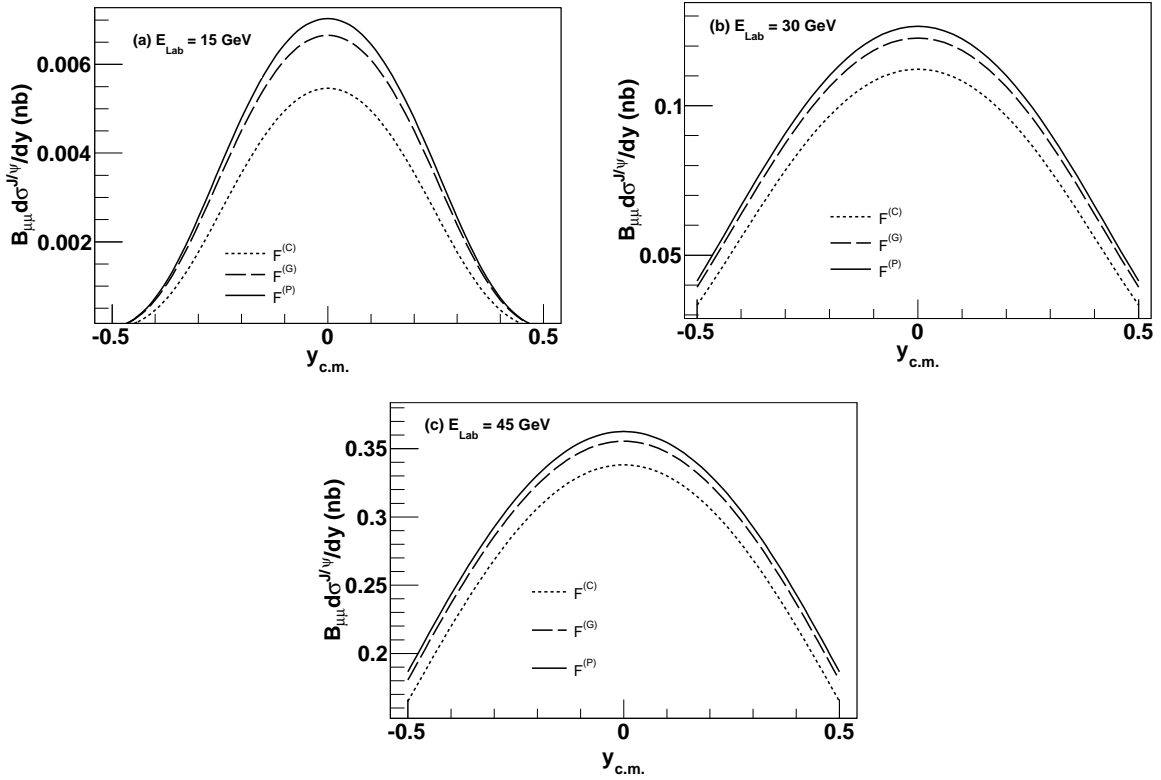


Figure 6.1: Rapidity distribution of J/ψ mesons produced in $p + p$ collisions in di-muon channel, for 15 GeV (top left panel), 30 GeV (top right panel) and 45 GeV (bottom panel) incident proton beams. Such measurements will be performed in the SIS-100 and SIS-300 rings of the upcoming CBM experiment at FAIR.

maximum beam energy at SIS-300 will be 35 (45) A GeV depending on their Z/A ratio. We note that at threshold energy for J/ψ production in the reaction $p + p \rightarrow p + p + J/\psi$ is about 12 GeV per nucleon in the laboratory frame. Thus at FAIR, J/ψ production will occur close to the kinematic production threshold.

6.2 J/ψ production in proton-induced collisions

6.2.1 $p + p$ collisions

For precise determination of the medium effects on J/ψ production in nuclear collisions, one quite essential pre-requisite is the measurement of J/ψ production cross sections in $p + p$ collisions, as discussed earlier. In these collisions J/ψ production is not affected by any kind of medium effects either primary or secondary. In the FAIR energy range, inclusive J/ψ production cross sections in $p + p$ collisions was indeed measured in the old experiments, as visible from Table 5.1 of chapter 5, though with large error bars.

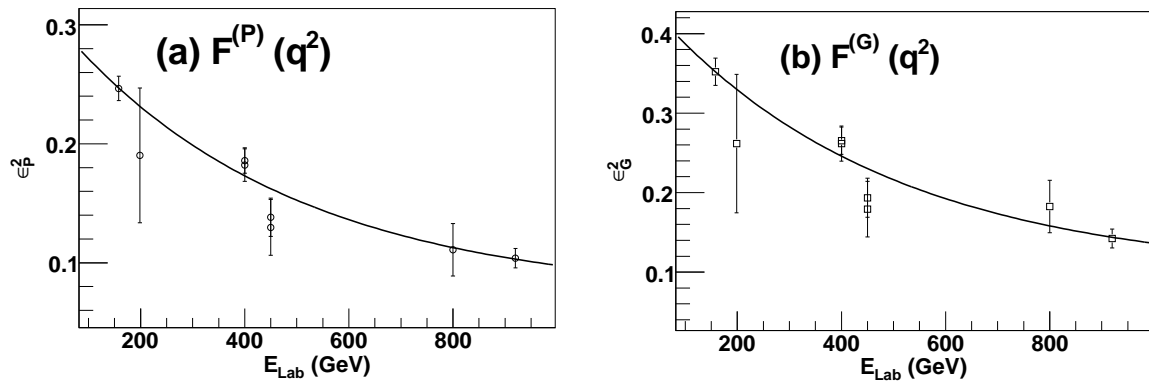


Figure 6.2: Variation of ε^2 with energy of the incident proton beam for a) $F^{(P)}(q^2)$ (left panel) and b) $F^{(G)}(q^2)$ (right panel). The points on the plots are taken from Table 5.4 of chapter 5. In both the cases the energy dependence has been parameterized following exponential functions.

Data suffer from low level of accuracy due to lack of statistics and limited experimental techniques. At FAIR, one can aim at measuring the multi-differential observables with the high intensity beams, for a fairly long data taking period.

In Fig. 6.1, we present the J/ψ rapidity distribution in protonic collisions with 15, 30 and 45 GeV proton beams, for all three different functional forms of the transition probability, $F_{c\bar{c} \rightarrow J/\psi}(q^2)$ [255]. As expected, the distributions are symmetric about the center of mass rapidity $y_{c.m.} = 0$, and the width of the distribution decreases with the decrease in the beam energy. The data for inclusive J/ψ production cross section, in this energy regime, are well accounted by all three different cases of formation mechanisms as seen in the previous chapter. However the differential cross sections take different values for different forms of $F_{c\bar{c} \rightarrow J/\psi}(q^2)$. The yield is found to be minimum for constant probability, $F^{(C)}(q^2)$ and maximum for power-law probability, $F^{(P)}(q^2)$, for all three beam energies, with the relative difference decreasing with increasing beam energy.

6.2.2 $p + A$ collisions

We now move on to the issue of J/ψ in $p+A$ collisions at FAIR [255]. For this purpose, we have parameterized the observed dependences of ε^2 (parameter in the model accounting for nuclear dissociation of the nascent $c\bar{c}$ pairs) on the energy of the incident proton beam, for both $F^{(G)}(q^2)$ and $F^{(P)}(q^2)$, using exponential functions. The parameterizations of $\varepsilon^2(E_{\text{Lab}})$ are shown in Fig. 6.2. These parametric relations can now be extrapolated to

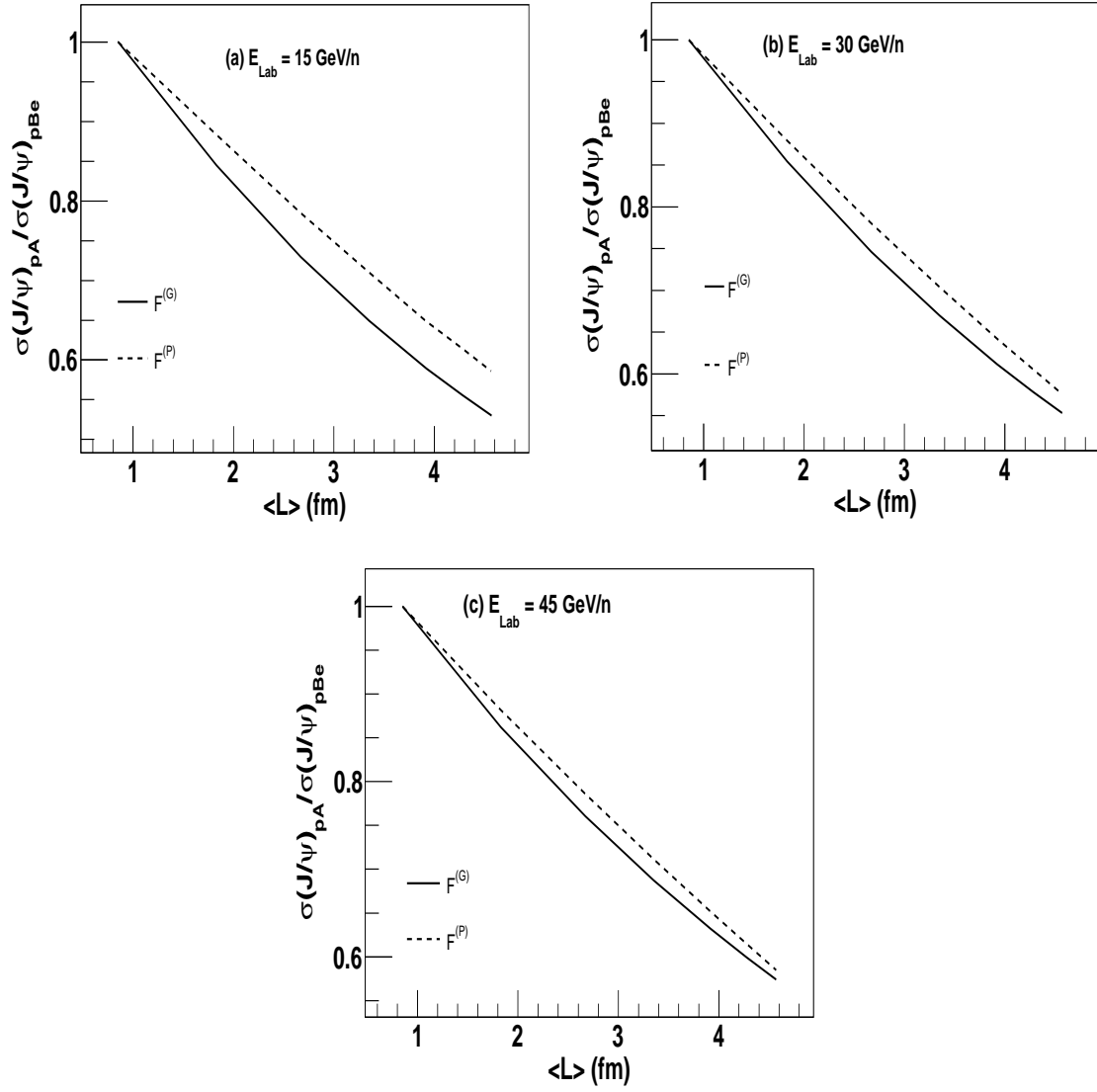


Figure 6.3: J/ψ production cross section ratios in $p+A$ collisions, as a function of $\langle L \rangle$ for different target nuclei in the FAIR energy domain, as predicted by our calculations. We have used both the Gaussian $F^{(G)}(q^2)$ as well as power law $F^{(P)}(q^2)$ forms of the transition probabilities for calculation of J/ψ yield. Lower be the energy of the incident proton beam the two different forms representing two different physical mechanisms of J/ψ formation is seen to generate different amount of suppression. Gaussian form ($F^{(G)}(q^2)$) is seen to generate more suppression than the power law ($F^{(P)}(q^2)$) form.

Table 6.1: J/ψ absorption cross section (σ_{abs}) in cold nuclear matter at FAIR energies. EPS09 parameterization has been used as an input for calculation of J/ψ production and thus the σ_{abs} characterizes only final state dissociation.

E_{lab} [GeV]	σ_{abs} [mb]
15	10.4 ± 1.79
30	10.1 ± 1.77
45	9.87 ± 1.76

derive the expected level of suppression at energies relevant to the CBM experiment at FAIR. In the Fig. 6.3 we have predicted the normal nuclear suppression in $p+A$ collisions, for $E_{Lab} = 15, 30$ and 45 GeV. Inclusive cross sections are obtained by integrating the single differential cross sections over the kinematic range: $-0.5 \leq y_{c.m.} \leq 0.5$. Following the same approach as NA60, we have calculated J/ψ cross section ratios (with Be as the reference) as a function of $\langle L \rangle$ for different target nuclei, for power-law and Gaussian transition probabilities. In case of $F^{(G)}(q^2)$, one can also find the corresponding final state absorption cross section, σ_{abs} , as might be extracted from the data that will be collected at FAIR. Results are given in Table 6.1. The value of σ_{abs} in the FAIR energy domain appears to be around 10 mb, which is larger compared to that obtained at 158 GeV. However the experimentally measured values can be larger than those reported here due to the interplay of the initial state parton shadowing effects. This fact can again be appreciated by looking the behavior of the shadowing functions in the lower energy regime, relevant for FAIR experiments. In Fig. 6.4, we have plotted the shadowing function, $S_{pA}^{J/\psi}$, for different nuclei as a function of $\langle L \rangle$ at a beam energy of 30 GeV of the incident proton beam. The inclusive production cross sections are calculated over a rapidity interval $-0.5 \leq y_{c.m.} \leq 0.5$. The contributions coming from the two leading order process namely gluon fusion and quark annihilation are shown separately along with their sum. As evident from the figure, incorporation of nuclear PDFs following EPS09 parameterization, results in reduction of the $c\bar{c}$ and hence J/ψ production for nuclear targets compared to the protonic collisions, for both the production processes. These observations can be understood by recalling the behavior of EPS09 nPDF distribution given in chapter 2. The rapidity interval at 30 GeV beam energy, considered in the present calculation, explores target x region, $\sim 0.24 < x_b <$

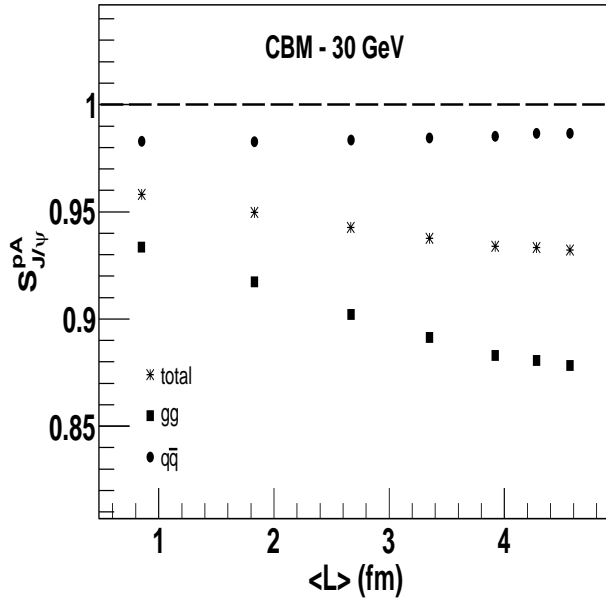


Figure 6.4: Variation of the shadowing factor $S_{J/\psi}^{pA}$, as function of the average path length $\langle L \rangle$, for a 30 GeV incident proton beam. Such measurements will be performed in the SIS-100 phase of the upcoming CBM experiment at FAIR.

0.66. In this region parton population in a nucleon bound inside a nucleus is depleted compared to a free nucleon. Since valence quark densities are more affected than the gluon densities, shadowing effects are more prominent for quark annihilation than gluon fusion. Thus, within the present theoretical scenario, a smaller dissociation cross section, compared to the free proton case might be required to describe the J/ψ suppression expected to occur at FAIR. Of course a conclusive picture can be drawn only after the measurements are performed.

In addition to the inclusive production cross sections, we also calculate the J/ψ rapidity distributions for different target nuclei. Fig. 6.5 illustrates the J/ψ differential production cross section at these three energies for three different $p + A$ systems. The obtained distributions can be fitted with the Gaussian functions. The corresponding best fit parameters are given in the Table 6.2.

One important outcome of the above study is the following. At SPS and higher energies, the calculated inclusive J/ψ yields employing both the forms of transition probabilities, are found to match the measured data for different $p + A$ systems, within error bars. Results for differential distributions are also in close proximity for the two cases. In other words none of the inclusive or differential measurements help us to select

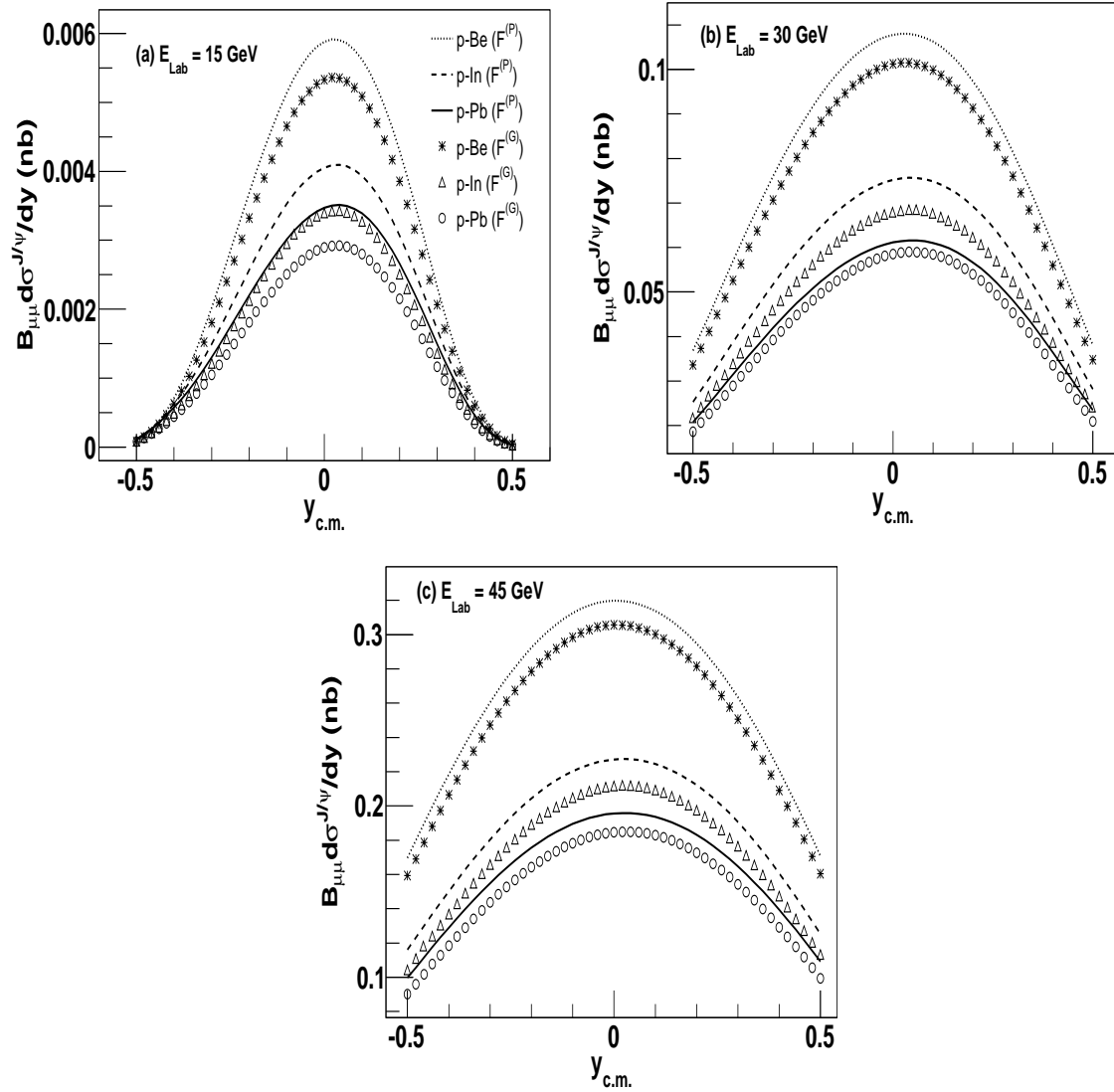


Figure 6.5: The differential J/ψ production cross section per nucleon as a function of the center of mass rapidity $y_{c.m.}$ for different target nuclei (Be, In and Pb) in the FAIR energy domain, at $E_{Lab} = 15$ GeV (top left panel), 30 GeV (top right panel), 45 GeV (bottom panel), as predicted by our calculations. Both the Gaussian $F^{(G)}(q^2)$ (markers) as well as power law $F^{(P)}(q^2)$ (lines) forms of the transition probabilities are used for calculation of J/ψ yield.

Table 6.2: Parameters of the Gaussian functions used to fit the J/ψ rapidity distributions in $p + A$ collisions for incident proton beam energies 15 GeV, 30 GeV and 45 GeV. The superscripts (P) and (G) respectively denote the power law and Gaussian parameterizations.

E_{Lab} [GeV]	$\mu_y^{(P)}$	$\mu_y^{(G)}$	$\sigma_y^{(P)}$	$\sigma_y^{(G)}$
15	1.34×10^{-2}	1.28×10^{-2}	2.11×10^{-1}	2.04×10^{-1}
30	1.81×10^{-2}	1.82×10^{-2}	3.57×10^{-1}	3.51×10^{-1}
45	1.78×10^{-2}	1.89×10^{-2}	4.52×10^{-1}	4.41×10^{-1}

either of the existing schemes of color neutralization. However the picture appears to be different at lower energies. The two possible hadronization schemes are found to generate different amount of suppressions. The Gaussian distribution gives higher suppression compared to the power law distribution. As the energy of the incident proton beam decreases, the difference between the J/ψ yields as predicted by two models increases. This might be attributed to the difference between the physical mechanisms incorporated in $F^{(G)}(q^2)$ and $F^{(P)}(q^2)$. As explained in chapter 2, $F^{(P)}(q^2)$ is associated with the radiation of soft gluons by the nascent $c\bar{c}$ pairs which in turn help them to reduce the pair invariant mass and thus facilitating the formation of J/ψ mesons. However, for the Gaussian probability $F^{(G)}(q^2)$, the related physical process is not assisted by any gluon radiation during the evolution. As a consequence, the J/ψ formation probability is highly suppressed for the $c\bar{c}$ pairs produced with large invariant mass. This results in a difference between the J/ψ production cross sections following two hadronization schemes, which becomes appreciable at lower beam energies. This can be quantitatively understood by looking at the invariant mass distribution of the produced $c\bar{c}$ pairs at different beam energies. Fig. 6.6 shows the distribution of the $c\bar{c}$ pairs produced at the initial stage (from gluon fusion and light quark annihilation) at the two energies $E_{Lab} = 30$ GeV and 400 GeV for p+Pb collisions. The shape of the distributions are quite different in two cases. At 400 GeV the produced pairs are almost uniformly distributed over the allowed phase space interval. However at 30 GeV, the production of large mass $c\bar{c}$ pairs is highly depleted due to the lack of available center of mass energy. Each of these input distributions are convoluted with the two different functional forms, $F^{(P)}(q^2)$ and $F^{(G)}(q^2)$, to obtain the final state distributions, as presented in Fig. 6.7.

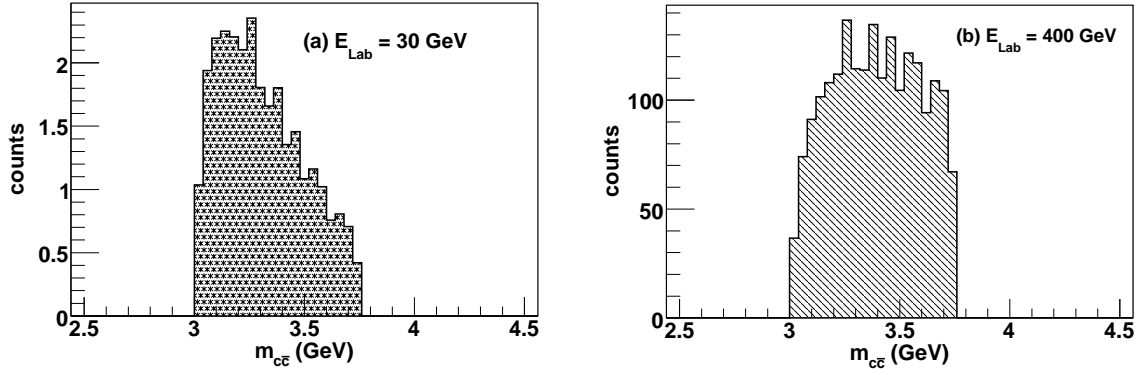


Figure 6.6: Histograms showing the invariant mass distribution of the initially produced $c\bar{c}$ pairs at $E_{Lab} = 30$ GeV (left panel) and $E_{Lab} = 400$ GeV (right panel) in p+Pb collisions.

At lower energy, the separation between the two distributions, corresponding to two different physical processes of hadronization, becomes higher. This ultimately results in the different production cross sections for two different processes. Now the accelerators at FAIR complex will deliver beams with unprecedentedly high intensities (note that the typical intensity for proton beam is $\sim 10^{13}s^{-1}$). If the data can be collected for a significantly long period, one can expect to have a data sample least affected by statistical uncertainties. On the other hand if the data for different target nuclei are measured in the same run, then one can expect to minimize the systematic errors particularly for the cross section ratios (σ_{pA}/σ_{pBe}). Thus in addition to the accurate normalization of the heavy-ion data, precise measurements of inclusive as well as differential J/ψ production cross sections in $p + p$ and $p + A$ collisions at FAIR might also help to distinguish the predictions for different scenarios and thereby pinning down the correct mechanism for color-neutralization.

6.3 J/ψ production in heavy-ion collisions

After the estimation of J/ψ production in proton induced collisions ($p + p$ and $p + A$) at FAIR, in this section, we investigate J/ψ production and its possible suppression in nucleus-nucleus collisions at FAIR [256, 286, 289]. For the heavy ion case we use Au+Au collisions as the colliding system in all our following calculations. First we extend our adapted version of the QVZ model to estimate the amount of charmonium production

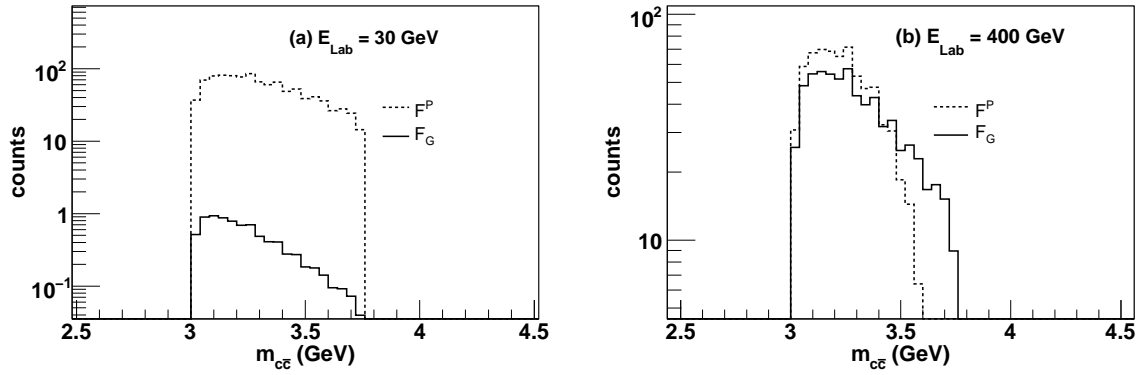


Figure 6.7: Histograms describing the invariant mass distribution of the $c\bar{c}$ pairs at $E_{Lab} = 30$ GeV and $E_{Lab} = 400$ GeV, at the final stage after they are convoluted with the transition probabilities $F^{(P)}(q^2)$ and $F^{(G)}(q^2)$ for J/ψ formation, in p+Pb collisions.

and suppression due cold nuclear effects at a beam energy of 25 A GeV, that will be within the reach of the FAIR accelerators. Next we explore the possible suppression effects induced by a dense baryonic medium, anticipated to be produced in the nuclear collisions at FAIR energy domain.

To understand the role of different CNM effects let us first investigate the behavior of the shadowing functions (introduced in chapter 5) that would tell us the role played by initial state effects. In addition to J/Ψ production we also calculate Drell-Yan productions in the FAIR energy domain. Like NA50 Collaboration at SPS, here also Drell-Yan di-muons can be used for characterization of J/ψ suppression. As earlier, inclusive cross sections are obtained at mid-rapidity ($-0.5 \leq y_{c.m.} \leq 0.5$). For Drell-Yan process, the corresponding mass range is $2.9 \leq m_{\mu\mu} \leq 4.5$ GeV/ c^2 . Results are presented in the Fig. 6.8, where we have plotted the shadowing functions for the two production processes as well as their ratios as a function of collision centrality expressed in terms of the magnitude of the impact parameter, **b**. Both the J/ψ as well as Drell-Yan productions exhibit shadowing, with Drell-Yan production showing stronger effects, where the production cross sections in central Au+Au collisions reduces by almost 50% compared to $p+p$ collisions. The way these shadowing and anti-shadowing corrections affect the J/ψ -to-Drell-Yan ratio at different collision energies, can again be attributed to the evolution of the EPS09 nuclear parton densities. Since at SPS and FAIR energies production is dominantly at mid-rapidity, so let us consider the region $y_{c.m.} \approx 0$, which would correspond to the kinematic domain $x_1 = x_2 = x = Q/\sqrt{s_{NN}}$. Hence at SPS ($\sqrt{s_{NN}} \approx 17.3$

GeV), we have $x_{SPS} \approx 0.18$, where both the gluons and valence quarks densities exhibit anti-shadowing whereas the sea quarks show shadowing effects. This is finally reflected in $S_{J/\psi} > 1$ and $S_{DY} < 1$ at SPS energies, as we have previously seen. On the other hand, in 25 A GeV Au+Au collisions at FAIR ($\sqrt{s_{NN}} \approx 6.9$ GeV), the kinematic region that will be probed is $x_{FAIR} \approx 0.45$. In this regime, gluon, valence quark as well as sea quark densities inside the nuclei get depleted (the so called EMC effect). Due to higher depletion of sea quarks, Drell-Yan process shows stronger reductions. Also even in the absence of the final state dissociation of the pre-resonance $c\bar{c}$ pairs, the initial state shadowing effects alone lead to a 10 -15 % suppression J/ψ production in Au+Au collisions. Eventually this also leads to lower values for the ratio $R_{J/\psi/DY}^{AA}$ compared to the SPS.

Let us now make quantitative predictions for J/ψ suppression 25 A GeV Au+Au collisions at FAIR due to cold matter effects, which can be directly contrasted with the data when available. We present our results both in terms of J/ψ -to-Drell-Yan ratio as well as nuclear modification factor (R_{AA}). In case the data for Drell-Yan production suffers from lack of sizable statistics, the suppressions can also be characterized in terms R_{AA} . Most of the present day experiments like those at RHIC or LHC are publishing their results on charmonium suppression in terms of R_{AA} . At FAIR energies also one can express the data in terms of R_{AA} , though our wish in that case would be a direct measurement of charmonium production cross sections in $p + p$ collisions, rather than the extrapolation of the $p + A$ results. Fig. 6.9 shows our model predictions for centrality dependence of J/ψ suppression in Au+Au collisions both in terms of J/ψ -to-Drell-Yan ratio as well as R_{AA} . The two theory curves, as usual correspond to two different parameterizations of $F(q^2)$. The corresponding values of ϵ^2 accounting for final state dissociation are obtained from the beam energy dependence of $\epsilon^2(E_b)$, parametrized in the previous section. Alike nuclear collisions at SPS, at FAIR also $F^{(G)}(q^2)$ generates larger suppressions for peripheral collisions. However with increasing collision centrality suppression invoked by power-law parametrization increases and for close to central suppression generated by power-law exceeds the Gaussian case. However both forms of transition probability produce a very large degree of nuclear suppression compared

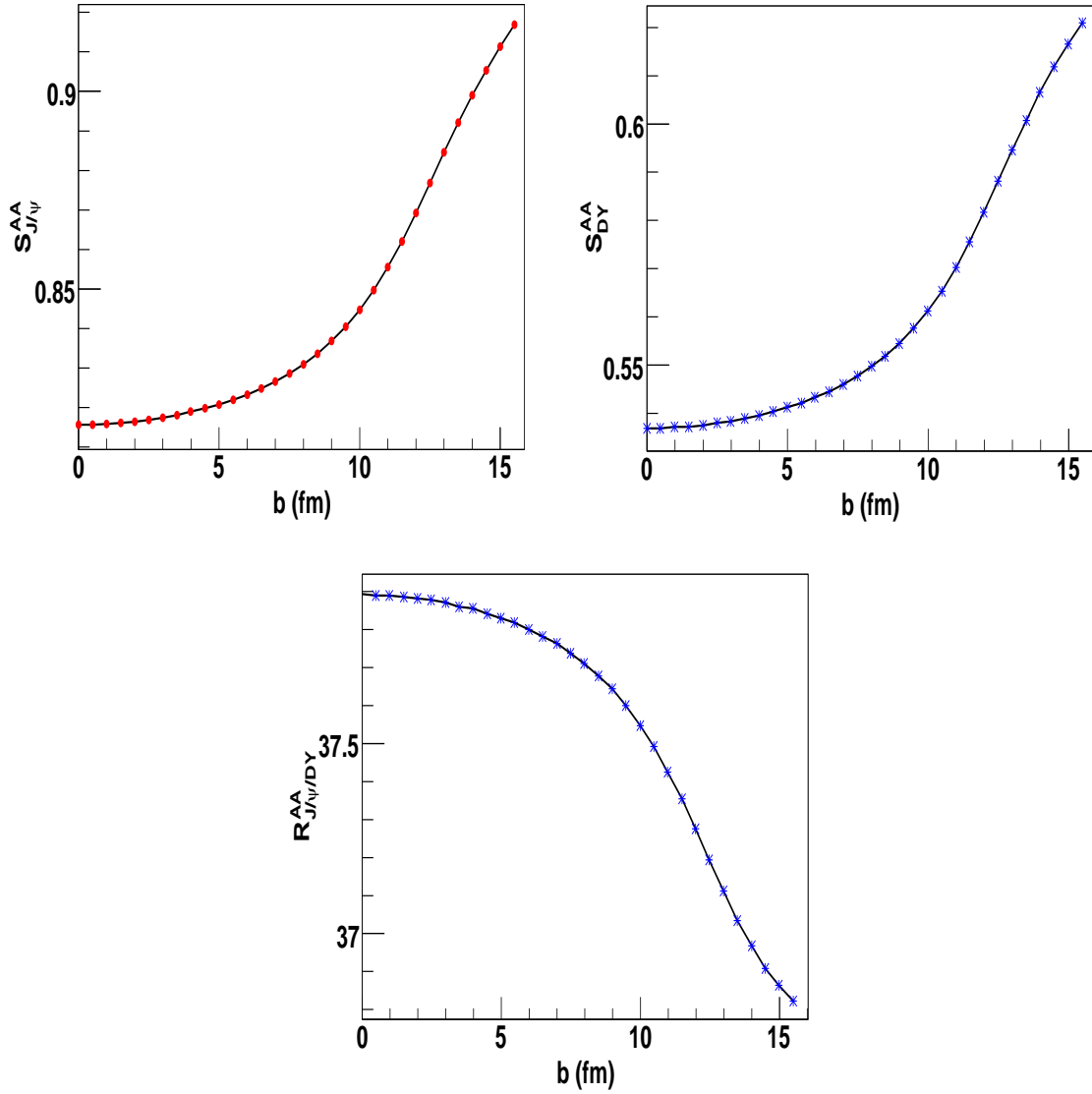


Figure 6.8: Impact parameter dependence of the shadowing functions, for (a) J/ψ (top left panel), (b) Drell-Yan productions (top right panel) and (c) the ratio of the two production cross sections (bottom panel) in absence of any final state interaction of J/ψ in the nuclear medium. Shadowing factors are evaluated at mid-rapidity, in 25 A GeV Au+Au collisions.

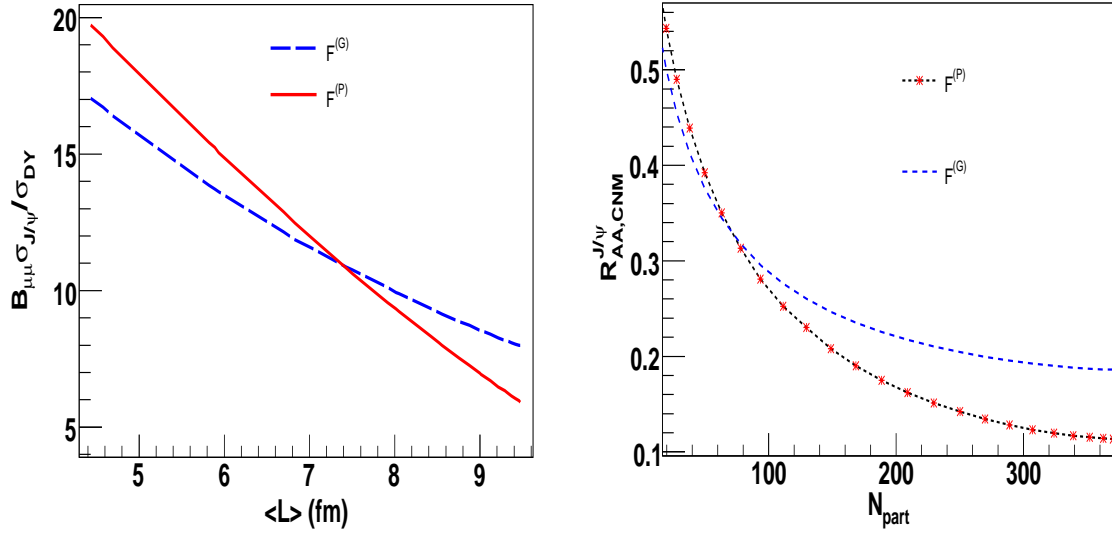


Figure 6.9: Model prediction for centrality dependence of the (a) J/ψ -to-Drell-Yan ratio and (b) nuclear modification factor of J/ψ ($R_{AA}^{J/\psi}$), in 25 A GeV Au+Au collisions. Calculations are for mid-rapidity. The CNM effects incorporated in the model calculations include the density dependent shadowing corrections in the initial state and final state dissociation of the pre-resonant $c\bar{c}$ pairs inside the nuclear medium. No hot medium effect is taken into account. Two theory curves, as usual correspond to the two different parametric forms of the J/ψ transition probability representing different color neutralization mechanisms.

to SPS. This can be attributed to the both initial and final state cold nuclear effects incorporated in our model calculations. At FAIR energies, both the quark and gluon densities results in a strong initial state shadowing. Also magnitude of the final state dissociation increases with decrease of beam energy. Thus unlike SPS energies, where the two effects compete and partially compensate each other, at FAIR they together generate remarkably large nuclear suppressions. Consider central ($b = 0$) Au+Au collisions for example. The Gaussian form $F^{(G)}(q^2)$ for which the resulting suppression is equivalent to that of Glauber model, generates around 80% reduction of the J/ψ yield compared to the $p + p$ collisions. The power law $F^{(P)}(q^2)$ form causes 90% suppression of the primordial yield. Explicit evaluation of the shadowing function indicates that initial state effects which is same for both the cases causes around 19% suppression. Rest is due to the multiple scattering of the $c\bar{c}$ pairs and dependent on the color neutralization scheme. Thus if at all there is any additional suppression effects caused by any secondary medium that would be operative on the remaining J/ψ s that would survive the large CNM effects. However it seems obvious from our study that most dominant contribution

to the observed J/ψ suppression at FAIR will come from the CNM effects.

6.4 Anomalous J/ψ suppression at FAIR

In the previous section we have seen that the nuclear effects are the most dominant source of J/ψ suppression in low energy nuclear collisions like those relevant at FAIR. Only a few of the primordial J/ψ mesons (10 – 20%) which can escape the nuclear dissociation will encounter the high baryon density medium subsequently produced in the collisions. As we pointed out earlier, that the degree of suppression induced by cold nuclear matter strongly depends on the passing time, $t_d = 2R_A/\gamma$, of the two colliding nuclei, where R_A is the nuclear radius and γ is the Lorentz contraction factor. At SPS energy ($E_{c.m.} \simeq 17.3$ GeV) the collision time is about 1 fm/ c and the magnitude of nuclear effects are large. At FAIR energies, the collision time ($t_d \simeq 3$ fm/ c) is even much longer and the J/ψ mesons during their evolution, will mostly encounter the (primary) nuclear medium rather than any secondary medium formed eventually due to the collision. Hence nuclear suppression are likely to play the most prominent role to govern the overall suppression pattern. In this section we would like to examine if on the top of this conventional source, the dense baryonic medium can cause additional J/ψ dissociation thereby reducing their yield further in the nuclear collisions at FAIR. One might remember that till date no measurement exists on charmonium production in heavy ion collisions below the top SPS energy, primarily due to the extremely low production cross sections. This in turn demands accelerators delivering extremely high intensity heavy ion beams and detectors with high rate handling capability. The upcoming Compressed Baryonic Matter (CBM) experiment at FAIR [290], in GSI, Germany, for the first time, is aiming at the measurement of charmonium production in low energy nuclear collisions, over a beam energy range $E_b=10-40$ A GeV. In this energy domain, highest possible baryon densities, around $(6 - 12)\rho_0$, where ρ_0 is the normal nuclear matter density, are expected to be produced at the center of the collision zone [291]. This might lead to a density driven QCD phase transition of the nuclear matter to a baryon rich quark-gluon plasma (QGP). The other possibility is the creation of high baryon density hadronic

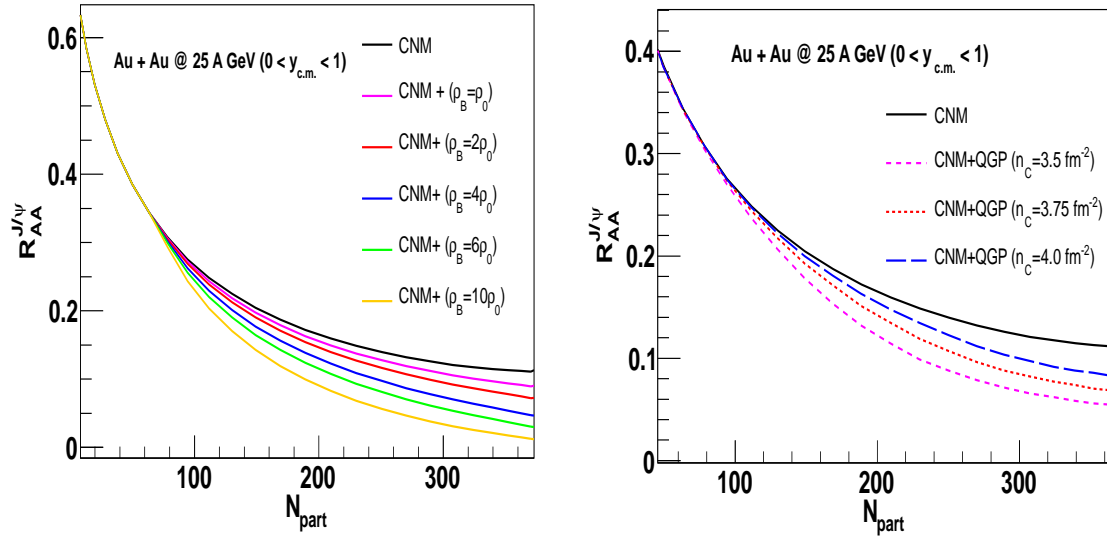


Figure 6.10: Centrality dependence of J/ψ suppression at 25 A GeV Au+Au collisions. In addition to nuclear effects, additional suppression due to high baryon density a) confined medium (left panel) and b) deconfined medium (right panel) are also shown.

medium. In this section we plan to investigate the possible effects of a dense baryonic medium on J/ψ production in heavy-ion collisions. To quantify the suppression effects exclusively due to possible secondary medium, we plan to calculate the centrality dependence of J/ψ suppression pattern, in Au+Au collisions [256, 289]. Suppression is characterized in terms of J/ψ survival probability which is estimated under two distinct scenarios namely, the suppression induced by a dense but confined baryonic medium (hadronic scenario) and that due to a deconfined plasma (partonic scenario).

Previously predictions of J/ψ survival probability at FAIR energy regime (25 A GeV Au+Au collisions) were made using HSD transport model [292]. Nuclear effects were incorporated through conventional Glauber suppression scenario. For simulating the anomalous suppression two different scenarios namely 'QGP threshold melting' and 'hadronic co-mover absorption' were independently studied. For partonic scenario, a variant of the geometrical threshold model [210] was used with different melting energy densities for different charmonium states. For the hadronic dissociation, inelastic collisions with different mesons was considered. However in those calculations, the magnitude of the CNM effects at FAIR is possibly underestimated as the value of effective absorption cross section was taken from the p+A measurements at 400 GeV. Our present estimates predict a much larger nuclear suppression

The anomalous suppression induced by a confined baryon dense medium can be schematically expressed as:

$$S_{J/\psi}^{\rho_B}(\mathbf{b}, \mathbf{s}) = \exp\left(-\int_{\tau_0}^{\tau_I} d\tau \rho_B(\mathbf{b}, \mathbf{s}, \tau) \langle v \sigma_{J/\psi-N} \rangle\right) \quad (6.1)$$

where $S_{J/\psi}^{\rho_B}(\mathbf{b}, \mathbf{s})$ denotes the J/ψ suffering dissociation due to inelastic collisions in a high baryon density medium at the point (\mathbf{b}, \mathbf{s}) in the transverse plane. In the above equation, $\sigma_{J/\psi-N} \sim 6.0$ mb [293] is the average inelastic cross section of the nucleons with the already formed J/ψ , $v \simeq 0.55$ [221] is J/ψ velocity and $\rho_B(\mathbf{b}, \mathbf{s}, \tau)$ is the net baryon density at proper time τ at the J/ψ 's position. The spatial dependence of the net baryon number density is set with the transverse profile of the participant density $n_{part}(\mathbf{b}, \mathbf{s})$ [294] as

$$\rho_B(\mathbf{b}, \mathbf{s}, \tau) \propto \rho_{B,0}(\tau) \times n_{part}(\mathbf{b}, \mathbf{s}) \quad (6.2)$$

One can compute $n_{part}(\mathbf{b}, \mathbf{s})$ using Glauber model as:

$$n_{part}(\mathbf{b}, \mathbf{s}) = T_A(\mathbf{s})(1 - e^{-\sigma_{NN}T_B(\mathbf{b}-\mathbf{s})}) + T_B(\mathbf{s})(1 - e^{-\sigma_{NN}T_A(\mathbf{b}-\mathbf{s})}) \quad (6.3)$$

where σ_{NN} is the nucleon-nucleon inelastic cross section and depends on the collision energy. For our present calculations we have used $\sigma_{NN} = 32$ mb. $T_A(\mathbf{s})$ is the nuclear thickness function, as defined earlier. Note that setting the density profile with participant density alone is a reasonable approximation in the low energy nuclear collisions like FAIR, where the effects of hard collisions on the bulk profile is expected to be negligible. τ_0 and τ_I respectively denotes the medium formation time and the interaction time up to which J/ψ 's will continue interacting with the medium. Both of them will depend on the path length through the nucleus and can be obtained using the standard prescriptions given in [221]. The evolution of baryon density with proper time τ can be followed from the equation for conservation of net baryonic current. If we neglect the transverse expansion (assuming that transverse expansion is slow and J/ψ suppression occurs much before the transverse expansion sets in), we are left with,

$$\tau_0 \rho_B^0 = \tau \rho_B \quad (6.4)$$

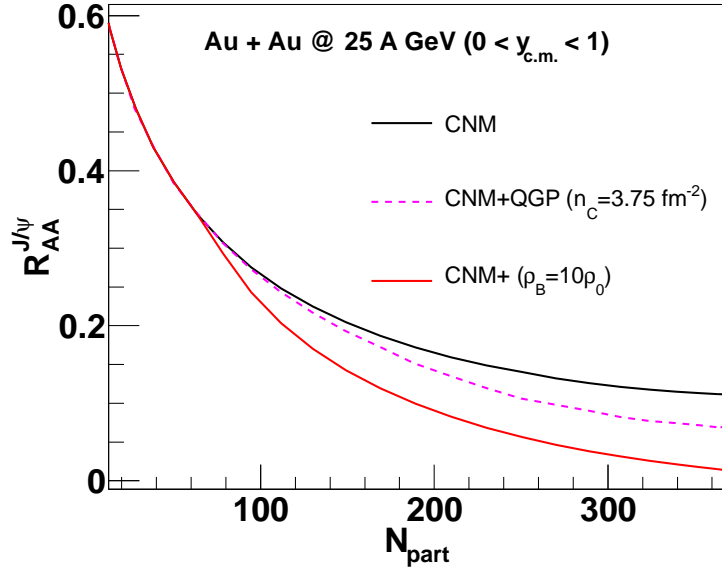


Figure 6.11: Comparison of the two different scenarios of J/ψ suppression in a compressed baryonic medium.

where ρ_B^0 is the initial net baryon density at time τ_0 when the hydrodynamic evolution starts. Using Eq. 6.4 and Eq. 6.1, one obtains the effective survival probability as

$$S_{J/\psi}^{\rho_B}(\mathbf{b}, \mathbf{s}) = \exp(-\rho_B^0(\mathbf{b}, \mathbf{s}) \langle v \sigma_{J/\psi-N} \rangle \ln(\frac{\tau_I}{\tau_0})) \quad (6.5)$$

Making use of Eq. 6.5, the suppression pattern induced by a confined compressed baryonic medium is shown in the left panel of Fig. 6.10. Calculations are performed for different peak densities varying from ρ_0 to $10\rho_0$. Higher be the density more violent is the suppression. If the maximum density of the produced medium is as high as $10\rho_0$, $R_{AA}^{J/\psi}$ approaches to zero and almost no J/ψ will survive. However if such high density is achieved in the initial phase of the collision, deconfinement might set in resulting a phase governed by partonic degrees of freedom. In a partonic phase, the J/ψ will interact differently with the medium. The interaction potential binding the c and \bar{c} together will be subject to Debye screening induced by the free color charges. To mimic the suppression pattern in a deconfined plasma, we follow the geometrical threshold model [210], without considering the detailed microscopic dynamics. In this model the

J/ψ suppression function, at an impact parameter b , can be written as:

$$S_{J/\psi}^{QGP}(b) = \int d^2\mathbf{s} \Theta(n_c - n_p(b, \mathbf{s})) \quad (6.6)$$

The density $n_p(b, \mathbf{s})$ in the step function is proportional to the local energy density of the matter at position (b, \mathbf{s}) . In the hot and dense part of the fireball where n_p is larger than a critical/threshold value n_c , all the J/ψ are absorbed in the medium and those outside this region only suffer normal suppression. The threshold density n_c in this model is a parameter, generally fixed from the data. However it has been observed earlier that a critical density $n_c \simeq 3.6 - 3.7 \text{ fm}^{-2}$ can reasonably describe both the data sets from SPS [211, 287] and RHIC [295]. n_c can be thought of to be proportional to the threshold dissociation energy density ($\epsilon_d^{J/\psi}$) required for melting of J/ψ . If we assume a constant value of the critical energy density ($\epsilon_c \simeq 1 \text{ GeV}/\text{fm}^3$), independent of baryon chemical potential μ_B , required for deconfinement transition, then by analogy the threshold dissociation energy density ($\epsilon_d^{J/\psi}$) and consequently the critical participant density, n_c , can be assumed to be constant. The right panel of Fig. 6.10, represents the behavior of $R_{AA}^{J/\psi}$ for three illustrative cases with three different critical densities. Smaller be the critical density, lower will be the energy density required for J/ψ melting and more will be the suppression. We put an end to this section by making a comparative study for these above two different mechanisms of anomalous suppression. For this purpose we consider two illustrative cases: a) confined baryonic medium with highest possible net baryon density ($\rho_B = 10\rho_0$) and b) deconfined medium with approximately constant threshold energy (and hence participant) density. The results are shown in Fig. 6.11. Two different mechanisms produce distinguishably different amount of suppressions. In a confined high baryon density medium, dissociation is more severe compared to that in QGP phase. Thus measurement of J/ψ production in nuclear collisions at FAIR might also furnish valuable information about the phase structure and the relevant degrees of freedom in such a high baryon density environment never observed before.

6.4.1 J/ψ suppression in a dynamically evolving medium

In the preceding sub-section we have discussed our first calculations of the effect of the compressed baryonic medium on the J/ψ suppression expected to be occurred at FAIR. However suppressions estimated both due to plasma screening and that caused by a baryon rich hadronic medium are based on rather simplified assumptions which do not really hold good in practice. For example, in case of simulating the effects of color screening inside the plasma, we followed the geometrical threshold model. Though found successful to describe the then available NA50 data on J/ψ -to-Drell-Yan ratio in Pb+Pb collisions, threshold model gives a crude description of the possible QGP scenario. It is a static model and does not incorporate the plasma dynamics. Similarly in case of hadronic dissociation due to the dense baryonic medium, the expansion dynamics is approximated by Bjorken's 1-D boost-invariant scaling flow. This might be well-justified for hydrodynamic evolution of matter around mid-rapidity interval at top RHIC energies and above. However in a rigorous calculation one should not pursue this assumption at lower energies, since at $\sqrt{s_{NN}} \simeq 20$ GeV and below it becomes invalid because of the absence of plateau in rapidity distribution of produced particles. Moreover evolution was set to start with somewhat arbitrary initial density varying from $\rho = (2 - 10)\rho_0$, instead of choosing the actual initial density from the temporal profile of the net-baryon density ($\rho_B(\tau)$), at a given collision energy. More reliable estimations in both the cases thus demand a more realistic simulation of the medium expansion. In this section we thus improve upon our previous estimations by quantifying the suppression effects in a deconfined/confined medium on a more reasonable ground through the inclusion of the medium dynamics following state-of-the-art model calculations. First we calculate the survival probability of J/ψ mesons in an evolving hot and baryonic QGP medium of finite space-time extent [289]. This will be followed by the suppression induced by an expanding hadronic medium of finite baryon density. For both the cases we now simulate the full (3+1)-D expansion of the hot and dense medium produced in the collision. The crucial inputs for this purpose, as will be described shortly, are the variation of the net baryon density (ρ_B) and total energy density (ϵ_d) as a function of time, calculated for Au+Au collisions. In the recent past, a number of existing dynamical models based on

transport or hydrodynamical equations have been employed to simulate central collisions of gold nuclei in the FAIR energy regime [291]. The employed models include UrQMD, PHSD, 3-fluid hydrodynamics, GIBIUU, QGSM among the others. For each case, central values of baryon density (ρ_B) and the total energy density (ϵ) are extracted as a function of time, for beam kinetic energies, $E_b = 5, 10, 20, 30$ and 40 A GeV. One striking observation of this study was that a large degree of mutual agreement among the results ($\rho_B(t)$ and $\epsilon(t)$) of the various models, despite of their very different mean fields and degrees of freedom. This is ascribed to the fact that both ρ_B and ϵ are mechanical variables and thus have well-defined values at all times. Particularly their extraction does not require the local thermal equilibrium to set in. Even if equilibrium is reached identical values of ρ_B and ϵ will generally lead to different values of the thermodynamic quantities from one model to other depending on the nature of the incorporated equation of state (EOS). By contrast the mechanical quantities ρ_B and ϵ are more robust variables and are subject to the local conservation laws. Since the various dynamical models abide by these basic conservation equations they will tend to give similar results for the corresponding quantities. Hence for our present calculations we resort to the UrQMD model to get $\rho_B(t)$ and $\epsilon(t)$, extracted for a central cell of unit thickness ($\Delta z = 1$ fm) in the longitudinal direction, in 30 A GeV Au+Au collisions. Note that all our earlier estimations for heavy-ion collisions at FAIR are based on 25 A GeV Au+Au collisions. However to take the advantage of the already existing simulations [291], we decide to go for 30 A GeV Au+Au collisions, as no data were simulated for the beam energy of 25 A GeV. Fig. 6.12 shows the variation of the central densities, $\rho_B(0, 0, 0, t)$ and $\epsilon(0, 0, 0, t)$, in central Au+Au collisions at 30 A GeV.

One might take note of the fact that the density values used in our calculations are those generated by a pure transport model calculations. Recently a hybrid model [50] has been developed where the pure UrQMD is coupled to a 3-D ideal hydrodynamic model for a better description of the hot and dense intermediate stage of the collision. The absolute values of $\rho_B(t)$ are shown to be very similar in the two cases. To account for the spatial non-uniformity of the medium, again as earlier we set the initial profiles of ρ_B and ϵ in the transverse plane of the collision, in proportion to the participant

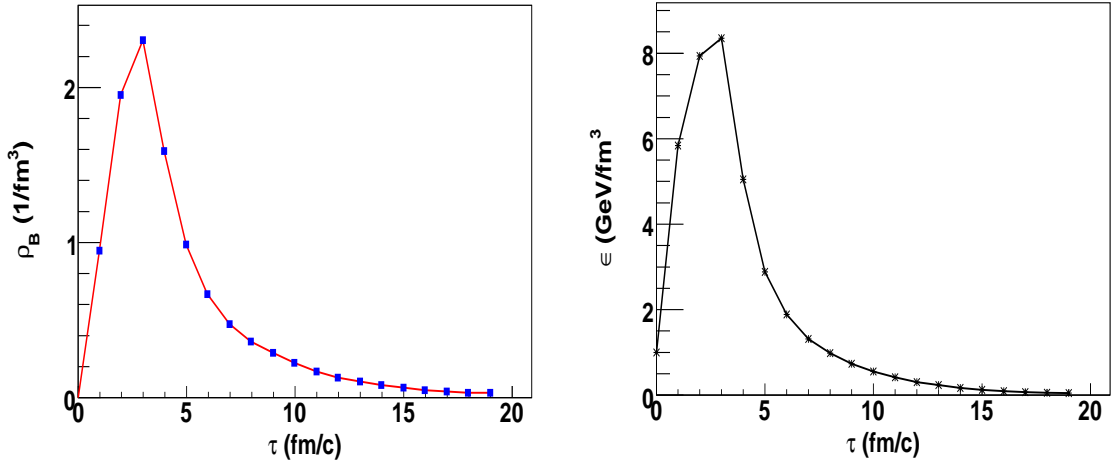


Figure 6.12: Variation of the central net baryon density, ρ_B (left panel) and total energy density, ϵ (right panel), as a function of proper time τ in central collisions of Au nuclei at 30 A GeV. The data points for these plots are obtained from [291].

density ($n_{part}(\mathbf{b}, \mathbf{s})$). Hence one can write

$$\epsilon(\mathbf{b}, \mathbf{s}, \tau) = k_1 \epsilon_0(\tau) \times n_{part}(\mathbf{b}, \mathbf{s}) \quad (6.7)$$

$$\rho_B(\mathbf{b}, \mathbf{s}, \tau) = k_2 \rho_{B,0}(\tau) \times n_{part}(\mathbf{b}, \mathbf{s}) \quad (6.8)$$

where the constants k_1 and k_2 take care of the corresponding normalizations. The normalization constants are fixed such a way that for $b = 0$ and at the point $(0, 0, 0)$ the central values are recovered. In short we thus obtain the local values of ρ_B and ϵ at each space-time point of an expanding medium. We require them for calculation for realistic J/ψ suppression patterns both inside a baryonic plasma and a hot hadronic medium with finite μ_B .

Suppression in a baryon-rich quark-gluon plasma

Let us start with the case of the suppression due to Debye screening inside a baryon-rich parton plasma. For this purpose we have developed a variant of the threshold model, which incorporates the complete plasma dynamics. Debye screening mass as a function of temperature and baryon chemical potential $m_D(T, \mu_B)$, in a dynamically evolving plasma is used to decide the fate of different charmonium state, implanted in the medium. Color

screening and its possible effects on the observed quarkonium suppression in nuclear collisions at SPS, RHIC and LHC have been studied at length in literature [229, 230, 231, 232, 233, 234, 212, 292], using geometrical screening models. They are based on semi-classical arguments assuming some sharply defined formation time and a suppression which is total or absent depending on the time spent inside plasma being shorter or longer than the formation time (for an alternative quantum mechanical prescription for the evolution of a $c\bar{c}$ wave packet in the plasma see [296]). The basic underlying theme is thus the existence of a characteristic threshold dissociation temperature (T_d) or equivalent energy density ($\epsilon_d \simeq T_d^4$), which encloses the plasma volume dense enough to cause the melting of a particular charmonium state. In other words, inside the volume the Debye screening length is shorter than the characteristic Bohr radius of a particular bound state. For easy visualization, let us consider a central nucleus-nucleus collision, which results in the formation of quark gluon plasma at some time τ_0 . Let us concentrate at the transverse plane $z = 0$ and the region of energy density, $\epsilon \geq \epsilon_d$. Assume that the $c\bar{c}$ pair is produced at the transverse position \mathbf{r} at $\tau = 0$ on the $z = 0$ plane with momentum \mathbf{p}_T . In the collision frame, the pair would take a time equal to $t_R = \tau_F \gamma_F = \tau_F m_T / M$ for the quarkonium to form, where $m_T = \sqrt{p_T^2 + M^2}$ and M is the mass of the quarkonium. τ_F denotes the intrinsic formation time of the quarkonium resonance under consideration and γ_F is the corresponding Lorentz dilation factor. During this time, the pair would have moved to the location $(\mathbf{r} + \tau_F \mathbf{p}_T / M)$. If at this instant, the plasma has cooled to an energy density less than ϵ_d , the pair would escape and quarkonium would be formed. If however, the energy density is still larger than ϵ_d , the resonance will not form leading to charmonium suppression. Resonance formation is thus forbidden for all $c\bar{c}$ pairs inside the region at the corresponding resonance formation time t_R , in the plasma frame. A complete suppression, as originally predicted, would however occur if the plasma were of infinite temporal and spatial extent because the evolving $c\bar{c}$ pairs would not form the resonances as long as $\epsilon \geq \epsilon_d$. The suppression would then be independent of plasma energy density ϵ and the velocity of the pair. However, in practice both the lifetime and volume of the QGP are finite and the formation time of the resonance is particularly important. Competition between t_R and the finite volume and

life time of the plasma, leads to the characteristic transverse momentum (p_T) dependent survival probability at central rapidity region. Finite lifetime sets an upper limit on the p_T at which charmonia are suppressed. As described in detail in the chapter 3, the characteristic T_d values for different charmonium states were initially estimated in [153], where the critical conditions for melting of quarkonia were obtained either through semi-classical approach or by solving numerically the Schrodinger equation with an in-medium generalized Cornell potential. The temperature dependence is inserted in the screening mass. More recently they are available from lattice QCD calculations at vanishingly small net baryon densities. In lattice QCD simulations two approaches are in vogue to find the quarkonia dissociation points in a quark-gluon plasma. In the first approach, the screening potential is directly obtained from the lattice estimations of the free energy of a static heavy quark-anti-quark pair. The other method relies on the direct evaluation of the quarkonia spectral functions $\sigma(\omega, T)$ in the appropriate quantum channel as a function of temperature T and $c\bar{c}$ binding energy ω . Two methods give different values of quarkonium dissociation temperatures particularly for J/ψ . Attempts have also been made to extract the critical dissociation temperatures by comparison with the data [212]. The common lore in all such calculations is that the deconfined medium formed in the nuclear collisions developed the thermal properties within a time comparable to the formation time of the primordial $c\bar{c}$ pairs in the collision frame. Hence these $c\bar{c}$ pairs would travel inside the plasma and those which satisfy the screening conditions, would not be able to evolve as the physical bound states. However the situation might be different at FAIR owing to different kinematic conditions. Due to large reduction in collision energies, much longer time will be required for the produced medium to attain thermalization compared to that at higher energies. Though thermalization in nuclear collisions is not yet understood clearly, it is commonly granted that the lower bound on the thermalization time can be estimated from the passing time, $t_d = 2R_A/\gamma\beta$, of the two colliding nuclei, where R_A is the nuclear radius and γ is the Lorentz contraction factor. At SPS energy ($\sqrt{s_{NN}} \approx 17.3$ GeV), t_d is about 1 fm/ c , whereas at FAIR energies $t_d \simeq 3 - 4$ fm/ c . On the other hand due to small available energy in the center of mass frame of the collision, the $c\bar{c}$ pairs will be produced with very small p_T , maximum

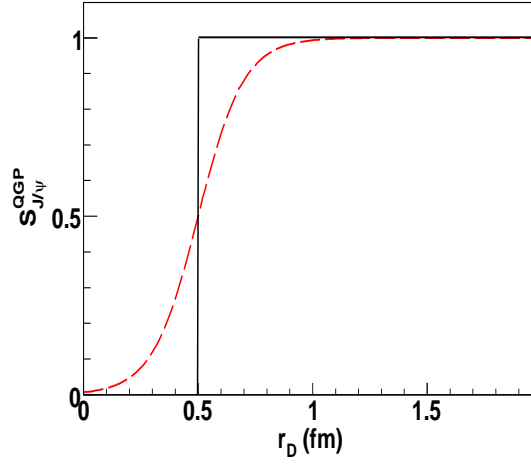


Figure 6.13: Schematic of the J/ψ survival probability suffering dissociation due to Debye screening inside the parton plasma. Suppression is modelled within the ambit of threshold scenario in terms of the Debye screening radius r_D . The continuous line represents an instantaneous dissociation whereas the dashed line includes gradual suppression scenario (see text for more details).

of $1 - 2$ GeV/ c . Consequently the Lorentz factor $\gamma_{R,i}$ by which the corresponding intrinsic formation time of the i^{th} resonance is dilated in the collision frame, would also be small ($\gamma_{R,i} \simeq 1$, so that $t_{R,i} = \gamma_{R,i}\tau_{R,i} \simeq \tau_{R,i}$). For the charmonium states like J/ψ , ψ' or χ_c , the intrinsic formation time is $\tau_{R,i} \approx 1 - 2$ fm [297]. Thus it might be reasonable to consider that at FAIR, different charmonium states will be formed in the pre-equilibrium stage and the plasma would encounter the already formed physical bound states rather than their precursors as believed to be the case at higher energies. Once plasma is produced, Debye screening would set in and if the local temperature $T(x)$ and chemical potential $\mu(x)$ inside the plasma are such that the screening radius $r_D(T(x), \mu(x)) \leq r_i$, the i^{th} state will melt, where r_i is the rms separation radius of the i^{th} charmonium state, calculated in non-relativistic quarkonium spectroscopy [105]. Hence, for an impact parameter \mathbf{b} , the survival probability at a transverse position \mathbf{s} , at time τ can be expressed as:

$$S_i^{QGP}(\mathbf{b}, \mathbf{s}, \tau) = \Theta(r_i - r_D(\mathbf{b}, \mathbf{s}, \tau)) \quad (6.9)$$

Modeling the dissociation by a theta function might be unrealistic as it completely ignores the time scale involved in the melting process. In [211], the authors showed that

their theoretical curve obtained using Θ function could not provide a perfect fit to the NA50 data points with smaller error bars. Fit quality can be improved by considering the gradual suppression mechanism which resulted in smearing of the Θ function by small amount. In the same spirit, we also modify the survival probability in Eq. 6.9 as:

$$S_i^{QGP}(\mathbf{b}, \mathbf{s}, \tau) = \frac{1}{2} \left(1 + \tanh\left(\frac{r_D(\mathbf{b}, \mathbf{s}, \tau) - r_i}{\lambda}\right) \right) \quad (6.10)$$

where λ denotes the smearing width; for each resonance state the corresponding smearing width is fixed to 10% of its corresponding separation radius ($\lambda = 0.1r_i$). The effect of the smearing can be viewed in Fig. 6.13, where the survival probabilities for J/ψ mesons are plotted as a function of the Debye screening radius (r_D) following Eqs. 6.9 and 6.10. Determination of survival probability now boils down to the estimation of in-medium Debye screening mass. Screening length is the inverse of the screening mass. ($m_D(T, \mu_B) = 1/r_D(T, \mu_B)$). At vanishing net baryon density, the color screening theory has been analyzed in quite some detail. Compared to this our knowledge at finite density is rather limited. In leading order perturbation theory, studied within real time formalism, the μ_B dependence of the Debye screening mass reads as [298]

$$m_D(T, \mu_q) = g(T, \mu_q) T \sqrt{\frac{N_c}{3} + \frac{N_f}{6} + \frac{N_f}{2\pi^2} \left(\frac{\mu_q}{T}\right)^2}, \quad (6.11)$$

where $\mu_q = \frac{\mu_B}{3}$ is the quark chemical potential and N_c and N_f respectively denotes the number of quark colors and flavors in the theory. In [299], screening mass at finite net-baryon density has been evaluated using thermo-field (TFD) dynamics. Within imaginary time method, the time-time component of the gluon self energy π^{00} is calculated which in the limit of ($q_0 = 0, \mathbf{q} \simeq \mathbf{0}$) yields the screening mass. Result obtained by this method is in complete agreement with that obtained in LO pQCD for any arbitrary net-baryon density, as expected. The NLO level estimates of Debye mass suffer from large uncertainties, particularly due to yet unresolved nature of the magnetic screening mass. In the temperature and density ranges expected at FAIR, application of perturbation theory is not beyond doubt. In lattice QCD, activities have been initiated to study the screening of static quark anti-quark sources in a medium with a non-vanishing net

quark density [170]. A small but finite baryon number density is included via Taylor expansion of the fermion determinant in μ_B . For temperatures above T_c , Debye screening masses are extracted from the large distance behavior of the free energies of the heavy quark pair. Analysis suggests that the screening length in a baryon or anti-baryon rich quark gluon plasma decreases with increasing value of the chemical potential. This is consistent with the expectation that a non-zero μ_B shifts the transition to lower temperatures. However the density dependence of screening masses has so far been analyzed for 2-flavor QCD and unrealistically large quark masses. In the present study, we thus desist from using lattice results and restrict ourselves to the LO pQCD estimations only, as given in Eq. 6.11. The (T, μ_B) dependence of the running coupling $g(T, \mu_B)$ is obtained from Ref. [300] as:

$$\alpha_s(T, \mu_q) = \frac{12\pi}{(33 - 2N_f)\log(M^2/\Lambda_{QCD}^2)} \quad (6.12)$$

where $g^2 = 4\pi\alpha_s$ and M denotes the effective momentum scale in the matter. Λ_{QCD} is the scale fixing parameter of QCD. In a medium at finite temperature and baryon density, the effective momentum scale can be approximated as

$$M^2 = \frac{4}{5}\mu_q^2 + 15.62T^2 \quad (6.13)$$

Substituting Eq. 6.13 in Eq. 6.12 and using $g^2 = 4\pi\alpha_s$ we get the running coupling as a function of T and μ_B . Our theory now requires the local T and μ_B of the fluid, as a function of collision energy and collision centrality. To get them we now make use of the local net baryon and energy densities. Space time dependent density values ($\rho_B(\mathbf{b}, \mathbf{s}, \tau)$ and $\epsilon(\mathbf{b}, \mathbf{s}, \tau)$) can then be plugged in some suitable partonic equations of state (EOS) to solve simultaneously for the corresponding values of local T and μ_B , as a function of collision energy and centrality. For our study, we employ phenomenological QGP EOS proposed by Kapusta [301]. It is so constructed that it matches with the lattice QCD simulation at $\mu_B \approx 0$ and to the known properties of ground state nuclear matter at zero temperature. The pressure (P), entropy density (s), baryon density (ρ_B) and energy

density (ε), in parametrized form are,

$$P = \left[\frac{\pi^2}{90} \left(16 + \frac{21N_f}{2} \right) T^4 + \frac{N_f}{18} \mu^2 T^2 + \frac{N_f}{324\pi^2} \mu^4 \right] - [CT^2 + D\mu^2 + B] \quad (6.14)$$

$$s = \frac{4\pi^2}{90} \left(16 + \frac{21N_f}{2} \right) T^3 + \frac{N_f}{9} \mu^2 T - 2CT \quad (6.15)$$

$$\rho_B = \frac{N_f}{9} \mu T^2 + \frac{N_f}{81\pi^2} \mu^3 - 2D\mu \quad (6.16)$$

$$\varepsilon = -P + Ts + \mu\rho_B \quad (6.17)$$

The first three terms within braces, in Eq. 6.14 corresponds to ideal gas equation for massless gluons and N_f quark flavors. The 2nd bracketed terms were included to account for the interaction, as observed in lattice simulations. $2C \approx 0.24$, $D \approx 0$, $B \approx T_0^4$, where T_0 can be identified with T_c the pseudo-critical temperature at $\mu_B \approx 0$. The critical energy density (ϵ_c), required for deconfinement at $\mu_B \approx 0$, can then be estimated by using Eq. 6.17. Since T_c as a function of μ_B is believed to follow a nearly constant density curve, we assume ϵ_c , to remain constant for increasing μ_B . Incorporation of ϵ_c thus endows the plasma with finite space-time extent. In principle, we now have all the ingredients to calculate the centrality dependence of the J/ψ suppression pattern due to screening in the QGP medium. In practice, it has been found that only about 60% of the observed J/ψ originate directly in hard collisions while 30% of them come from the decay of χ_c and 10% from the ψ' . Hence, the total survival probability of J/ψ becomes,

$$S^{tot} = 0.6S_{J/\psi} + 0.3S_{\chi_c} + 0.1S_{\psi'} \quad (6.18)$$

Inclusive survival probability for different states, can be obtained by integrating Eq. 6.10 over space-time. In order to do so, we distribute J/ψ in the transverse plane, following the transverse density of binary collisions $n_{coll}(\mathbf{b}, \mathbf{s})$, since they are produced in the initial hard collisions. Glauber model can again be used to calculate n_{coll} as

$$n_{coll}(\mathbf{b}, \mathbf{s}) = \sigma_{NN} T_A(\mathbf{s}) T_B(\mathbf{b} - \mathbf{s}) \quad (6.19)$$

Screening effects remain operational on a bound state, over the time it spends inside

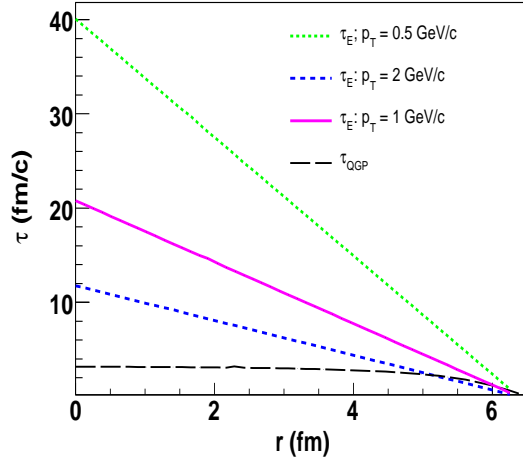


Figure 6.14: Variation of the minimum escape time of J/ψ , τ_E with three different constant values of p_T and variation of the plasma life time, τ_{QGP} as a function of the transverse co-ordinate r . Calculations are performed for 30 A GeV central Au+Au collisions.

the plasma. The lower limit of the screening time is assumed to coincide with the thermalization time of the medium (t_{th}). It might be reasonable to assume that relaxation to local equilibrium cannot occur earlier than a certain time needed for the Lorentz contracted nuclei to completely pass through each other. We calculate τ_{th} following Ref. [302] as

$$\tau_{th} = \left(\frac{2R_A}{\gamma\beta}\right) + \left(\frac{\Delta z}{2\beta}\right) \quad (6.20)$$

where R_A denotes the nuclear radius and Δz denotes the thickness of the central cell in the longitudinal direction, chosen for extraction of densities. Eq. 6.20 gives the lower bound of thermalization time. For beam kinetic energy $E_b = 30$ A GeV, and for a central cell of longitudinal width $\Delta z = 1$ fm, as used in our present analysis, thermal equilibration time comes out to be $\tau_{QGP} \simeq 3.7$ fm (in natural units where $c = 1$).

A charmonium state of mass m , inserted at a point \mathbf{r} , in the transverse plane ($z = 0$) of the plasma, with velocity \mathbf{v} will travel a distance

$$d = -r\cos\phi + \sqrt{R_A^2 - r^2\sin^2\phi} \quad (6.21)$$

in the time interval $\tau_E = M_T d/p_T$, before it escapes from the partonic system of trans-

verse extension R_A , ϕ being the angle between the vectors \mathbf{r} and \mathbf{v} and $M_T(M_T = \sqrt{(p_T^2 + m_\psi^2)})$ denotes the transverse mass. For a given p_T , τ_E would be minimum for $\phi = 0$. Hence if τ_{ex} denotes the plasma extinction time, minimum between the two time scales τ_E and τ_{ex} should fix the upper limit of duration a bound state suffers dissociation due to screening. However as pointed out earlier, the quarkonia produced at FAIR energies in the mid-rapidity ($p_z \simeq 0$) are expected to have very small p_T . Experiments measuring J/ψ production cross sections in $p + A$ collisions at BNL-AGS [149] and CERN-PS [303] in the same energy domain as FAIR, follows the p_T distribution to be $p_T \simeq \exp(-6p_T)$ or $p_T \simeq \exp(-ap_T^2)$ with $a = 1.6 \text{ GeV}^{-2}$. Such anzatzes correspond to an average transverse momentum of $\langle p_T \rangle \simeq 0.34 \text{ GeV}$ (exponential distribution) or $\langle p_T \rangle \simeq 0.7 \text{ GeV}$ (Gaussian distribution). For such small p_T , the charmonia are found to remain inside the plasma, as long as the plasma is alive. This would essentially result p_T independent survival probability. This argument of p_T independent survival probability can be elucidated in a more quantitative fashion in the following way. Note that for a J/ψ with a given p_T , the escape time, τ_E , will be minimum when $\phi = 0$. In the Fig. 6.14, we have thus plotted the minimal escape time, τ_E^{min} as a function of the transverse co-ordinate r , for three different arbitrarily chosen constant values of charmonium $p_T = 0.5, 1, 2 \text{ GeV}$. In addition the plasma life time, τ_{QGP} is also plotted in the same panel. For a given r , τ_{QGP} is defined as $\tau_{QGP}(r) = \tau_{ex}(r) - \tau_{th}$. Plasma extinction time τ_{ex} is the time when the energy density of the medium drops down to the critical energy density, ϵ_c , required for plasma formation. As seen from the figure, even for a p_T value as high as 2 GeV, life time of the plasma is much smaller than the corresponding minimal escape time, τ_E^{min} . For smaller values of p_T , τ_E^{min} is even larger. Note that in practice neither all the J/ψ will have $\phi = 0$, nor all of them will be produced with p_T as high as 1 – 2 GeV. In fact due to want of enough center of mass energy most the J/ψ will have very small p_T close to zero. For both the cases of small p_T or $\phi > 0$ τ_E will be even larger than the present estimates. Hence unlike the cases of SPS, RHIC or LHC, at FAIR we will have p_T independent J/ψ survival probability so far as dissociation due to plasma screening is concerned.

After discussing our theoretical framework, let us now start describing the numerical

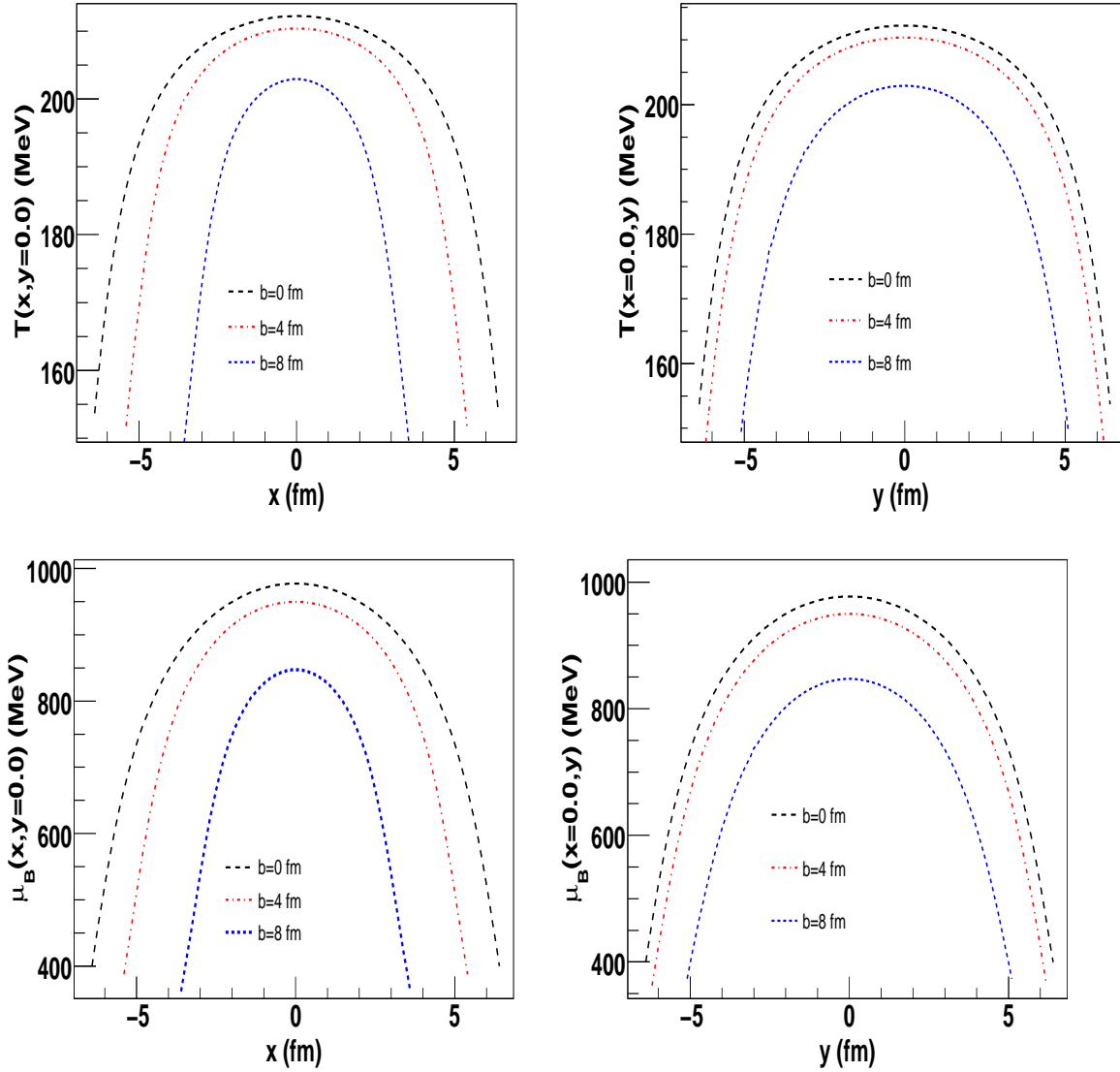


Figure 6.15: Spatial variation of the local temperature (T) and baryon chemical potential (μ_B), in the transverse plane of the plasma, for 30 A GeV Au+Au collisions. The curves are generated at an instant $\tau = 4$ fm/ c , for various values of the collision impact parameter.

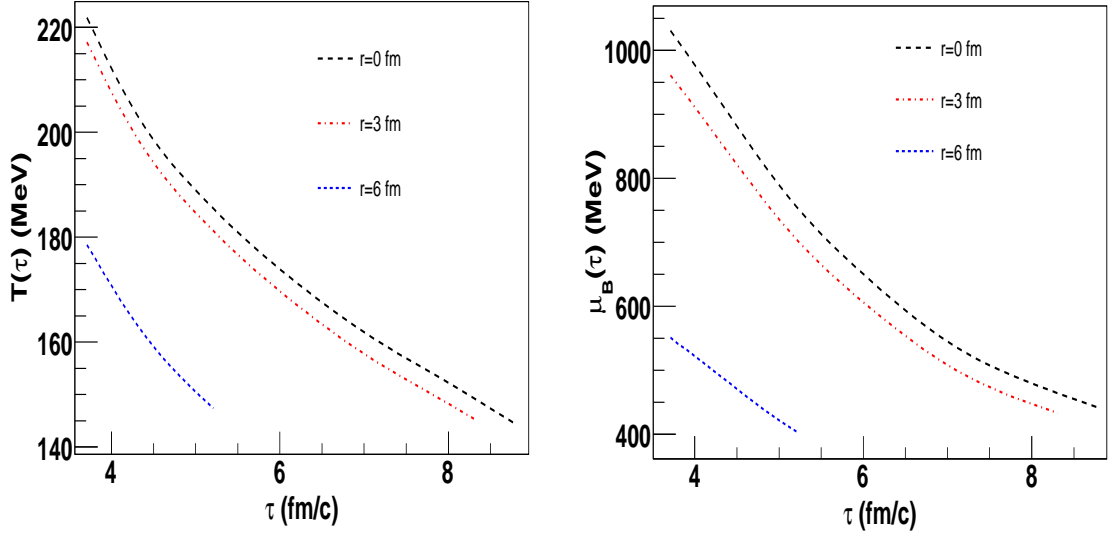


Figure 6.16: Temporal variation of the local temperature (T) and chemical potential (μ_B) of the plasma in 30 A GeV central Au+Au collisions. The curves are generated for three different values of the transverse coordinate r , as shown in the figure.

results from our model simulations. The ultimate goal is to estimate the centrality dependence of the J/ψ suppression pattern in a baryonic QGP medium, as anticipated in FAIR energy collisions. For this we consider 30 A GeV Au+Au collisions as our reference system. However before calculating the survival probability, it might be interesting to take a look on the general characteristics of the plasma, produced in the collisions. We begin with the space-time evolution of the local T and μ_B inside the plasma, as obtained from the UrQMD calculated density values using the Kapusta EOS given in the previous section. In Fig. 6.15, we have shown the snapshot of the spatial profile of T and μ_B , in the transverse plane of the collision, at an instant $\tau = 4$ fm/c, just after the formation of the plasma, for different collision impact parameters. As expected the temperature and the chemical potential attain their maximum values at the center. For central collisions the T and μ_B profiles are identical along x and y directions due to azimuthal symmetry of the overlap zone. In case of non-central collisions, owing the spatial asymmetry of the overlap zone, the distributions are more elongated along y direction. Fig. 6.16 represents the temporal evolution of fluid temperature and chemical potential at three different transverse positions, in central Au+Au collisions. Evolution starts at $\tau \approx 3.7$ fm, plasma formation time. As expected the fluid cells at the center having highest densities evolve for the longest time.

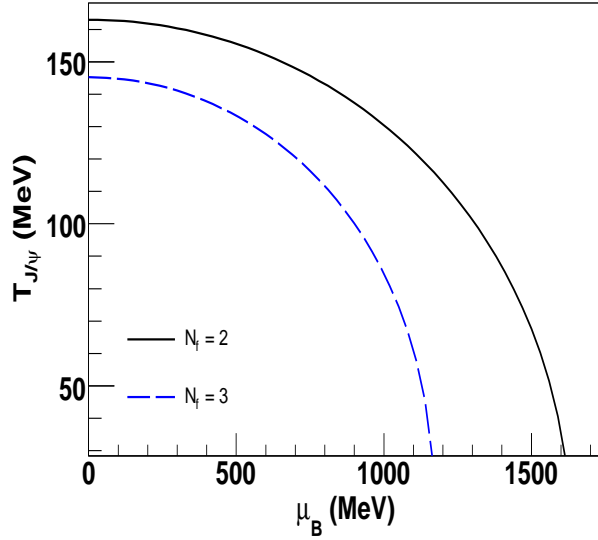


Figure 6.17: Relation between critical temperature and critical baryon chemical potential for dissociation of J/ψ , as obtained within our model calculations. Calculations are done both for two flavor ($N_f = 2$) as well as three flavor ($N_f = 3$) systems. Critical value of the screening radius has been set to 0.5 fm, the separation radius of J/ψ .

It might also be interesting to look at the dependence of the critical temperature of J/ψ melting ($T_{J/\psi}$) as a function μ_B , as obtained within our model approach. Fig. 6.17 shows the variation of $T_{J/\psi}$ with μ_B for $N_f = 2$ and $N_f = 3$. Melting temperature decreases with increase of baryon density. $T_{J/\psi}$ for $N_f = 2$ is larger than $N_f = 3$ and the separation between two curves increases with increasing quark chemical potential. For other charmonium states the corresponding critical screening radii would be even larger which make them to melt at lower temperatures and densities. The results obtained here are in qualitative agreement with that obtained in [299], though the absolute values in our case are smaller. This could be corresponded to the differences in the criticality (of screening) conditions employed in the two cases. At zero density the J/ψ dissociation temperature is smaller than that obtained by lattice QCD.

Let us now move on to the quantitative estimation of charmonium suppression induced by Debye screening in the baryonic plasma. In Fig. 6.18 we present the inclusive survival probability as a function of impact parameter b for different charmonium states (J/ψ , ψ' and χ_c), suffering dissociation due to plasma screening, in 30 A GeV Au+Au collisions. The total J/ψ survival probability, which is actually measured in experiments and that includes the contributions from the sequential decays of the excited states is also

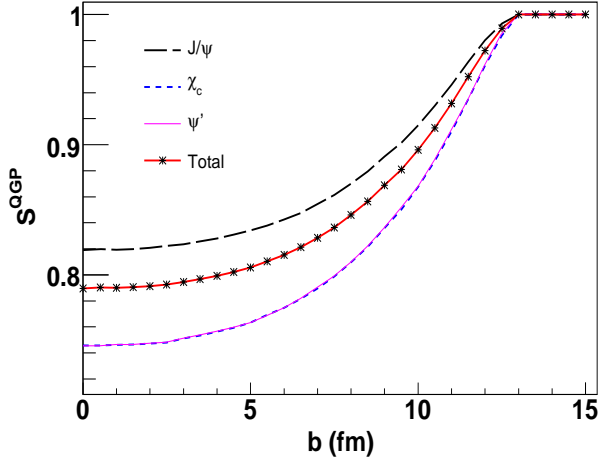


Figure 6.18: Centrality dependence of the inclusive survival probability of different charmonium states in a baryon rich QGP medium, assumed to be created in 30 A GeV Au+Au collisions. Dissociation is exclusively due to Debye color screening. Centrality is expressed in terms of collision impact parameter, b . In addition to the different directly produced charmonium states (J/ψ , ψ' and χ_c), total J/ψ survival probability including the feed down contributions is also shown. ψ' and χ_c are found to undergo visibly same amount of suppressions.

shown. As expected the excited states are found to be more suppressed compared to the ground state J/ψ . The excited states are found to undergo identical dissociation. All the curves are generated for $N_f = 2$ and $T_0 = 154$ MeV. The flavor dependence of the suppression pattern is found to be very small and thus not shown explicitly. However for our present calculations it is more reasonable to model the plasma using up and down quarks only. For low energy collisions like those at FAIR, excitation of the strange quarks will be rather small. Also we have assumed in our calculations $\mu_q = \mu_B/3$ which is not valid for massive strange quarks.

Now it might be interesting to investigate the sensitivity of the suppression pattern to the different input parameters used in our model calculations. In order to estimate the sensitivity of the screening dissociation on the plasma EOS, survival probabilities are calculated with three different values of T_0 , which also corresponded to different values of threshold energy density ϵ_c . A smaller value of ϵ_c in turn indicates longer life time as well as spatial extent of the plasma. The reason for these particular choices of $T_0 = 140, 154, 175$ MeV is the following. Guided by the current state-of-the-art lattice simulations of T_c [304], we have chosen $T_0 = 154$ MeV. Note that for $\mu_B = 0$, T_0 coincides with T_c . The lowest value ($T_0 = 140$ MeV) thus arises from the hope that T_c cannot be

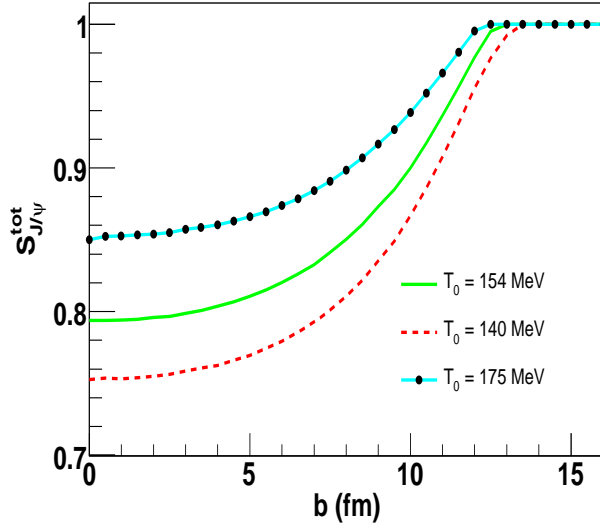


Figure 6.19: Centrality dependence of the inclusive J/ψ survival probability suffering dissociation due to Debye screening, in a baryon rich QGP medium, produced in 30 A GeV Au+Au collisions. Curves are generated for $N_f = 2$ and different input values of T_0 .

less than the pion rest mass. The highest value ($T_0 = 175$ MeV) is inspired from [305]. Results are shown in Fig. 6.19. Suppression is indeed found to be sensitive to the choice T_0 . A higher T_0 in turn results in higher ϵ_c for required deconfinement transition and thus shrinks the spatio-temporal extent of the plasma. For purely central collisions ($b = 0$) the difference in the maximum suppression from $T_0 = 140$ MeV to $T_0 = 175$ MeV increases by 10%.

Next we want to check the dependence of the J/ψ survival probability on the choice of thermalization time (τ_0), from where the screening starts to be operative. As we discussed above thermalization in heavy ion collisions is one of the grey areas that remains unsolved till today. In our calculations, we have estimated $\tau_0 = 3.7$ fm, from the transit time of the two colliding nuclei, following Eq. 6.20. It is the time by which all the initial baryon baryon scatterings have taken place between the two colliding nuclei. However we need to remember that such estimations are based on geometrical arguments and thermalization is a dynamic phenomenon. For example if one looks at the time evolution of the central baryon density in 30 A GeV central Au+Au collision, peak of the distribution occurs at time $\tau \simeq 3$ fm. It might be possible that at the centre of the collision zone plasma is formed at time $\tau \sim 3$ fm, earlier than that at the corona.

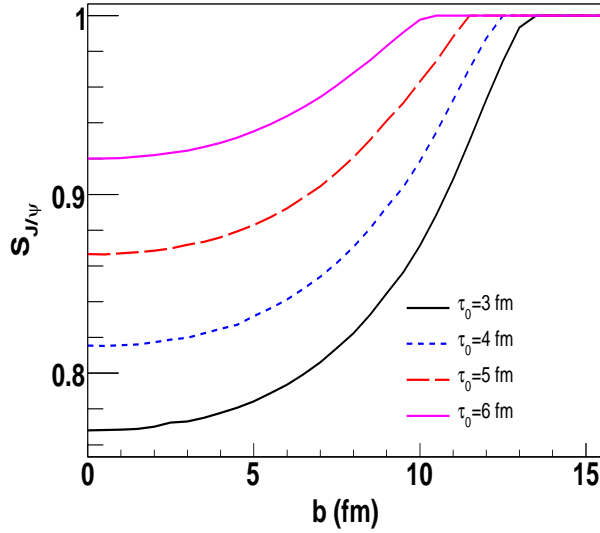


Figure 6.20: Sensitivity of the J/ψ suppression pattern on the choice of thermalization time. The curves depict the impact parameter dependence of the inclusive J/ψ survival probability, suffering dissociation due to Debye screening, in a baryon rich QGP medium, produced in 30 A GeV Au+Au collisions. Curves are generated for $N_f = 2$, $T_0 = 154$ MeV and different input values of τ_0 .

On the other hand as discussed in Ref. [302], Eq. 6.20 gives the minimum value of τ_0 and actual equilibration time can be higher than that. However we do not wish to engage in calculations based on local thermalization time $\tau_0(\mathbf{b}, \mathbf{s})$. Rather we use a single value of τ_0 for all collision centralities and transverse positions, which is a common practice in standard hydrodynamical approaches. τ_0 should be viewed as some sort of average thermalization time. Hence we calculate the J/ψ suppression pattern for different input values of τ_0 between 3 - 6 fm as shown in the Fig. 6.20. The suppression decreases for late thermalization (larger τ_0) due to reduced screening effects. For a typical value of $\tau_0 = 6$ fm, the maximum suppression at $b = 0$ is even less than 10%.

It might also be interesting to find out the sensitivity of the suppression pattern on the medium expansion dynamics, particularly the role of transverse flow in deciding the screening effects. Most of the existing calculations so far, generally assume the plasma to expand following Bjorken 1-D boost invariant scaling solutions. As we said earlier, it is basically driven by the expectation that the suppression occurs before the transverse expansion could set in. In our present calculations, we have followed the time evolution of the densities from UrQMD which includes the full 3-D expansion of the fireball. For a better understanding of the role played by transverse dynamics, we

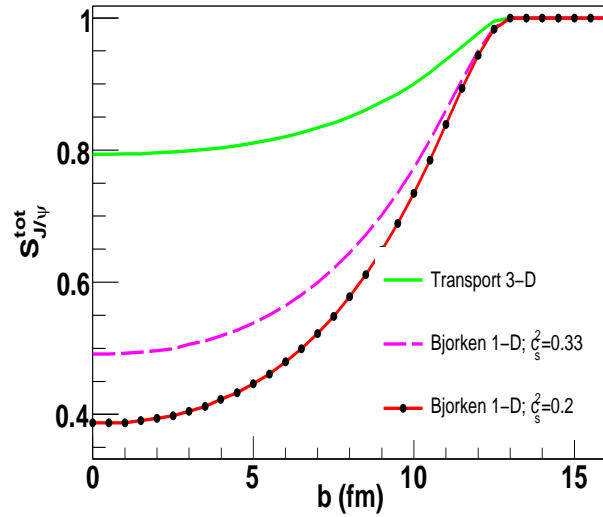


Figure 6.21: Sensitivity of total inclusive J/ψ survival probability in 30 A GeV Au+Au collisions, to the plasma expansion dynamics. Curves are generated for $N_f = 2$ and $T_0 = 154$ MeV. Fluid is assumed to expand with and without transverse expansion. In case of longitudinal Bjorken type expansion, two different c_s^2 values are considered.

have also calculated the suppression for a case where the fluid dynamics is governed by Bjorken 1-D hydrodynamical expansion, though such cases are really not feasible in practice. For such cases the net baryon density would evolve following Eq. 6.4 and the energy densities would evolve as

$$\epsilon \tau^{1+c_s^2} = \text{constant}, \quad (6.22)$$

where c_s denotes the speed of sound in the plasma. For ideal massless relativistic gas $c_s^2 = 0.33$. For a massive interacting system c_s^2 would be less than that. In Fig. 6.21, we have shown comparative suppressions between 3-D and 1-D expansions of the partonic fluid. Magnitude of suppression exhibits a strong dependence on the medium expansion dynamics, with larger suppression occurring in absence of transverse expansion. This can be clearly understood by looking at Fig. 6.22, where we have plotted the time evolution of various plasma parameters in the central fluid cell for 30 A GeV central Au+Au collisions. The quantities are allowed to evolve till the plasma extinction point is reached. In case of J/ψ mesons for example, the screening is effective as long as $r_D < r_{J/\psi} \sim 0.5$ fm. In the absence of transverse expansion, plasma expands slowly and hence screening would operate for a longer time. Expansion rate in such cases, would

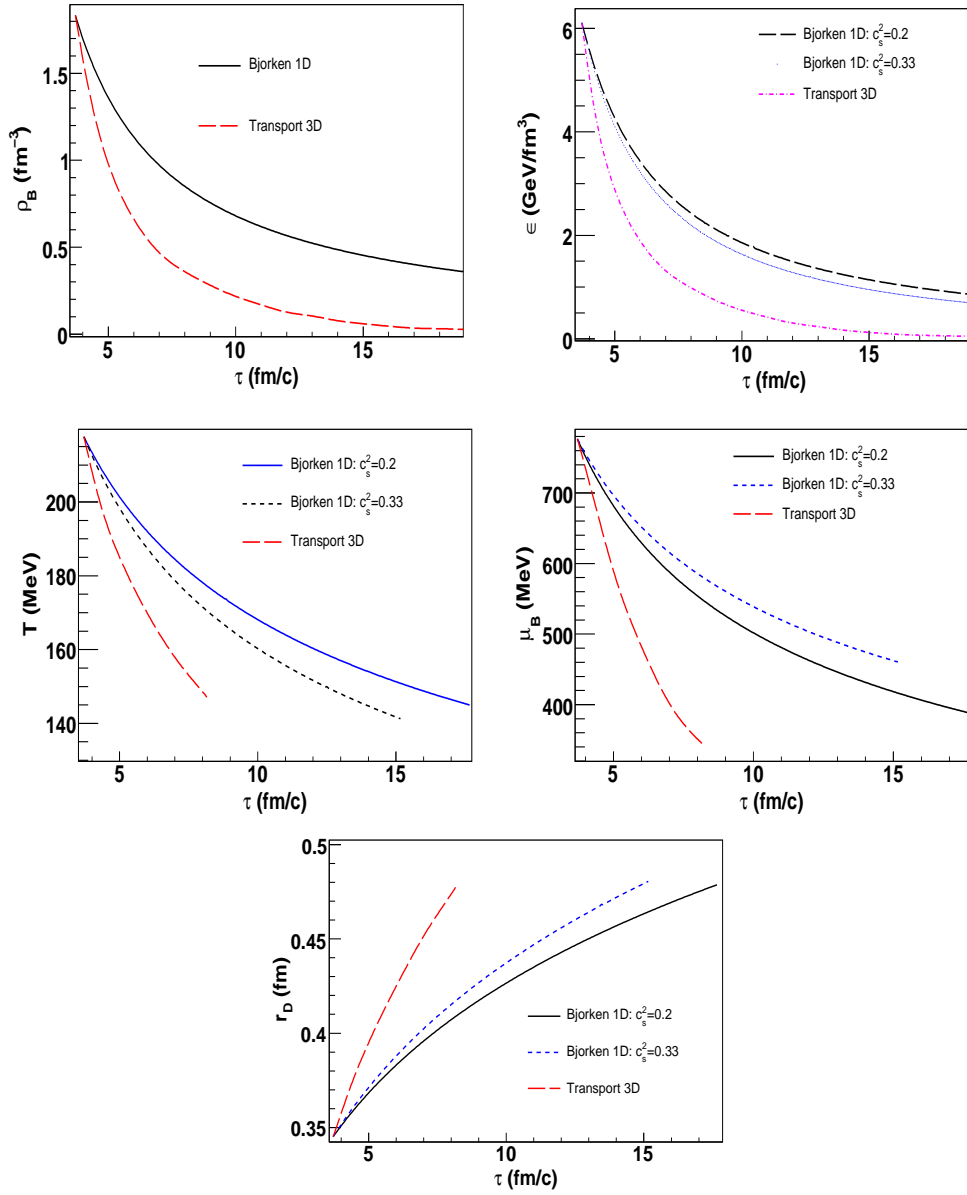


Figure 6.22: Time evolution of various physical quantities in the central fluid cell for 30 A GeV central Au+Au collisions. Top panel shows the variation of central values of energy density and net baryon density. Intermediate panel shows the evolution of the corresponding temperature and baryon chemical potential. Bottom panel shows the variation of screening length. The curves are generated both for a full (3+1)-D space-time expansion of the medium as well as for a (1+1)-D expansion assuming boost invariance. Evolution is fastest in presence of transverse expansion. In absence of transverse dynamics, rate of expansion is governed by c_s , the speed of sound.

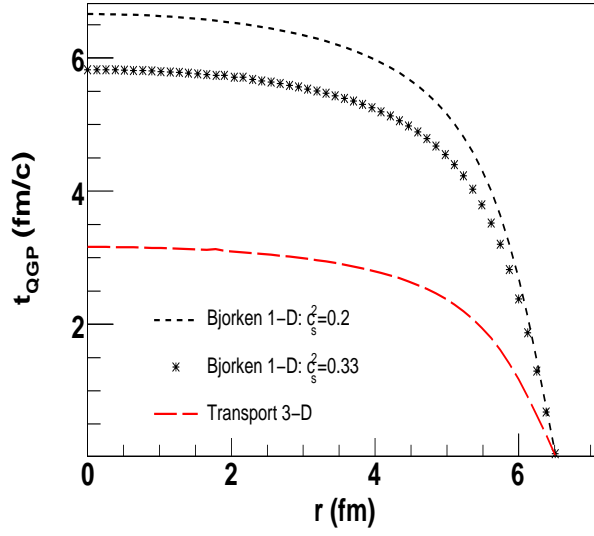


Figure 6.23: Dependence of the the plasma life time on the medium expansion dynamics.

be controlled by the value of c_s^2 . Among the three cases considered, slowest possible expansion occurs for $c_s^2 = 0.2$, giving largest suppression effects. On the other hand presence of the transverse expansion accelerates the rate of expansion thereby shortens the plasma life, which would increase the chances for J/ψ to escape the dissociation. This is also visible from Fig. 6.23, where we have plotted the plasma life time as a function of transverse co-ordinate r for the different expansion dynamics discussed above.

Finally, before we end this discussion it might be worth estimating the sensitivity of our results on the estimation of screening mass. In the preset paper, we have used a simple leading order perturbative ansatz for estimation of Debye screening mass, due to want of suitable calculations at finite density. At $\mu_B \approx 0$, lattice studies [170] indicate that for $T \leq 1.5T_c$, LO pQCD estimations of m_D are underestimated by a factor $A \approx 1.4$. Such non-perturbative effects might also be important at FAIR energy domain. Again if Debye masses, at finite μ_B , are evaluated at next-to-leading order level following the prescriptions in [306], they come out to be on an average about 1.9 times larger than the LO estimates. To explicitly check the effect of non-perturbative corrections to the screening masses on the charmonium suppression pattern, we have calculated the inclusive survival probability of the direct J/ψ mesons for an arbitrarily chosen large non-perturbative correction factor $A = 2$, as shown in Fig. 6.24. The suppression merely increases at the most by 5 – 6% in near central collisions. Such small changes would

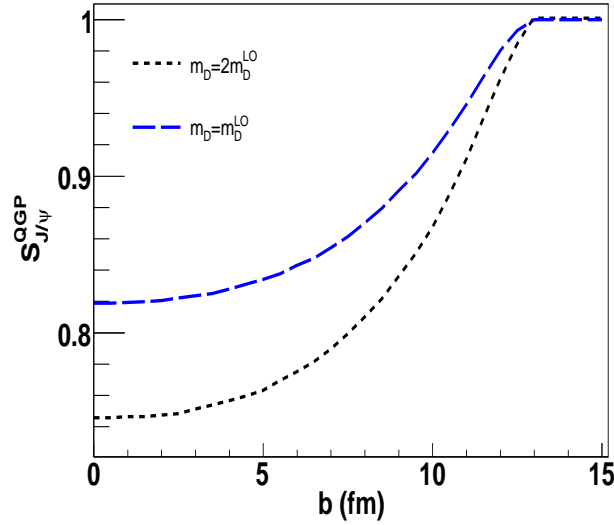


Figure 6.24: Sensitivity of the centrality dependence of inclusive survival probability of J/ψ on the non-perturbative effects in the Debye screening mass.

probably be too meagre to affect the overall suppression and possibly will not be detected within finite experimental resolution.

With the above results we in principle end our discussions on studying the anomalous J/ψ suppression in a baryon rich parton plasma. But it might be useful to note that the J/ψ suppression due to screening effects inside the plasma are quantified through the impact parameter dependence of the inclusive J/ψ survival probability. For theoretical studies such observables could be used to investigate the centrality dependence of suppression. However in order to have a direct quantitative comparison with the data to be collected at FAIR, more direct observables are required. Hence before closing this discussion, we express the suppression pattern in terms of the N_{part} dependence of J/ψ R_{AA} for 30 A GeV Au+Au collisions, an observable that can be directly contrasted with the data. In this case the suppression comes from both cold nuclear matter effects in the pre-equilibrium phase as well as color screening due to the formation of plasma after thermal equilibration. Note that since CNM effects and Debye screening effects become operative at different time scales, one can write

$$R_{AA} = R_{AA}^{CNM} \times S_{QGP} \quad (6.23)$$

As earlier we calculate the R_{AA}^{CNM} for 30 A GeV Au+Au collisions using the QVZ ap-

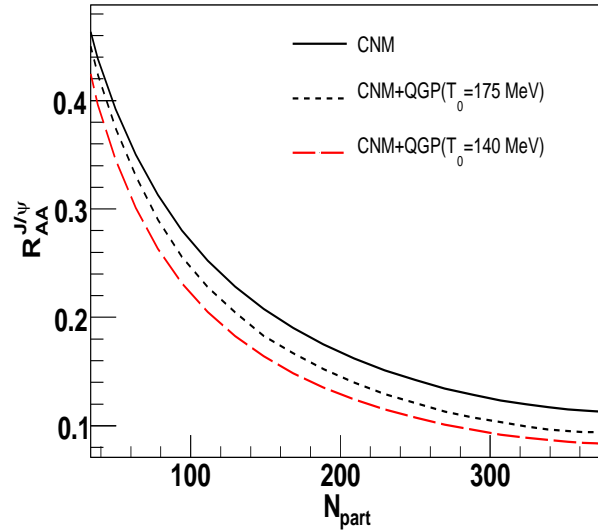


Figure 6.25: Model predictions for the centrality dependence of the nuclear modification factor for J/ψ ($R_{AA}^{J/\psi}$) in 30 A GeV Au+Au collisions. J/ψ s are mostly suppressed due to CNM effect. Formation of the deconfined matter enhances the dissociation, maximum by a factor of 15 – 25% depending on the choice of T_0 , an input parameter of the plasma EOS.

proach. As we know in the QVZ model, different parametric forms have been formulated for the transition probability, $F_{c\bar{c} \rightarrow J/\psi}(q^2)$, of a $c\bar{c}$ pair with relative momentum square q^2 to evolve into a physical meson, following the existing prescriptions of color neutralization. Out of them the power law form ($F^{(P)}(q^2)$) has been seen earlier to describe the latest J/ψ production cross section data at SPS, in p+A, as well as in In+In and Pb+Pb collisions reasonably well, without incorporating any additional hot medium effects. Hence in the present calculation we opt for the power law form. Results are shown in Fig. 6.25 with and without the QGP suppression effect. As evident from the figure, the overwhelming contribution to the observed J/ψ suppression comes from the CNM effects, a feature that has already been seen earlier for 25 A GeV collisions. This itself is a very important observation. It tells us that at FAIR energies, the suppression of J/ψ in baryon rich matter will be dominated by the CNM effects. The CNM effects thus will need to be understood in detail before any discussion of thermal effects and details of them will become of relevance. Explicit evaluation of the shadowing functions (see section 6.3 for a detailed discussion on shadowing functions in nuclear collisions at FAIR) at this particular energy, in absence of any final state dissociation ($R_{AA}^{CNM}(\epsilon^2 = 0)$), indicates that around 15% reduction of the primordial production cross section arises

due to the initial state shadowing effects; rest 75% can be attributed to the final state nuclear dissociation resulting an overall about 90% reduction of the charmonium yield compared to $p+p$ collisions in central Au+Au collisions, due to nuclear effects alone. Remaining 10% surviving the cold matter suppression, would then encounter the secondary medium subsequently produced in the collisions. Depending on the plasma characteristics, Debye screening would then dissolve 15 – 20% of these remaining J/ψ traversing through the medium. One can take note that the differences of R_{AA} with and without plasma screening effects are very little. In the deconfined medium, the contribution to the color screening mass from quarks is dominant and that from gluons is small at low temperatures. At high temperatures, the contributions to the screening mass come from both quarks and gluons and thus color screening effects would be more stronger, higher be the temperature of the plasma. However the plasma anticipated to be produced at FAIR, will have smaller temperatures and higher baryon densities compared to that at SPS or RHIC. Consequently the screening effects will be weaker resulting small suppression due to plasma screening. Hence experimental distinction of the exclusive plasma effects, if any, in turn demands very accurate data set, with lowest possible systematic and statistical errors, to be collected at FAIR.

Suppression in a baryon rich hadronic medium

For completeness, it is now time to discuss the fate of the charmonium states implanted in a high baryon density hadronic medium. However the calculations in [291] suggest that at FAIR energy collisions very large compression is expected to occur. For example, in central Au+Au collisions at $E_b = 30$ A GeV, the peak baryon density at the center is as high as $\rho_B \sim 2.3/\text{fm}^3$ which is about 15 times larger than the saturation density ($\rho_0 \sim 0.16/\text{fm}^3$) of normal nuclear matter. Following common wisdom, a rough estimate of the critical baryon density for deconfinement transition can be made with the assumption that the deconfinement sets in ground state nuclear matter ($T = 0, \rho_B = \rho_0$) under extreme compression, when the internuclear separation is of the order of mean nucleon radius (i.e. all nucleons start overlapping with each other). Considering mean nucleon radius, $\langle r_N \rangle \approx 1$ fm, the critical density comes out to be $\rho_c = (3 - 4)\rho_0$. Thus

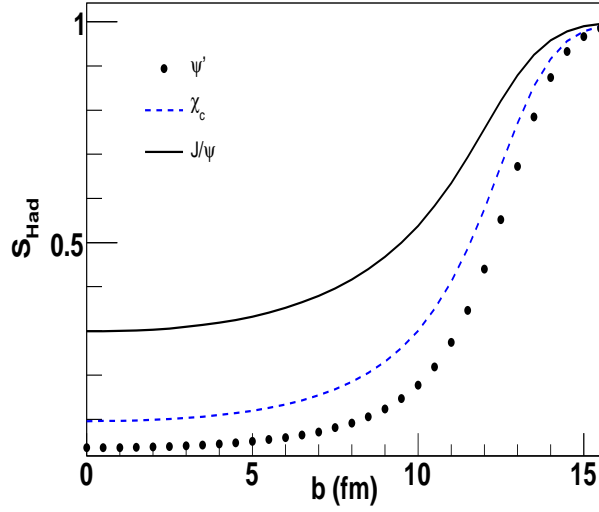


Figure 6.26: Centrality dependence of the survival probability of different charmonium states, undergoing dissociation in a high baryon density hadronic medium.

in the near central Au+Au collisions at FAIR, plasma formation seems to be inevitable. However no first principle QCD calculations are available till now at such high baryon densities. Also an experimental validation of color deconfinement in low energy nuclear collisions is yet to be done. Data collected at the Bevalac and BNL Alternating Gradient Synchrotron (AGS) showed no clear experimental evidence for QGP formation. However the baryon densities achieved in these collisions at the center were found to be around $(2 - 4)\rho_0$. Hence it might be interesting to assume a case where the FAIR energy collisions lead to a highly dense but confined baryonic medium. Such compressed baryonic medium could also lead to substantial reduction in the observed charmonium yield through inelastic nucleon-charmonium collisions. As argued earlier, due to low collision energies at FAIR, the secondary medium eventually formed in the nuclear collisions would likely to encounter the physical resonances rather their precursors. The survival probability in such a dense baryonic medium is already given by the Eq. 6.1. Of course there the suppression pattern is calculated under various simplifying assumptions like Bjorken's 1-D scaling solution for the evolution of net baryon density, arbitrary choice of central initial density. Here we plan to use the full (3+1)-D density evolution profile as calculated within UrQMD simulations. For a smooth and continuous reading we reproduce the formula below once again. The suppression induced by a secondary

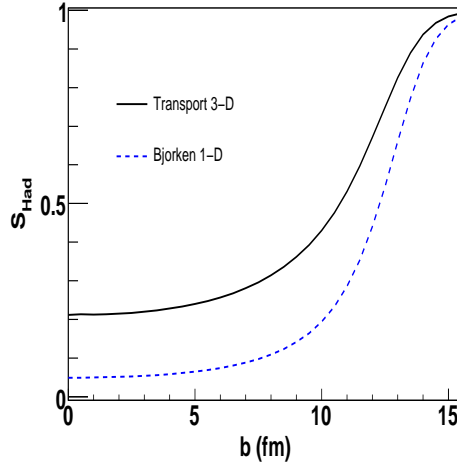


Figure 6.27: Sensitivity of the J/ψ suppression pattern to the expansion dynamics of the dense baryonic medium. The full 3-D expansion is followed from UrQMD calculations. For 1-D longitudinal expansion Bjorken boost invariant scaling solutions are assumed to be obeyed.

baryon dense confined medium can be schematically expressed as:

$$S_{Had}^i(\mathbf{b}, \mathbf{s}) = \exp\left(-\int_{t_0}^{t_I} d\tau \rho_B(\mathbf{b}, \mathbf{s}, \tau) \langle v \sigma_{\psi-N} \rangle\right) \quad (6.24)$$

where all the symbols have their usual meanings. Note as earlier t_0 denotes the medium formation time which to start with we assume to coincide with the passing time of the two colliding nuclei ($t_0 = (\frac{2R_A}{\gamma\beta} + \frac{\Delta z}{2\beta})$). t_I denotes the time up till which the J/ψ mesons interact with the medium. In principle t_I should be the minimum between the two time values namely the J/ψ escape time from the medium t_b and the chemical freeze-out time of the medium t_F at which all the inelastic interactions cease. However in this case as well, due low p_T of the charmonium states, baryonic dissociation will continue to operate till the expanding medium becomes too dilute to support inelastic collisions and t_F instead of t_b sets the upper limit of temporal integration. As earlier following Ref. [293], the average inelastic cross section of the nucleons with the already formed J/ψ , is taken to be $\sigma_{J/\psi-N} = 6$. mb. For any other resonance state ψ , we estimate the corresponding dissociation cross sections by geometrical scaling: $\sigma_{\psi-N} = (R_{psi}/R_{J/\psi})^2 \sigma_{\psi-N}$, where R_ψ denotes the radius of the state ψ . Note that in our previous calculation of baryonic dissociation excited states are not taken into account. Results are shown in Fig. 6.26, for different resonance states. For all three states suppression due to hadronic dissociation

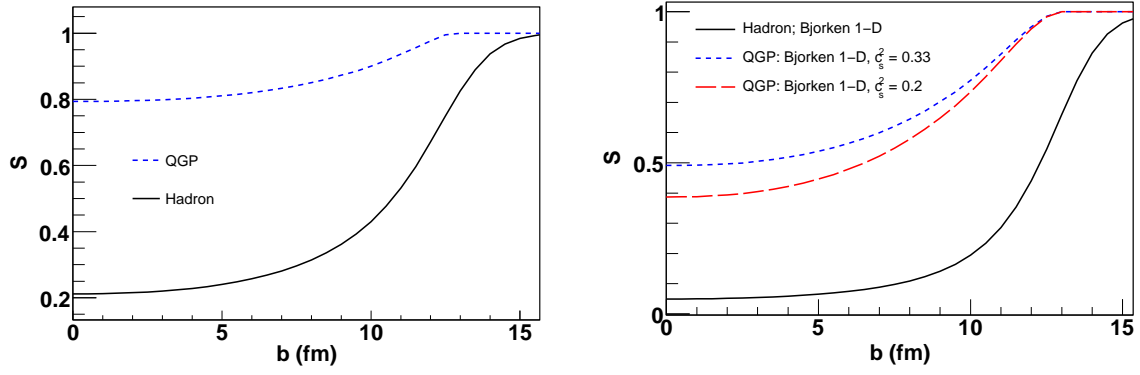


Figure 6.28: Comparison of the anomalous J/ψ suppression pattern due to plasma screening and baryonic dissociation, in 30 A GeV Au+Au collisions.

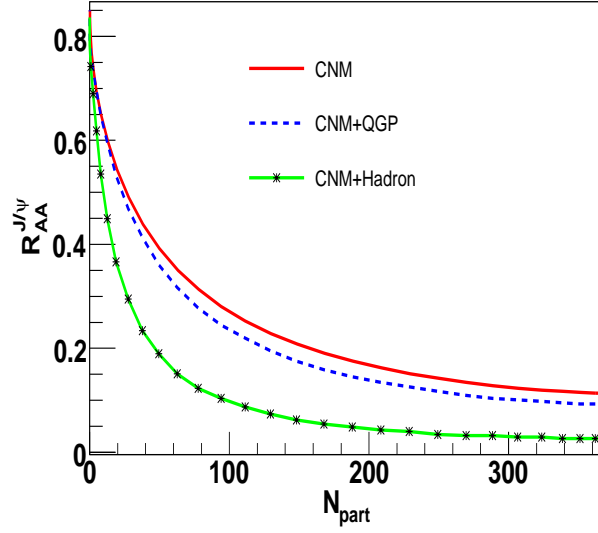


Figure 6.29: Model predictions for $J/\psi R_{AA}$ in 30 A GeV Au+Au collisions. Anomalous suppression due to QGP and hadronic medium are separately shown.

is much larger compared to that inside a deconfined medium occurred due to plasma screening. In contrast to the plasma case, amount of suppression is visibly different for $J/\psi, \chi_c$ and ψ' , with ψ' suffering from largest degree of suppression. For purely central collisions almost all those ψ' which escape cold matter suppression get dissociated. This could be attributed to the different suppression mechanisms in the two cases. In case of a confined medium the inelastic dissociation cross section scales with the square of the size of the respective bound state, thus significantly magnifying the dissociation for the weakly bound excited states.

Like the QGP case, for the hadronic case as well, we can check the effect of the transverse expansion on the overall suppression pattern. In absence of the transverse

motion, the medium expansion follows $\rho_B\tau = \text{constant}$, provided Bjorken's boost invariant scaling solutions are obeyed. Fig. 6.27 represents a comparative study of the two cases, where we have plotted the total (including the contribution from feed down decays) inclusive survival probability of J/ψ as a function of b . As expected absence of transverse cooling, magnifies the dissociation to a much larger extent reducing the J/ψ survival probability from around 20% to below 5% for central Au+Au collisions. Finally, in the Fig. 6.28 we have compared and contrasted the suppression patterns for the two distinct cases namely partonic suppression due to plasma screening and hadronic suppression due to collisional dissociation. For completeness we have plotted both the full 3-D expansion scenario, the so called realistic case and the longitudinal expansion scenario. Magnitude of suppression is found to be much larger in case of a confined dense baryonic medium than a baryon rich plasma. This observations are surely in qualitative agreement with our earlier investigations based on much simpler and cruder approximations. We conclude this chapter by showing the variation of $J/\psi R_{AA}$ with N_{part} in Fig. 6.29 in presence of the anomalous suppression induced by the compressed baryonic matter. For completeness anomalous suppression due to plasma effects are also shown. As clearly shown in the figure, suppression in the two cases is distinguishably different. Hence data at FAIR might help in experimental settlement of the yet unresolved issue of anomalous suppression.

6.5 Summary

In this chapter we describe the results of our theoretical investigations on J/ψ production and suppression in the FAIR energy regime. We start our discussion with J/ψ production in proton induced ($p + A$) reactions. Collision of proton beams off the nuclear targets gives us the opportunity to estimate the level of normal J/ψ suppression induced by cold nuclear matter (CNM) effects. Such estimations are absolutely necessary to isolate the genuine hot and nuclear matter effects leading to anomalous J/ψ suppression in heavy-ion collisions. The adapted version of QVZ model has been employed to estimate the CNM suppression at FAIR energies. Unlike the SPS energy domain, in the kinematic

region of the FAIR both the quark as well as gluon densities inside the target nucleons are found to exhibit strong shadowing effects. Moreover final state dissociation of the nascent $c\bar{c}$ pairs is also found to increase with decrease in the beam energy. Together these two effects lead to a large CNM suppression at FAIR energy collisions. Moreover at FAIR, the suppression pattern generated by two different parametrizations of $F(q^2)$, representing different mechanisms of resonance binding, are found to be distinguishably different. A precision measurement of the J/ψ production cross sections for different nuclear targets, may also help us to shed light on the much debated issue of color neutralization of a $c\bar{c}$ pair leading to the formation of hidden charm mesons.

After depicting the $p + A$ collisions, we move on to the issue of J/ψ suppression in heavy ion collisions at FAIR. First we have estimated the normal nuclear suppressions due to CNM effects. In case of nucleus-nucleus collisions parton densities both inside projectile and target nucleons are affected by the shadowing effects and the shadowing factors depend on the collision centrality. We have estimated the shadowing functions both for J/ψ as well as Drell-Yan (DY) productions. Both the processes show an overall shadowing with the effect being stronger for DY process which can be comprehended by differences in quark and gluon shadowing factors. The final results on J/ψ suppression exclusively due to CNM effects are calculated for 25 A GeV Au+Au collisions. Results are given in terms of centrality dependence of nuclear modification factor (R_{AA}) and J/ψ -to-DY ratio. Depending on the employed form of $F(q^2)$, about 80 – 90% of the primordial J/ψ s are seen to get dissociated due to cold matter effects. Out of this, 10 – 15% reduction occurs from the initial state shadowing and the rest is due to final state dissociation.

In addition to the CNM effects, we have also computed the possible anomalous J/ψ suppression induced by the high baryon density medium anticipated in low energy nuclear collisions at FAIR. Such high densities might lead to the color deconfinement transition resulting in the formation of a baryon rich quark-gluon plasma. In our calculations we have explored both the partonic scenario as well as hadronic scenario. Initially we assume some simplistic scenarios for both the cases. Suppression due to plasma screening is modeled via geometrical threshold model. Threshold model is a static model and does

not incorporate the medium dynamics. Dissociation in high baryon density hadronic medium results from the inelastic collisions of the nucleons with the fully formed J/ψ mesons. In this case we include the longitudinal expansion of the medium following Bjorken's boost invariant 1-D hydrodynamics. For both the scenarios suppression effects are quantified through the centrality dependence of $J/\psi R_{AA}$. A comparison of these two distinct scenarios reveals a much larger suppression in the compressed baryonic medium.

The simple calculations mentioned above are improved later by inclusion of realistic medium evolution dynamics. To model the dissociation due to plasma screening, we have developed a variant of the threshold model where the in medium Debye screening mass ($m_D(T, \mu_B)$) is used to decide the fate of a charmonium state implanted inside the medium. Incorporation of medium expansion, drastically reduces the suppression effects. The same feature is observed for the baryon dense hadronic medium, where inclusion of transverse acceleration of the medium results in much smaller suppression pattern. Largest contribution to the overall J/ψ suppression in nuclear collisions, is found to come from the CNM effects. One advantage of charmonium measurements at FAIR is that the initial suppression effects would possibly not get compensated by subsequent regeneration effects. Thus any additional suppression, if observed in data above the CNM effects, can then be attributed to the dense baryonic medium eventually produced in the collisions. The degree the additional suppression appears to be sensitive to the confining status of the medium. Hence measurement of J/ψ suppression in heavy ion collisions at FAIR might help in experimental settlement of the mechanism of anomalous suppression, an issue which unfortunately can not be resolved from the existing measurements.

Chapter 7

J/ψ detection at FAIR

7.1 Introduction

In the previous chapters we have presented the theoretical predictions about the J/ψ production in the FAIR energy domain. In this chapter we will discuss about the feasibility of J/ψ measurements in the CBM experiment at FAIR. J/ψ will be detected via its decay into di-lepton channel. As we know, the strategy of the CBM experimental program is to perform the charmonium measurements both via di-electron as well as di-muon channel. However in our study we will particularly focus on the J/ψ identification in the muon channel. In this context we will describe in detail the design-simulation of the MUon CHamber detector system (MUCH), one of the detector systems at CBM, aimed to study rare probes via the identification of the muon pairs produced in the high energy heavy-ion collisions in the beam energy range 8 to 35 A GeV. A brief outline of the different sub detector systems of the CBM experimental has been given in chapter 2. The measurement of the lepton pairs is a central part of the CBM physics program, as they are believed to be very sensitive diagnostic probes of the conditions inside the fireball produced in the nuclear collisions. The physics goal of the MUCH setup is the reconstruction of the full di-muon spectrum in heavy-ion collisions at FAIR. At low invariant masses, dileptons provide information on the in-medium modification of vector mesons which is a promising observable for the restoration of chiral symmetry. At intermediate invariant masses, the dilepton spectrum is dominated by thermal radi-

ation from the fireball reflecting its temperature. At invariant masses around $3 \text{ GeV}/c^2$, dileptons are the appropriate tool to study anomalous charmonium suppression in the deconfined phase. In the CBM experiment both electrons and muons will be measured, within the same kinematic coverage, in order to obtain a consistent and comprehensive picture of dilepton physics.

The MUCH project is to be realized in collaboration of institutes from India, Russia and Germany. The detector system will be constructed and installed into the CBM experiment for the start of FAIR operation in the year 2018.

7.2 Conceptual layout of the CBM muon detection system

The general philosophy of a muon detector system used in a high energy physics (HEP) experiment any where in the world is the following. The system comprises of absorber capable of absorbing hadrons and a set of detectors for identification of muons. The basic idea is that all other particles produced in the high energy nuclear collisions get absorbed inside the absorber and the muons being highly non-interacting penetrate through the absorbers and reach the detector. One important quantity for designing the hadron absorber is the nuclear or hadronic interaction length (λ_I) of the absorber material. For a given medium, λ_I is defined as the average distance traversed by a high energy hadron inside the medium before it undergoes a nuclear interaction and can be calculated as:

$$\lambda_I = \frac{A}{N_A \sigma_{inel} \rho} \quad (7.1)$$

where A is the atomic mass number of the material, ρ is its density, N_A denotes the Avogadro's number and σ_{inel} is the total inelastic cross section for hadron nucleus interaction. For a nucleus-nucleus interaction, σ_{inel} is given by:

$$\sigma_{inel} = \sigma_0 (A_{projectile}^{1/3} + A_{target}^{1/3} - \delta)^2 \quad (7.2)$$

where $\sigma_0 = 68.8 \text{ mb}$ and $\delta = 1.32$ [307]. Empirically one can calculate the hadronic

interaction length as: $\lambda_I \sim 35A^{1/3} \text{ gmcm}^{-2}$.

The CBM muon setup is being so designed to stand the high luminosity and huge background produced in reactions of a relativistic Au ion beam impinging on Au target of thickness 1% interaction length. To face such a severe environment and meet the specific experimental conditions related to di-muon and in particular J/ψ measurements following major design considerations have been kept in mind:

- The total space occupied by the muon detector system should be kept as minimum as possible, in order to minimize the combinatorial background due to meson decays. Thus one should choose materials with sufficient high A to have λ_I as small as possible resulting in a compact design.
- The vector mesons, $\rho, \omega, \phi, J/\psi, \psi'$, are identified through their di-muon decay channel; the mass resolution should be as good as possible in order to resolve the ψ' and J/ψ as well as ϕ and $\rho + \omega$.
- High luminosity is demanded for di-muons with mass above $2 \text{ GeV}/c^2$ as their cross section is extremely small; this in turn demands detectors with very high rate capability particularly close to the interaction point where particle density is substantially large.

One of the major experimental challenges of muon measurements in heavy-ion collisions in the FAIR energy regime is the identification of low momentum muons, originating from the decay of low-mass vector mesons, in a very high particle density environment. The novel feature of the muon detection system for the CBM experiment, as compared to the muon detectors in other HEP experiments, is that the total absorber is sliced and detectors are placed in between absorbers to facilitate momentum dependent track identification. This is to improve the capturing efficiency of low momentum muons, which would have been otherwise stopped by the thick absorber. The high efficiency for detection of low momentum muons is a prerequisite to reconstruct the low mass vector mesons in the muon chambers (MUCH). The layout of the MUCH system, i.e. the number, thickness and material of the absorber slices, and the number and granularity of the tracking detectors, has been optimized by simulations of central Au+Au collisions

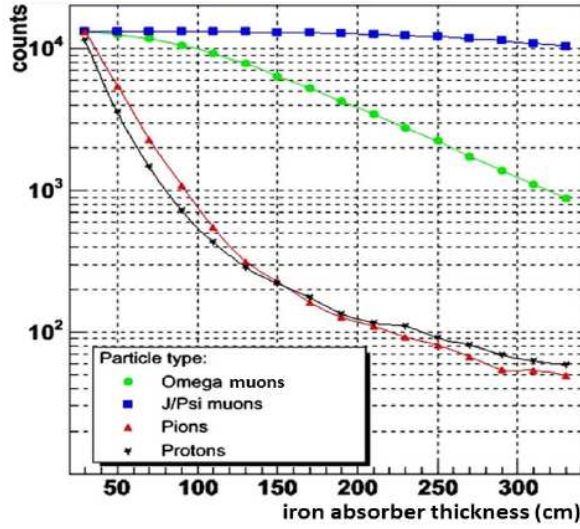


Figure 7.1: Number of particles as function of traversed length in iron. Momentum distribution of the particles are taken from the simulation of central Au+Au collisions at a beam kinetic energy of 25 A GeV. The muons decayed from J/ψ and ω mesons, are generated by PLUTO event generator while rest of the particles are generated by UrQMD event generator.

at 25 A GeV beam energy generated by the UrQMD event generator. The emitted particles are transported through the absorber and the tracking chambers using the GEANT3 transport engine. Iron has been chosen as the principal component of the hadron absorber with the goal to retain as much as possible the huge number of hadrons produced in Au+Au collisions, prior to their decay into muons. Principal contribution to the background muons comes from the weak decays of pions (eg: $\pi^+ \rightarrow \mu^+ + \nu$) and kaons. These decay muons constitute the resonance background and should be reduced to the minimum. Simultaneously the absorber materials must be appropriate to reduce the multiple scattering suffered by the muons, since this instrumental effect is the main cause for the increase of fake matches which finally increases mismatched background tracks. (Note that if the momentum of the tracks are measured after the pass through the absorber, multiple scattering causes large degradation of the momentum resolution which finally leads to poor mass resolution for the reconstructed pair. Fortunately this is not the case for CBM as will be explained later). A compromise should be found between the interaction length λ_I , which is proportional to $A^{1/3}$ of the component material and the radiation length, X_0 ($X_0 \propto A/Z^2$). λ_I should be small enough to absorb the hadrons in a reasonable absorber length, and X_0 should be as large as possible in order to reduce

Table 7.1: Characteristics of the materials used as hadron absorbers

Material	λ_I (cm)	ρ (gm/cm ³)	X_0 (cm)
C	44.72	1.93	22.1
Fe	18.32	7.2	1.92
W	10.4	17.8	0.38
Pb	3.98	11.35	0.55

the multiple scattering.

In Table 7.1 we have quoted the characteristics of a few materials that are generally used as absorbers. Note that multiple scattering is anti-correlated to X_0 through the scattering angle:

$$\theta_0 = \frac{13.6}{\beta p} z \sqrt{\frac{z}{X_0}} [1 + 0.038 \ln(\frac{x}{X_0})] \quad (7.3)$$

where β , p and z are the velocity, momentum and charge number of the incident particle, and $\frac{x}{X_0}$ is the thickness of the scattering medium in units of radiation lengths. Taken these demands into account, iron has been found as the optimum choice as the absorber material. The required thickness of the hadron absorbers for the measurement of low-mass vector mesons and charmonia can be estimated from Fig. 7.1 where the absorption of various particles is shown as a function of the thickness of an iron block. Whereas the muons from J/ψ traverse a distance up to 250 cm in iron without having any considerable suppression, low momentum muons from ω mesons get absorbed by a factor of 10 in such a thick absorber. Moreover, it can be seen that beyond an iron thickness of 1.5 m the slope of absorption for muons from omega mesons and of pions and protons are similar, which means that the signal-to-background ratio (S/B) will not improve further. In conclusion, for the efficient detection of low mass vector mesons the iron absorber thickness should not exceed 1.5 m, whereas for the measurement of muons from J/ψ decays one should add an iron absorber of about 1 m thickness together with a number of detector layers. In practice the total absorber thickness for detection of low mass vector mesons has been fixed to 125 cm of iron which amounts to be $7.5\lambda_I$. For J/ψ mesons the total absorber thickness is set to 225 cm of iron which is equivalent to $13.5\lambda_I$.

Apart from the total absorber thickness one has to optimize the thickness of the individual absorber layers in the MUCH system. Particularly important is the thickness

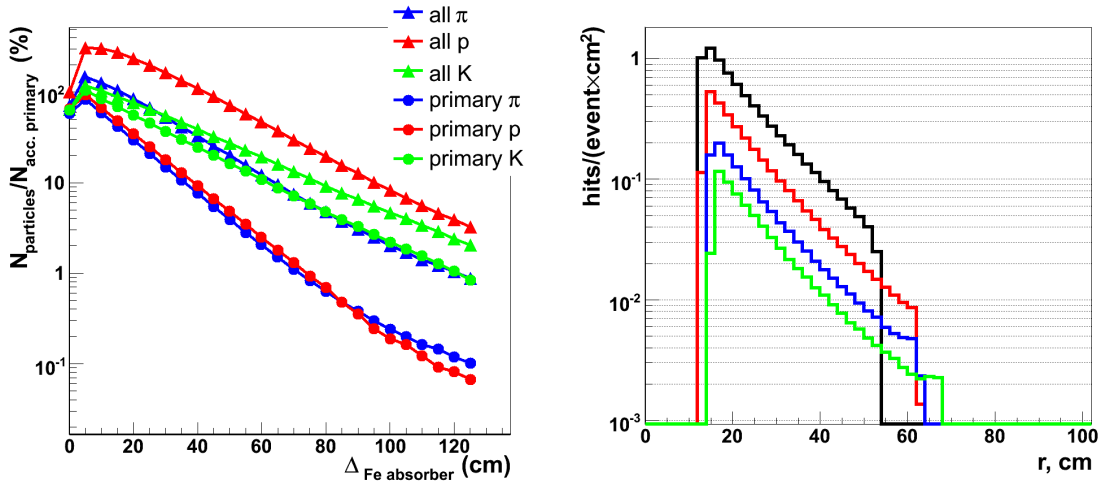


Figure 7.2: (Left) Variation of particle multiplicity (primary + secondary), per central Au+Au collision at 25 A GeV (expressed in terms of primary particles within detector acceptance), as a function of the thickness of an iron absorber. (Right) Radial distribution of particle density behind an iron block of various thicknesses. The thickness (Δ_{Fe} values used in the simulation are 10 cm (black line), 20 cm (red line), 30 cm (blue line) and 40 cm (green line).

and the material of the first absorber slice where one has to find a compromise between hadron absorption and multiple scattering [308]. The absorber should be sufficiently thick to reduce the hadron multiplicity and the hit density that decides the rate that has to be handled by the tracking chambers placed immediately after the absorber. On the other hand, a thick absorber increases multiple scattering and, hence, the number of mismatched tracks (fake tracks) which finally results an increase of the combinatorial background and a poor S/B ratio. In the left panel of Fig. 7.2 we have shown the variation of particle multiplicity as a function of thickness of the first iron absorber for central 25 A GeV Au+Au collisions. The right panel of the same figure shows the radial distribution of the particle density, for the same set of collisions, on the tracking chambers just after the first absorber of different thicknesses varying between 10 cm to 40 cm. The simulations indicate that for the particle multiplicity is dominated by the yield of secondary electrons that rises initially and then drops with increasing material thickness. Similarly for a thin absorber of 10 cm thickness the maximum particle density is 1 hit/cm 2 /event which for a peak event rate of 10 MHz translates into a particle rate of 10 7 /cm 2 /s incident on the tracking chambers. Such high rates are too large to be handled by the existing feasible detector technologies. From these considerations a

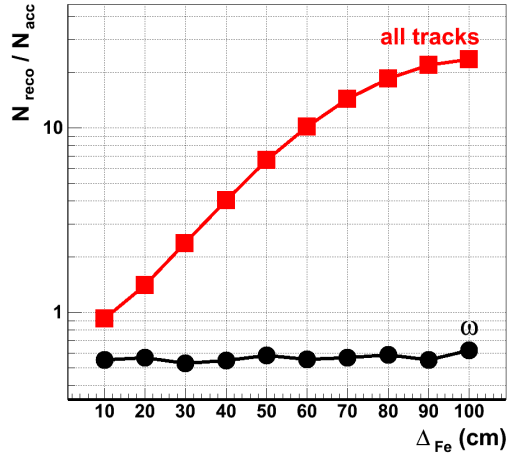


Figure 7.3: Variation of the ratio of the reconstructed tracks to the accepted tracks in the muon detection system as a function of the thickness of the first absorber block. The simulation was performed for iron as the absorber material.

thick absorber slice having thickness 40 cm seems to be preferred as the first absorber. However, as mentioned above, another important criterion for the optimization of the thickness of the first hadron absorber is the small-angle multiple scattering, which increases with the absorber thickness, and thus decreases the matching efficiency between the incoming and outgoing tracks. This reduction in matching efficiency results in an increased number of mismatches, and, finally, in a larger number of falsely reconstructed background tracks. This effect is illustrated in Fig. 7.3 where the ratio of the reconstructed tracks to the accepted tracks is shown as a function of the thickness of the first absorber. The simulation clearly shows a strong increase of reconstructed background tracks with increasing absorber thickness. The resulting invariant mass spectrum from the reconstructed tracks, which represents background for the di-muon measurement is plotted in Fig. 7.4. The result shows that the background increases by almost a factor of 10 when the thickness of the first iron absorber is increased from 10 cm to 40 cm. Thus, a first iron absorber of 20 - 30 cm thickness seems to be an optimum choice between hit density and background tracks. We have fixed the thickness of the first absorber to be 20 cm of iron.

Even though iron was taken to be the only absorber material in early days of simulation studies, more recently a carbon absorber (graphite block) of 60 cm thickness, equivalent to 20 cm of iron in terms of interaction length, is found to be more preferable

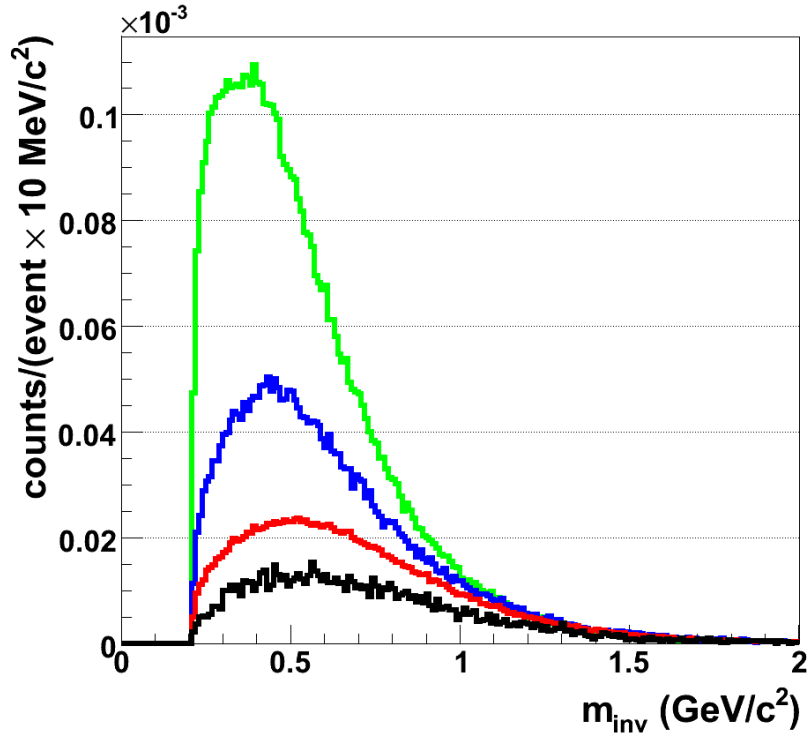


Figure 7.4: The reconstructed invariant mass spectrum for the combinatorial background for different thicknesses of the first iron absorber block. The thickness values used in the simulation are 10 cm (black line), 20 cm (red line), 30 cm (blue line) and 40 cm (green line). The total absorber thickness in all the cases is fixed to 125 cm of iron.

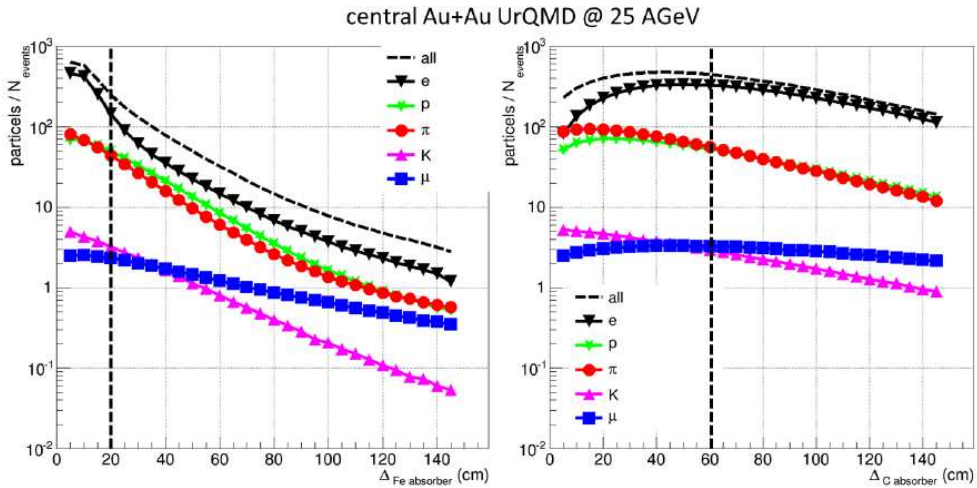


Figure 7.5: Variation of particle multiplicity (primary + secondary) per central Au+Au collision at 25 A GeV as a function of the thickness of an iron absorber (left) and a carbon absorber (right).

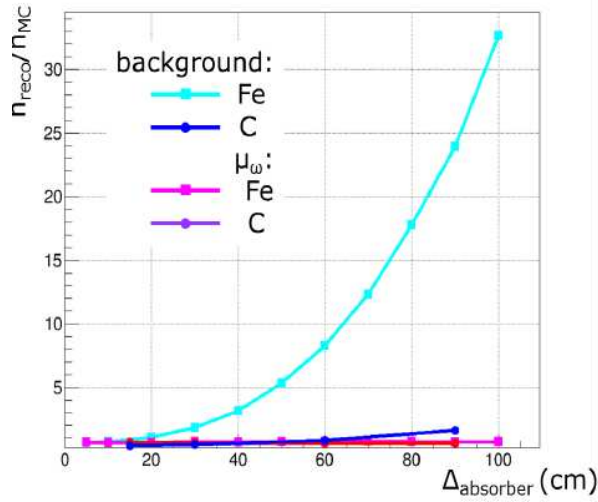


Figure 7.6: Variation of the ratio of the reconstructed tracks to the accepted tracks in the muon detection system as a function of the thickness of the first absorber. The simulations are performed for iron and carbon as absorber materials.

as the first absorber slice. It can be seen in Fig. 7.5 that the multiplicity of particles, in 25 A GeV Au+Au collisions, which traversed 60 cm carbon or 20 cm iron is very similar [309]. Also the hit densities after a 60 cm carbon block is of same order of magnitude as that after a 20 cm iron block. Note that according to the existing design of the CBM muon set up, the first absorber will be placed inside the high magnetic field of the CBM dipole magnet. Hence taking into consideration the aspect of mechanical integration, carbon (graphite) is preferable over iron. There is one additional advantage of using carbon as the absorber material as well. Due to larger radiation length, the amount of multiple scattering suffered by the tracks traversed through carbon is much less. This helps to improve the matching efficiency and thus reduces the number of fake background tracks. This can be clearly visualized in Fig. 7.6 where we plotted the variation of the ratio of the reconstructed and input Monte Carlo tracks as a function of thickness for both iron and carbon as the absorber materials. Apart from the first one, rest all absorber slices are made up of iron to maintain the compactness of the total detector system and to reduce the meson decay effects discussed earlier. They are not also crucial in terms of fake tracks due to reduced track densities. So far as practical design is concerned, the first absorber is divided into two pieces. The 40 cm thick first piece is housed inside the dipole magnet where as the rest 20 cm is placed outside the magnet. Note that even though all the iron absorbers are placed outside the magnet

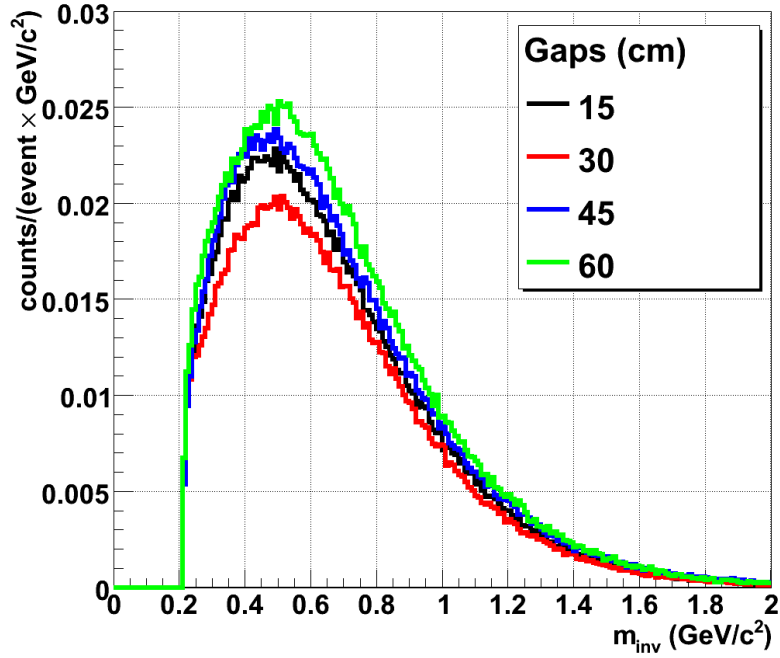


Figure 7.7: Reconstructed invariant mass distribution of the combinatorial background for various values of the gap between the absorbers. The total absorber thickness as well as thickness of the individual segmented absorbers is kept same for different gap widths. Iron has been used as the only absorber material.

to avoid the effect of any residual magnetic field they all are made up of stainless steel instead of soft iron which is non magnetic in nature.

The sketch of the muon detection system optimized for heavy-ion collisions at SIS300 energies is shown in Fig. 7.9. It comprises of 6 absorbers, first one made of carbon and rest of iron, and 6 tracking stations. Each tracking station consists of three layers of detectors located in the air gap after each absorber layer. The air gap between the two successive absorbers has been optimized to 30 cm. Note that to reduce the combinatorial background coming from the weak decays, one needs to design the set up as compact as possible. With the increase of the gap between the absorbers total size of the MUCH increases. It also results in an enhanced combinatorial background as seen in Fig. 7.7, where the invariant mass distribution for the combinatorial background relevant for lm_{vm} measurements, is plotted for four gap values of 15, 30, 45 and 60 cm. Results indicate that the background is minimum for a 30 cm of air gap between the two absorbers. For higher gap widths the background increases due to increased fraction of meson decays. For smaller gap the background increases due to the short

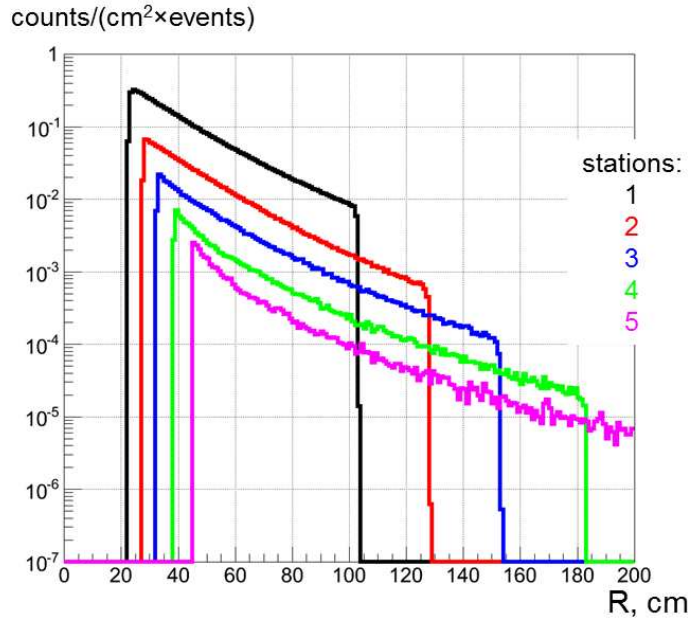


Figure 7.8: Hit densities in the tracking chambers of stations 1 - 5 for central Au+Au collisions at 25 A GeV as calculated with the UrQMD event generator and the GEANT3 transport code. For a given station the hit density is averaged over the three layers (gas chambers).

range secondary electrons that are emitted from the absorber and can easily reach the following detector stations for small gaps. The total number of detector chambers is 18 (3 behind each absorber). Also a gap of 30 cm between two successive absorbers is required to accommodate the total detector profile including cooling arrangements, mechanical structure among the others. The total absorber length in the current design amounts to 265 cm divided into 60 cm carbon and (20 + 20 + 30 + 35 + 100) cm of iron which is equivalent to 13.5 times λ_I . This geometry can be used both for the identification of charmonium and low mass vector mesons at top FAIR energy. For the latter, only hits in front of the last 100 cm absorber are relevant, i.e the effective number of detector layers for low-mass vector meson measurement is 15, and the corresponding total hadron absorber thickness is 60 cm of carbon and 1.05 m of iron. The angular acceptance of the detector spans from $\approx \pm 5^\circ$ to $\pm 25^\circ$. The lateral size of the absorbers is sufficient to completely shield the detectors from the primary particles emitted from the target. The last station behind the 100 cm thick absorber is also used for charmonium trigger as will be discussed latter.

We have performed simulations to estimate the hit density in the tracking chambers

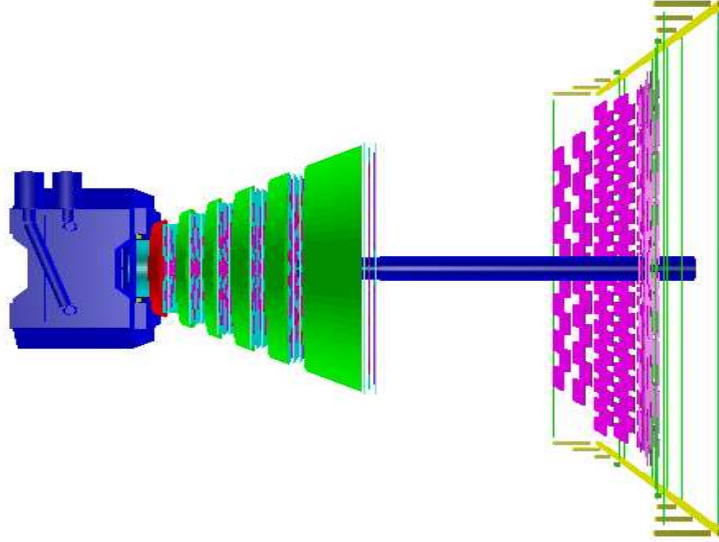


Figure 7.9: A schematic view of MUCH SIS300 layout. It consists of 18 detector layers and 6 absorbers with total absorber thickness of 265 cm of carbon + iron. The time-of-flight (TOF) wall is shown in the setup.

placed behind the absorbers. The results are shown in Fig. 7.8 in terms of counts per cm^2 per event as function of the distance from the beam axis for central Au+Au collision at 25 A GeV, for the stations 1 - 5 with the UrQMD event generator and the GEANT3 transport code. The hit density in the first station reaches values up to $0.3/\text{cm}^2/\text{event}$, in the innermost part (i.e. for small polar emission angles). This value asks for a small detector pad size of the order of $10\text{-}15 \text{ mm}^2$, at least for the inner part of the first detector station, in order to keep the occupancy at a reasonably low level (5%). In case of minimum bias collision the particle densities are expected to lower by a factor of 4. Hence for a total reaction rate of 10 MHz, the peak rate to handled by the tracking chambers in the first station comes out to be $0.75 \text{ MHz}/\text{cm}^2$.

Apart from the SIS-300 configuration, MUCH will be taking data in the start version of FAIR where proton beams with 30 GeV energy and Au ions up to 11 A GeV will be available. As there is likely to be a time gap between the operation of start version using SIS100 ring and the full version with SIS300, we have optimized a start version of

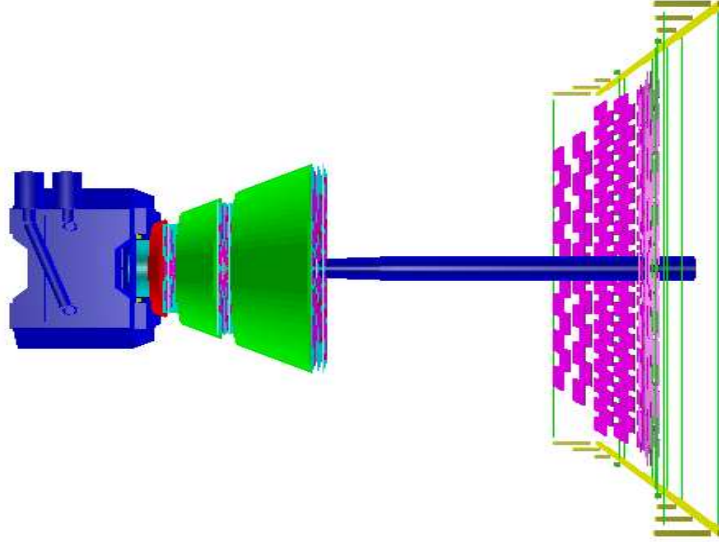


Figure 7.10: A schematic view of MUCH SIS100 layout. It consists of 9 detector layers and 3 absorbers. The last 3 layers are used for charmonium trigger. TOF wall will be also common to all the configurations.

MUCH at CBM for SIS100 collisions. As shown in the Fig. 7.10, SIS100 configuration will consist of 3 stations each consisting 3 layers. Total absorber thickness will be same as of SIS-300, except that the absorber segments will be relocated to make 3 absorber layers: 60 cm carbon and two iron blocks of varying thickness, making a total iron absorber of 205cm thick. This configuration is for J/ψ measurement only and therefore 3 tracking stations are expected to be adequate with the last station to be used for muon trigger.

The detectors planned to be used for the first stations are GEM-chambers [310], a detailed discussion on which can be found in the technical design report (TDR) of MUCH. For inclusion of a realistic scenario, modular structure has been implemented in simulation. The covered active area of each layer has been divided into trapezoidal sector-shaped modules. Each module is arranged on a support structure, having thickness around 2 cm. Detector modules are attached at the front and the back sides of the support structure and filled with argon based gas mixture as the active medium.

As per present status, all stations will have gaseous detectors of different technologies. This allows us to use gas as sensitive medium throughout. The gas thickness is set to 3 mm. Cables, gas tubes, PCBs and front-end-electronics are not included in the present version of simulation. The distance between the centers of detector layers is 10 cm to provide enough space for accommodating the detector profile that includes electronics boards, mechanics, cooling arrangement among the others. The spacing between layer and absorber is 5 cm. The modules are arranged in rows on both sides of each support plane keeping 2 mm overlap in azimuth of sensitive volumes to avoid dead zones along the radial direction. The number of sectors in a particular detector plane depends on the radii of the stations. It might be important to note here that earlier we have also used rectangular modules instead of sector shaped modules. Each detector layer was divided in several modules of size 30 cm \times 30 cm as the maximum size of the modules was limited by the GEM foil production technology. The practical disadvantage of this modular design is the non-availability of large size GEM modules which in turn results in complex detector design and large number of dead zones. One possible solution to this problem that has been identified is to divide the detector planes into several sectors instead of modules. In case of sector design, large GEM foils limited by 50 cm size (width) in one direction and no limitation in length are available and prototypes are being made by CMS and other experiments. These GEMs are produced using single-mask technology which gives significantly larger yield of good foils compared to the conventional double-mask GEM. Considering all the above advantages, we have presently switched over to the sectorized geometry option. In Fig. 7.11 the layout of one layer of the first station with trapezoidal sectors is shown. To accommodate detector electronics, cooling systems etc. half of the total set of sectors are arranged in the front face and rest half in the back face. The number of sectors that can be accommodated in a detector layer is indeed a tunable parameter in simulation. However in a given layer, we have fixed the total number of sectors in the following way. As mentioned the maximum width of the trapezoidal GEM foils is 50 cm. Assuming that 10 cm will be required for support arrangement etc. the usable width of one foil comes out to be 40 cm. Hence for a layer of outer radius R_{out} (in cm) the number of sectors is calculated using the relation, $N_{sec} = \frac{2\pi R_{out}}{40}$. It should

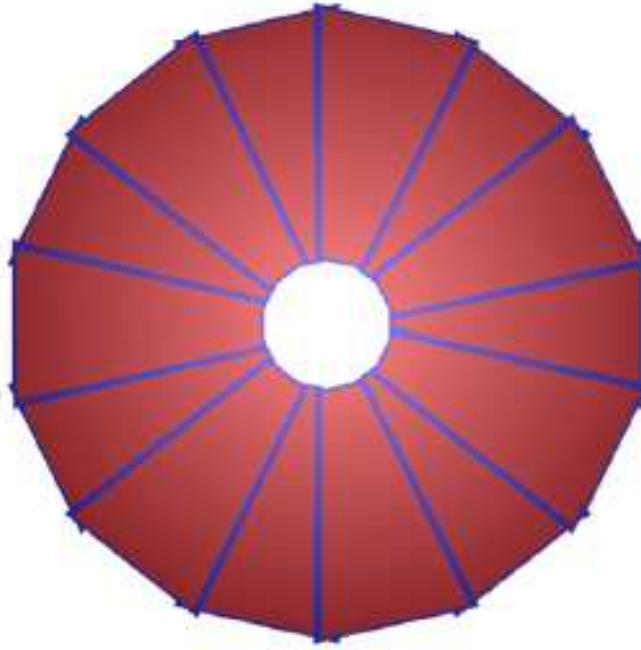


Figure 7.11: Schematic view of the layout of the muon chambers with trapezoidal overlapping sectors

be mentioned that for the simulation results presented here, detectors in all six stations are taken to be made -of GEM for ease of implementation in simulation geometry. Even though in actual setup, other technological options like straw tubes or an existing Transition Radiation Detector will be used. However, given the realistic segmentation, gas detector response of those chambers will be same as present implementation.

7.3 Simulation procedure of MUCH

7.3.1 Simulation framework

The simulation chain performed using the UrQMD event generator and the GEANT3 transport engine can be summarized by the block diagram given in Fig. 7.12. It consists of following fundamental blocks: (a) geometry implementation and transport, (b) segmentation and digitization, (c) hit formation, (d) track propagation in MUCH chambers, and (e) selection of tracks as muon candidates. The final identification of muon tracks is part of the di-muon analysis.

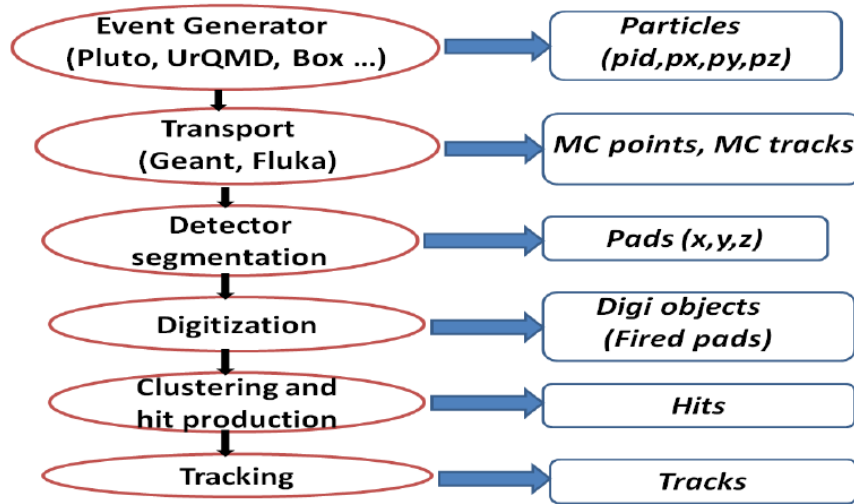


Figure 7.12: Block diagram showing a schematic layout of the simulation chain in MUCH

- Geometry implementation and transport:** MUCH aims to study the propagation of tracks inside the segmented absorbers. The study of geometry therefore involves in implementation of conical absorbers of varying sizes placed around the conical beam pipe. Conical absorbers are used to accept the forward focused produced particles. The detector modules are of trapezoidal profiles that are placed behind each absorber block. For effective tracking, each tracking station consists of 3 layers of tracking chambers. Each tracking layer consists of a thin support structure and an equal number of sector-shaped modules are placed on two faces of the support structure. For reducing the dead-space, modules on two faces are placed in such a way that a border of the module on one side has overlap with an active zone of the module on the opposite side. The number of stations, their shape, size and number of modules are varied for optimization of efficiency and signal to background ratio (S/B) for detecting low-mass vector mesons and charmonia.
- Digitization:** GEANT3 provides the position of energy deposition inside the detector module. These locations along with the energy depositions taken together are called MUCH points. To account for realistic detector geometry, the read-out planes of the modules are segmented in pads for obtaining final detectable response. The procedure of distributing the MUCH points to pads, known as digitization involves the detailed procedure of implementing the response of the gas

detector to the energy deposition inside the chamber as described in detail later. The projective segmentation scheme has been implemented as per the optimization requirements of the modules. The pad dimensions are varied to reduce the pad occupancy and the multi-hit probability in a pad. In the *simple* digitization scheme, points falling inside a given pad area are added together to obtain a *digit*, and in the *advanced* digitization scheme, MUCH points are subjected to create primary ionization, multiplication and signal generation inside the gas volume. For the results presented here, *advanced* digitization scheme has been used.

- **Clustering and HitFinder:** Digits are grouped into *clusters* using a suitable clustering algorithm. Based on the particle multiplicity and associated cluster overlap, the clusters are either broken into several sub-clusters which have been treated as hits (advanced hit finder) or each cluster is treated as one hit (simple hit finder). The centroids of the sub-clusters in case of advanced hit finder or of the main cluster in case of simple hit finder is assigned to be the location of a MUCH-hit which are then taken as candidates for track propagation.
- **Track propagation:** Tracks reconstructed in STS are propagated using the Kalman Filter technique to pass through the MUCH layers. MUCH hits located around the propagation point are taken as the candidates of the propagated track. For analysis of MUCH, χ^2 of track fitting, number of STS and MUCH layers associated to the propagated tracks are taken as track validation parameters.

7.3.2 Detector segmentation, digitization, clustering and hit formation

The muon tracking chambers will be under the conditions of high hit density and large event rates (10 MHz). The aim of the segmentation study is to get a realistic and optimized detector layout with respect to the physics measurements. In order to take into account the variation of hit density with the radial distance from the beam pipe (density falls as $1/r$), the muon detector readout planes are segmented in different annular regions with pads of appropriate shapes and sizes required to achieve the desired pad occupancy.

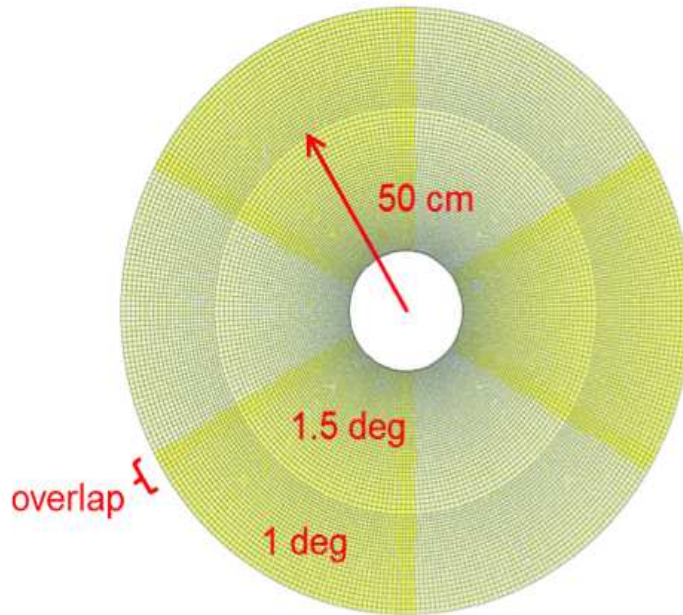


Figure 7.13: Schematic views of the segmentations of the sectorized modules, entire area has been divided into projective pads of 1 degree angular regions and with two rings of different angular dimensions

Apart from the hit-occupancy, another constraint is the spatial resolution that limits the maximal pad size.

At the transport level, only basic gas volumes are created, while the detailed pad readout structure is simulated a posteriori with a segmentation algorithm. In case of sector geometry, projective pads of radially increasing size are implemented in segmentation as shown in Fig. 7.13. The dimensions of the pads are determined by the angular separation on transverse plane. The implemented segmentation algorithm determines angular dimensions and positions of the pads automatically depending on radius in such a way that the radial dimension of each pad is kept approximately equal to the azimuthal dimension ($\Delta r \sim r\Delta\phi$) at a given radius. The entire region could be divided into pads of uniform or varying angular regions as shown in the figure. For our present implementation, pads are used resulting in 1-degree separation in azimuthal angle. Total number of pads over all the six stations comes out to be 8,02,320 for a case when all the stations have pad readout. It is likely that only first three stations will be made of GEM, but the segmentations in some other technology options are likely to remain same and therefore this number is useful from the point of view of total number of required readout channels. There is a possibility that straw and TRD might use strip readout

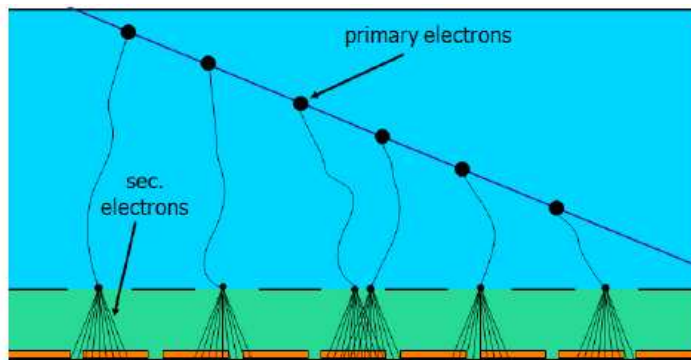


Figure 7.14: Schematic representation of the signal generation in GEM

and the number of readout channels will be somewhat reduced. Even though all results shown here are for 1 degree pads, which results in large pad size in the outer periphery of layers, as a part of future optimization of the segmentation, if required, we have the option to divide the pads at larger radii into smaller than 1 degree intervals.

Simulation of GEM detector response (digitization), which is schematically shown in Fig. 7.14 is based on a simple assumption that a GEM active gas volume can be split into the drift and avalanche regions. This means that the triple-GEM structure is ignored in the simulation at the moment. The digitization algorithm can be logically split into several steps:

- Determination of the number of primary electrons emitted in the drift volume for each Monte-Carlo point is based on the Landau distribution for an argon-based gas mixture, track length in the drift volume and particle type and energy. Parameters of the Landau distribution namely the expectation value and the variance are determined with the HEED [311] package. Primary electrons so produced are then distributed randomly according to Poisson law along the direction of the incident track.
- Determination of the number of secondary electrons emitted in the avalanche region for each primary electron. Exponential gas gain distribution with a default mean gas gain of 10^4 is used in this step. The transversal diffusion of the avalanche which gives the measure of the spot size is assumed to be constant.
- Intersection of secondary electron spots with the pad structure of a module and

determination of the charge arrived at each pad. The default spot radius is set to 0.6 mm as measured for the triple-GEM detectors during beam tests. Charge arrival time is calculated from the Monte-Carlo point time plus the primary electron drift time: $t = d/v$ (d -distance traveled by the primary electron towards the avalanche region, v - drift velocity, $v = 100 \mu\text{m/ns}$ by default).

- Time-dependent summation of charges from all Monte-Carlo points pad-by-pad and conversion of the charge-vs-time distribution into the timing response of the foreseen MUCH readout electronics. Timing response on a delta-function-like charge from secondary electrons is simulated by the linear peaking period of 20 ns and the falling edge described as an exponential decrease with 40 ns slope. Response to several delta-function-like charge signals is described as a convolution in time of responses from several delta-functions. Random noise of the readout electronics is also added at this step.
- Application of the threshold to the readout response and determination of the time stamp (a moment when the response exceeds the threshold value). The charge information is converted into ADC channels with one of the three methods: amplitude with the flash discriminator, Wilkinson integration or time-over-threshold approach.
- The time stamp and the ADC information is decoded into 32-bit word and stored in the array of CbmMuchDigi objects together with the 32-bit channel Id for subsequent processing.

Fig. 7.15 illustrates the results obtained with the digitization algorithm showing the reconstructed charge on pads corresponding to Monte-Carlo track projections. In addition to the visual control of the fired pad to MC track correspondence, the quality assurance algorithm has been developed. One of the quality criteria is the distribution of the full charge from the track as function of energy and particle type. An example of the charge vs. energy logarithm distributions is shown on Fig. 7.16. The obtained distributions agree well with the Bethe-Bloch dependence of the most-probable value of the input Landau shape corrected for the mean gas gain (see black line). Fig. 7.17 shows

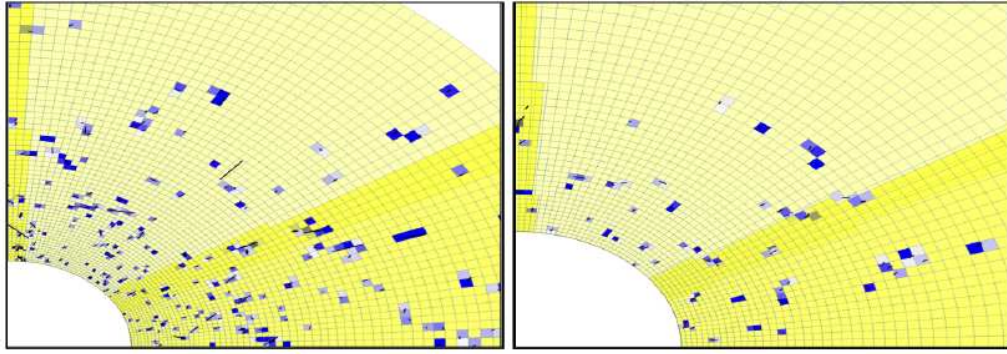


Figure 7.15: Illustration of digitization scheme for station 1(left panel) and station 2 (right panel)

the distributions of deposited charges by the minimum ionizing particles. The charge deposition spectrum follows the Landau distribution as expected.

The detector parameters are tunable and could take values depending on the exact micro-pattern detector technology. The spot radius is chosen such as to reproduce the existing experimental data. The avalanche spot for each primary electron is projected to the pad plane and the sum of charges at each pad is calculated. Apart from the spot radius one can also tune the parameters like total number of ADC channels, the maximum charge that can be collected by a pad and the threshold charge. The maximum charge defines the dynamic range of the readout ASIC. If for a particular channel, the corresponding energy deposition goes beyond the specified dynamic range, the channel gets saturated. The threshold charge is set above the expected noise level. However, in the present implementation, as no additional noise has been introduced in the simulation, the applied threshold cuts signal thereby reducing the efficiency. The noise threshold has therefore been kept at a reasonably low level. In the current study, we set following values to the above parameters: (i) Number of ADC Channels: 2048, (ii) Q_{max} : 100 fc, (iii) Q_{th} : 1.0 fc ,(iv) GEM spot radius: 600 μm . Note that muons are minimum ionizing particles (MIP). Within a argon filled drift volume a MIP typically produces 100 - 120 primary electrons per cm Hence for a drift gap of 3 mm, the number of primary electrons would be approximately 30 - 40. For an average gain of 10^4 , the total number of electrons created by an incident muon track will be $\sim 30 \times 10^4$ which is equivalent to a deposited charge of 45 fc (1 fc = 6,600 electrons). Hence setting up a noise threshold

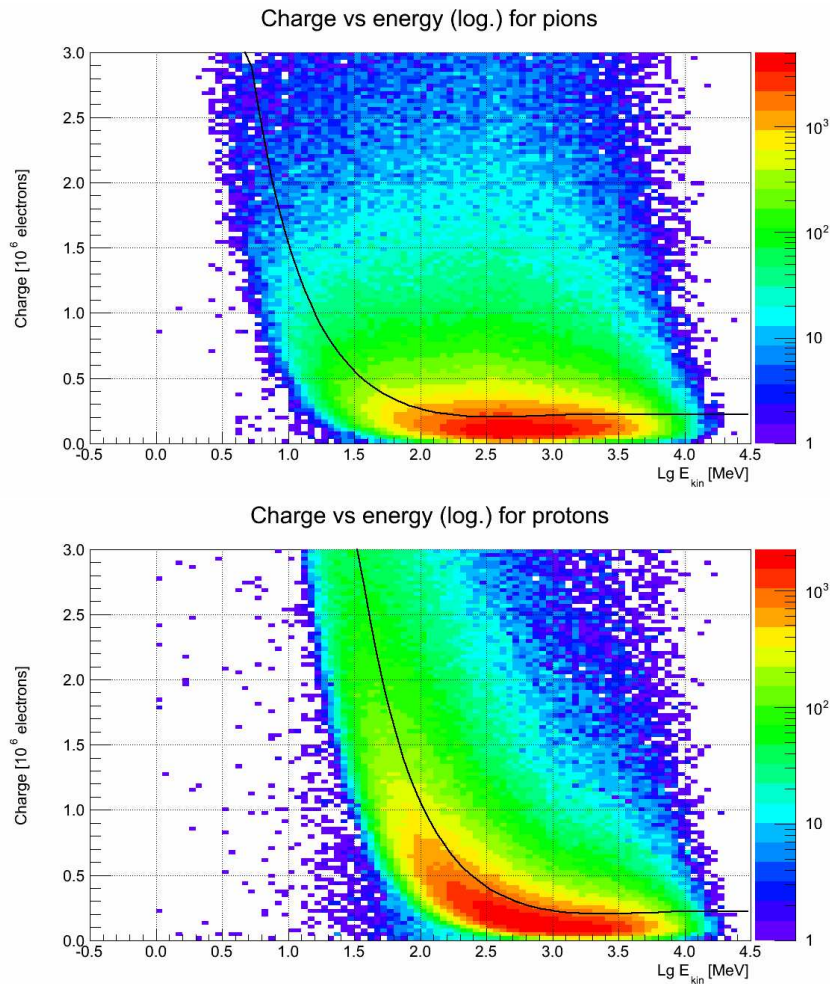


Figure 7.16: Total charge created by the incident tracks inside the active volume of the detector. The gas depth is set to 3mm in simulation. The figure describes deposited charge versus particle kinetic energy for pions and protons. The black lines result from a Bethe-Block fit to the mean values.

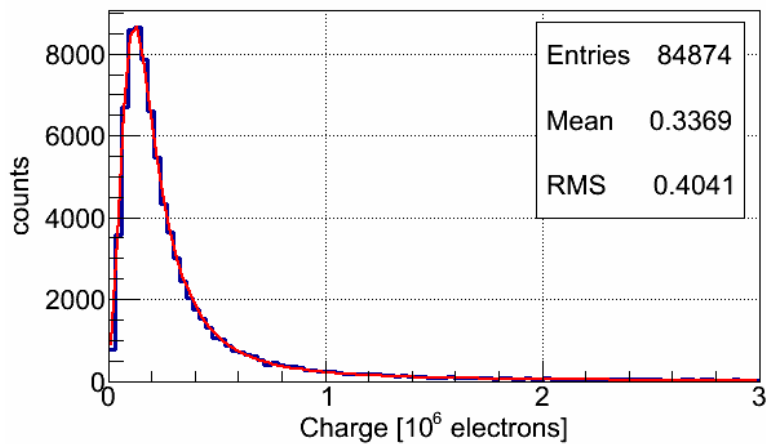


Figure 7.17: Charge deposition by a minimum ionization particle (MIP) in the gas volume of the detector. The mean gas gain has been set to 10^4 in simulation. Hence each MIP creates on the average about 33 primary electrons along its track inside the 3 mm gas volume.

of $Q_{th} = 1$ fc is not likely to significantly affect the signal.

The *digits* formed by the procedure discussed above are clubbed together to form clusters, which are then deconvoluted to form hits. The following algorithms have been implemented for the cluster deconvolution and hit finding:

- **one hit per pad** A trivial algorithm when a hit is created for each fired pad. The hit positions correspond to pad centers, while the hit uncertainties are taken as pad dimensions divided by $\sqrt{12}$. Main advantages of this algorithm are the simplicity of implementation and low CPU consumption. The main disadvantage is that too many hits are created, many of them appear to be far from real track positions. Many additional hits lead also to huge combinatorics and inefficiency at the track finding level.
- **one hit per cluster** One hit per cluster is created. Hit coordinates are determined by center-of-gravity averaging with weights equal to charges induced on pads. This algorithm is also quite simple and fast. In the case of small pads, this algorithm allows to define track position much better than in the previous case. In the case of large clusters, this algorithm may cause too large difference between reconstructed hit positions and real track coordinates (see fig. 7.18, center, for example).
- **search for local maxima** A search for local maxima in the charge distribution is performed cluster-by-cluster. Hit coordinates are assigned to centers of pads, corresponding to local maxima. If cluster dimensions are less than 2x2 pads, *one hit per cluster* algorithm is used to determine hit coordinates for small clusters with better precision. The main advantage of the method is that it works for large clusters, it allows to find several single track hits that contributed to one cluster (see fig. 7.18, right for example). Nevertheless, in the case of long clusters (usually produced by single but very inclined low-energy electrons) local maxima may originate from random fluctuations of charge on pads. Therefore search for local maxima may lead to creation of fake hits, which do not correspond to real tracks. Moreover, one should keep in mind that some tracks still could remain unresolved by this algorithm (see fig. 7.18, right).

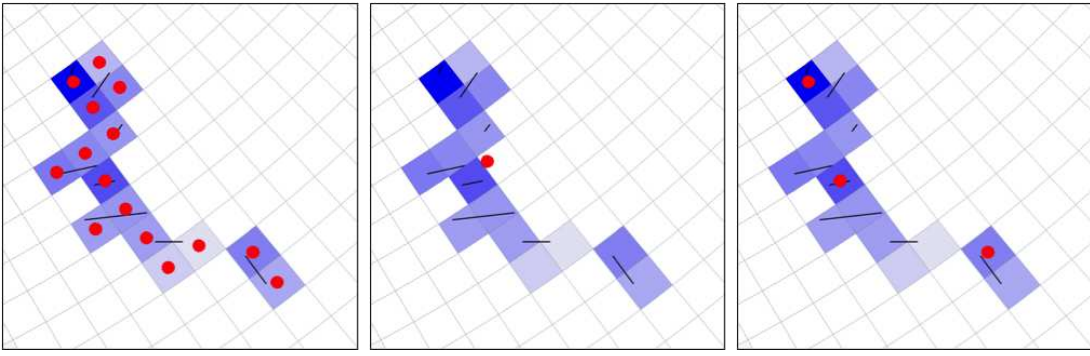


Figure 7.18: Illustration of three types of hit finder scheme

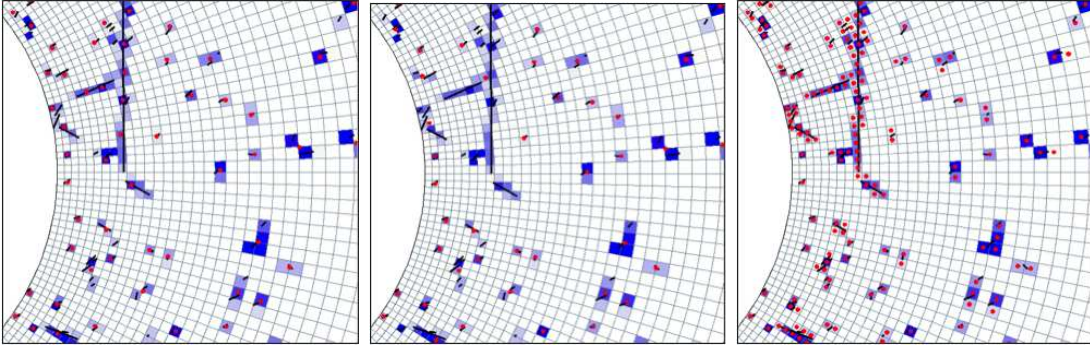


Figure 7.19: Illustration of different hit-finder algorithms in an event

The **search for local maxima** is used as a default algorithm in the MUCH simulations. The developed algorithms for the cluster and hit finding can be used not only for simulation purposes but also for the reconstruction of real data.

The performance of the hit finding algorithms is illustrated in Fig. 7.18 for one of large clusters. Fig. 7.19 represents the results for the central region of the first MUCH station where one expects maximum occupancies. Fig. 7.19 illustrates that track positions are correctly reconstructed in majority of cases.

7.3.3 MUCH Track Reconstruction

The main challenge of the track recognition in the CBM-MUCH detector results from the large multiplicity in heavy-ion collisions. About 1000 charged particles are produced in central Au + Au collisions at CBM energies. This high charged particles multiplicity leads to a high track and hit density in the MUCH detector, especially on the first detector planes (see Figure 7.20).

The developed track reconstruction algorithm in MUCH is based on track following

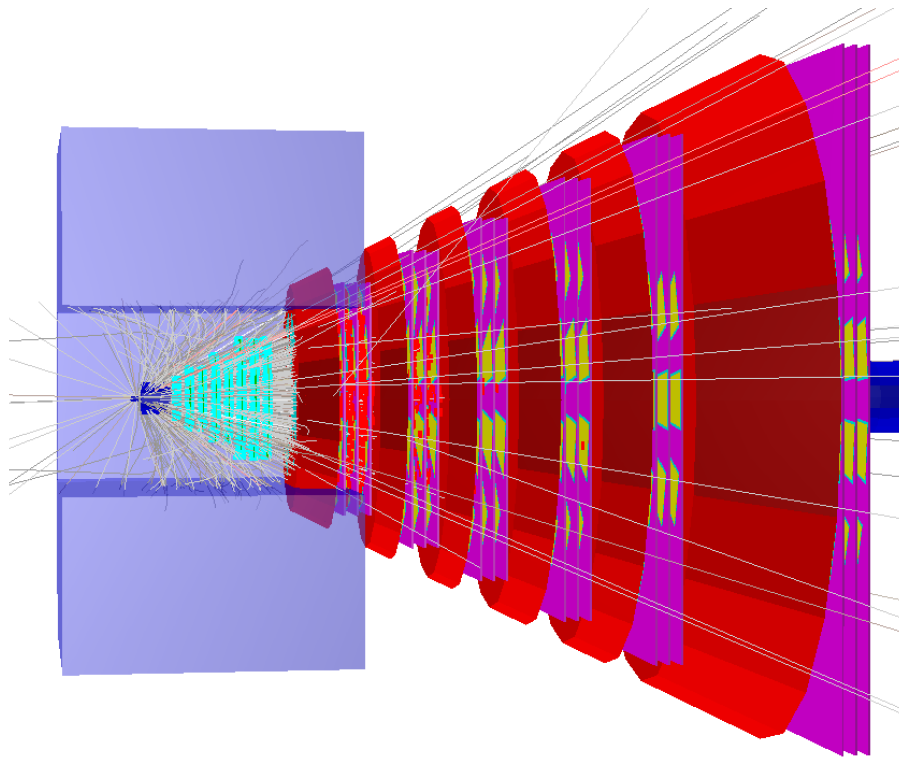


Figure 7.20: Visualization of one simulated central Au + Au collision at 25 A GeV.

using reconstructed tracks in the STS as seeds. The STS track reconstruction is based on the cellular automation method [312] and STS track parameters are used as starting point for the subsequent track prolongation. This track following is based on the standard Kalman filter technique [313] and is used for the estimation of track parameters [314] and trajectory recognition. Main logical components are track propagation, track finding, track fitting and finally a selection of good tracks. Each of the steps will be described in the following in some more detail.

Track propagation

The track propagation algorithm estimates the trajectory and its errors in a covariance matrix while taking into account three physics processes that influence the trajectory, i.e. energy loss, multiple scattering and the influence of a magnetic field. The influence of the material on the track momentum is taken into account by calculating the expected average energy loss due to ionization (Bethe-Bloch formula) and bremsstrahlung (Bethe-Heitler formula) [315]. Adding process noise in the track propagation includes the influence on the error, i.e. the covariance matrix due to multiple scattering. Here, a

Gaussian approximation using the Highland formula [315] is used to estimate the average scattering angle. The propagation of the trajectory is done according to the equation of motion. If the track passes a magnetic field the equation of motion for a charged particle is solved applying the 4th order Runge-Kutta method [316]. For passing a field free region, a straight line is used for propagation and the transport matrix calculation. The transport matrix is calculated by integrating the derivatives along the so-called zero trajectory [317]. A detailed description of the developed track propagation can be found in [318].

Track finding

In the track finding algorithm hits are attached to the propagated track at each detector station using two different methods. In the *nearest-neighbour* method just the nearest hit is attached to the track. In the *branching method*, on the other hand, all hits within a certain environment are included. For the first method, only one track is further propagated, the branching method allows for several track branches to be followed, one for each attached hit. Common techniques to these methods are the above described track following, the Kalman Filter and the calculation of the validation region for hits.

Assignment of new hits is done step by step at each detector station. After the track propagation to the next station possible hits are attached and track parameters are updated by the Kalman Filter. For the attachment of hits a validation gate is calculated in order to allow for a high degree of confidence in the hit-to-track assignment. The validation gate is defined based on the residual vector r (distance between fitted track and the hit) and the residual covariance matrix R . In the context of Kalman-based tracking filters, a validation gate can be expressed as $v = rR^{-1}r^T < d$. The cut value d is chosen such that a defined probability of rejecting the correct hit is achieved, here this probability is chosen to be 0.001. Values for d can be taken from χ^2 tables in dependence on the number of effective degrees of freedom. Here the effective degree of freedom is 1 for a straw tube detector hits and 2 for hits from pads in a GEM detector. The algorithm takes into account possibly missing hits due to detector inefficiencies, dead zones in the detector, inefficiency of hit finder algorithm etc.

The two methods which can be chosen for hit assignment to tracks differ in the way how a situation is dealt with in which several hits lie within the validation gate. In case of the branching method, a new track branch is created for each hit lying within the validation gate. Since the number of branches can grow exponentially, the χ^2 value is calculated for each track branch and unlikely ones are rejected. Also for each input track seeds number of created branches is calculated and if it exceeds the limit than the tracking continues using nearest neighbor approach. For the second method no track branches are created. The nearest neighbor method attaches the hit with the smallest v , if lying in the validation region at all.

Vertex determination

For each reconstructed MUCH track, the primary vertex determination has already been done by the associated STS track.

MUCH Reconstruction Performance

After track finding, so called clone tracks (consisting of a very similar set of hits) and ghost tracks (consisting of a random set of hits) have to be rejected while keeping correctly found tracks with high efficiency. The selection algorithm works in two steps. First, tracks are sorted by their quality which is defined by the track length and χ^2 . Then, starting from the highest quality tracks all hits belonging to a track are checked. In particular, the number of hits shared with other tracks is calculated and the track is rejected if more than 15% of the hits are shared. The results presented here are based on studies performed with standard simulations for central Au + Au collisions at 25 A GeV beam energy. Events were generated with the UrQMD event generator [38]. In order to enhance statistics and investigate the MUCH response to primary muons, ten J/ψ particles decaying into $\mu^+ \mu^-$ pair were embedded into each UrQMD event. The SIS300 detector setup has been used for simulations.

The performance of the algorithms was obtained using information from the Monte Carlo input. During the efficiency calculation the level of correspondence between the found and simulated tracks is estimated. A track is defined as correctly found if it has

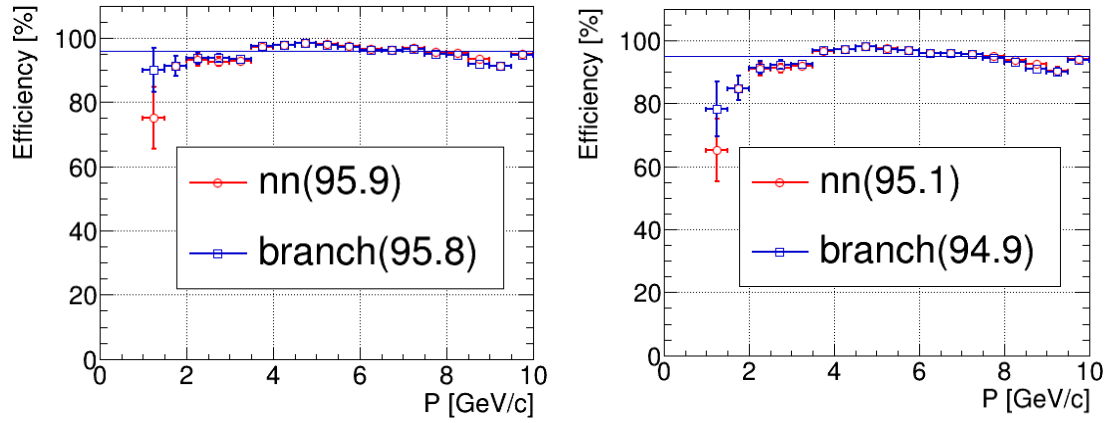


Figure 7.21: Track reconstruction efficiency for primary muon tracks from J/ψ as a function of track momentum for two tracking algorithms: nearest neighbor (red) and branching (blue). Left plot shows MUCH tracking efficiency, right plot shows STS-MUCH tracking efficiency. Horizontal lines represent numbers integrated over momentum.

more than 70% of hits from one Monte-Carlo track, otherwise a track is defined as ghost track. The track reconstruction efficiency is defined as $\epsilon_{track} = N_{reconstructed}/N_{accepted}$. $N_{reconstructed}$ is the number of correctly found tracks after reconstruction, $N_{accepted}$ is the number of reconstructable tracks in the MUCH acceptance, i.e. tracks that have at least 6 detected hits in the MUCH. Results shown here are for muon tracks since these are the most important for the muon simulations.

Fig. 7.21 shows the track reconstruction efficiency in dependence on momentum for MUCH and global tracking efficiency for STS-MUCH for 25AGeV beam energy. The MUCH track reconstruction efficiency integrated over the momentum range 0-10GeV/c is 95.9% for nearest neighbor method and 95.8% for branching method. The mean efficiency for tracking in STS-MUCH is 95.1% for nearest neighbor and 94.9% for branching method. Both methods show the same efficiency but nearest neighbor approach have some advantages: it is easier to implement and it is faster. This method was used by default in event reconstruction.

7.3.4 Muon identification and analysis

From the global reconstructed tracks, we apply a set of cuts at the analysis level to identify muon tracks likely to be originated from J/ψ . The aim is to reduce background

due to non-muonic tracks and muons from weak decays of pions and kaons. The cuts which have been used on reconstructed tracks for selection of muon candidates are (a) from STS: number of hits in STS and χ^2 of STS segment of the track and (b) from MUCH: number of much layers, χ^2 of the MUCH segment of the track. Additionally, a cut on χ^2_{vertex} is also applied. Based on the separation power of these cuts, we obtain a set of final cuts that have been used in this analysis for selection of muon candidates. It should be noted that for selection of muons from low-mass vector mesons and charmonia, the numbers of MUCH layers in a track are taken to be different. Muons originating from the decay of J/ψ are relatively harder and thus expected to cross the full absorber and reach the last station (trigger station). For selecting track candidates for J/ψ the track should have at least 16 MUCH hits. On the other hand tracks coming from lmvms are much softer they are expected to stop inside the last 100 cm thick iron block. Hence for them the required number of MUCH hits dose not exceed 15.

We have performed various tests using MC data to evaluate the performance of MUCH. One of the first tests performed was to test the survival of different types of primary and secondary particles with the variation of number of hits in STS and χ^2 . As there is no muon from UrQMD output, decay muons are present only in the secondary samples. It is seen that the use of a cut using minimum 6 STS hits and χ^2 less than 2.0 removes most of the pions and other particles without removing muons significantly. It should be mentioned that for the discussions to follow, final efficiency results are obtained after the use of final cuts that is aimed at reducing the background in addition to increased efficiency. The cuts used therefore works as the effect of absorber in addition to acceptance and track finding. The efficiency results obtained in subsequent discussions should be viewed in that context when compared with the results shown in previous section while describing tracking efficiency.

Each reconstructed muon track satisfying the above set of cuts are now selected for di-muon invariant mass analysis. Each selected track is represented by its 4-momentum vector:

$$P_\mu = (E_\mu, \vec{p}_\mu) \quad (7.4)$$

where $E_\mu = \sqrt{m_\mu^2 + \vec{p}_\mu^2}$.

The di-muon 4-momentum vector can be constructed from the 4-momentum vector of the single muon tracks and can be written as:

$$P_{\mu_1\mu_2} = P_{\mu_1} + P_{\mu_2} = (E_{\mu_1} + E_{\mu_2}, \vec{p}_{\mu_1} + \vec{p}_{\mu_2}) \quad (7.5)$$

From this one can construct the invariant mass (m_{inv}) of the di-muon pair, which due to energy-momentum conservation should be equal to the mass of the J/ψ . The invariant mass formula is given by:

$$m_{inv}^2 = P_{\mu_1\mu_2}^2 = 2m_\mu^2 + 2(E_{\mu_1}E_{\mu_2} - \vec{p}_{\mu_1} \cdot \vec{p}_{\mu_2}) \quad (7.6)$$

where $m_\mu = 105$ MeV is the rest mass of the muon. Being norm of a 4-vector m_{inv} is invariant under Lorentz transformation. Apart from the pair mass, the other fundamental di-muon kinematic variables are the pair p_T , pair rapidity (Y) and the decay/opening angle ($\theta_{\mu_1\mu_2}$) defined as the angle between \vec{p}_{μ_1} and \vec{p}_{μ_2} . Neglecting the muon mass in Eq 7.6, one obtains,

$$m_{inv} \simeq \sqrt{2p_1p_2[1 - \cos\theta_1\cos\theta_2 - \sin\theta_1\sin\theta_2\cos(\phi_1 - \phi_2)]} \quad (7.7)$$

where p_i , θ_i and ϕ_i are the magnitude of 3-momentum, polar and azimuthal angles of the single muon tracks.

From the 4-momentum conservation the pair p_T can be written as

$$p_{T,\mu_1\mu_2} = \sqrt{p_{x,\mu_1\mu_2}^2 + p_{y,\mu_1\mu_2}^2} \quad (7.8)$$

where

$$p_{i,\mu_1\mu_2} = p_{i,\mu_1} + p_{i,\mu_2}; (i = x, y, z) \quad (7.9)$$

On the other hand the pair rapidity in the laboratory frame takes the form

$$Y_L = \frac{1}{2} \log\left(\frac{E + p_z}{E - p_z}\right) \quad (7.10)$$

where E and p_z denote the pair energy and longitudinal momentum in the laboratory frame. One can easily get the pair rapidity in the centre of mass frame of the collision (Y^*) using the following relation

$$Y_L = Y^* + Y_{CM} \quad (7.11)$$

where Y_{CM} is the rapidity of the centre of mass system in the laboratory and can be expressed as

$$Y_{CM} = \frac{1}{2} \log\left(\frac{1 + \beta_c}{1 - \beta_c}\right) \quad (7.12)$$

where β_c is the velocity of the center of mass of the collision system in the laboratory and can be calculated as

$$\beta_c = \frac{|\vec{P}_{lab}|}{E_{lab}} = \frac{|\vec{P}_{beam}|}{E_{beam} + m_{tgt}} \quad (7.13)$$

where \vec{P}_{beam} and E_{beam} are projectile momentum and energy and m_{tgt} is the mass of the target. For 25 A GeV Au+Au collisions, we have $Y_{beam} = 3.99$ and $Y_{CM} = 1.99$.

Kinematics Resolution

In general the kinematic resolutions the di-muon experiments are governed by three factors:

- the multiple scattering of the muons in the target and the hadron absorber
- the energy loss of the muons in the hadron absorber
- the proper error of the measurement in the tracking chambers

The last one being negligible compared with the previous two. Now, one novel feature of the CBM experiment compared to the previous and existing experiments is that the full tracking will be performed in the STS detector system upstream to the absorber. Hence the momentum measurements will not be affected by the multiple scattering or energy loss effects inside the absorber. Also the target thickness of CBM

is much smaller ($1\%\lambda_I$) compared to the existing measurements (for example the target thickness in NA50 experiment was varied between $7-30\%\lambda_I$), which also helps to reduce the multiple scattering and thus improve upon the momentum resolution. Under such conditions, the momentum resolution will be considerably affected by magnetic field only. Note that for a dipolar magnetic field of strength B and extended over a length L , the momentum resolution of a track having momentum p can be written as:

$$\frac{\Delta p}{p} \propto \frac{p}{BL^2} \quad (7.14)$$

With the existing dipole magnet designed for tracking, the momentum resolution of the muon tracks are $\frac{\Delta p}{p} \sim 1\%$. So far as di-muon mass resolution is concerned, note that from Eq. 7.6, neglecting the muon mass, we can write

$$m_{inv}^2 = 2p_{\mu 1}p_{\mu 2}(1 - \cos(\theta_{\mu 1\mu 2})) \quad (7.15)$$

where the symbols carry their usual meanings. Since the average single momentum strongly increases with mass, the multiple scattering which contributes to the angular resolution ($\Delta\theta_{\mu 1\mu 2}$) is more important at low masses and has negligible effect in the high mass (eg: J/ψ , ψ') regime. On the other hand energy loss of the single muons has a stronger contribution which in our case is also not very prominent as explained above. Neglecting the angular resolution, we can estimate the expected mass resolution as:

$$\frac{\Delta m_{inv}}{m_{inv}} = \frac{\Delta p_{\mu}}{\sqrt{2}p_{\mu}} \quad (7.16)$$

which comes out to be 0.7%.

7.4 Physics performance studies

7.4.1 Input

Simulations for the optimization of the detector design in the di-muon measurement setup have been performed within the *cbmroot* framework that allows full event simula-

tion and reconstruction. Apart from cbmroot, the event generators PLUTO [319] and UrQMD3.3 [320] have been used for generating signals and background events, respectively, as will be detailed below.

J/ψ phase space distribution

PLUTO generates the J/ψ mesons following a thermal fireball model with thermal m_T and Gaussian rapidity distributions in the centre of mass frame of the collision. The p_T/m_T distributions are generated according to the form:

$$\frac{dN}{m_T dm_T} = \frac{dN}{p_T dp_T} = m_T K_1\left(\frac{m_T}{T}\right) \quad (7.17)$$

where $m_T = \sqrt{(p_T^2 + m^2)}$, with m being the particle rest mass, denotes the transverse mass. K_1 denotes the Bessel function of second kind and first order in $\frac{m_T}{T}$:

$$K_1\left(\frac{m_T}{T}\right) = \frac{e^{-(m_T/T)}}{\sqrt{(m_T/T)}} P_6(T/m_T) \quad (7.18)$$

where P_6 is a polynomial of order 6. The inverse ‘slope’ parameter T can be identified with the kinetic freeze-out temperature T_f , at which particles decouple from the fireball.

The rapidity distributions are generated in the centre of mass frame using Gaussian function with a mean $\mu_y = 0$ and width σ_y as

$$\frac{dN}{dy} = \exp\left(\frac{-y^2}{2\sigma_y^2}\right) \quad (7.19)$$

where y denotes the J/ψ rapidity in the centre of mass frame.

T_f and σ_y are the free parameters, whose values are required to be set. Unfortunately, there is not data on J/ψ production in heavy-ion collisions below 158 A GeV, which could have otherwise guided our choice of input parameters. The existing data on J/ψ production from the $p + A$ collisions, at FAIR energies are also based on inclusive measurements rather than differential distributions. In absence of any experimental guidance we go by the following arguments. The NA50 Collaboration at SPS measured the m_T spectra of J/ψ and ψ' in 158 A GeV Pb+Pb collisions. The distributions were

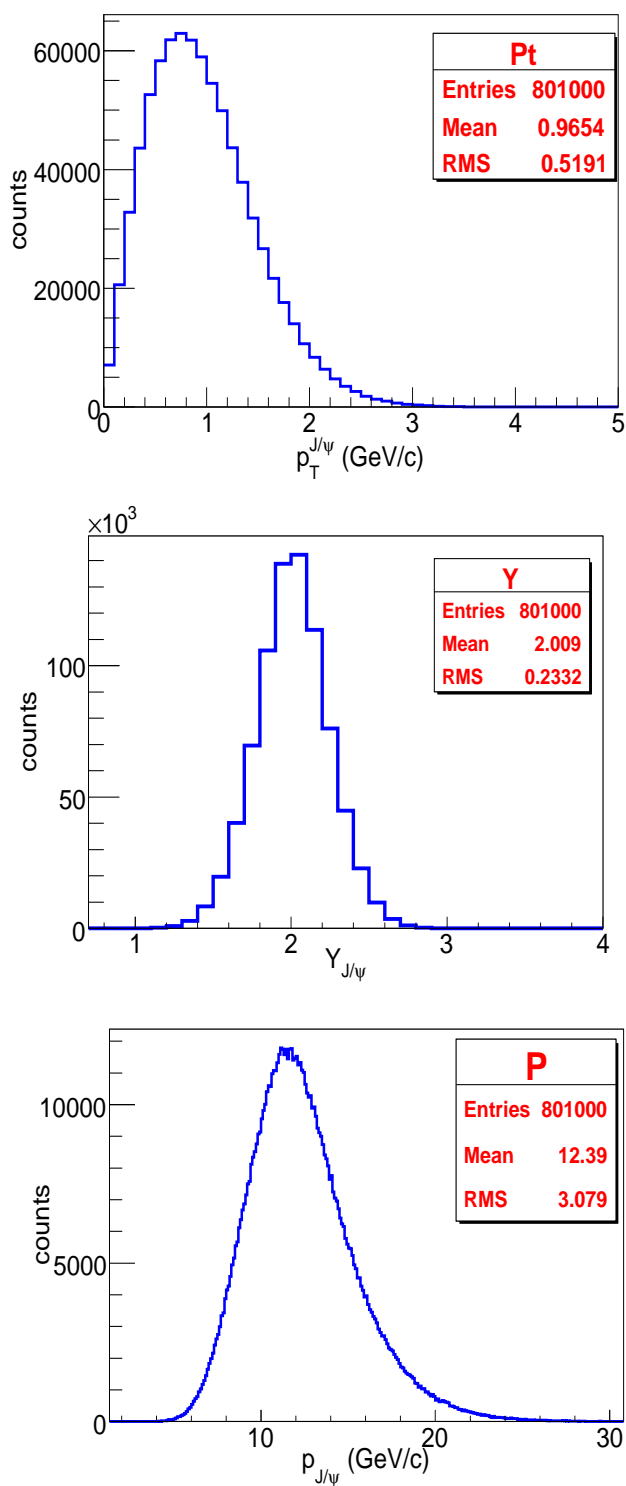


Figure 7.22: Input distributions of different kinematic variables for J/ψ as obtained from PLUTO. The p_T distribution is shown at the top and rapidity distribution in the laboratory frame is shown in the middle panel. The bottom panel contains the J/ψ 3-momentum distribution in the laboratory frame. Due to boost in the forward direction, $p_{J/\psi}$ is much larger than $p_T^{J/\psi}$.

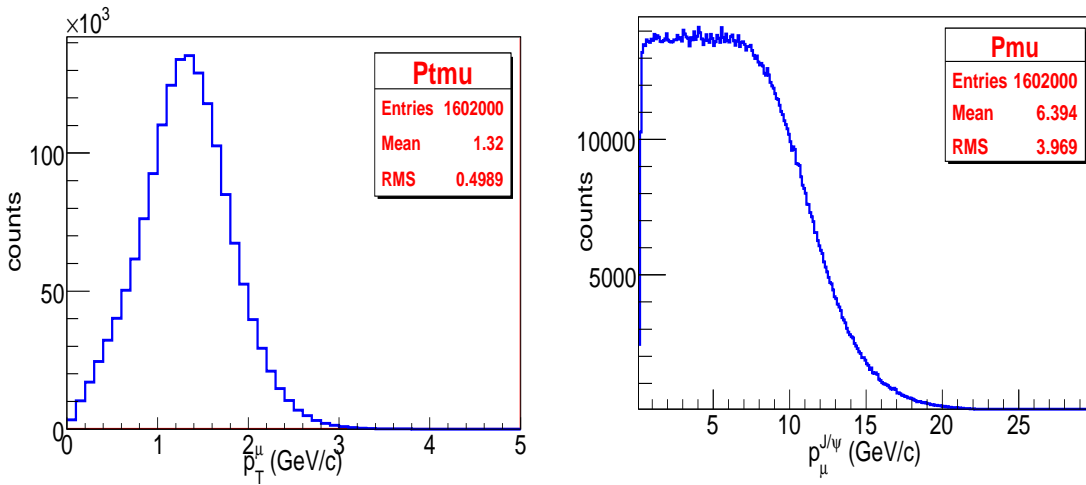


Figure 7.23: Input momentum distributions of the single muons generated from the decay of J/ψ . Left figure shows the p_T spectra and the right figure shows the 3-momentum spectra of the muons.

found to be fitted with a thermal distribution as given in Eq. 7.17, with an inverse slope parameter $T^* \simeq 220$ MeV. Subsequent analysis within a hydrodynamical model of QGP expansion and hadronization revealed that the data could be reproduced with a common freeze-out temperature $T_f \simeq 170$ MeV and average collective transverse expansion velocity $\bar{v}_T \simeq 0.2$. On the other hand the equilibrium hadron gas (HG) model describes remarkably well the hadron multiplicities measured in $A + A$ collisions at top SPS and RHIC energies. The extracted hadronization temperature parameter is similar for both energies $T_H = 170 \pm 10$ MeV. It was thus argued that unlike the lighter particles (eg: pion), the kinetic freeze-out of the J/ψ and ψ' mesons takes place directly at the hadronization, after the transition of the QGP to the hadron gas, due to their large mass and small hadronic cross sections. At RHIC energies ($\sqrt{s_{NN}} = 200$ GeV), T_f was assumed to be the same in accordance with T_H whereas the transverse hydrodynamic flow was expected to be stronger. If T_f remains the same as we go down from top RHIC to top SPS energy, we can safely assume the same value of $T_f = 170$ MeV at FAIR as well. However at FAIR, dominant contribution of J/ψ production comes from primordial hard $N - N$ collisions and the statistical production of charmonia at hadronization is expected to be negligibly small. In other words J/ψ s are unlikely to get equilibrated and inherit the flow of the medium. We thus assume $\bar{v}_T = 0$ and $T_f = 170$ MeV to generate the transverse momentum distribution of J/ψ .

So far as rapidity distribution is concerned, σ_y is fixed at a given energy in the following way. The width of the pion rapidity distribution is estimated using Landau formula. Width of rapidity distribution for any heavier meson is decreased proportionally to the maximum rapidity with which such a meson can be produced for a given \sqrt{s} . Hence we have

$$\sigma_y^{J/\psi} = \sigma_y^\pi \times \frac{y_{max}^{J/\psi}}{y_{max}^\pi} \quad (7.20)$$

where following Landau's expression,

$$\sigma_y^\pi = \sqrt{\log(\sqrt{s}/2m_N)} \quad (7.21)$$

where m_N being the nucleon mass. The maximum rapidity for a particle of mass m is given by

$$y^{max} = \log(\sqrt{s}/m) \quad (7.22)$$

With the above formulation, the width of J/ψ rapidity distribution comes out to be $\sigma_y^{J/\psi} = 0.24$, for 25 A GeV Au+Au collisions. This above parametrization for generating rapidity distributions has been used by several experiments as it describes reasonably well the existing measurements. In Fig. 7.22, we have given the input transverse momentum (p_T), rapidity (y) and three momentum (p) distributions of the J/ψ mesons produced with the parameters $T_f = 170$ MeV and $\sigma_y^{J/\psi} = 0.24$. Another commonly used function for generating rapidity distributions is of the form $\frac{1}{\cosh^2(ay)}$ which is similar to a Gaussian distribution of width $\sigma_y = 0.75/a$. The J/ψ mass distribution is assumed to be a Dirac Delta function, with mass 3.097 GeV/ c^2 since its natural width ($\Gamma_{J/\psi} = 87$ KeV) is orders of magnitude smaller than the experimental resolution. It is also assumed that J/ψ is directly produced in the collision, without taking into account the fraction of events that come from the decay of the higher states. Once the J/ψ 's are produced they are decayed into di-muons following isotropic angular distributions. The input momentum distributions for the single muons decayed from J/ψ are shown in Fig. 7.23.

Table 7.2: Elementary nucleon-nucleon J/ψ production cross section (nb), in dimuon channel at 25 A GeV following different parameterizations

Schuler	E771	Lourenco	Scaling
0.066	0.063	0.062	0.065

Estimation of J/ψ multiplicity

Apart from the kinematic distributions, another quantity required for estimation of S/B ratio of J/ψ detection is the multiplicity of J/ψ production in 25 A Ge Au+Au collisions. PLUTO does not give any information on J/ψ multiplicity. The common practice in the CBM simulations is to pick up the multiplicity values for different signal particles from the HSD transport code. However instead of doing that we perform the following exercises to calculate J/ψ multiplicity in 25 A GeV Au+Au collisions at a given impact parameter \mathbf{b} . In chapter 3, we have made a survey of the different parameterizations available in literature, for inclusive J/ψ production in elementary NN collisions, as obtained from different fixed target experiments. The important parameterizations include the (i) Schuler parametrization from E672 Collaboration, (ii) parametrization from the E771 Collaboration (iii) parametrization given by Lourenco (iv) and finally the more recent parametrization for near threshold charmonium production based on scaling analysis. All of these parameterizations agree reasonably well with the existing data on inclusive J/ψ production in $p + A$ collisions in the FAIR energy domain. The mean values of σ_{NN} in the di-muon channel, as obtained from different parameterizations for a beam kinetic energy 25 A GeV is given in Table 7.2. As seen from the table all the above parameterizations predict nearly similar values of J/ψ cross sections in elementary collisions. For a conservative estimation of J/ψ multiplicity in heavy-ion collisions, let us choose $\sigma_{NN} = 0.062$ nb. Since at FAIR energies, J/ψ production will be dominated by initial hard scatterings, in absence of all possible medium effects the J/ψ multiplicity in 25 A GeV Au+Au collisions, at an impact parameter \mathbf{b} can be written as:

$$N_{J/\psi}^{Au+Au}(\mathbf{b}) = T_{AuAu}(\mathbf{b}) \times \sigma_{J/\psi}^{pp} \quad (7.23)$$

where, T_{AuAu} is the nuclear overlap function calculable using Glauber model. At large impact parameter, not every encounter of two nuclei leads to an inelastic collision.

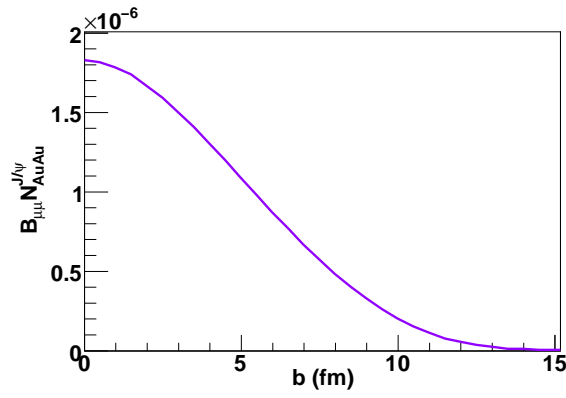


Figure 7.24: Variation of J/ψ multiplicity in the di-muon channel with collision impact parameter in 25 A GeV Au+Au collisions.

Hence to compute the multiplicity, one needs to consider the probability of an inelastic collision, given by, $p_{inel}^{Au+Au}(\mathbf{b}) = 1 - \exp(-N_{coll}(b))$, where $N_{coll}(b)$ is the number of binary collisions, defined as $N_{coll}(b) = \sigma_{NN} \times T_{AB}(b)$. σ_{NN} denotes the inelastic nucleon-nucleon inelastic cross section, and at FAIR energies we have assumed $\sigma_{NN} \sim 32$ mb. The impact parameter dependence of J/ψ multiplicity in 25 A GeV Au+Au collisions is given in Fig. 7.24. J/ψ multiplicity in the di-muon channel (i.e. yield times branching ratio) in purely central Au+Au collisions is $N_{J/\psi}(b=0) = 1.83 \times 10^{-6}$. Our multiplicity values are somewhat larger than that obtained with HSD model. In a minimum bias Au+Au collision, the average J/ψ multiplicity is given by

$$N_{J/\psi}^{Au+Au} = \frac{\int d^2b p_{inel}^{Au+Au} N_{J/\psi}(\mathbf{b})}{\int d^2b p_{inel}^{Au+Au}} \quad (7.24)$$

This comes out to be

$$\langle N_{J/\psi} \rangle^{Au+Au} = \sigma_{pp}^{J/\psi} \langle T_{AuAu} \rangle = 62.94 \times \sigma_{pp}^{J/\psi} \quad (7.25)$$

where, $\langle T_{AuAu} \rangle = 62.94 \text{ fm}^{-2}$. Substituting $\sigma_{pp}^{J/\psi} = 0.062$ nb (1 nb = 10^{-7} fm²), the J/ψ multiplicity in 25 A GeV minimum bias Au+Au collisions comes out to be 3.9×10^{-7} .

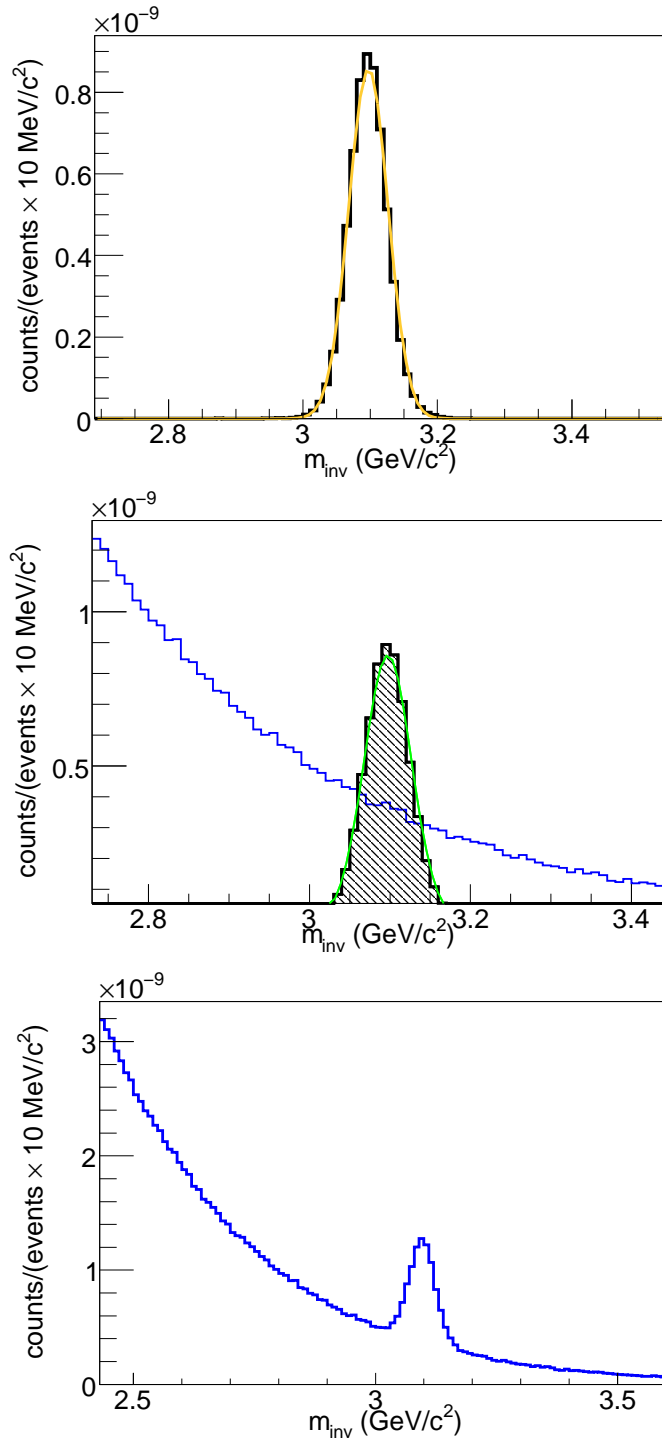


Figure 7.25: Reconstructed invariant mass spectra of J/ψ mesons in 25 A GeV central Au+Au collisions. Top panel shows the pure J/ψ signal, middle panel shows the signal superposed on the combinatorial background and the bottom panel depicts the total spectra where properly weighted signal and background are added together.

Table 7.3: Dependence of J/ψ reconstruction efficiency and S/B ratio on various track selection cuts

Much hits	STS hits	χ_{vertex}^2	χ_{STS}^2	χ_{Much}^2	$\epsilon_{J/\psi}(\%)$	S/B	$\sigma_{J/\psi}$ (MeV)
16	4	3.0	3.0	3.0	24.5	0.35	29.1
16	5	3.0	3.0	3.0	24.26	0.362	28.9
16	6	3.0	3.0	3.0	23.77	0.41	28.7
16	7	3.0	3.0	3.0	22.64	0.51	28.3
16	7	3.0	3.0	3.0	22.64	0.51	28.3
17	7	3.0	3.0	3.0	20.74	0.59	28.2
17	6	3.0	3.0	3.0	21.76	0.474	28.73
17	7	3.0	3.0	2.0	17	0.93	28.13
17	7	3.0	3.0	2.0	17	0.93	28.13
17	7	3.0	2.0	2.0	16.73	0.94	28
17	7	2.0	2.0	2.0	12.54	1.08	27.4
17	7	2.0	1.5	2.0	12.22	1.11	27.92
17	7	2.0	1.5	1.5	7.53	1.57	27.72
17	7	1.5	1.5	1.5	5.44	1.6	27.4
16	6	1.5	1.5	1.5	6.16	1.35	28.3
16	6	2.0	2.0	2.0	14.3	0.91	27.7
17	6	2.0	2.0	2.0	13.16	0.95	27.6

7.4.2 Results for SIS-300 collisions

In this section we give the final results of our feasibility study on J/ψ detection via di-muon channel in 25 A GeV Au+Au collisions at FAIR. Note that the measurement of J/ψ mesons is favored by the absorber technique as the decay muons from charmonium exhibit harder momentum spectra compared to those from ρ or ω mesons, and, hence, are much less absorbed.

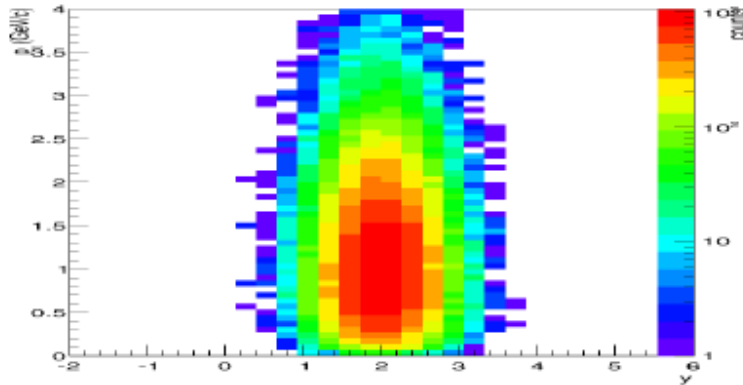


Figure 7.26: Phase space distribution of the reconstructed J/ψ mesons, in $Y - p_T$ plane, for 25 A GeV central Au+Au collisions.

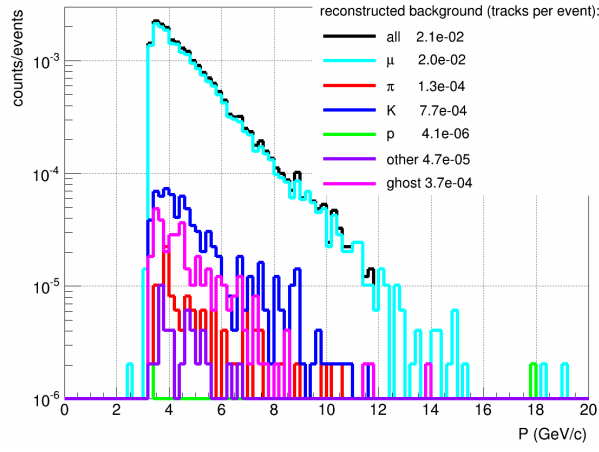


Figure 7.27: Composition of the reconstructed background tracks in 25 A GeV central Au+Au collisions. Only those tracks are selected with satisfy the required criteria for J/ψ analysis (see text for details).

The two quantities required to quantify the performance of the CBM muon set up are the J/ψ reconstruction efficiency and the signal-to-background (S/B) ratio. The J/ψ reconstruction efficiency is defined as the ratio of the numbers of the reconstructed and generated Monte-Carlo J/ψ . The di-muon efficiency is related to the reconstruction efficiency of the single muon tracks satisfying all the specified reconstruction and selection cuts for J/ψ analysis. Reconstruction of single muons is directly related to the chamber detection efficiency. If ϵ_μ is the efficiency for single muon tracks originated from J/ψ , the J/ψ detection efficiency can be written as:

$$\epsilon_{J/\psi} = \epsilon_{\mu^+} \times \epsilon_{\mu^-} \quad (7.26)$$

Use of harder track selection cuts results in decrease of $\epsilon_{J/\psi}$ but helps to increase the S/B ratio by reducing the background. Higher reconstruction efficiency ensures a larger data sample over a given time period whereas S/B represents the actual figure-of-merit of any measurement. One thus has to find an optimized choice between these two quantities. In order to do so, we have calculated the J/ψ reconstruction efficiency and S/B ratio for a set of values of the track selection cuts as shown in Table 7.3. The optimum results ($\epsilon_{J/\psi} = 12.12\%$ and $S/B = 1.11$) are obtained for selected tracks having ≥ 7 sts hits, ≥ 17 much hits, $\chi_{vertex}^2 < 2.0$, $\chi_{STS}^2 < 1.5$ and $\chi_{Much}^2 < 2.0$. These tracks selected with optimal set of analysis cuts are now projected to the TOF plane

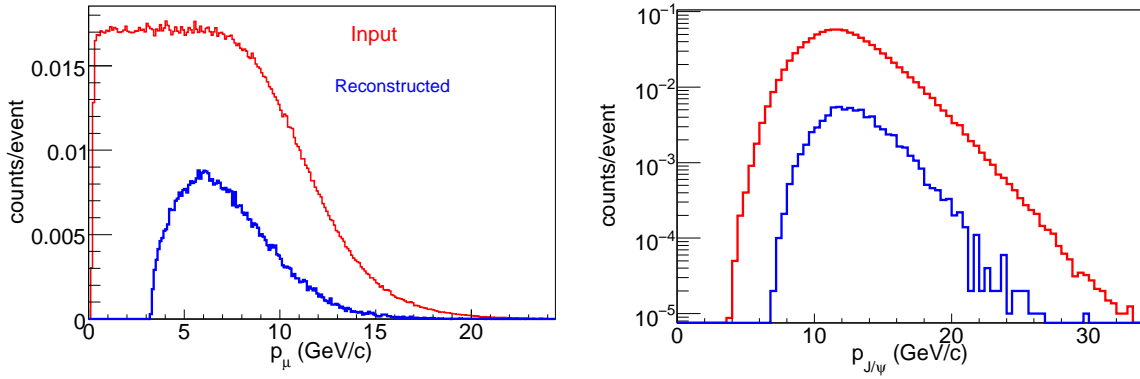


Figure 7.28: Momentum distribution of the reconstructed signal muons (left) and J/ψ mesons (right), in 25 A GeV central Au+Au collisions. Both the distributions are superposed on their respective input distributions.

where we apply the TOF mass cut as the final selection cut. The resulting invariant mass spectra are shown in Fig. 7.25. The top panel shows the pure signal, middle panel depicts the properly scaled invariant mass spectra separately for signal and background superposed on each other. The J/ψ peak is clearly visible and can be nicely fitted with a symmetric Gaussian function. The bottom panel shows the total spectra in the J/ψ mass region where signal and combinatorial background are added together according to their respective weights. The reconstruction efficiency and S/B ratio are 5% and 2 respectively. The mass resolution comes out to be $\sigma_{J/\psi} = 28$ MeV. The basic important features of the invariant mass spectra are the following:

- The input Dirac Delta function for J/ψ mass distribution degenerate into Gaussian distribution at the reconstruction level. This can be attributed to the finite momentum (and angular resolution) of the single muon tracks. Note that the mass distribution is a pure Gaussian without having non symmetrical mass dependent dispersion tails even at a region away from the pole mass. This itself is a novel feature compared to the previous experiments like NA50 and NA60 at SPS, where the muon momenta were measured after they pass through the hadron absorber and J/ψ reconstructed mass distributions were found to be described by asymmetric Gaussian distributions with increasing smearing tails. The observed asymmetry between Right and left tails was caused by two effects: while multiple scattering inside the hadron absorber affected in the same way, both right and left tails, the

energy loss ($\frac{dE}{dx}$) affects more the left tail, since muons energy whose straggling corresponds to the Landau tail of energy loss is not totally compensated in the reconstruction process, just a mean correction was performed. On the other hand, in case of CBM experiment the muon momentum is fully determined at STS where they least affected by either of the above effects due to low material budget. This the reconstructed mass shapes do not show any taily nature.

- The J/ψ mass resolution is found to be $\sigma_{J/\psi} \sim 28$ MeV which is factor of 4 better compared to NA50 ($\sigma_{J/\psi}(NA50) \sim 100$ MeV) and factor of 3 better compared to NA60 ($\sigma_{J/\psi}(NA60) \sim 70$ MeV). In NA50 experiment, the complete momentum determination was performed in the muon spectrometer placed after the hadron absorber which in turn results is poor momentum and angular resolution of the reconstructed tracks. In NA60 this situation was improved by additional momentum measurement in the silicon vertex telescope upstream the absorber and momentum matching between the reconstructed tracks before and after the absorber. In CBM complete momentum determination is performed upstream the absorber in the STS detector system which results in a momentum resolution of $\sim 1\%$. From Eq. 7.16 we see that such a good momentum resolution would approximately lead to a mass resolution $\sigma \sim 0.7 \times m_{J/\psi} \sim 20$ MeV.
- We have not simulated the 2s charmonium state ψ' . However J/ψ mass resolution of the order of 30 MeV clearly indicates that J/ψ and ψ' will be completely separable in the CBM muon set up.
- The S/B ratio is calculated by estimating the background within $\pm 2\sigma$ around the signal mass peak. Improvement in σ itself also helps to improve the S/B ratio.

The acceptance plot of the reconstructed J/ψ mesons is shown in Fig. 7.26 illustrating that the majority of the phase-space is covered. Let us now analyze the results in some more detail. Note that in all our calculations the background continuum comes from the combinatorial contribution only. The composition of the reconstructed background tracks per event for J/ψ mesons from central Au+Au collisions at 25 A GeV is shown in Fig. 7.27. The background is completely dominated by muons from weak decays of

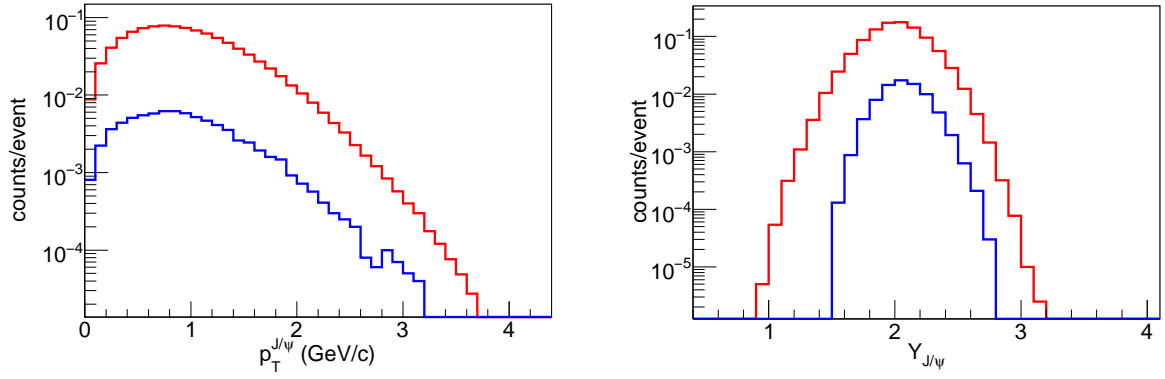


Figure 7.29: Transverse momentum and rapidity distributions of the reconstructed J/ψ mesons, in 25 A GeV central Au+Au collisions. The corresponding input distributions are also plotted in the same canvas.

pions and kaons. Next to understand the effect of absorbers on the signal muons, we plot in Fig. 7.28 reconstructed momentum distribution of the single muons originated from the decay of J/ψ along with their input distribution obtained from PLUTO. As evident from the figures the hadron absorbers introduce a threshold of $p_\mu^{min} = 3.2$ GeV/ c on the single momentum level below which all the signal muons are absorbed. The corresponding threshold momentum for J/ψ is $p_{J/\psi}^{min} \sim 6.5$ GeV/ c below which no J/ψ is reconstructed. Since the absorbers are placed along the forward direction, they induce the cut on the longitudinal component rather than the transverse component of the momentum. This can be clearly visualized in Fig. 7.29, where we have separately shown the p_T and rapidity distribution of the reconstructed J/ψ mesons. The p_T range for input and reconstructed mesons are identical down to $p_T = 0$, where as in case of rapidity distribution (reflecting the p_Z distribution) the low rapidity J/ψ mesons are absorbed. Rapidity of the reconstructed J/ψ correspond to the range: $< 1.5 < Y_{J/\psi} < 2.8$ in the laboratory frame. Following Eq. 7.12, the rapidity of the centre-of-mass at a beam energy of 25 A GeV is $Y_{CM} \sim 2.0$. Hence from Eq. 7.11, rapidity coverage of the J/ψ mesons in the centre-of-mass frame appears to be $-0.5 < Y_{J/\psi}^* < 0.8$, which reflects the combined effects of finite geometrical acceptance of the CBM muon set up as well as the hadron absorbers that absorbs the low momentum muons as well.

In addition to the central collisions it might also be interesting to look at the J/ψ invariant mass spectra in 25 A GeV minimum bias Au+Au which will be measured experimentally in practice. In Fig. 7.30 we have shown the total invariant mass spectra

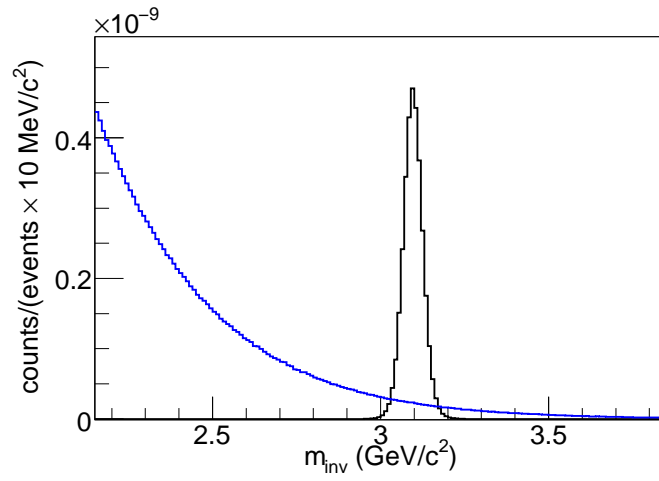


Figure 7.30: Reconstructed invariant mass spectra of J/ψ in 25 A GeV minimum bias Au+Au collisions. Properly normalized signal and background spectra are superposed on each other.

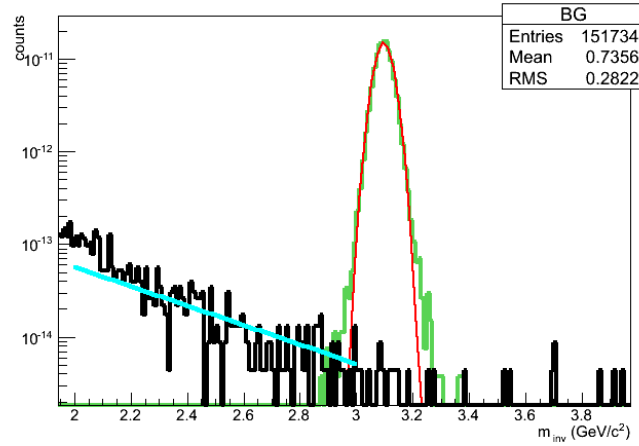


Figure 7.31: Reconstructed invariant mass spectra of J/ψ in 30 GeV p+Au collisions. Such measurements are an integral part of the SIS-100 physics program.

in the J/ψ mass region. The reconstruction efficiency and S/B respectively comes out to be 11.3% and 10. The mass resolution is found to be 30 MeV.

7.4.3 Results for SIS-100 collisions

In addition to the Au+Au collisions, we have also studied the feasibility of J/ψ measurements in $p + A$. Measurements of J/ψ production in $p + A$ collisions is extremely important in order to study the cold nuclear matter effects which are required to be isolated in case of heavy-ion data to identify the genuine hot and dense medium effects. To study $p + A$ collisions we have chosen 30 GeV p+Au collisions as our reference system,

which is an important part of SIS-100 physics program. Fig. 7.31 depicts the invariant mass distributions for J/ψ mesons in the SIS100 configuration (see Fig. 7.10) for p+Au collisions at 30 GeV beam energy. The J/ψ reconstruction efficiency was found to be 30%. Even after processing of 5 million UrQMD events without signal, the background below the J/ψ peak region has been found to be extremely small. Therefore, the shape of the background shown in Fig. 7.31 has been estimated from a superevent analysis, and then fitted with an exponential function to the few background events obtained with an event-by-event analysis. In spite of the uncertainties in the estimation of background, the identification of J/ψ mesons in proton-nucleus collisions at top SIS100 energy seems to be easily feasible. It remains to be demonstrated how far one can go down in energy before losing the signal.

7.4.4 Estimation of J/ψ collection rate

After showing the feasibility of J/ψ measurements through di-muon channel in 25 A GeV Au+Au collisions it is now important to have an estimate of the J/ψ yield that will be collected over a given beam time period. In any experiment, the event rate (R_e) defined as the number of collisions per second, can be written as:

$$R_e = L_{in} \times \sigma_{inel} \quad (7.27)$$

where, L_{in} is the instantaneous luminosity of the beam delivered by the accelerator. In a fixed target experiment L_{in} can be defined as:

$$L_{in} = I_b \times n_T \times \Delta_T \quad (7.28)$$

where, n_T is the number density of the target and Δ_T denotes the target thickness. Thus using thicker targets one can increase the event rate. Instead of L_{in} , different experiments sometimes also quote their integrated beam luminosity (L_{int}) defined as $L_{int} = \int L_{in} dt$, where the time integration is over the entire data taking period. The number density of the target material can be calculated as:

$$n_T = (N_A \times \rho)/A_{target} \quad (7.29)$$

Thus substituting for n_T in Eq. 7.28 and using Eq. 7.1 in Eq. 7.27 one gets:

$$R_e = \frac{I_b \times L_T}{\lambda_I} \quad (7.30)$$

Now the FAIR accelerators are so designed to deliver proton beams of intensity $4 \times 10^{13}/s$ and Au beams of intensity $10^9 - 10^{10}$ ions/s. Note that these intensities are unprecedented and about 5 orders of magnitude higher in case of proton beams and 100 - 1000 times higher in case of the heavy-ions beams available at CERN-SPS machine. The thickness of the Au target as optimized through simulations is set to $250 \mu m$ for muon runs. Following Eq. 7.1, this would correspond to $1\% \lambda_I$ of Au target ($\lambda_I^{Au} \sim 2.4$ cm). Such a thin target (even thinner than the thinnest target for SPS) would surely help to avoid the re-interactions in the target. Thus the event rate (see Eq. 7.30) for Au+Au collisions, with a conservative estimation of beam intensity of 10^9 ions/s, comes out to be 10 MHz. The J/ψ multiplicity in the di-muon channel in 25 A GeV minimum bias Au+Au collisions is found to be 3.9×10^{-7} . Hence the J/ψ production rate in the di-muon channel at FAIR, in absence of any medium effect is around 3.9 per second. To calculate the number of detected J/ψ need to take into account the geometrical acceptance of the CBM detector system as well as the J/ψ reconstruction efficiency. We have seen that with a realistic design of the muon system, the product of geometrical acceptance and pair reconstruction efficiency comes out to be 11%. Hence the J/ψ collection rate at CBM will be $\sim 0.39 J/\psi$ per second. For a typical data taking period of 2 months (2 months $\sim 5.2 \times 10^6$ s) the total number of J/ψ collected in the di-muon channel, in absence of any medium effect will then be 2.02×10^6 . Similar estimates can also be made for J/ψ production in p+Au collisions. For a $250 \mu m$ thick Au target, the event rate in p+Au collisions is $4 \times 10^{11}/s$. On the other J/ψ production cross section in elementary N-N collisions in the di-muon is ~ 0.1 nb. The corresponding value of J/ψ multiplicity in 30 GeV p+Au collisions is $\sim 66 \times 10^{-8}$. Considering the 30% J/ψ reconstruction efficiency, the J/ψ yield in di-muon channel comes out to be $7.92 \times 10^4/s$.

Table 7.4: Basic features of J/ψ measurement by NA50 Collaboration at SPS [322].

Year	Energy (GeV)	Collision System	Sub-targets	Target thickness	Intensity (10^7 ions/sec)	$N_{J/\psi}$ ($\times 10^3$)
1995	158	Pb+Pb	7 (in air)	$17\%\lambda_I$	0.63	50
1996	158	Pb+Pb	7 (in air)	$30\%\lambda_I$	1.04	190
1998	158	Pb+Pb	7 (in air)	$7\%\lambda_I$	1.15	49
2000	158	Pb+Pb	7 (in vacuum)	$10\%\lambda_I$	1.46	129
1996 1998	450	p+A	Be, Al, Cu, Ag, W	$26 - 39\%\lambda_I$	40:130	350:800
1998 2000	450	p+A	Be, Al, Cu, Ag, W	$26 - 39\%\lambda_I$	8:25	80:180
2000	400	p+A	Be, Al, Cu, Ag, W, Pb	$26 - 39\%\lambda_I$	90:130	38:68

Hence for the same data taking period of 2 months, the typical number of J/ψ that will be collected in absence of any suppression effects is $\sim 4 \times 10^{11}$. However in practice J/ψ production in $p + A$ and in $A + A$ collisions at FAIR will be reduced than what has been estimated due to suppressions induced by cold nuclear matter effects and hot and dense matter effects in case of heavy-ion collisions. Depending on the magnitude of suppression the yield will be accordingly lower.

It might also be interesting to know how does the J/ψ yields estimated for CBM compare with the existing measurements from the NA50 Collaboration at SPS. The SPS ring had usually operated at two energies: 450 GeV, which corresponds to extraction of proton beams at 450 GeV incident beam kinetic energy and 400 GeV allowing the extraction of protons with 400 GeV and fully stripped Pb ions (Pb_{208}^{82+}) with 158 GeV per nucleon beam kinetic energy (note $E_A = (\frac{Z}{A}) \times E_p$, where E_A and E_p are the beam kinetic energies of the nucleus and proton respectively). For $A + B$ collisions, the intensity was $\sim 7 \times 10^7$ ions in a beam cycle of 19.2 s, and an effective spill of 4.8 s. The ion nominal intensity was limited by pile-up, which needed to kept under control to avoid re-interactions in the target which might finally lead to ambiguities in the energy measurements. Depending on the objective of the collision, NA50 experiment used several targets. For $p + A$ collisions, Be, Al, Cu, Ag, W and Pb targets were used. In Pb+Pb collisions, depending on the data taking period, a Pb sub-targets system was used: a single sub-target in the 1998 and 2000 runs and several ones in the 1995 and 1996 ones. The target thickness was varied between 7% and $30\%\lambda_I$ for heavy-ion runs

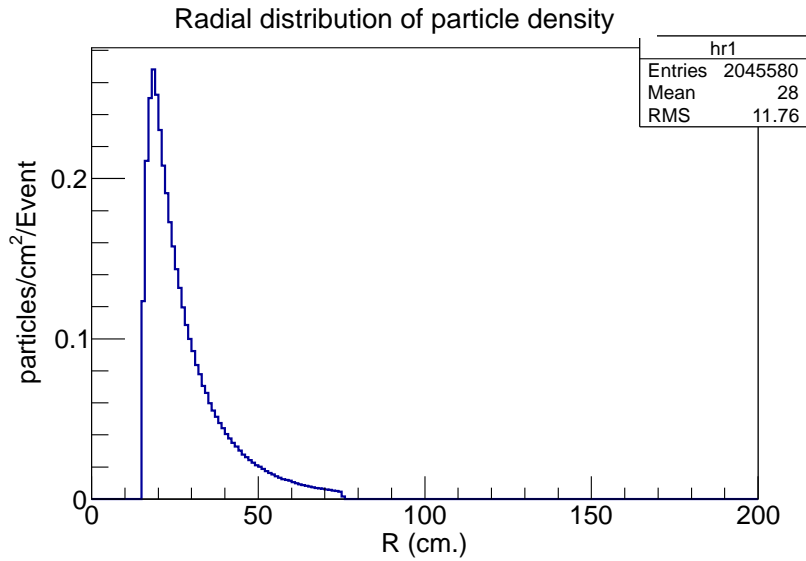


Figure 7.32: Radial distribution of the density of the MUCH points (MUCH points/cm²/event) in the first station (average over three layers), after 60 cm of carbon (chosen as the first absorber block), for 25 A GeV central Au+Au collisions.

and $26 - 39\% \lambda_I$ for $p + A$ runs. In Table 7.4 we summarize the basic features of J/ψ measurement by the NA50 Collaboration.

7.5 Data rate on chambers

The CBM experiment is designed to measure rare diagnostic probes of the fireball, and hence, will be operated at reaction rates of up to 10 MHz. This poses challenges with respect to the rate capability and radiation hardness on the muon chambers. We have studied two parameters in detail that are related to the rate capability: the particle density and the detector occupancy. The density of the Monte Carlo (MC) points on the much detectors i.e. the number of MUCH points per unit area per event on the chamber planes gives an estimate of the particle rate incident on the chamber planes. The particle density is maximum at the first station and reduces for the chambers downstream. In Fig. 7.32 we have plotted the radial distribution of MUCH points in the first MUCH station (average over the three layers). As input we have used 1000 central Au+Au collisions at 25 A GeV. For minimum bias collisions, the numbers will be around 25 % of the central values. As expected, the density is maximum near the beam pipe and falls off as we go to the edges. For 1 cm² pads, the envisaged maximum data rate in the

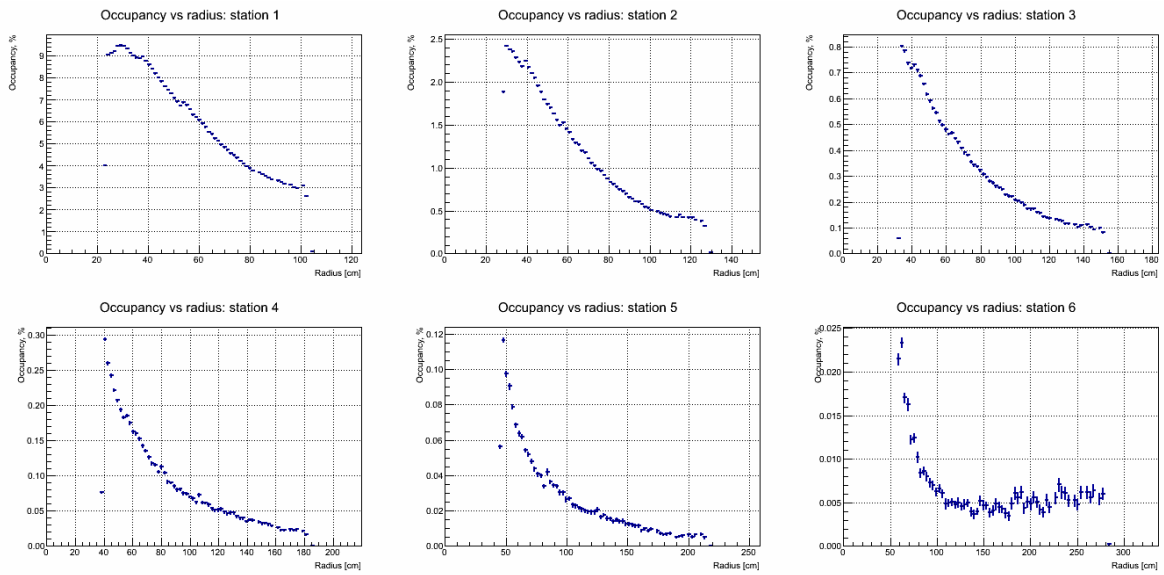


Figure 7.33: Radial distribution of occupancy for six stations of SIS300 MUCH geometry with trapezoidal modules. The plot is generated for central Au + Au collisions at 25 A GeV beam energy

central zone, for a peak event rate of 10 MHz will be $0.31 \times 0.25 \times 10 \text{ MHz} = 0.75 \text{ MHz}$, on the first station. After digitization, the ionization process (primary and avalanche) adds to the profile of much points and thereby increases the data volume accordingly. The data rate shown for 1 cm^2 pad reduces according to the pad size. The occupancy defined as the fraction of total number of pads fired per event gives an estimate of the actual data rate. In Fig. 7.33, we have shown the radial distributions of occupancy for trapezoidal modules, for all six stations of the SIS-300 geometry, for 25 A GeV central Au+Au collisions. Again for the self-triggered system, more useful quantity from the data rate requirement will be the occupancy for minimum bias events, which is roughly 2% at a region of the first station near the beam pipe. These quantities are extremely useful in designing the layout of the readout boards in the detector plane.

The number of pads fired in the first station is maximum due to the highest particle density. Ideally for a projective segmentation, if the pad area is projected according to the hit rate, then the occupancy should remain constant over the entire radial distance. In our case, we have taken a square pad approximation in which the length of the pad corresponds to 1 degree in azimuth. This therefore results in falling occupancy as shown in Fig. 7.33. However, even for beam energy of 25 A GeV the maximum occupancy at the first station is 8% and falling rapidly. The pad size therefore is close to what

is expected for a design value of 5% occupancy. In case of trapezoidal modules, where radially increasing pads of angular width 1 degree in azimuth is used, the maximum occupancy is observed in the first station, that translates into a peak data rate of 200 KHz, for minimum bias Au+Au collisions. Difference with the extrapolated value from Fig. 7.32, can be attributed to the implementation of actual pad area (which comes out to be factor of 10 down compared to 1 cm²) in the occupancy estimation as well as the inclusion of full detector response including ionization.

7.6 Trigger simulation with MUCH

We have seen above that at FAIR energies, J/ψ production cross sections are extremely small which drives the necessity for an extreme interaction rate of 10 MHz. The foreseen data acquisition (DAQ) system will be able to record events at a rate of 25 kHz. Thus, efficient on-line selection of events rich in J/ψ is mandatory. We have made an effort to develop an algorithm to trigger on J/ψ online [323] and the rejection of background events based on the information from a subset of the muon detectors only. It is envisaged that this algorithm could be applied on the data available using the First-Level Event Selection (FLES) algorithms running on the computer farm [324]. The scheme of the trigger logic is depicted in Fig. 7.34. Our aim is to select events on-line which contain muon pairs coming from charmonium decay. We have run the algorithm both in SIS-300 and SIS-100 MUCH geometries. For faster selection, we have used hits only from the 3 layers of the last station positioned after the 1 m thick iron absorber, which we call trigger station. Since our muon detection system is placed outside the magnetic field, high momentum muons coming from decay of J/ψ mesons will go approximately straight up to the last station. The present algorithm is based on following steps:

(a) Take 3 hits from the trigger station with one from each of the 3 layers and fit the hits with straight line both in X-Z and Y-Z plane passing through the origin (0, 0) i.e.
 $X = m_0 \times Z$; $Y = m_1 \times Z$

(b) Make all possible combinations

(c) Find χ^2 and apply cut on both χ_X^2 and χ_Y^2

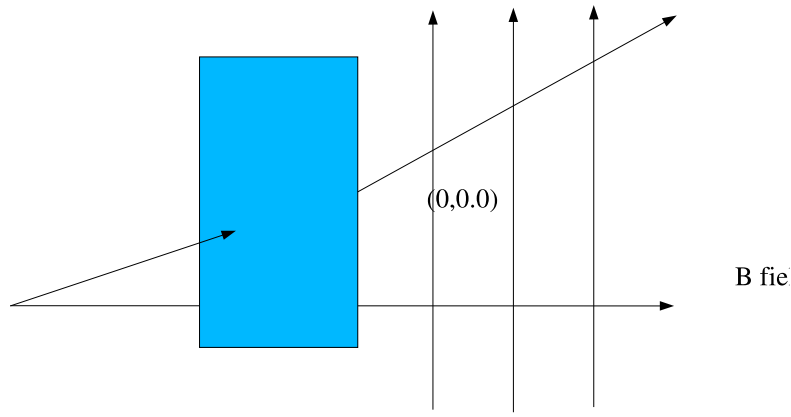


Figure 7.34: Schematic of the trigger logic

- (d) Hit combinations satisfying the cuts are called triplets.
- (e) Hit once used for formation of a valid triplet has not been used further
- (f) Find m_0 and m_1 of the fitted straight lines
- (g) Define a parameter $\alpha = \sqrt{(m_0^2 + m_1^2)}$
- (h) Apply a cut on α .

The cuts are applied in sequential order.

For estimating the performance of the proposed algorithm, we have simulated 80K minimum bias UrQMD events for 25 A GeV Au + Au collisions for simulating the background and 1K Pluto events for signals from J/ψ decayed into muons. The results for background suppression factors (BSF) and the J/ψ efficiency are shown in Table 7.5. In the table the specification of the cuts are as follows. Cut-1 demands that an event should have at least one triplet, whereas those events having two triplets satisfy cut-2. Cut-3 specifies that at least one of the two triplets satisfies the α cut, whereas cut-4 signifies that both the triplets satisfy the α cut. The J/ψ reconstruction efficiency is obtained after full reconstruction of tracks and measurement of area under the invariant mass peak. It has been found from the study on the effect of different trigger cuts on the acceptance of J/ψ that there is no significant change in the phase space coverage of the accepted J/ψ for the events accepted after application of trigger cuts. It has also been shown that a similar algorithm can be employed to select J/ψ enriched events at

Table 7.5: Efficiency and suppression factors for different cuts in trigger algorithm developed for selection of charmonium trigger in 25 A GeV minimum bias Au+Au collisions.

Cut	$\epsilon_{overall}(\%)$	Suppression factor
No cut	29.3	-
1	29.2	30
2	24.5	314
3	24.2	879
4	15.3	1430

SIS100 energy.

7.7 Summary

This chapter describes in detail the different aspects of the design simulation and physics performance of the MUCH system, of the CBM experiment at FAIR. The detector system is so designed to identify muon pairs which are produced in high energy heavy ion collisions in the beam energy range from 2 to 40 A GeV. In this thesis we particularly focus on the identification of muon pairs from J/ψ mesons that would populate the high mass region of the di-muon spectrum and believed to carry promising information on the occurrence of deconfinement transition. The experimental challenge for muon measurements in heavy ion collisions at FAIR energies is to identify low-momentum muons in an environment of high particle densities. The CBM strategy is to track the particles through a hadron absorber system, and to perform a momentum-dependent muon identification. This concept is realized by an instrumented hadron absorber, consisting of staggered absorber plates and tracking stations. The hadron absorbers vary in material and thickness, and the tracking stations consist of detector triplets based on different technologies. The MuCh system is placed downstream of the dipole magnet hosting the Silicon Tracking System (STS) which determines the particle momentum. In order to reduce pion and kaon weak decays into muons the absorber/detector system has to be as compact as possible.

Detailed simulations have been performed to optimize the detector system with respect to efficiency, signal-to-background ratio, and phase-space coverage. The event generator UrQMD and the transport code GEANT3 have been used within the CBM-

root framework to simulate for example the worst-case background scenario, i.e. central Au+Au collisions. As a result, the actual realistic design of the MuCh system consists of 6 hadron absorber layers (60 cm carbon and iron plates of 2 x 20 cm, 30 cm, 35 cm, and 100 cm thickness) and 6 gaseous tracking chamber triplets behind each iron slab. The tracking chambers are based micropattern gas detector (GEM) technology capable of handling high rates. The physics performance studies of the MuCh system are based on a realistic detector segmentation and response. Digitization and clustering algorithms have been developed in order to define the hits which then are used to reconstruct the particle trajectories. The trajectories in the MuCh are reconstructed by a track following method using the reconstructed tracks in the STS as seeds. The track reconstruction in the STS is based on the Cellular Automaton method. For track following from the STS into the MuCh the Kalman filter technique is used. Trajectories which do not point to the primary vertex or do not fit well to a certain number of hits are rejected in order to suppress weak decays and mismatches of tracks in the STS with tracks in the MuCh. The tracks which survive the quality cuts are used to calculate the combinatorial background. For the feasibility studies, the background is calculated for central Au+Au collisions using the UrQMD code. The signal muon pairs from decays of J/ψ mesons are imbedded in UrQMD events, and then reconstructed. For central Au+Au collisions at 25 A GeV the signal-to-background ratio for the J/ψ a value of $S/B=1.7$ is found whereas for minimum bias collisions at the same energy and for same colliding system the value is ~ 10 . At SIS100 energies, J/ψ mesons produced in 30 GeV p+Au collisions can be already identified even with a reduced configuration made up of 3 absorber layers and 3 tracking stations. Detailed simulation with realistic detector system thus clearly establishes the J/ψ measurements via di-muon channel in the FAIR energy collisions.

Chapter 8

Summary and discussions

The quantitative understanding of the rich phenomenology of strong interaction physics is a fascinating challenge for modern day fundamental research and the prime focus of the upcoming FAIR accelerator facility at GSI, Darmstadt, Germany. Relativistic heavy ion collisions in the FAIR energy domain will provide the unique possibility to create and investigate compressed nuclear matter in the laboratory and hence the experimental program is named as the Compressed Baryonic Matter (CBM) experiment. The main objective of the CBM experiment is to explore the phase structure of the strongly interacting matter in the region of moderate temperatures and extremely high net baryon densities. J/ψ suppression has long been recognized as an important signature for the occurrence of color deconfinement in nuclear collisions. Measurement of J/ψ suppression in the CBM environment has been identified as a potential probe to look for the signatures of deconfinement transition from hadronic to quark-gluon plasma phase at high baryon densities. Till date no measurement exists on J/ψ production in heavy ion collisions below the top SPS energy, primarily due to their low production cross sections. The CBM experiment at FAIR, is planning to perform for the first time, a detailed study of charmonium production in nuclear collisions, at beam energies $E_b = 10 - 40$ A GeV. The J/ψ mesons produced at an early stage of the collisions might help in characterizing the confining status of the highly compressed baryonic medium, anticipated to be produced in these collisions. Charmonium measurements at FAIR energies are particularly challenging due to the very low charm production cross section which requires heavy ion

beams with unprecedented high intensities and very fast detectors capable of handling high rates. J/ψ mesons will be detected at CBM via their di-lepton decay channel. As per present plan the experiment will take data both in di-electron (e^+e^-) and di-muon ($\mu^+\mu^-$) channels. A detector system is being developed to enable to di-muon measurements at FAIR. This thesis is dedicated to study the different aspects of charmonium physics at FAIR. The motivation of the present thesis work has been two fold: (i) to theoretically estimate the J/ψ production cross sections and (ii) to study the design simulation of the muon detector system and its physics performance for detection of J/ψ in the di-muon decay channel.

In chapter 1 of the thesis we have given a brief general introduction to the physics of quark-gluon plasma produced in relativistic heavy ion collisions. After a short discussion on the historical perspective of QGP studies we briefly mention about the contemporary understanding on the phases of strongly interacting matter. Next we discuss about the QGP production in relativistic heavy ion collision experiments. First we describe the space time evolution picture of the hot and dense fireball produced in the collision, next we mention about the different theoretical approaches to model the evolution dynamics which is followed by a small discussion on the different experimental facilities around the world, dedicated for the QGP study. We end the chapter with a discussion on some of the various signatures of QGP that has studied over the years.

Chapter 2 presents a general overview of the CBM experiment at FAIR. The outline of the FAIR accelerator facility is depicted first followed by the discussion on the different physics goals of the CBM experiment and the corresponding potential observables required to probe the high density matter anticipated at FAIR. The chapter ends with a brief account on the configuration of CBM experimental setup and each of its sub systems.

A non comprehensive review of the pioneering works available on literature related to the charmonium production in nuclear collisions is given in chapter 3. Starting with the simultaneous discovery of J/ψ mesons at BN and SLAC, we first give a brief account of the quarkonium spectroscopy in vacuum. This is followed by the short description of the spectral properties of charmonium in a thermal medium. The goal of this study is

find out the dissociation points of different quarkonium states inside a global medium in thermodynamic equilibrium. For a baryonless medium ($\mu_B \sim 0$), two methods are in vogue to compute the dissociation points of different quarkonium states. The first method is the potential model approach where the interaction potential of a static heavy $c\bar{c}$ pair is either directly configured phenomenologically or extracted from the lattice estimation of the free energy. The other method relies on the direct evaluation of the quarkonia spectral functions in the appropriate quantum channel as a function of temperature T and $c\bar{c}$ binding energy ω . Two methods give different values of quarkonium dissociation temperatures particularly for J/ψ . The status of the existing calculations to extend the problem of determining the dissociation temperatures at finite μ_B is also briefly mentioned. The chapter ends with a brief overview of charmonium production in nuclear collisions. Here we have first discussed the issue of charmonium production in hadronic collisions. Different QCD inspired models have been developed over the years to account for quarkonium production in hadronic collisions. The models which are most commonly found in literature are the Color Evaporation model (CEM), Color Singlet Model (CSM) and Non-Relativistic QCD (NRQCD). Short descriptions on each of these approaches are given. Next we move on to the issue of charmonium production in proton-nucleus ($p + A$) collisions where J/ψ production is presumably suppressed due to the prevailing cold nuclear matter (CNM) effects. Two main aspects arising from charmonium production in $p + A$ collisions are the initial state nuclear modification of the parton densities and final state absorptions of the nascent $c\bar{c}$ pairs during their passage through the nucleus. Both the aspects are discussed in some detail and operational methods for quantifying the CNM suppression effects in experimental studies are also specified. Finally we go the issue of charmonium production and suppression in nuclear collisions. Several possible and quite different effects have been proposed in literature as consequences of the produced secondary medium on charmonium production. They include charmonium (i) suppression due to Debye color screening inside the plasma (partonic scenario) (ii) dissociation due to inelastic collision co-moving hadrons (iii) enhancement due to regeneration of the exogamous $c\bar{c}$ pairs via recombination process at the phase boundary during hadronization of the QGP. Salient features of each

approach is discussed. Finally we close the chapter with a summary of experimental results for J/ψ suppression in heavy ion collisions as observed at SPS, RHIC and LHC.

As a part of this thesis, we have worked on two aspects of understanding the high density nuclear matter using charmonia as a probe. The works are on: (i) theoretical formulation and estimation of J/ψ production cross sections in FAIR energy collisions and (ii) feasibility studies of J/ψ detection in di-muon channel at CBM. In chapter 4 we have described in detail our theoretical formulation, for calculation of J/ψ production cross sections in nuclear collisions. Our formulation is based on the QVZ approach. For our present work we have extended the model in several aspects though keeping the main features unchanged. Following QVZ framework, we model the J/ψ production in elementary hadronic interactions as a factorizable two component process. First stage is the perturbative production of $c\bar{c}$ pairs, followed at a much later stage by non-perturbative formation of J/ψ resonance. The corresponding $A + B \rightarrow J/\psi + X$ production cross section at leading order in strong coupling is dependent on the transition probability, $F(q^2)$ for $c\bar{c}$ to evolve into a final state J/ψ meson, where q^2 denotes the relative four momentum of the $c\bar{c}$ pair. Various J/ψ formation mechanisms can be accommodated via suitable functional form of $F(q^2)$. In case of a nuclear medium, as present in $p + A$ or $A + A$ collisions, the model includes J/ψ suppression via multiple parton scatterings of the preresonant $c\bar{c}$ pairs in cold nuclear matter only. The model does not consider any further suppression in the hot medium later created in the nuclear collisions. Multiple scattering of the $c\bar{c}$ pair increases the q^2 of the pair and thus reducing the overlap with $F(q^2)$ which finally results in reduction of J/ψ production cross section in $p + A$ and $A + A$ collisions. More be the scattering larger is the reduction. Effect of the heavy quark re-scattering in the cold nuclear medium is modeled with a constant shift in q^2 linear in nuclear path length: $q^2 \rightarrow q^2 + \Delta q^2 = q^2 + \varepsilon^2 \langle L \rangle$, where ε^2 denotes the gain in the relative momentum square due to scatterings per unit path length and $\langle L \rangle$ denotes the average path length traversed by the $c\bar{c}$ pair in the nuclear medium. In addition to final state dissociation, our calculations also incorporate the another important CNM effect i.e– the initial state nuclear modification of the parton densities (shadowing effects), ignored in the original prescription, which affects the perturbation

$c\bar{c}$ production cross sections. In case of nucleus-nucleus collisions we further implement the spatial dependence of the shadowing functions in proportion with the local nuclear density. This finally results in centrality dependent initial state effects a precise estimation of which is necessary for a correct interpretation of the different CNM effects in the heavy ion data. Apart from these above two cold matter effects no other medium effect (either primary or secondary) is implemented in our calculations. We end this chapter with a short description of standard method required for calculation of Drell-Yan (DY) production cross section. A proper estimation of Drell-Yan process is required as often the data on J/ψ suppression is reported in terms of ψ -to-DY ratio.

In chapter 5 we have calibrated our previously formulated QVZ model by analyzing the available data on J/ψ production cross sections for different colliding systems from different fixed target experiments. Model parameters have been tuned from the analysis of the data from the proton induced reactions. Both the absolute J/ψ production cross sections as well as ψ -to-DY ratio have been calculated and contrasted with the data. Over a wide range of beam energies model results with different forms of $F(q^2)$ mimicking various mechanisms of color neutralization are found to be in fair agreement with the data. Model with all its parameters optimized from $p + A$ reactions is then applied to examine the heavy ion data available from NA50 and NA60 Collaborations. For NA50 experiment, we have analyzed both the data sets for centrality dependence of ψ -to-DY ratio and nuclear modification factor (R_{AA}) in 158 A GeV Pb+Pb collisions. For NA60 experiment we have examined centrality dependence of R_{AA} in 158 A GeV In+In collisions. The NA60 data have been again found to be well explained by different forms of $F(q^2)$ accommodated in the model. For the Pb+Pb case however only the power law form of $F(q^2)$, that includes soft gluon radiation from the nascent $c\bar{c}$ pairs for color neutralization, is found to match the data for all centrality bins. The Gaussian form of $F(q^2)$, which bears essential features of color singlet model and is equivalent to Glauber systematics for nuclear absorption, underestimates the observed suppression in near central collisions. However full description of the heavy ion data (using power law parametrization of $F(q^2)$) within the QVZ approach does not allow any room for further anomalous suppression mechanisms to set in. Cold nuclear matter effects alone

are found to be sufficient to generate the required suppressions even in most central Pb+Pb collisions at SPS, provided the final state dissociation effects are quantified in terms of heavy quark re-scatterings inside the nuclear medium. Detailed investigations are also made on the effects of initial state modification of the parton densities on J/ψ and Drell-Yan production cross sections. The two processes are found to be affected differently due to shadowing effects. In the kinematic domain of SPS, J/ψ production observes antishadowing enhancements whereas shadowing effects are visible for Drell-Yan process.

In chapter 6 we have given predictions for FAIR energy collisions using our modified version of QVZ model, tuned previously using SPS data. We have started with the rapidity distribution of J/ψ mesons in $p+p$ collisions at different beam kinetic energies. Calculations are made for different parametrizations of J/ψ formation probability, $F(q^2)$, all of which can describe the existing inclusive production cross sections in this energy domain. Next we have calculated the J/ψ production cross sections in $p+A$ collisions, as we know $p+A$ collisions enable us opportunity to study the CNM effects on charmonium production. CNM effects (the final state dissociations) are more significant with lowering the beam energy and thus will play an important role at FAIR. The most string observation in this respect is that our calculations with two different forms of $F(q^2)$ predict distinguishably different amount of suppressions and the difference increases with the decrease in beam energy, a feature unobserved at higher collision energies. Thus in addition to probe the effects of confined medium, data on J/ψ cross sections in $p+A$ collisions at FAIR, might also help to throw some light on the yet unresolved issue of color neutralization and resonance formation. Finally we move on to the topic of J/ψ suppression in heavy ion collisions. We have calculated the centrality dependence of both the observables R_{AA} and ψ -to-DY ratio for 25 A GeV Au+Au collisions. Our calculations reveal that about 80–90% of the initially produced J/ψ mesons are dissociated due to CNM effects. A detailed analysis of the CNM suppression further shows that in the kinematic regime of FAIR experiments, both the quark as well as gluon densities, in nuclear collisions, exhibit shadowing effects leading to about 10–20% suppression in J/ψ production compared to the $p+p$ reactions. Rest comes from the dissociation of the

evolving $c\bar{c}$ pairs during their passage through the nuclear medium. In addition to the normal nuclear suppression induced by CNM effects, we have also computed the possible anomalous suppression pattern induced by a compressed baryonic medium anticipated at FAIR energy collisions. We have explored both the possible scenarios namely the suppression caused by Debye screening in a baryon rich QGP as well as dissociation inside a high baryon density hadronic medium. Realistic medium expansion scenarios are incorporated following UrQMD transport model calculations. Anomalous suppression in either case is found to be much smaller compared to the CNM suppression effects. However suppression in the hadronic scenario is found to be visibly larger than in the partonic scenario. Thus heavy ion data at FAIR might offer us with golden opportunity to experimentally settle the theorized origin of anomalous J/ψ suppression that have not yet resolved by the existing measurements.

So far we have discussed about our theoretical estimation of charmonium production and its various probable in medium dissociations in the FAIR energy domain. In chapter 7 we have engaged in a description of the simulation studies to explore the feasibility of J/ψ detection via the di-muon decay channel, under the CBM experimental conditions. Having started with the conceptual design of the muon detector system we describe the different steps towards optimization of the configuration of the muon set up. In CBM muon system, tracking chambers are gas filled detectors and they are placed in between the segmented absorbers. Optimizations are made in terms of absorber materials, their thickness, thickness of the gap between the absorber and detector chamber, choice of detector granularity among the others. The optimized set up is the used for identification of J/ψ mesons buried in a background composed of high momentum hadrons, decay muons and secondaries generated from various passive materials. In this respect we have described the entire simulation chain required for selection of di-muon track candidates within a realistic scenario. Reconstruction of the invariant mass spectra clearly shows the J/ψ mass peak above the continuum from combinatorial background. Estimations are made for both central as well as minimum bias Au+Au collisions. So far as $p + A$ collisions are concerned, even a reduced version of the standard muon system is found to be sufficient for J/ψ identification in 30 GeV $p + A$ collisions. In addition, an

estimate of the expected J/ψ collection rate with foreseen beam conditions is also made which clearly establishes the feasibility of the measurement of such rare probes in the low energy collisions. These primary studies are also supplemented by additional studies like simulation of data rate, chamber occupancy etc. specifically required for detector design. We end this chapter with a conceptual design of an online trigger logic required for selection of charmed events and thus to suppress the rate to recordable events to a level that can be handled by the foreseen data acquisition systems.

In summary, in the work presented in this thesis, we have worked on both estimating the J/ψ production and the feasibility of their detection in the FAIR energy domain. Based on formulating a J/ψ production mechanism using the extended QVZ model which has been calibrated using the available $p + p$ and $p + A$ data, it has been shown that CNM effects play a major role in J/ψ suppression in heavy ion collisions at FAIR energies. Modeling of the anomalous J/ψ suppression scenario indicates that there are competitions between hadronic and partonic scenarios is dissociation of J/ψ in the dense baryonic medium anticipated in the nuclear collisions at FAIR. We have established a case that it is of utmost importance to perform high precision J/ψ measurements in the CBM experiment at FAIR.

In our work therefore, we have also carried out detailed realistic simulation of a muon detector system using segmented absorbers and have established the feasibility of J/ψ measurements via the di-muon decay channel, in the FAIR energy range for both nucleon-nucleus and nucleus-nucleus collisions.

Bibliography

- [1] <http://www.had2know.com/academics/water-ice-density-temperature-calculator.html>
- [2] V. E. Fortov *et al.*, Phys. Rev. Lett. **99** (2007) 185001.
- [3] S. Mrowczynski, M.H. Thoma, Ann. Rev. Nucl. Part. Sci. **57** (2007) 61.
- [4] N. F. Mott, Rev. Mod. Phys. **40** (1968) 677.
- [5] F. Gebhard, *The Mott Metal-Insulator Transition* (Springer, Berlin, 1997).
- [6] S. Chandrasekhar, Astrophys. J. **74** (1931) 81.
- [7] S. L. Shapiro and S. A. Teukolsky, *Black Holes, White Dwarfs and Neutron Stars* (John Wiley & Sons, New York, 1983).
- [8] W. Heisenberg, Z. Phys. **101** (1936) 533; Z. Phys. **113** (1939) 61.
- [9] E. Fermi, Progr. Theor. Phys. (Japan) **5** (1950) 570.
- [10] I. Ya. Pomeranchuk, Doklady Akad. Nauk. SSSR **78** (1951) 889.
- [11] L. D. Landau, Izv. Akad. Nauk SSSR **17** (1953) 51;
- [12] R. Hagedorn, Nuovo Cim. Suppl. **3** (1965) 147; Nuovo Cim. **56A** (1968) 1027.
- [13] H. Fritzsche, M. Gell-Mann, H. Leutwyler, Phys. Lett. B **47** (1973) 365.
- [14] Y. Nambu, Phys. Rev. Lett. **4** (1964) 380.
- [15] O. W. Greenberg, Phys. Rev. Lett. **13** (1964) 598.

- [16] D.J.Gross, F. Wilczek, Phys. Rev. Lett. **30** (1973) 1343; H.D. Politzer, Phys. Rev. Lett. **30** (1973) 1346.
- [17] H. Satz, Fortsch. Physik **33** (1985) 259.
- [18] F. Karsch, Lect. Notes Phys. **583** (2002) 209 [hep-lat/0106019]; F. Karsch, E. Laermann, hep-lat/0305025; E. Laermann, O. Philipsen, hep-ph/0303042.
- [19] A. Basavov *et al.*, arXiv:1111.1710v1.
- [20] Z. Fodor and S. D. Katz, Phys. Lett. B **534** (2002) 87.
- [21] P. de Forcrand and O. Philipsen, Nucl. Phys. B **642** (2002) 290.
- [22] C. R. Allton *et al.*, Phys. Rev. D **68** (2003) 014507.
- [23] For a recent review see: O. Philipsen, PoS Lat2005:016 (2006), [hep-lat/0510077].
- [24] S. C. Frautschi, Phys. Rev. D **3** (1971) 2821.
- [25] N. Cabbibo, G. Parisi, Phys. Lett. B **59** (1975) 67.
- [26] J.C. Collins, M.J. Perry, Phys. Rev. Lett. **34** (1975) 1353.
- [27] T. D. Lee and G. C. Wick, Phys. Rev. D **9** (1974) 2291.
- [28] T. D. Lee, Rev. Mod. Phys. **47** (1975) 267.
- [29] E.V. Shuryak, Phys. Lett B. **78** (1978) 150.
- [30] K. Fukushima and T. Hatsuda, Rept. Prog. Phys. **74** (2011) 014001
- [31] S. Borsanyi *et al.*, JHEP **1009**(2010) 073.
- [32] Y. Aoki *et al.*, Nature **443** (2006) 675.
- [33] Z. Fodor and S.D. Katz, JHEP **0404** (2004) 050.
- [34] A. Andronic *et al.*, Nucl. Phys. A **837** (2010) 65.
- [35] See e.g., M. G. Alford *et al.*, Rev. Mod. Phys. **80** (2008) 1455.

- [36] S. R. De Groot, W. A. Van Leeuwen and C. G. Van Weert, *Relativistic Kinetic Theory. Principles And Applications*, Amsterdam, Netherlands: North-holland (1980) 417p.
- [37] Z. W. Lin and C. M. Ko, Phys. Rev. C **65** (2002) 034904; Z. W. Lin, C. M. Ko, B. A. Lin, B. Zhang and S. Pal, Phys. Rev. C **72** (2005) 064901.
- [38] S.A. Bass et al, Prog. Part. Nucl. Phys. **41** (1998) 225.
- [39] W. Ehehalt and W. Cassing, Nucl. Phys. A **602** (1996) 449;
- [40] W. Cassing and E. L. Bratkovskaya, Nucl. Phys. A **831** (2009) 215, [arXiv:0907.5331 [nucl-th]].
- [41] T. Hirano, Phys. Rev. C **65** (2002) 011901, [arXiv:nucl-th/0108004].
- [42] P. F. Kolb and U. W. Heinz, arXiv:nucl-th/0305084.
- [43] C. Nonaka and S. A. Bass, Phys. Rev. C **75** (2007) 014902.
- [44] R. B. Clare and D. Strottman, Phys. Rept. **141** (1986) 177.
- [45] P. F. Kolb, P. Huovinen, U. W. Heinz and H. Heiselberg, Phys. Lett. B **500** (2001) 232.
- [46] P. F. Kolb, U. W. Heinz, P. Huovinen, K. J. Eskola and K. Tuominen, Nucl. Phys. A **696** (2001) 197.
- [47] P. Huovinen, P. F. Kolb, U. W. Heinz, P. V. Ruuskanen and S. A. Voloshin, Phys. Lett. B **503** (2001) 58.
- [48] C. E. Aguiar, T. Kodama, T. Koide and Y. Hama, Braz. J. Phys. **37**, 95 (2007).
- [49] V. V. Skokov and V. D. Toneev, Phys. Rev. C **73** (2006) 021902.
- [50] H. Petersen, J. Steinheimer, G. Burau, M. Bleicher and H. Stocker, Phys. Rev. C **78** (2008) 044901, [arXiv:0806.1695 [nucl-th]].
- [51] C.A. Ogilvie, Nucl. Phys. A **698** (2002) 3c [nucl-ex/0104010]; M.A. Lisa, Nucl. Phys. A **698** (2002) 185c [nucl-ex/0104012].

- [52] U. Heinz and M. Jacob, nucl-th/0002042 and references therein.
- [53] L. McLerran, hep-ph/0202025; J. Nagle, T. Ullrich, nucl-ex/0203007; P. Jacobs, hep-ex/0211031; D. Kharzeev, Nucl. Phys. A **715** (() 2003) 441c, [nucl-th/0211083]; <http://www.bnl.gov/rhic/>
- [54] K. Kajantie, Nucl. Phys. A **715** (() 2003) 432c; P. Giubellino, Nucl. Phys. A **715** (() 2003) 441c; R.J. Fries, B. Müller, nucl-th/0307043.
- [55] http://www.gsi.de/zukunftsprojekt/index_e.html
- [56] K. Kajantie, L. McLerran, Ann. Rev. Nucl. Part. Sci. **37** (() 1987) 293; Berndt Muller, Rep. Prog. Phys.**58** (1995) 611; J.W. Harris, B. Müller, Ann. Rev. Nucl. Part. Sci. 46 (71) 1996 [hep-ph/9602235]; S.A. Bass, M. Gyulassy, H. Stöcker, and W. Greiner, J. Phys. G **25** (1999) R1, [hep-ph/9810281].
- [57] C. Y. Wong, *Introduction to high energy heavy ion collisions*, World Scientific, Singapore (1994).
- [58] Ramona Vogt, *Ultrarelativistic Heavy-Ion Collisions*, Elsevier, The Netherlands, 2007.
- [59] B. Müller, *The Physics of Quark Gluon Plasma*, Springer, Heidelberg, 1985.
- [60] S. Sarkar, H. Satz and B. Sinha (Eds), *The Physics of the Quark-Gluon Plasma: Introductory Lectures*, Lect. Notes Phys.**785**, Springer, Heidelberg, 2010.
- [61] J. Stachel and P. Braun-Munzinger, Phys. Lett. B, **216** (1989) 1.
- [62] J.D. Bjorken, Phys. Rev. D **27** (1983) 140.
- [63] M. Kataja *et al.*, Phys. Rev. D **34** (1986) 2755
- [64] L. Van Hove, Phys. Lett. **B118** (1982) 138.
- [65] S. Sarkar *et al.*, Phys. Rev. C **51** (1995) 318.[Erratum:ibid C**51** (1995) 2845.]
- [66] A. Dumitru *et al.*, Z. Phys. **A353** (1995) 187.

- [67] D. Kharzeev and M. Nardi, Phys. Lett. **B507** (2001) 121.
- [68] J. Rafelski and B. Muller, Phys. Rev. Lett. **48** (1982) 1066.
- [69] P. Koch, B. Muller and J. Rafelski, Phys. Rep. **142** (1986) 165.
- [70] J. Rafelski and R. Hagedron, "From Hadron Gas To Quark Matter. 2", in *Statistical Mechanics of Quarks and Hadrons*, H. Satz, ed. (North Holland 1980) pp.253-272, also; Preprint CERN-TH-2969, October 1980.
- [71] E. L. Feinberg, Nuovo Cimento Sco. Ital. Fis. A **34** (1976) 39.
- [72] J. Kapusta, P. Lichard, and D. Seibert. Phys. Rev. D **44** (1991) 2774, *Erratum-ibid* **47** (1993) 4171.
- [73] S. A. Bass, B. Müller, and D. K. Srivastava, Phys. Rev. Lett. **93** (2004) 162301; S. A. Bass, B. Müller, and D. K. Srivastava, Phys. Rev. Lett. **90** (2003) 082301; *ibid*, Phys. Rev. C **66** (2002) 061902; T. Renk, S. A. Bass, and D. K. Srivastava, Phys. Lett. B **632** (2006) 632.
- [74] R. Chatterjee, E. Frodermann, U. Heinz, and D. K. Srivastava, Phys. Rev. Lett. **96** (2006) 202302; U. Heinz, R. Chatterjee, E. Frodermann, C. Gale, and D. K. Srivastava, Nucl. Phys. A **783** (2007) 379.
- [75] R. Chatterjee and D. K. Srivastava, Phys. Rev. C **79** (2009) 021901, [arXiv:0809.0548 [nucl-th]].
- [76] R. J. Fries, B. Müller, and D. K. Srivastava, Phys. Rev. Lett. **90** (2003) 132301.
- [77] K. Kajantie, J. Kapusta, L. McLerran, and A. Mekijan, Phys. Rev. D **34** (1986) 2746.
- [78] P. Mohanty, J. Alam and B. Mohanty, Phys. Rev. C **84** (2011) 024903.
- [79] J. Alam, B. Sinha and S. Raha, Phys. Rept. **273** (1996) 243; J. Alam, S. Sarkar, P. Roy, T. Hatsuda and B. Sinha, Annals Phys. **286** (2001) 159, [hep-ph/9909267].

- [80] R. Chatterjee, L. Bhattacharya and D. K. Srivastava, Lect. Notes Phys. **785** (2010) 219,[arXiv:0901.3610 [nucl-th]].
- [81] P. Mohanty, S. Ghosh and S. Mitra, Adv. High Energy Phys. **2013** (2013) 176578.
- [82] M. M. Aggarwal *et al.* (WA98 Collaboration), Phys. Rev. Lett. **85** (2000) 3595.
- [83] S. S. Adler *et al.* (PHENIX Collaboration), Phys. Rev. Lett. **94** (2005) 232301;
S. S. Adler *et al.* (PHENIX Collaboration), Phys. Rev. C **76** (2007) 034904.
- [84] D. K. Srivastava, J. Phys. G **35** (2008) 104026.
- [85] D.K. Srivastava *et al.*, Phys. Lett. **B276** (1992) 285.
- [86] M. Strickland, Phys. Lett. **B331** (1994) 245.
- [87] D. K. Srivastava and B. Sinha, Phys. Rev. C **64** (2001) 034902.
- [88] J. Cleymans, K. Redlich, and D. K. Srivastava, Phys. Rev. C **55** (1997) 1431.
- [89] S. Turbide, R. Rapp, and C. Gale, Phys. Rev. C **69** (2004) 014903.
- [90] J. Alam, S. Sarkar, T. Hatsuda, T. K. Nayak, and B. Sinha, Phys. Rev. C **63** (2001) 021901.
- [91] P. Huovinen, P. V. Ruuskanen, and S. S. Rasanen, Phys. Lett. B **535** (2002) 109;
S. S. Rasanen, Nucl Phys. A **715** (2003) 717; H. Niemi, S. S. Rasanen, and P. V. Ruuskanen, CERN Yellow Report CERN-2004-009, arXiv:0311131 [hep-ph].
- [92] J. Alam, J. K. Nayak, P. Roy, A. K. Dutta-Mazumder, and B. Sinha, J. Phys. G **34** (2007) 871.
- [93] D. G. d'Enterria and D. Peressounko, Eur. Phys. J. C **46** (2006) 451.
- [94] S. Turbide, C. Gale, E. Frodermann, and U. Heinz, Phys. Rev. C **77** (2008) 024909.
- [95] J. K. Nayak, J. Alam, S. Sarkar and B. Sinha, Phys. Rev. C **78** (2008) 034903.

- [96] J. K. Nayak and J. Alam, Phys. Rev. C **80** (2009) 064906; P. Mohanty, J. K. Nayak, J. Alam and S. K. Das, Phys. Rev. C **82** (2010) 034901.
- [97] P. Mohanty, V. Roy, S. Ghosh, S. K. Das, B. Mohanty, S. Sarkar, J. Alam and A. K. Chaudhuri, Phys. Rev. C **85** (2012) 031903 (R).
- [98] P. Roy, S. Sarkar, J. Alam, B. Dutta-Roy, and B. Sinha, Phys. Rev. C **59** (1999) 2778.
- [99] S. Weinberg, Phys. Rev. Lett. **18** (1967) 507.
- [100] J. Kapusta and E.V. Shuryak, Phys. Rev. D **49** (1994) 4694.
- [101] R. Rapp, J. Wambach, Eur. J. Phys. A **6** (1999) 415; R. Rapp and J. Wambach, Adv. Nucl. Phys. **25** (2000) 1; H. van Hees, R. Rapp, Phys. Rev. Lett. **97** (2006) 102301; H. Van Hees, R. Rapp, arXiv:0711.3444 [hep-ph].
- [102] G. Agakichiev *et al.*, (CERES Collaboration), Phys. Rev. Lett. **75** (1995) 1275; G. Agakichiev *et al.*, CERES Collaboration, Phys. Lett. B **422** (1998) 405; D. Adamova *et al.*, (CERES Collaboration), Eur. Phys. J. C **41** (2005) 475; D. Adamova *et al.*, (CERES Collaboration), Phys. Rev. Lett. **91** (2003) 042301.
- [103] R. Arnaldi *et al.*, (NA60 Collaboration), Phys. Rev. Lett. **96** (2006) 162302.
- [104] G.E. Brown, Nucl. Phys. A **488** (1988) 689; G.E. Brown and M. Rho, Phys. Rev. Lett. **66** (1991) 2720; G. E. Brown and M. Rho, Phys. Rept. **269**, 333 (1996).
- [105] H. Satz, Rept. Prog. Phys. **63** (2000) 1511, [hep-ph/0007069]; H. Satz, J. Phys. G **32** (2006) R25; H. Satz, Nucl. Phys. A **783**, 249 (2007), [hep-ph/0609197]; L. Klumberg and H. Satz, arXiv:0901.3831 [hep-ph];
- [106] T. Matsui and H. Satz, Phys. Lett. B **178** (1986) 416.
- [107] S. Digal, P. Petreczky and H. Satz, Phys. Rev. D **64** (2001) 094015.
- [108] C. Baglin *et al.*, (NA38 Collaboration), Phys. Lett. B **220** (1989) 471.

- [109] C. Gerschel and J. Huefner, Phys. Lett. B **207** (1988) 253. C. Gerschel and J. Huefner, Z. Phys. C **56** (1992) 171. C. Gerschel and J. Huefner, Ann. Rev. Nucl. Part. Sci. **49** (1999) 255; hep-ph/9802245.
- [110] M.C. Abreu, NA50 Collaboration, Phys. Lett. B **410** (1997) 377.
- [111] V. N. Gribov and L. N. Lipatov; Sov. J. Nucl. Phys. **15**,438 (1972); V. N. Gribov and L. N. Lipatov; Yad. Fiz. **15**,781 (1972); G. Altarelli and G. Parisi; Nucl. Phys. **B 126**, 298 (1977); Y. L. Dokshitzer; Sov. Phys. JTEP **46**, 641 (1977); Y. L. Dokshitzer; Zh. Eksp. Teor. Fiz. **73**, 1216 (1977) .
- [112] Y. Akiba *et al.*, (PHENIX Collaboration), Nucl. Phys. A**774** (2006) 403, S.S. Adler *et al.*, (PHENIX Collaboration), Phys. Rev. C**76** (2007) 034904.
- [113] J. Y. Ollitrault, Phys. Rev. D **46** (1992) 229.
- [114] S. Voloshin, Y. Zhang, Phys. C **70** (1996) 665, hep-ph/9407282.
- [115] S. Voloshin, A. M. Poskanzer, R. Snellings, *Landolt-Boernstein: Relativistic Heavy Ion Physics* volume 1/23 (Springer-Verlag, 2010), pp. 5–54, 0809.2949.
- [116] R. Snellings, New J. Phys. **13** (2011) 055008.
- [117] B. B. Back *et al.*, Nucl. Phys. A **757** (2005) 28.
- [118] I. Arsene *et al.* (BRAHMS Collaboration), Nucl. Phys. A **757**, 1 (2005)
- [119] K. Adcox *et al.* (PHENIX Collaboration), Nucl. Phys. A **757**, 184 (2005)
- [120] J. Adams *et al.* (STAR Collaboration), Nucl. Phys. A **757**, 102 (2005)
- [121] B. Müller, J. L. Nagle, Ann .Rev. Nucl .Part. Sci. **56** (2006) 93; nucl-th/0602029.
- [122] D. Teaney, *Quark-Gluon Plasma 4* (World Scientific, Singapore, 2010), chap. Viscous Hydrodynamics and the Quark Gluon Plasma; arXiv:0905.2433.
- [123] J. Nagle, P. Steinberg, W. Zajc, Phys. Rev. C **81** (2010) 024901.
- [124] K. Aamodt *et al.*, (ALICE Collaboration), Phys. Rev. Lett. **105** (2010) 252302.

- [125] N. Armesto *et al.*, J. Phys. G **35** (2008) 054001; arXiv:0711.0974.
- [126] P. Sorensen, J. Phys. G **37** (2010) 094011; arXiv:1002.4878.
- [127] B. Alver, G. Roland, Phys. Rev. C **81** (2010) 054905; arXiv:1003.0194.
- [128] H. Heiselberg, Phys. Rep.**351** (2001) 161 and the refernces therein.
- [129] S. Jeon and V. Koch, Phys. Rev. Lett. **83** (1999) 5435.
- [130] S. Jeon and V. Koch, Phys. Rev. Lett. **85** (2000) 2076.
- [131] S. Gavin and C. Pruneau, nucl-th/9906060 and nucl-th/9907040.
- [132] J. Adams *et al.*, (STAR Collaboration), Phys. Rev. C **68** (2003) 044905.
- [133] J. Adams *et al.*, (STAR Collaboration), Phys. Rev. C **71** (2005) 064906, H. Appelhauser *et al.*, (NA49 Collaboration) Phys. Lett. **B459** (1999) 679.
- [134] T. Akesson *et al.*, (HELIOS Collaboration) Z. Phys. **C38** (1988) 383, H. Heiselberg *et al.*, Phys. Rev. Lett. **67** (1991) 2946, B. Blattel *et al.*, Nucl. Phys. **A544** (1992) 479c.
- [135] M.I. Gorenstein *et al.*, Phys. Lett. **B585** (2004) 237.
- [136] B. Mohanty and J. Serreau, Phys. Rep.**414** (2005) 263.
- [137] J. M. Heuser, (CBM Collaboration), Nucl. Phys. A **904** (2013) 941c.
- [138] A. Schmah, arXiv:1202.2389v1.
- [139] A. Aduszkiewicz *et al.*, Acta Physica Polonica B43 (2012) 635
- [140] NICA White Paper, <http://nica.jinr.ru/files/WhitePaper.pdf>
- [141] FAIR Baseline Technical Report 2006, <http://www.gsi.de/fair/reports/btr.html>
- [142] W. Cassing, E.L. Bratkovskaya, and A. Sibirtsev, Nucl. Phys. A691 (2001) 753, and E.L. Bratkovskaya, priv. comm.
- [143] A. Andronic, P. Braun-Munzinger, J. Stachel, Nucl. Phys. A772 (2006) 167

- [144] CBM Report 2012-01, <http://www.gsi.de/documents/DOC-2011-Aug-29-1.pdf>
- [145] B. Friman *et al.* (Eds.), *The CBM Physics Book*, Lect. Notes Phys. 814, Springer-Verlag Berlin Heidelberg 2011
- [146] R.J. Porter *et al.* (DLS Collaboration), Phys. Rev. Lett. **79** (1997) 1229.
- [147] G. Agakichiev *et al.* (HADES Collaboration), Phys.Rev.C84 (2011) 014902
- [148] G. Agakichiev *et al.* (CERES/NA45 Collaboration), Eur. Phys. J. C41, 475 (2005);
- [149] J.J. Aubert *et al.*, Phys. Rev. Lett. **33**, 1404 (1974).
- [150] J. E. Augustin *et al.*, Phys. Rev. Lett. **33** (1974) 1406.
- [151] P. P. Bhaduri, P. Hegde, H. Satz and P. Tribedy, Lect. Notes Phys. **785**, 179 (2010); [arXiv:0812.3856 [hep-ph]].
- [152] E. Eichten *et al.*, Phys. Rev. D **17** (1978) 3090; Phys. Rev. D **21** (1980) 203.
- [153] F. Karsch, M. T. Mehr, and H. Satz, Z. Phys. C **37** (1988) 617.
- [154] V. V. Dixit, Mod. Phys. Lett. A **5** (1990) 227.
- [155] S. Digal, P. Petreczky and H. Satz, Phys. Lett. B **514** (2001) 57.
- [156] E. Shuryak and I. Zahed, Phys. Rev. D **70**, 054507 (2004).
- [157] C.-Y. Wong, Phys. Rev. C **72** (2004) 034906;
C.-Y. Wong, hep-ph/0509088;
C.-Y. Wong, Phys. Rev. C **76** (2007) 014902.
- [158] W. Alberico *et al.*, Phys. Rev. D **72** (2005) 114011.
- [159] S. Digal *et al.*, Eur. Phys. J. C **43** (2005) 71.
- [160] X. Guo, S. Shi and P. Zhuang, Phys. Lett. B **718** (2012) 143.
- [161] Y. Liu, N. Xu and P. Zhuang, Phys. Lett. B **724** (2013) 73.
- [162] T. Umeda *et al.*, Int. J. Mod. Phys. A **16** (2001) 2215.

- [163] M. Asakawa and T. Hatsuda, Phys. Rev. Lett. **92** (2004).
- [164] S. Datta *et al.*, Phys. Rev. D **69** (2004) 094507
- [165] H. Iida *et al.*, PoS LAT2005 (2006) 184.
- [166] A. Jacovac *et al.*, Phys. Rev. D **75** (2007) 014506.
- [167] R. Morrin *et al.*, PoS LAT2005 (2006) 176;
G. Aarts *et al.*, Nucl. Phys. A **785** (2007) 198.
- [168] M. Laine *et al.*, JHEP **0703** (2007) 054; M. Laine, JHEP **0705** (2007) 028
Y. Burnier, M. Laine and M. Vepsalainen, JHEP **0801** (2008) 043.
- [169] A. Mocsy, P. Petreczky and M. Strickland, Int. J. of Mod. Phys. A, **28**, (2013) 1340012.
- [170] M. Doring, S. Ejiri, O. Kaczmarek, F. Karsch and E. Laermann, Eur. Phys. J. C **46** (2006) 179.
- [171] Purnendu Chakraborty and Subhasis Chattopadhyay, arXiv:1401:1110v1 [hep-ph].
- [172] M.B. Einhorn and S.D. Ellis, Phys. Rev. D **12** (1975) 2007; H. Fritzsch, Phys. Lett. B **67** (1977) 217; M. Glück, J.F. Owens and E. Reya, Phys. Rev. D **17** (1978) 2324; J. Babcock, D. Sivers and S. Wolfram, Phys. Rev. D **18** (1978) 168.
- [173] E. Braaten, S. Fleming, and T. C. Yuan, Ann. Rev. Nucl. Part. Sci. **46** (1996) 97; [arXiv:hep-ph/9602374].
- [174] C. H. Chang, Nucl. Phys. B **172** (1980) 425; E. L. Berger and D. Jones, Phys. Rev. D **23** (1981) 1521; R. Baier and R. Rückl, Phys. Lett. B **102** (1981) 364.
- [175] G.T. Bodwin, E. Braaten, and G.P. Lepage, Phys. Rev. D **51** (1995) 1125; [Erratum-ibid. D **55** (1997) 5853].
- [176] G.A. Schuler, Habilitationsschrift, Univ. Hamburg, Germany, 1994, CERN-TH-7170-94, arXiv:hep-ph/9403387.
- [177] F. Abe *et al.* (CDF Collaboration), Phys. Rev. Lett. **71** (1993) 3421.

- [178] P. Artoisenet, J. P. Lansberg, and F. Maltoni, Phys. Lett. B **653** (2007) 60.
- [179] J. M. Campbell, F. Maltoni, and F. Tramontano, Phys. Rev. Lett. **98** (2007) 252002.
- [180] P. Artoisenet, J. M. Campbell, J. P. Lansberg, F. Maltoni, and F. Tramontano, Phys. Rev. Lett. **101** (2008) 152001.
- [181] N. Brambilla *et al.*, CERN-2005-005, (CERN, Geneva, 2005),
- [182] H. Satz and X.-N. Wang (Eds.), *Hard Processes in Hadronic Interactions*, Int. J. Mod. Phys. A **10** (1995) 2881;
- [183] Y. Lemoigne *et al.*, Phys. Lett. B **113** (1982) 509;
L. Antoniazzi *et al.*, Phys. Rev. D **46** (1992) 4828; Phys. Rev. Lett. **70** (1993) 383;
HERA B.
- [184] A. Bamberger *et al.*, Nucl. Phys. B **134** (1978) 1.
- [185] M. J. Corden *et al.*, (WA39 Collaboration), Phys. Lett. B **98** (1981) 220.
- [186] J. Badier *et al.*, (NA3 Collaboration), Z. Phys. C **20** (1983) 101.
- [187] M. C. Abreu *et al.*, (NA51 Collaboration), Phys. Lett. B **438** (1998) 35.
- [188] V. Abramov *et al.*, (E672 Collaboration), Fermilab-PUB-91/62-E, March, 1991.
- [189] T. Alexopoulos *et al.*, (E771 Collaboration), Phys. Lett. B **374** (1996) 271.
- [190] C. Lourenco, Nucl. Phys. A **610** (1996) 552c.
- [191] P. P. Bhaduri and S. Gupta, Phys. Rev. C **88** (2013) 045205.
- [192] M. C. Abreu *et al.*, NA38 Collaboration, Phys. Lett. B **466** (1999) 408; O. Draiper *et al.*, NA38 Collaboration, Nucl. Phys. A **544** (1992) 209c.
- [193] J. G. Branson *et al.*, (E331 Collaboration), Phys. Rev. Lett. **38** (1977) 1331.
- [194] M. C. Abreu *et al.*, (NA38 Collaboration), Phys. Lett. B **444** (1998), 516.

- [195] R. Cases (NA38 Collaboration), Ph. D. Thesis, Valencia University (1989), Spain, unpublished.
- [196] B. Alessandro *et al.*, (NA50 Collaboration), Euro. J. Phys **48** 329 (2006).
- [197] R. Arnaldi *et al.* (NA60 Collaboration), Phys. Rev. Lett. **99** (2007) 132302.
- [198] B. Alessandro *et al.* (NA50 Collaboration), Euro. J.Phys **33** 31 (2004).
- [199] D. M. Alde *et al.*, Phys. Rev. Lett. **66** (1991) 133.
- [200] M. H. Schub *et al.* (E789 Collaboration), Phys. Rev. D. **52** (1995) 1307.
- [201] M. J. Leitch *et al.* (E789 Collaboration), Phys. Rev. D. **52** (1995) 4251.
- [202] M. J. Leitch *et al.*, (E866 Collaboration), Phys. Rev. Lett. **84** (2000) 3256.
- [203] I. Abt *et al.*, (HERA-B Collaboration), Eur. Phys. J. C **60** (2009) 525.
- [204] R. J. Glauber, in Lectures in Theoretical Physics, ed. W. E. Britten and L. G. Dunham, *Interscience*, N. Y. (1959).
- [205] D. Kharzeev, C. Lourenco, M. Nardi and H. Satz, Z. Phys. C**74** (1997) 307.
- [206] C. Lourenco, R. Vogt and H. K. Wohri, JHEP **0902** (2009) 014.
- [207] F. Karsch and H. Satz, Z. Phys. C **51** (1991) 209.
- [208] S. Gupta and H. Satz, Phys. Lett. B **283** (1992) 439.
- [209] D. Kharzeev, F. Karsch and H. Satz, Phys. Lett. B **637** (2006) 75.
- [210] J. P. Blaizot and J.Y Ollitrault, Phys. Rev. Lett. **77** (1996) 1703.
- [211] J. P. Blaizot, P. M. Dinh and J.Y. Ollitrault, Phys. Rev. Lett. **85** (2000) 4012.
- [212] T. Gunji, H. Hamagaki, T. Hatsuda and T. Hirano, Phys. Rev. C **76** (2007) 051901 (R); A. K. Chaudhuri, Phys. Rev. C **80** (2009) 047901;
- [213] O. Linnyk, E. L. Bratkovskaya, W. Cassing and H. Stocker, Nucl. Phys. A **786** (2007) 183.

- [214] L. Grandchamp and R. Rapp, Phys. Lett. B **523** (2001) 60; L. Grandchamp and R. Rapp, Nucl. Phys. A **709** (2002) 415; L. Grandchamp, R. Rapp and G. E. Brown, Phys. Rev. Lett. **92** (2004) 212301.
- [215] D. Kharzeev and H. Satz, Phys. Lett. B **334** (1994) 155.
- [216] Y. Park, K. I. Kim, T. Song, S. H. Lee and C. Y. Wong, Phys. Rev. C **76** (2007) 044907.
- [217] J. Ftacnik, P. Lichard and J. Pisut, Phys. Lett. B **207** (1988) 194.
- [218] S. Gavin, M. Gyulassy and A. Jackson, Phys. Lett. B **207** (1988) 257.
- [219] R. Vogt, M. Prakash and P. Koch, Phys. Lett. B **207** (1988) 263.
- [220] A. Capella, E. J. Feireiro and A. B. Kaidalov, Phys. Rev. Lett. **85** (2000) 2080; A. Capella, A. B. Kaidalov, D. Sousa, Phys. Rev. C **65** (2002) 054908.
- [221] R. Vogt, Physics Reports **310**, (1999) 197.
- [222] S. J. Brodsky and A. H. Mueller, Phys. Lett. B **206** (1988) 685; N. Armesto and A. Capella, Phys. Lett. B **430** (1998) 23.
- [223] P. Braun-Munzinger and J. Stachel, Nucl. Phys. A **690** (2001) 119.
- [224] R. L. Thews, Martin Schroedter and Johann Rafelski, Phys. Rev. C **63** (2001) 054905; R. L. Thews, AIP Conf. Proc. 631 (2002) 490, arXiv:hep-ph/0206179; R. L. Thews, arXiv:hep-ph/0302050; R. L. Thews, J.Phys. G30 (2004) S369; R. L. Thews and M. L. Mangano, Phys.Rev. C **73** (2006) 014904
- [225] P. Braun-Munzinger and J. Stachel, arXiv:0901.2500 [nucl-th] ; A. Andronic, P. Braun-Munzinger, K. Redlich and J.Stachel, Phys. Lett. B **571** (2003) 36; Phys. Lett. B **652** (2007) 259.
- [226] D. Kharzeev, M. Nardi and H. Satz, Phys. Lett. B **405** (1997) 14.
- [227] S. Gavin and M. Gyulassy, Phys. Lett. B **214** (1988) 241; J. Hüfner, Y. Kurihara and H. J. Pirner, Phys. Lett. B **215** (1988) 218;

- [228] R. L. Thews and M. Mangano, Phys. Rev. C **73** (2006) 014904; R. L. Thews, AIP Conf. Proc. **828** (2006) 303 [hep-ph/0510390].
- [229] J. P. Blaizot and J. Y. Ollitrault, Phys. Lett. B **199** 499 (1987).
- [230] M. C. Chu and T. Matsui, Phys. Rev. D. **37**, 1851 (1988).
- [231] F. Karsch and R. Petronzio, Phys. Lett. B **193** 105 (1987).
- [232] R. Vogt, Phys. Lett. B **430** (1998) 15.
- [233] D. Pal, B. K. Patra and D. K. Srivastava, Eur. Phys. J. C **17** (2000) 179;
- [234] M. Mishra, C. P. Singh, V. J. Menon and Ritesh Kumar Dubey, Phys. Lett. B **656**, 45 (2007); P.K.Srivastava, M. Mishra and C. P. Singh, Phys. Rev. C. **87** (2013) 034903
- [235] H. Liu, K. Rajagopal and U. A. Wiedemann, Phys. Rev. Lett. **97** (2006) 182301.
- [236] E. Scomparin *et al.* (NA60 Collaboration), Nucl. Phys. A **830** (2009) 239C.
- [237] A. Adare *et al.*, (PHENIX Collaboration), Phys. Rev. C **84** (2011) 054912; arXiv:1103.6269 v1.
- [238] A. Adare *et al.*, (PHENIX Collaboration), arXiv:1105.1960.
- [239] L. Adamczyk *et al.*, (STAR Collaboration), Phys. Rev. Lett. **111** (2013) 052301, arXiv:1212.2304.
- [240] L. Adamczyk *et al.*, (STAR Collaboration), Phys. Lett. B **722** (2013) 55; arXiv:1208.2736.
- [241] L. Adamczyk *et al.*, (STAR Collaboration), (2013), arXiv:1310.3563.
- [242] L. Adamczyk *et al.*, (STAR Collaboration), Phys. Lett. B **735** (2014) 127; arXiv:1312.3675.
- [243] C. Aidala *et al.*, (PHENIX Collaboration), (2014) arXiv:1404.1873.
- [244] H. Masui and Z. Tang, (STAR Collaboration), J. Phys. G **38** (2011) 124002.

- [245] H. Brambilla *et al.*, Eur. Phys. J. C **71** (2011) 1534.
- [246] R. Arnaldi, talk given at EMMI workshop: ‘Quarkonia in deconfined matter’ (<http://www2.physik.uni-bielefeld.de/quarkonia.html>), September 28-30, 2011, Acitrezza (Italy).
- [247] K. Aamodt *et al.*, (ALICE Collaboration), Phys. Lett. B **704** (2011) 442.
- [248] G. Aad *et al.*, (ATLAS Collaboration), Nucl. Phys. B **850** (2011) 387; arXiv:1012.5419v1.
- [249] S. Chatrchyan *et al.*, (CMS Collaboration), arXiv:1111.1557.
- [250] R. Aaij *et al.*, (LHCb Collaboration), Eur. Phys. J. C **71** (2011) 1645; arXiv:1103.0423v2.
- [251] P. Pillot, (ALICE Collaboration), J. Phys. G **38** (2011) 124111.
- [252] T. Dahms, (CMS Collaboration), J. Phys. G **38** (2011) 124105.
- [253] J. Qiu, J.P. Vary and X. Zhang, Nucl. Phys. A **698**, (2002) 571; Phys. Rev. Lett. **88** (2002) 232301.
- [254] M. C. Abreu *et al.*, (NA50 Collaboration), Phys. Lett. B **477** (2000) 28.
- [255] P. P. Bhaduri, A. K. Chaudhuri and S. Chattopadhyay, Phys. Rev. C **84** (2011) 054914; [arXiv:1110.4268 [hep-ph]].
- [256] P. P. Bhaduri, A. K. Chaudhuri and S. Chattopadhyay, Phys. Rev. C **85** (2012) 064911; [arXiv:1206.0822 [hep-ph]].
- [257] A. K. Chaudhuri, Phys. Rev. Lett. **88** (2002) 232302.
- [258] A. K. Chaudhuri, Phys. Rev. C **66** (2002) 021902.
- [259] J.C. Collins, D.E. Soper and G. Sterman, Nucl. Phys. B **263** (1986) 37.
- [260] C. Benesh, J.-W. Qiu and J.P. Vary, Phys. Rev. C **50** (1994) 1015.

- [261] A.D. Martin, W.J. Stirling, R.S. Thorne, G. Watt, Eur.Phys.J.C **63**:189-285,2009;
A.D. Martin, W.J. Stirling, R.S. Thorne, G. Watt, Eur.Phys.J.C **64**:653-680,2009;
A.D. Martin, W.J. Stirling, R.S. Thorne, G. Watt, Eur.Phys.J.C **70**:51-72,2010.
- [262] H. Fritzsch, Phys. Lett. **B67**, 215 (1977); M. Gluck, J. F. Owens , and E. Reya,
Phys. Rev. D**17** (1978) 2324.
- [263] K. J. Eskola, Nucl. Phys. A **910-911** (2013) 163. [arXiv:1209.1546 [hep-ph]].
- [264] K.J. Eskola, H. Paukkunen and C.A. Salgado, JHEP**04** (2009) 065.
- [265] J.-W. Qiu, J.P. Vary and X.-F. Zhang, private communication.
- [266] M. Luo, J.-W. Qiu and G. Sterman, Phys. Rev. D **49** (1994) 4493.
- [267] V. Emel'yanov *et al.*, Phys. Rev. C **59** (1999) 1860R.
- [268] S.R. Klein and R. Vogt, Phys. Rev. Lett. **91** (2003) 142301.
- [269] I. Helenius, K. J. Eskola, H. Honkanen and C. A. Salgado, JHEP **1207** (2012)
073, [arXiv:1205.5359 [hep-ph]].
- [270] R. Arnaldi, P. Cortese and E. Scomparin, Phys. Rev. C **81** (2010) 014903.
- [271] Yu. M. Antipov *et al.*, Phys. Lett. B **60** (1976) 309.
- [272] K. J. Anderson *et al.*, Phys. Rev. Lett. **36** (1976) 237.
- [273] K. J. Anderson *et al.*, Phys. Rev. Lett. **37** (1976) 799.
- [274] K. J. Anderson *et al.*, (E331 Collaboration), Phys. Rev. Lett.**42** (1979) 944.
- [275] L. Antoniazzi *et al.*, Phys. Rev. Lett. **70** (1993) 383.
- [276] C. Morel *et al.*, (UA6 Collaboration), Phys. Lett. B **251** (1990) 505.
- [277] H. D. Synder *et al.*, (E288 Collaboration), Phys. Rev. Lett. **36** (1976) 1415.
- [278] C. Kourkoumelis *et al.*, Phys. Lett. B **91** (1980) 481.
- [279] A. G. Clark *al.*, Nucl. Phys. B **142** (1978) 29.

- [280] F. W. Busser *et al.*, Phys. Lett. B **56** (1975) 482.
- [281] E. Nagy *et. al.*, Phys. Lett. B **60** (1975) 96.
- [282] E. Amaldi *et. al.*, Lett. Nuovo Cimento **19** (1977) 152.
- [283] M. Bargiotti *et. al.*, (HERA-B Collaboration), HERA-B-Physics/05-012.
- [284] K.J. Eskola, V. J. Kolhinen and C.A. Salgado, Eur.Phys.J. C **9** (1999) 61.
- [285] K.J. Eskola, H. Paukkunen and C.A. Salgado, JHEP **0807** (2008) 102.
- [286] P. P. Bhaduri, A. K. Chaudhuri and S. Chattopadhyay, Phys. Rev. C **89** (2014) 044912; arXiv:1404.3260 [hep-ph].
- [287] A. K. Chaudhuri, Phys. Rev. C **64** (2001) 054903, Phys. Lett. B **527** (2002) 80.
- [288] L. Grandchamp, R. Rapp and G. E. Brown, Phys. Rev. Lett. **92** (2004) 212301.
- [289] P. P. Bhaduri, A. K. Chaudhuri and S. Chattopadhyay, Phys. Rev. C. **88** (2013) 061902 (R); [arXiv:1310.3616 [hep-ph]].
- [290] J. M. Heuser (CBM Collaboration), Nucl. Phys. A **830** (2009) 563C; P. Senger, Nucl. Phys. A **862-863** (2011) 139.
- [291] I. C. Arsene *et al.*, Phys. Rev. C **75** (2007) 034902.
- [292] O. Linnyk, E. L. Bratkovskaya, W. Cassing and H. Stocker, Nucl. Phys. A **786** (2007) 183.
- [293] R. Molina, C. W. Xiao and E. Oset, Phys. Rev. C **86** (2012) 014604 [arXiv:1203.0979 [nucl-th]].
- [294] P. F. Kolb, U. Heinz P. Huovinen, K. J. Eskola and K. Tuominen, Nucl. Phys. A **696** (2001) 197.
- [295] A. K. Chaudhuri, Phys. Rev. C **75** (2007) 044902.
- [296] J. Cugnon and P. B. Gossiaux, Phys. Lett. B **359** (1995) 375.

- [297] F. Karsch and H. Satz, *Z. Phys. C* **51** (1991) 209; J. P. Blaizot and J. Y. Ollitrault, *Phys. Lett. B* **199** (1987) 499.
- [298] T. Toimela, *Phys. Lett. B* **124** (1983) 407.
- [299] S. Gao, B. Liu and W. Q. Chao, *Phys. Lett. B* **378** (1996) 23.
- [300] H. Stoecker, *Nucl. Phys. A* **418** (1984) 587.
- [301] J. I. Kapusta, *Phys. Rev. C* **81** (2010) 055201.
- [302] L. V. Bravina *et al.*, *Phys. Rev. C* **78** (2008) 014907.
- [303] A. M. Bamberger *et al.*, *Nucl. Phys. B* **134**, (1978) 1.
- [304] A. Bazavov *et al.*, (HotQCD Collaboration), *Phys. Rev. D* **85**,(2012) 054503.
- [305] S. Gupta, X. Luo, B. Mohanty, H. G. Ritter, N. Xu, *Science* **332** (2011) 1525.
- [306] C. Hong, L. Bo and H. Ze-jun, *Chin. Phys. Lett.* **15** (1998) 787.
- [307] PhD Thesis, Helena de Santos, (NA50 Collaboration), Universidade Técnica de Lisboa-IST, Lisbon, 2004.
- [308] A. Kiseleva *et al.*, CBM Progress Report **2008**, Darmstadt 2009, p. 27.
- [309] S. Ahamad, P. P. Bhaduri *et al.*, paper draft submitted to NIM-A.
- [310] S. Chattopadhyay *et al.*, CBM Progress Report **2009**, Darmstadt 2010, p 28; please also see Muon Chamber Technical Design Report for details.
- [311] I. Smirnov, HEED simulation program for energy loss, St. Petersburg
- [312] I. Kisel, *Nucl Inst and Methods A* **566** (2006) 85.
- [313] R. Kalman *Transactions of the ASME, Journal of Basic Engineering Series D* **82** (1960) 35
- [314] R. Fruhwirth, *Nucl. Inst. and Methods A* **262** (1987) 444
- [315] C. Amstel, *The Review of Particle Physics, Phys. Lett B* **667** (2008)

- [316] W. Press, *Numerical Recipes: The Art of Scientific Computing*, Cambridge Univ Press (2007).
- [317] R. Fruhwirth *et. al.*, *Data analysis techniques in high energy physics*, Cambridge Univ Press (2000).
- [318] A. Lebedev and G. Ososkov, LIT track propagation for CBM , CBM Note (2008).
- [319] www-hades.gsi.de/pluto.
- [320] <http://urqmd.org/documentation/urqmd-3.3.pdf>.
- [321] E.Bratkovskaya,<http://fias.uni-frankfurt.de/brat/hsd.html>.
- [322] G. Borges for NA50 Collaboration, talk given at XXXX-th Rencontres de Moriond, La Thuile, Italy, March 12-19, 2005.
- [323] P. P. Bhaduri and S. Chattopadhyay, CBM Progress Report **2009**, Darmstadt 2010, p. 68.
- [324] V. Singhal, P. P. Bhaduri *et. al.*, CBM Progress Report **2012**, Darmstadt 2013, p. 97.